Fluorine Chemistry in Rechargeable Batteries: Challenges, Progress, and Perspectives

Yao Wang,[†] Xu Yang,[†] Yuefeng Meng,[†] Zuxin Wen, Ran Han, Xia Hu, Bing Sun, Feiyu Kang, Baohua Li,* Dong Zhou,* Chunsheng Wang,* and Guoxiu Wang*
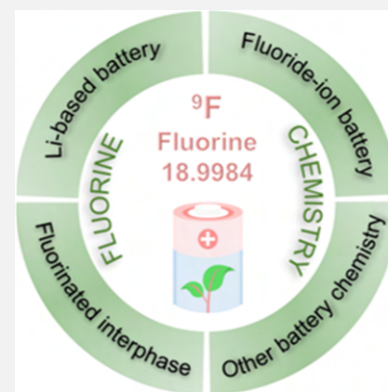
ACCESS | ⬚ Metrics & More | 📖 Article Recommendations

ABSTRACT: The renewable energy industry demands rechargeable batteries that can be manufactured at low cost using abundant resources while offering high energy density, good safety, wide operating temperature windows, and long lifespans. Utilizing fluorine chemistry to redesign battery configurations/components is considered a critical strategy to fulfill these requirements due to the natural abundance, robust bond strength, and extraordinary electronegativity of fluorine and the high free energy of fluoride formation, which enables the fluorinated components with cost effectiveness, nonflammability, and intrinsic stability. In particular, fluorinated materials and electrode|electrolyte interphases have been demonstrated to significantly affect reaction reversibility/kinetics, safety, and temperature tolerance of rechargeable batteries. However, the underlining principles governing material design and the mechanistic insights of interphases at the atomic level have been largely overlooked. This review covers a wide range of topics from the exploration of fluorine-containing electrodes, fluorinated electrolyte constituents, and other fluorinated battery components for metal-ion shuttle batteries to constructing fluoride-ion batteries, dual-ion batteries, and other new chemistries. In doing so, this review aims to provide a comprehensive understanding of the structure–property interactions, the features of fluorinated interphases, and cutting-edge techniques for elucidating the role of fluorine chemistry in rechargeable batteries. Further, we present current challenges and promising strategies for employing fluorine chemistry, aiming to advance the electrochemical performance, wide temperature operation, and safety attributes of rechargeable batteries.

CONTENTS

1. INTRODUCTION

To satisfy the ever-growing demand for energy storage, the development of next-generation rechargeable batteries hinges on advanced materials that possess low cost, abundant resources, long lifespan, and high safety, especially when considering high energy/power density, wide temperature range, and high-voltage operation applications.[1−4] Significant advancements in fulfilling these requirements have been successfully achieved by utilizing fluorine chemistry to redesign the battery configurations/components toward specific targeted applications. It is known that fluorine chemistry research can be traced to 1886 when Henri Moissan first isolated elemental fluorine.[5,6] Over the past century, fluorine chemistry has significantly contributed to technological innovations, which began with the creation of Freon for refrigeration applications in the 1930s.[7,8] Currently, fluorine chemistry has been successfully utilized in various fields, including pharmaceutical/agrochemical industries and fluoropolymer industry. The extraordinary electronegativity of fluorine and the high free energy of fluoride formation endow the fluorides with intrinsic high stability along with non/low flammability (Figure 1a). In addition, as the 13th most abundant element in the Earth's crust (∼585 ppm),[9,10] fluorine (mined as CaF_2) demonstrates an advantage in terms of raw material cost (Figure 1b).[11] However, the availability of resources remains a significant concern for essential elements employed in Li-based electrodes (e.g., Co and Ni are ∼25 and ∼84 ppm in the Earth's crust, respectively).[10] In this context, the integration of fluorine chemistry into battery components and novel configurations is thus a promising avenue for advancing battery technology, which has garnered growing interest among the research community. The rapid development of employing fluorine chemistry in various types of rechargeable batteries necessitates a comprehensive review. However, unlocking fluorine chemistry at the atomic scale presents a big challenge. More importantly, the design principles of fluorinated materials and the mechanistic understandings of fluorinated electrodelelectrolyte interphases as well as their effects on the ionic conductivity and reaction kinetics/stability of charge carriers under extreme conditions (e.g., fast cycling rate, wide temperature range, and high working voltage) have been long overlooked.

In this review, we begin by providing a short overview of the operating mechanisms, characteristics, and current limitations of Li-based batteries along with beyond Li battery chemistry based on either low-cost metal ions or fluorine-containing charge carriers prior to moving into an in-depth and specific discussion of fluorine chemistry in rechargeable battery systems. From the physicochemical and electrochemical properties to the safety aspects related to battery operation, key research progress and technical achievements for the application of fluorine chemistry in battery materials are summarized, spanning from designing fluorine-containing electrodes, fluorinated electrolyte constituents (e.g., conducting salt, cosolvent/solvent, additive), and other fluorinated battery components for metal-ion shuttle batteries (e.g., Li-based batteries) to constructing rechargeable fluoride-ion batteries (FIBs), dual-ion batteries (DIBs), and beyond chemistries. We highlight the relationship between fluorinated materials and battery performance, the characteristics of
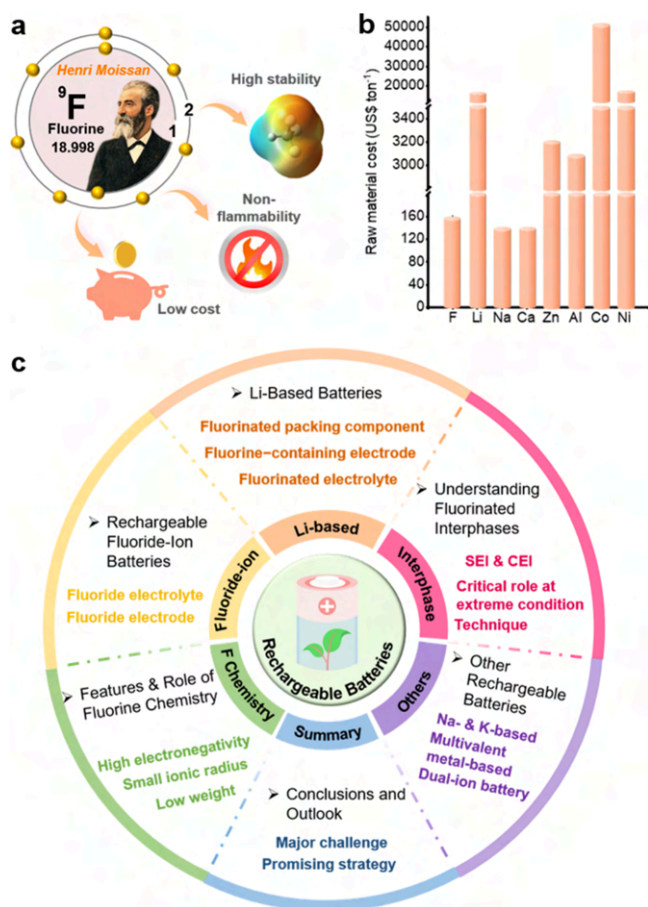
Figure 1. Features and interest of fluorine chemistry for use in rechargeable batteries. (a) Discovery and features of fluorine chemistry. (b) Comparisons of raw material costs of F (mined as CaF_2), Li (Li_2CO_3), Na (Na_2CO_3), Ca (CaO), Zn, Al, Co, and Ni in 2021. Data extracted from ref 11. (c) Schematic diagram of the main aspects covered in this review.

fluorinated interphases, along with the cutting-edge characterization techniques available for elucidating fluorine chemistry. We also identify the current major restrictions and design strategies for utilizing fluorine chemistry toward improving the performance of rechargeable batteries (Figure 1c).

1.1. Brief Background on Rechargeable Li-Based Batteries and Beyond

Since the inception of lithium-ion batteries (LIBs) in the 1970s, extensive work has been conducted on the quest for a higher energy density and longer lifespan, solidifying LIBs as the most promising candidate for many applications. Typically, LIBs rely on the insertion of Li^+ into host structures with a variety of layered oxides (e.g., $LiCoO_2$, $LiFePO_4$, and $LiMn_2O_4$) and graphite as the cathode and anode materials, respectively. They were developed by John B. Goodenough and other researchers over the past four decades.[12] Nevertheless, the energy density of LIBs is expected to reach its intrinsic limits within a few years (around 300 Wh kg^{-1}), which is incapable of satisfying the escalating demands for high energy density.[13] To further increase the energy density, the cathode and anode must offer high specific capacities and a substantial voltage gap between them. For instance, cathode materials with higher capacity and voltage platforms have been developed, such as Li-rich Mn-based materials ($xLi_2MnO_3(1 -$

$x)LiTMO_2$ (TM = Ni, Mn, Co, etc.; $0 < x < 1$)) and Ni-rich $LiNi_xMnyCo_{1-x-y}O_2$ (NMC, $x \geq 0.5$, $x + y < 1$),[14−18] in addition to advanced anodes (e.g., Li metal or Si/C anode) with low reaction potential and ultrahigh specific capacity.[19−30] Unfortunately, these electrode materials usually experience severe capacity fading especially in extreme conditions due to structure deterioration and side reactions. More significantly, safety issues and low Coulombic efficiency (CE) resulting from notorious Li dendrites (in the case of Li metal anode) or Li deposition on the non-Li metal anodes have not been fully addressed. Meanwhile, it is imperative to redesign electrolyte systems that exhibit sufficient antioxidative stability (typically >4.5 V vs Li/Li$^+$), high compatibility toward both electrodes (i.e., robust electrode|electrolyte interphases), excellent temperature tolerance (from −60 to +60 °C), and high safety characteristics (e.g., the risk of fire and explosion), which are critical for adapting to high energy density Li-based batteries.[31]

Alternative rechargeable batteries based on more abundant elements promise higher energy density and improved safety features. Among them, sodium-ion batteries (SIBs) and potassium-ion batteries (PIBs), utilizing the Earth's crust's sixth and seventh most abundant elements, are considered as outstanding complementary technologies to Li-based batteries.[32] Although they have with similar chemistry with Li-based batteries, SIBs and PIBs are facing several challenges due to their larger ionic radii (Shannon ionic radii: 1.02, 1.38, and 0.76 Å for Na^+, K^+, and Li^+, respectively), higher redox potentials (−2.71 V for Na, −2.936 V for K, compared with −3.04 V for Li vs standard hydrogen electrode (SHE)), greater atomic masses (23, 39, and 7 g mol^{-1} for Na, K, and Li, respectively), resulting in low specific capacity, poor rate capability, reduced lifespan, and low theoretical energy density.[33−35] In contrast, multivalent metal-based (e.g., Mg^{2+}, Ca^{2+}, Zn^{2+}, Al^{3+}) batteries offer high energy density and low cost, benefiting from their multielectron redox capability and Earth's crust abundance. However, their larger ionic radii and greater charge density pose great challenges in ion transport, polarization, and reversibility.[36,37]

Anions, as charge carriers, typically offer faster mobilities due to their less effective nuclear charge and corresponding reduced solvation compared to cations with similar absolute charge. This feature has prompted the development of anion shuttle batteries, exemplified by FIBs employing the F$^-$ anion as the charge carrier, which utilize abundant materials to achieve high theoretical energy density.[9,38−42] Specifically, F$^-$ ions are released from the cathode material and transfer to the anode side during discharging, whereas the process occurs in reverse upon charging.[9] The high electronegativity of fluorine imparts the F$^-$ anion with high oxidative stability, facilitating high-voltage redox reactions. The utilization of F$^-$ also contributes to high theoretical energy densities from multiple-electron electrochemical processes,[9,39,43−45] along with dendrite-free anode reactions due to the absence of the metal plating process, highly enhancing safety over alkali metal batteries. Nevertheless, FIBs present several unique challenges, including significant volume changes in electrode materials during fluoridation and defluoridation, contact loss, and interphase degradation. In addition, the electrode dissolution in electrolytes exacerbates self-discharge and capacity decay. More importantly, development of chemically/electrochemically stable electrolytes possessing high room- temperature (RT) conductivity is crucial for FIB commercialization, which is still at an incipient stage.[9]
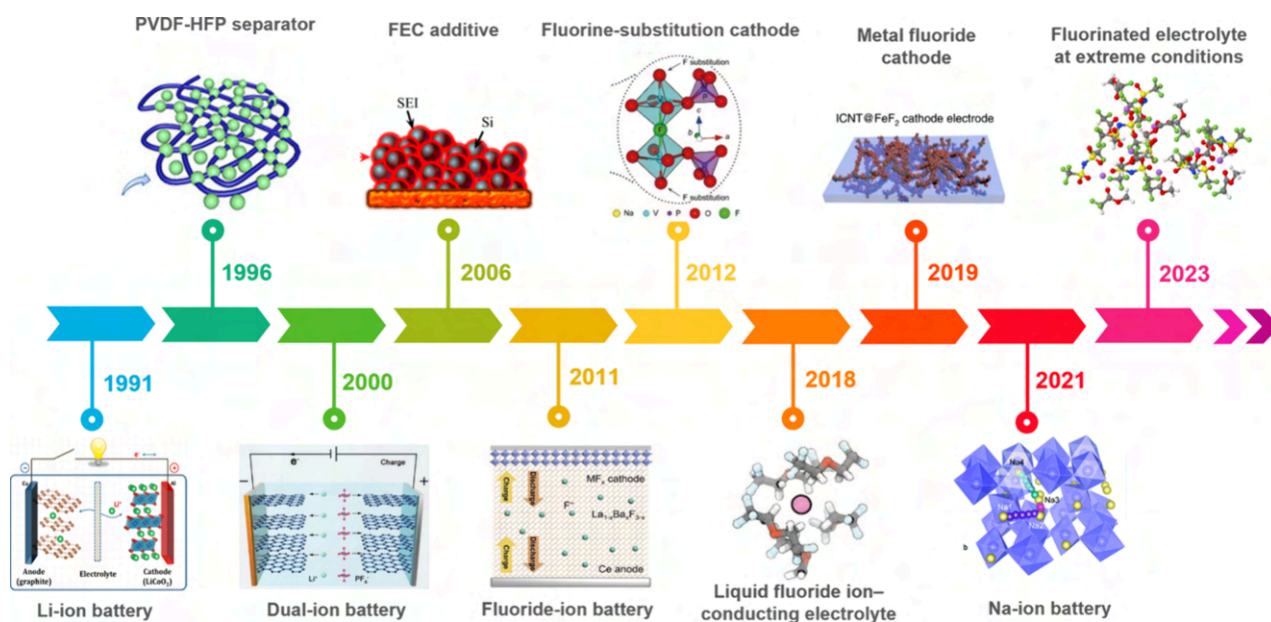
Figure 2. Timeline of the application of fluorine chemistry in rechargeable batteries. Reproduced with permission from ref 48. Copyright 2013 American Chemical Society. Reproduced with permission from ref 49. Copyright 1996 Elsevier. Reproduced with permission from ref 47. Copyright 2021 Wiley-VCH. Reproduced with permission from ref 38. Copyright 2021 Elsevier. Reproduced with permission from ref 50. Copyright 2012 Elsevier. Reproduced with permission from ref 51. Copyright 2006 Elsevier. Reproduced with permission from ref 52. Copyright 2018 American Association for the Advancement of Science. Reproduced with permission from ref 53. Copyright 2019 Springer Nature. Reproduced with permission from ref 54. Copyright 2021 Elsevier. Reproduced with permission from ref 55. Copyright 2023 Springer Nature.

Combining the cation and anion storage, DIBs provide advantages of low cost, material availability, safety, and high voltage. They operate by simultaneously incorporating anions into the cathode and cations into the anode upon charging with both ions being released back into the electrolyte during discharging.[46,47] Particularly, the deinsertion/insertion of anions occurring at high voltage is beneficial for enhancing the energy density. However, the insufficient oxidative stability and poor electrode compatibility of conventional organic electrolytes and the scarcity of electrode materials with high storage capacity and structural stability present substantial obstacles. Furthermore, emerging battery chemistries such as reverse dual-ion batteries (RDIBs) face significant challenges due to the lack of suitable electrolytes, impeding their practical advancement.

1.2. Role of Fluorine Chemistry in Rechargeable Batteries

Fluorine, as the most electronegative element with a comparably low atomic weight, small ionic size (1.33 Å), and natural abundance,[56] drives new levels of performance and safety in rechargeable batteries. To elucidate the role of fluorine chemistry in rechargeable batteries, the key progress and brief development history are presented, as outlined in Figure 2.

Owing to the electron-withdrawing properties of F atoms and the delocalized charge of anions, F-containing Li salts (e.g., lithium hexafluorophosphate, $LiPF_6$) are generally highly soluble in dipolar aprotic solvents with good electrochemical stability at high voltage. The development of these salts for commercial LIBs dates back to the early 1990s,[57−60] but their chemical and thermal instability has prompted the search for alternative conducting salts, usually at the expense of other performance attributes. The utilization of fluorine has been extended to advanced battery components (e.g., separators, binders, current collectors) for Li-based batteries. Efforts can

be traced to 1996, when Tarascon et al. developed a fluorinated polymer (i.e., poly(vinylidenefluoride-hexafluoro-propylene), PVDF-HFP) separator for the first time.[49] After that, fluorinated copolymers and grafted commercial separators by F-containing groups have been intensively utilized, enhancing the oxidation stability, thermal stability, ionic conductivity, and safety for battery operations. Moreover, due to the electron-withdrawing inductive effect, the substitution of fluorine to a hydrogen of electrolyte cosolvent/solvents and additives typically decreases the highest occupied molecular orbital (HOMO) and lowest unoccupied molecular orbital (LUMO) energy levels simultaneously, leading to higher resistance toward oxidation and poorer resistance to reduction.[61−67] Specifically, the prior reduction of fluorinated additives benefits the anode by generating an effective solid electrolyte interphase (SEI),[68−70] among which fluoroethylene carbonate (FEC) stands out as the most popular additive with excellent film-forming ability on various electrodes.[51] Besides the film-forming ability, the introduction of fluorine demonstrates unique physicochemical and electro-chemical properties, including high oxidative stability, wide temperature range, and nonflammability. In particular, fluorinated interphases are pivotal for Li-based batteries under extreme conditions such as wide temperature range, extended cycling, fast cycling rate, and high-voltage operation. Significant progress was reported recently by Wang et al., designing a fluorinated electrolyte that yielded LiF-rich interphases on both the cathode and the anode, which enhanced the battery performance across the temperature range from −60 °C to +60 °C with high-voltage and fast-charging characteristics.[55] Despite advances, electrode materials remain a major bottleneck for energy density enhancement. The highly ionic character of the metal−fluorine bond and the light atom mass of the F element endow fluorinated cathodes with higher voltage and/or higher capacity.[53] Additionally, F-

Table 1. Comparisons of the Electrochemical Performance of F-Based Electrodes for LIBs

electrode materials	discharge voltage vs Li/Li$^+$ (V)	current density (mA g^{-1})	initial discharge capacity (mAh g^{-1})	retained discharge capacity (mAh g^{-1})	capacity retention	cycle number	ref
CuF	2.7	0.106	523	80	15.3%	5	95
FeF$_2$	2.2	0.3	700	525	75%	50	96
Cu$_{0.5}$Fe$_{0.5}$F$_2$	2.5	9.2	580	475	81.9%	5	102
FeF$_2$	2	50	650	450	69.2%	100	53
FeF$_3$	3	2000	92	90	97.8	100	97
Cu$_{0.25}$Ni$_{0.75}$F$_2$	2	0.055	550	210	38.2%	6	98
CoF$_2$	2	100	360	335	93%	200	99
CoF$_3$	1.5	5	1000	400	40%	14	100
MnF$_2$	0.5	6000	300	270	90%	4000	101
VO$_2$F	3	13.1	200	150	75%	50	103
BiOF	2.5	30	343	148	43.1%	40	104
FeOF	2	10	500	355	71%	30	105
TiOF$_2$	2	0.26	200	180	90%	30	106
NbO$_2$F	1.3	30	650	180	27.7%	20	107

related chemistry involved in the modification strategy can improve the interphase stability and rate capability of the electrodes.

Apart from Li-based batteries, fluorine chemistry is integral to other univalent metal-based batteries such as SIBs and PIBs, where the increase of ionic M−X bonds in fluorides promotes redox reactions of transition metal cations instead of oxygen anions at high voltage. The lower molecular weight of the fluorine cation compared to polyanions enhances the specific capacity. Additionally, F-based compounds are considered to be more stable against oxidation, making metal fluorinated materials highly appealing. The diversity in compositions, structures, and properties of fluorinated electrode materials offers vast opportunities for cathode design. On the anode side, F doping improves the surface disorder of carbonaceous materials, creating large amounts of defects for facilitating K$^+$ adsorption.[71] In aqueous multivalent metal-based systems (i.e., Zn-ion batteries, ZIBs), fluorine chemistry enables the formation of fluoride-rich interphases for dendrite suppression and electrolyte stability. In nonaqueous systems, fluorinated materials accelerate plating kinetics in Mg-ion and Ca-ion batteries, thus expediting their practical applications.

Since the first proof-of-concept rechargeable FIB demonstrated by Fichtner et al. in 2011,[43] fluorine chemistry has been utilized in FIB developments, spanning from electrode materials to electrolyte formulations. The F$^-$ anion displays exceptional antioxidation stability, enabling the utilization of high-voltage redox couples. Besides, the F$^-$ storage is typically involved in multiple-electron reactions and metal fluoride formation reactions, which are characterized by substantial Gibbs free energy change, realizing high voltages. As the charge carrier, the F$^-$ anion possesses a smaller ionic radius and lower weight compared to Cl$^-$, thus assisting in fast ionic transport and having a high theoretical energy density of 5000 Wh L^{-1}.[9,39,43,52,72−75] FIBs are experiencing many challenges with electrodes and electrolytes, among which suitable electrolytes with sufficient F$^-$ conductivity is crucial. A significant advancement by Jones et al. in 2018 designed a novel fluoride salt possessing high RT ionic conductivity, a broad electrochemical stability window, and sufficient chemical stability in ether solvents, enabling a reversible/stable FIB at RT.[52] Ongoing efforts should be devoted to developing diverse conversion and intercalation-based electrode materials and fast

F$^-$ conducting electrolytes to make FIBs a promising option for commercial-grade batteries.[76]

As for DIBs, Dahn et al. studied the intercalation mechanism of the PF$_6^-$ anion into graphite cathodes in 2000 for the first time, proving staged phases of graphite via in situ X-ray diffraction (XRD).[77] Various anions with F-containing groups such as PF$_6^-$,[78−81] bis(trifluoromethanesulfonyl)imide (TFSI$^-$),[82,83] bis(fluorosulfonyl)imide (FSI$^-$),[83−86] fluorosulfonyl-(trifluoromethanesulfonyl)imide (FTFSI$^-$),[87,88] tetrafluoroborate (BF$_4^-$),[89,90] difluoro(oxalato)borate (DFOB$^-$),[91] trifluoromethanesulfonic (CF$_3$SO$_3^-$),[92] and tetrafluoroaluminate (AlF$_4^-$)[93] have been extensively explored for their unique characteristics and electrochemical behavior. Besides, fluorination of other electrolyte components in DIBs imparts advantages such as a wide voltage window, a broad temperature range, nonflammability, and enhanced electrode/electrolyte compatibility, enhancing the reversibility/kinetics of anion insertion. Fluorine can also be introduced to cathode materials for boosting and stabilizing the properties of anion intercalation.

2. FLUORINE CHEMISTRY IN LI-BASED BATTERIES

2.1. Fluorine-Containing Electrode Materials

The increasing demands for high energy density batteries with a long lifespan and low cost have prompted the research of advanced electrode materials, especially fluorine-containing materials. This is because fluorine elements are widely distributed on Earth and the strong electronegativity of fluorine endows the fluorine-containing materials with a high free energy of formation, generally leading to a high electrochemical energy density and stability. Here, we present a comprehensive review to reveal the roles of F chemistry in advanced fluoride electrodes and fluorine-doping materials.

2.1.1. Metal Fluorides. Metal fluoride cathodes for LIBs have been widely investigated as a promising next-generation rechargeable battery with high theoretical voltage and energy density owing to the highly ionic metal−fluorine bonding and low atom mass of the F element[94] as well as the multielectron transfer characteristics of the transition metal (M) in metal fluoride cathodes. The battery reaction of metal fluoride-based LIBs follows the following reaction

$$MF_x + xLi = M + xLiF \quad (2)$$
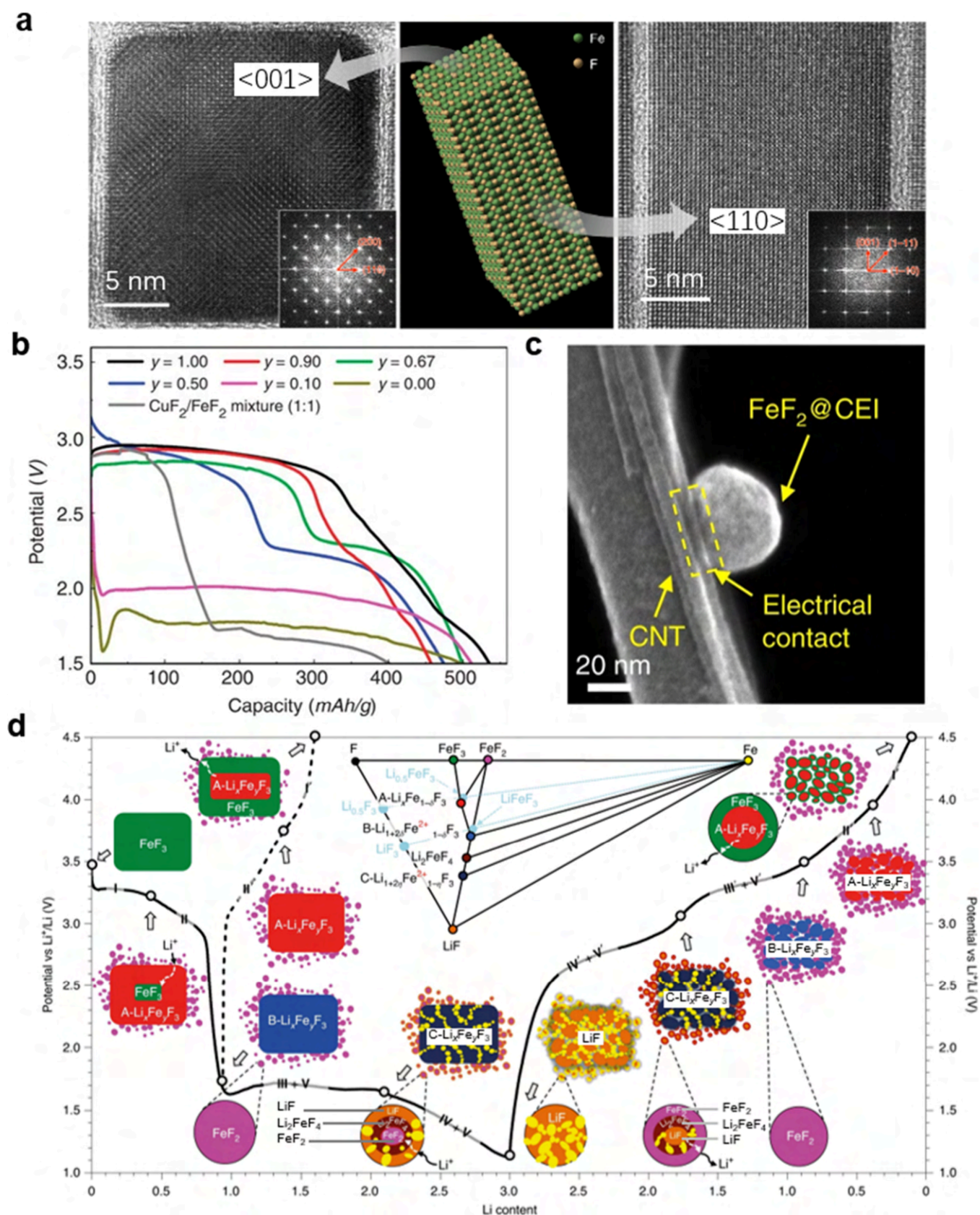
Figure 3. Metal fluorides as electrode materials for LIBs. (a) HRTEM images of a single FeF$_2$ nanorod, and space-filling model of a single nanorod derived from the standard CIF file of FeF$_2$. Reproduced with permission from ref 96. Copyright 2020 Springer Nature. (b) Voltage profiles (first discharge at a current of 5 mA g^{-1}) of the Cu$_y$Fe$_{1-y}$F$_2$ series along with a simple mixture of CuF$_2$ and FeF$_2$. Reproduced with permission from ref 102. Copyright 2015 Springer Nature. (c) Scanning transmission electron microscopy (STEM) image of an FeF$_2$ particle on a single CNT. Reproduced with permission from ref 53. Copyright 2019 Springer Nature. (d) Simplified Li−Fe−F ternary phase diagram, and illustration of the reaction pathways of the FeF$_3$−FeF$_2$ system (with voltage curves for insertion charge and full reaction cycle, respectively, denoted using dashed and

Figure 3. continued

solid lines). The reference phases in the phase diagram are labeled and indicated by light blue circles to show the positions of the A- and B-$Li_xFe_yF_3$, whose Fe concentration is off-stoichiometric. The color of each phase in the phase diagram is consistent with that in the pathway illustration. Impeded external and internal Li transport is indicated by black solid and white dashed arrows, respectively. Reproduced with permission from ref 108. Copyright 2021 Springer Nature.
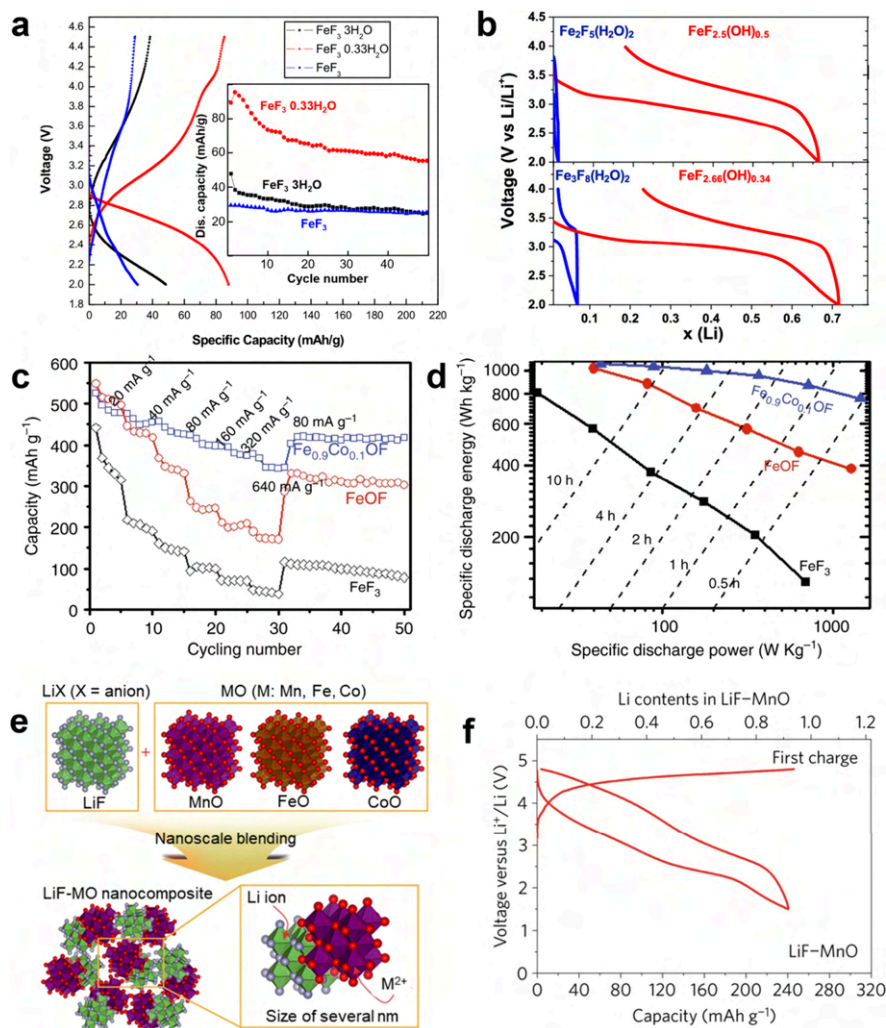
Figure 4. Metal hydroxyfluorides and oxyfluorides for LIBs. (a) Discharge and charge profiles of $FeF_3·3H_2O$, $FeF_3·0.33H_2O$, and anhydrous FeF_3 at 0.5 C. (Inset) Cycling stability curves of $FeF_3·3H_2O$, $FeF_3·0.33H_2O$, and FeF_3 at 0.5 C in the voltage range of 2.0−4.5 V. Reproduced with permission from ref 109. Copyright 2013 Elsevier. (b) First cycle voltage−composition curves for Li/iron fluoride cells in the LP30 electrolyte at 0.05 C. (Upper panel) Comparison of $Fe_2F_5(H_2O)_2$ and $FeF_{2.5}(OH)_{0.5}$. (Lower panel) Comparison of $Fe_3F_8(H_2O)_2$ and $FeF_{2.66}(OH)_{0.34}$. Reproduced with permission from ref 110. Copyright 2019 American Chemical Society. (c) Rate capability for $Fe_{0.9}Co_{0.1}OF$, FeOF, and FeF_3 cathode materials. (d) Ragone plot of FeF_3, FeOF, and $Fe_{0.9}Co_{0.1}OF$ (based on active mass). Reproduced with permission from ref 111. Copyright 2018 Springer Nature. (e) Schematic of the positive electrode material design strategy using metal monoxide (MO). Metal monoxides that had electrochemical activity only as the negative electrode were designed as a positive electrode material by forming mixtures with LiF in nanoscale under high-energy ball milling. After mechanochemical mixing, LiF and MO exist without chemical reaction in the several nanometer scale. The crystal structure of all compounds is described by a polyhedral image: red, O; gray, F; green, Li; purple, Mn; brown, Fe; blue, Co. (f) First discharge and second charge profiles of LiF−MnO nanocomposites after the initial activating charge protocol as a positive electrode (1.5−4.8 V) in 1 M $LiPF_6$ in ethyl carbonate/dimethyl carbonate (EC/DMC, 1:1 by volume) electrolyte at a 20 mA g^{-1} (0.03 mA cm^{-2}) constant current rate. Reproduced with permission from ref 112. Copyright 2017 Springer Nature.

Abundant types of metal fluorides, including copper fluorides (CuF_2),[95] iron fluorides (FeF_3/FeF_2),[53,96,97] nickel fluorides (NiF_2),[98] cobalt fluorides (CoF_3/CoF_2),[99,100] and manganese fluorides (MnF_2),[101] and multimetal fluoride solid−solutions have been investigated, and their attractive merits in terms of specific capacity, cycling stability, and rate performance have been verified (Table 1).

Iron(II) fluoride is a typical metal fluoride cathode for LIBs owing to its high theoretical specific capacity and abundant raw material resources.[96] However, the performance of the as-reported iron(II) fluoride cathode is not satisfactory for practical application, and the failure mechanism remains blurred. In 2020, Pasta and colleagues reported a single-crystalline, monodisperse FeF_2 nanorod synthesized by a facile

colloidal method.[96] As shown in Figure 3a, the as-obtained 20 nm wide nanorods were single crystalline, monodisperse, and faceted. This FeF_2 cathode can deliver a high specific capacity (close to the theoretical value of 570 mA h g^{-1}) and cycling stability (capacity retention > 90%) for more than 200 cycles at higher rates (0.5 C, 1 C = 570 mA g^{-1}) and temperatures (50 °C) within an ionic liquid electrolyte. Based on the complex morphological features, lattice orientation relationships, and oxidation state changes from high-resolution transmission electron microscopy (HRTEM) analysis, the transformation mechanism of the FeF_2 nanorod was comprehensively estimated. This mechanism provided a new expiation that the phase evolution, diffusion kinetics, and cell failure were all critically affected by surface-specific reactions of the FeF_2 nanorod. Topotactic cation diffusion through an invariant lattice of F$^-$ ions and the nucleation of metallic particles on semicoherent interphases synergistically affected the reversibility of the FeF_2 cathode.

Feng and colleagues developed a ternary metal fluoride ($Cu_yFe_{1-y}F_2$ solid solution) via a mechanochemical reaction method.[102] Synchrotron XRD and TEM characterization verified the distorted rutile structure of $Cu_yFe_{1-y}F_2$ solid−solution in the form of complex agglomerates composed of small nanocrystallites under different Cu/Fe ratios (y = 0, 0.1, 0.33, 0.5, 0.67, 0.9, 1). In the corresponding discharge voltage profiles in Figure 3b, no typical voltage dip of pure FeF_2 was found. This indicated that the electrochemical properties of $Cu_yFe_{1-y}F_2$ solid−solution was significantly affected by the cooperative redox of Cu and Fe sitting on the same lattice. This ternary metal fluoride $Cu_yFe_{1-y}F_2$ achieved the reversible Cu redox reaction (Cu$^{2+/0}$) with a low-voltage hysteresis (<148 mV), which was uncommon in binary fluorides. The thermodynamics and kinetics of the lithium (re)conversion reactions following a two-stage (de)lithiation path of $Cu_yFe_{1-y}F_2$ were supported by X-ray absorption spectroscopy (XAS) and TEM-electron energy loss spectrometer (EELS) characterization. Initially, Cu^{2+} reduces into metallic Cu^0 with the concomitant formation of disordered FeF_2 followed by Fe$^{2+/0}$ reduction. In contrast, the delithiation path undergoes a different process, where Fe^0 is partially oxidized to Fe^{3+} as a rutile framework followed by the reconversion of Cu^{2+} to form a disordered rutile-like Cu−Fe−F final phase. This work promotes the development of Cu-based ternary metal fluorides as promising cathode candidates for LIBs. However, the reversible specific capacity of Cu conversion faded rapidly, which can be ascribed to the Cu$^+$ dissolution on the cathode−electrolyte interphase (CEI). Thus, construction of a stable CEI layer is one of the strategies to improve the cycling stability of metal fluoride cathodes in LIBs. Accordingly, Yushin and co-workers introduced solid polymer electrolytes (SPEs) to pair with a carbon nanotube (CNT)@FeF_2 composite cathode.[53] The obtained solid-state cells delivered a high specific capacity of more than 450 mAh g^{-1} and a long cycle stability of over 300 cycles at 50 mA g^{-1} and 50 °C. The introduction of SPE not only prompted the formation of an elastic, thin, and stable CEI on the FeF_2 surface (Figure 3c) but also reduced the electrolyte decomposition and maintained the cathode structural stability due to the enhanced mechanical properties. This work motivated research on the CEI, which will guarantee an improved lifespan of the metal fluoride cathode with merits of low cost and high energy density.

Although it has been widely accepted that metal fluorides are conversion-type cathodes for LIBs, Gray and colleagues demonstrated a different viewpoint of reaction mechanisms in metal fluoride cathodes.[108] The material structure was well measured by X-ray total scattering and electron diffraction techniques over multiple length scales and analyzed by density functional theory (DFT) calculations. The results indicated that the mobility difference of displaced species affected the diffusion rate during the (de)lithiation of metal fluorides. The illustration of the reaction pathways of the FeF_3 system is demonstrated in Figure 3d. During a typical lithiation process, FeF_3 initially transforms into FeF_2 and a cation-ordered and stacking-disordered phase (A-Li$_x$Fe$_y$F$_3$) on the surface of the cathode particles; then, the transition phase product successively converts into B-, C-Li$_x$Fe$_y$F$_3$ and ends in LiF and Fe as the final discharge products. The subsequent delithiation process follows a reversible pathway. This new mechanistic principle provides a reference model to develop more isomorphic metal fluorides as cathodes for high energy density LIBs.

2.1.2. Metal Hydroxyfluorides and Oxyfluorides. Metal fluoride hydrates have also been investigated as cathode materials for LIBs. In 2013, Wang and co-workers synthesized a series of iron fluoride hydrates with different hydration water contents via the liquid-phase method.[109] Pure crystalline $FeF_3 \cdot 3H_2O$, $FeF_3 \cdot 0.33H_2O$, and FeF_3 were obtained during the dehydration process at increasing calcination temperature, which was verified by the XRD patterns and their Rietveld refinements. When applied in liquid LIBs, the orthorhombic $FeF_3 \cdot 0.33H_2O$ cathode delivered the highest discharge specific capacity of 88.0 mAh g^{-1} and the lowest polarization among all three samples (Figure 4a). The authors attributed this better electrochemical performance of $FeF_3 \cdot 0.33H_2O$ to its huge hexagonal cavity for faster Li$^+$ transfer. These iron fluoride hydrates were simply ball milled with acetylene black to form high electronic conductive composite cathodes, and the initial discharge specific capacity of the $FeF_3 \cdot 0.33H_2O$/C cathode was improved to 177.6 mAh g^{-1} at 0.1 C (1 C = 237 mA g^{-1}) with a high retention of 83.8% after 100 cycles. This reveals that optimization of the crystal structure is important in the development of high-performance metal fluoride hydrate cathodes for LIBs.

Later, in 2019, Lhoste and colleagues further investigated the structural effects of iron hydroxyfluorides as cathodes in LIBs.[110] First, two anion-deficient iron fluoride hydrates $Fe_2F_5(H_2O)_2$ and $Fe_3F_8(H_2O)_2$ were synthesized by a facile microwave synthesis method, which were unstable under the ambient atmosphere. After special heating treatments, two stable iron hydroxyfluorides $FeF_{2.5}(OH)_{0.5}$ (pyrochlore structure) and $FeF_{2.66}(OH)_{0.34}$ (hexagonal tungsten bronze structure) were obtained. When applied as cathodes in LIBs, the dehydrated iron hydroxyfluorides delivered a higher reversible specific capacity than their hydrated opponents (Figure 4b). The structure analysis by XRD and Mössbauer spectrometry proved that removal of structural water molecules within the hexagonal cavities opened the Li diffusion channels for the battery cycling process.

Metal oxyfluorides, such as VO_2F,[103] BiOF,[104] FeOF,[105,111] $TiOF_2$,[106] and NbO_2F[107] (Table 1), have shown great potential as cathodes for LIBs owing to their high specific capacity, high voltage, good conductivity, and good cycling stability.[113] The battery reaction of metal oxyfluoride (MO_xF_y)-based LIBs follows the following reaction:

$$MO_xF_y + (2x + y)Li \leftrightarrow M + xLi_2O + yLiF \qquad (3)$$
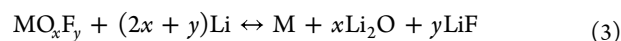
In 2018, Wang and coauthors reported a cobalt-doped iron oxyfluoride ($Fe_{0.9}Co_{0.1}OF$) synthesized by a solvothermal method.[111] The specific capacity of $Fe_{0.9}Co_{0.1}OF$ was much higher than that of the pristine FeOF and FeF_3 (Figure 4c), achieving a high energy density of ~1000 Wh kg^{-1} (Figure 4d). This $Fe_{0.9}Co_{0.1}OF$ cathode delivered a high specific capacity of 350 mAh g^{-1} for 1000 cycles at 500 mA g^{-1}, and the voltage hysteresis was reduced to 0.27 V. Combined with TEM techniques, pair distribution function (PDF) analysis, and first-principles calculations, the author verified that the reaction kinetics of $Fe_{0.9}Co_{0.1}OF$ was enhanced by the cosubstituted anion (O) and cation (Co) in $Fe_{0.9}Co_{0.1}OF$. In this case, the less reversible conversion reaction was replaced by a highly reversible intercalation−extrusion reaction due to the decrease in particle size and abundance of metallic Fe(Co). Hence, this cosubstitution strategy inspired the development of other conversion-type electrode materials with similar reversibility problems.

Unlike the crystalline oxyfluorides, Kang and colleagues reported a special LiF−metal monoxide (MO, M = Mn, Fe, Co) nanocomposite as a Li-free cathode for LIBs,[112] which was synthesized by blending the transition metal monoxides and nanosized lithium fluoride in a high-energy ball miller under an argon atmosphere (Figure 4e). This cathode material delivered a high specific capacity after the first charging step with a high voltage (e.g., average voltage of 3.1 V for LiF−MnO, Figure 4f). In contrast with the conventional Li intercalation, the reaction mechanism of the LiF−MO nanocomposite cathode can be ascribed to a surface conversion reaction as follows:

$$MO + LiF \leftrightarrow MOF + Li \qquad (4)$$

Moreover, the performance of the LiF−MO nanocomposite cathode can be further improved by decreasing the particle size of the metal compounds. This novel mechanism is expected to be expanded to other transition metal compounds and Li salt couples for advanced cathode materials in LIBs.

2.1.3. Fluorine-Substitution Electrode Materials. To achieve higher electrochemical performance, fluorides are added to electrodes to improve the properties of the original cathode materials. Silver vanadium oxide ($Ag_2O \cdot xV_2O_5$) has been commercialized as a cathode material in primary Li batteries for high-rate applications. The increase of the Ag:V ratio can extend the high-voltage plateau but is accompanied by poor kinetics and low conductivity. In 2005, Poeppelmeier and colleagues reported the synthesis of single crystals of $Ag_4V_2O_6F_2$ ($Ag_2O \cdot V_2O_5 \cdot 2AgF$) via a low-temperature hydrothermal technique.[114] Introduction of the AgF phase increased the Ag:V ratio and the reaction potential of the cathode. At the same time, the dimensionality of the vanadium oxide framework was partially reserved (Figure 5a), which served as the Li-ion conduction pathway between vanadium centers. Therefore, the $Ag_4V_2O_6F_2$ cathode delivered an enhanced initial discharge plateau and higher specific capacity above 3 V (3.52 V and 148 mAh g^{-1}) compared to the undoped silver vanadium oxides (3.22 V and 100 mAh g^{-1}, Figure 5b).

The strategy of fluoride doping can also multiply the rate energy density and performance of the cathode material. The low electronic conductivity and limited specific capacity are the main drawbacks of conventional polyanion compound cathodes,[117] including $LiFePO_4$ phosphates, $LiMBO_3$ borates, Li_2MSiO_4 silicates, and $Li_2Fe(SO_4)_2$. In 2015, Kang and co-workers reported a fluorinated polyanion compound cathode ($LiVPO_4F$) for LIBs,[115] which was synthesized by a scalable
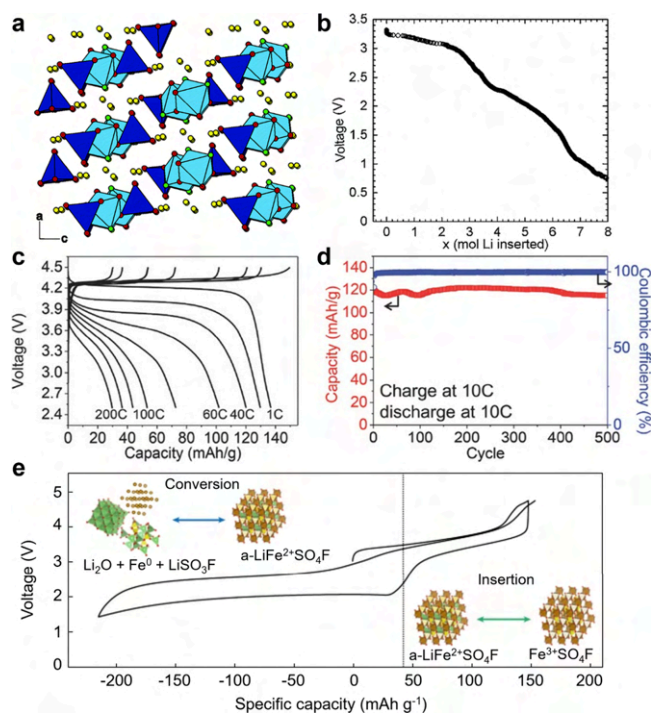
Figure 5. Fluoride-containing electrode materials. (a) Three-dimensional packing diagrams of $Ag_4V_2O_6F_2$. Yellow spheres represent silver atoms, vanadium oxide fluoride octahedra are in light blue, and vanadium oxide tetrahedra are in dark blue. (b) Constant current discharge curve of $Ag_4V_2O_6F_2$. Reproduced with permission from ref 114. Copyright 2005 American Chemical Society. (c) Charge/discharge voltage profiles of C-coated $LiVPO_4F$ at various rates (right to left: discharging at 1, 20, 40, 60, 80, 100, 120, 150, and 200 C and charging at 1 C without a voltage hold). (d) Capacity retentions at 10 C charge/10 C discharge for 500 cycles. The cutoff voltage was 2.5−5 V (only for cycle retention). Reproduced with permission from ref 115. Copyright 2015 Wiley-VCH. (e) Charge/discharge profile with a schematic of the two-step reaction mechanism of a-$LiFeSO_4F$ as insertion and conversion reactions. Reproduced with permission from ref 116. Copyright 2022 Springer Nature.

single-step solid-state reaction. As shown in Figure 5c, the Li‖$LiVPO_4F$ cell achieved superior rate capability up to 200 C with low polarization and maintained a high specific capacity of ~120 mAh g^{-1} at 10 C for 500 cycles with >95% retention efficiency (Figure 5d). Owing to its higher operating voltage (>3.45 V), $LiVPO_4F$ can achieve a higher energy density (~521 Wh g^{-1} at 20 C, 1 C = 158 mA g^{-1}) than $LiFePO_4$. The smaller particle size, negligible number of antisite defects, and minimal surface oxidation endowed this $LiVPO_4F$ cathode material with remarkable rate capability and energy density, overwhelming the commercial $LiFePO_4$ cathode materials.

Moreover, fluorosulfates such as $LiFeSO_4F$[118] and Li-$(Fe_{1-\delta}Mn_\delta)SO_4F$[119] have been investigated as cathode materials for LIBs for decades owing to the low cost and the abundant distribution of these transition metal elements on Earth. However, the low gravimetric specific capacity of the heavy polyanion group in the cathode materials restricts its commercial application. In 2022, Kang and colleagues reported an amorphous iron fluorosulfate (a-$LiFeSO_4F$) synthesized by a simple ball-milling process of LiF and $FeSO_4$.[116] This fluoride-doping polyanion cathode demonstrated a high specific capacity of 360 mAh g^{-1} with ~98.6% specific capacity retention after 200 cycles even at 60 °C. With an average
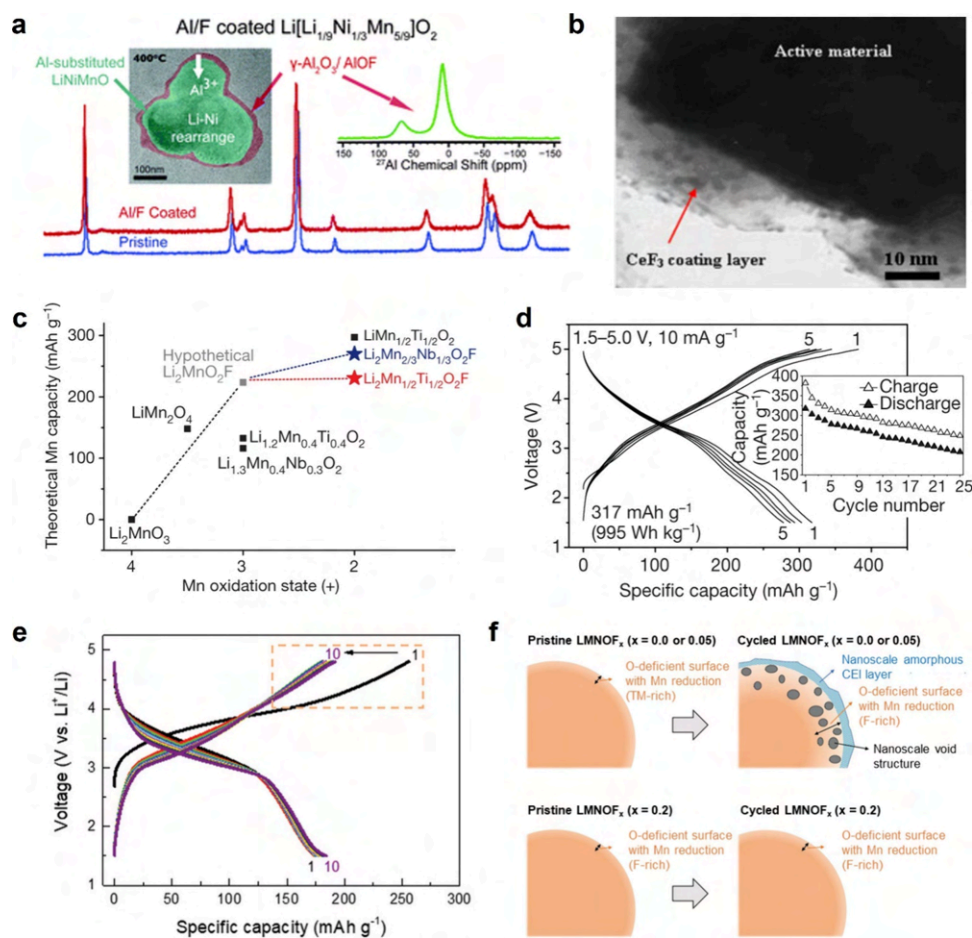
Figure 6. F-modified electrode materials. (a) Powder XRD pattern, TEM images, and ^{27}Al NMR spectra of pristine and Al/F-coated Li[Li$_{1/9}$Ni$_{1/3}$Mn$_{5/9}$]O$_2$. Reproduced with permission from ref 121. Copyright 2012 Royal Society of Chemistry. (b) TEM image of 2 wt % CeF$_3$-coated Li[Li$_{0.2}$Mn$_{0.54}$Ni$_{0.13}$Co$_{0.13}$]O$_2$. Reproduced with permission from ref 122. Copyright 2014 Elsevier. (c) Theoretical Mn redox capacity of various Mn-based cathode materials. (d) Voltage profiles and capacity retention of Li$_2$Mn$_{2/3}$Nb$_{1/3}$O$_2$F under 1.5−5.0 V, 10 mA g^{-1}. Reproduced with permission from ref 123. Copyright 2022 Springer Nature. (e) Voltage profiles at a higher voltage region during the first 10 cycles for LMNOF$_{0.2}$. (f) Schematics summarizing the observation of the structural and chemical evolutions in the LMNOF$_x$ cathode particles. (Upper panel) For the LMNOF$_x$ cathodes with zero or low F concentration (x = 0, 0.05), the cycling process leads to the formation of nanoscale amorphous CEI layers on the surface and void-like nanoregions featuring severe loss of O, Mn, and Li at the subsurface, all of which can be detrimental to Li transport. (Lower panel) For the LMNOF$_x$ cathodes with high F concentration (x = 0.2), the crystalline structure at the cathode surface and the stoichiometric elemental distribution at the subsurface is mostly well preserved after cycling, which ensures facile Li transport at the surface. Reproduced with permission from ref 124. Copyright 2021 Wiley-VCH.

discharge voltage of ∼2.52 V, a high energy density of 906 Wh kg^{-1} was achieved by a-LiFeSO$_4$F cathode. Different from the conventional crystalline polymorphic LiFeSO$_4$F, the a-LiFe-SO$_4$F with a unique inherent amorphous structure underwent a three-electron redox reaction based on combined intercalation and conversion (Figure 5e), which maintained intact structural integrity for reversible cycle stability. This multimechanistic lithiation process of the amorphous intercalation material is promising for the development of high-capacity and low-cost cathodes for LIBs.

2.1.4. Fluorinated Surface Modification. F-modification technologies such as fluoride coating and fluorine substitution are widely used to improve the performance of conventional oxide-based cathodes for LIBs. The high electronic and ionic resistance caused by unstable CEI limits the rate capability and cycle life of Co-free layered oxide cathode materials.[120] In 2012, Grey and coauthors investigated the coating strategy of a layered Li[Li$_{1/9}$Ni$_{1/3}$Mn$_{5/9}$]O$_2$ cathode processed by the commercial aluminum fluoride (AlF$_3$) aqueous suspension

and followed by heat treatment.[121] As shown in Figure 6a, the XRD, TEM, energy-dispersive X-ray (EDX), and ^{27}Al nuclear magnetic resonance (NMR) results proved that a uniform layer of fluorinated amorphous aluminum oxide (Al$_2$O$_3$) was successfully coated on the surface of the cathode material. The Li[Li$_{1/9}$Ni$_{1/3}$Mn$_{5/9}$]O$_2$ cathode with a low coating layer (1 mol % Al/F) delivered a specific capacity of 215 mA h g^{-1} with a cutoff charging voltage of 4.6 V. Zhang and co-workers reported an amorphous CeF$_3$-coated layered lithium-rich oxide cathode via a facile chemical deposition method.[122] A 10 nm thick CeF$_3$ layer (2 wt %) was evenly deposited on the surface of Li$_{1.2}$Mn$_{0.54}$Ni$_{0.13}$Co$_{0.13}$O$_2$ cathode particles (Figure 6b). This CeF$_3$-coated cathode demonstrated a higher capacity retention (97.1%) than that of the pristine sample (82.1%) after 50 cycles. Additionally, the rate performance of the CeF$_3$-coated cathode also surpassed that of the pristine sample at 1250 mA g^{-1} (103.1 vs 82.2 mAh g^{-1}). The authors attributed the outstanding enhancement to this amorphous CeF$_3$ coating layer, which effectively hindered the continuous decomposition
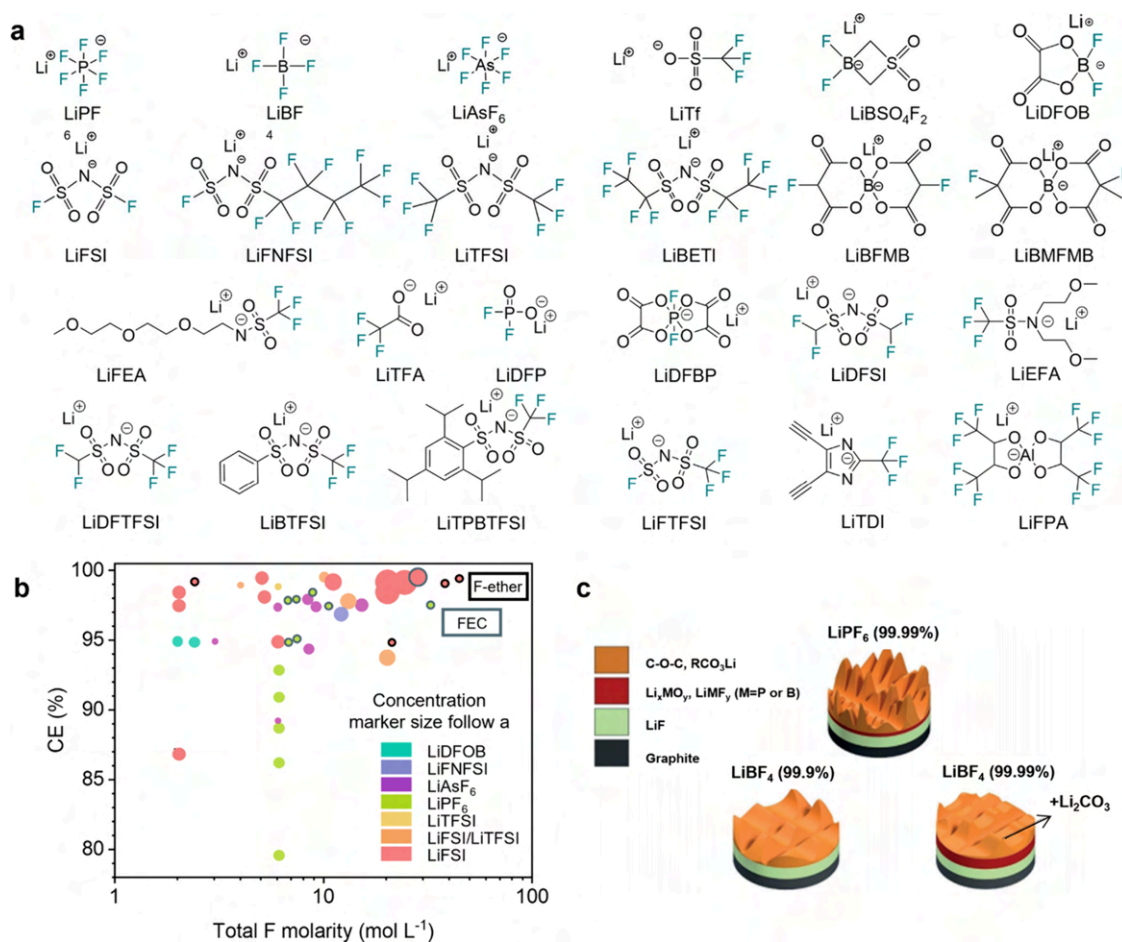
Figure 7. Fluorinated salts for Li-based batteries. (a) Structural formulas of the different Li salts. (b) CEs of Li||Cu cells with Li salts of different F molarity. Reproduced with permission from ref 24. Copyright 2021 Springer Nature. (c) Schematic illustration of the SEI film obtained from electrolyte formulations based on $LiPF_6$ (99.99% battery grade purity), $LiBF_4$ (99.9% purity), and $LiBF_4$ (99.99% battery grade purity). Reproduced with permission from ref 131. Copyright 2013 Elsevier.

of the electrolyte on the cathode surface, thus controlling the growth of the insulated passivated interlayer and maintaining the structural stability of the cathode.

The fluorine substitution strategy was also utilized to improve the performance of electrode materials for LIBs. In 2018, Ceder and colleagues reported Co/Ni-free disordered-rocksalt Li-rich intercalation cathodes $Li_2Mn_{2/3}Nb_{1/3}O_2F$ realized by the partial substitution of the fluoride anion and high-valent cation,[123] which have a Mn^{2+}-involved theoretical specific capacity of 270 mAh g^{-1}, much higher than that of a typical Mn-based Li-rich cathode (Figure 6c). As shown in Figure 6d, this cathode delivered a high discharge specific capacity of 317 mAh g^{-1} and reached a state-of-the-art high-energy content of 995 Wh kg^{-1} (3761 Wh l^{-1}) due to the high amount of Mn^{2+}/Mn^{4+} redox couples combined with a small amount of O redox reactions. Giving rise to this strategy, the structural stability of the Mn-based Li-rich cathode was not affected by the extensive O redox, thus leading to high cathode performance.

The surface stability of disordered rocksalt cathodes can also be enhanced by fluorine substitution. Wang and coauthors unveiled the relationship between high-level fluorine sub-stitution and good surface stability.[124] The Mn-based disordered rocksalt cathodes with various fluorine substitutions ($Li_{1.2}Mn_{0.6+x/2}Nb_{0.2-x/2}O_{2.0-x}F_x$, LMNOF$_x$, x = 0−0.2) were synthesized and compared in terms of electrochemistry and

characterization. The cycling stability of the LMNOF$_x$ cathode was significantly improved by increasing the F content from 0 to 0.2, while the O redox peaks nearly disappeared (Figure 6e). The results demonstrated that the increased fluorine substitution level in the disordered rocksalt cathode reduced the amorphous CEI layers at the top of the cathode surface, prevented damage to the internal crystal structure of the cathode, and maintained the uniform chemical distribution at the subsurface of the cathode particles (Figure 6f).

Fluorine chemistry is crucial in the development of Li-based batteries with high energy density and reversibility. High-voltage metal fluoride and oxyfluoride electrodes show great promise to improve the energy densities of Li-based batteries. In particular, metal fluorides based on multiple electron transfer reactions are expected to address the limitations of conventional cathode materials in LIBs.

2.2. Fluorinated Electrolytes

Electrolytes play a particularly essential and complex role in LIBs and Li metal batteries (LMBs). As the battery component is in contact with other active and passive parts of the battery, the electrolyte must fulfill the following requirements: a high degree of Li-ion conductivity, good thermal and chemical stability, electronic insulation to avoid self-discharge, relative nontoxicity to avoid environmental hazards, and low cost. Commonly used commercial electrolytes consist of a
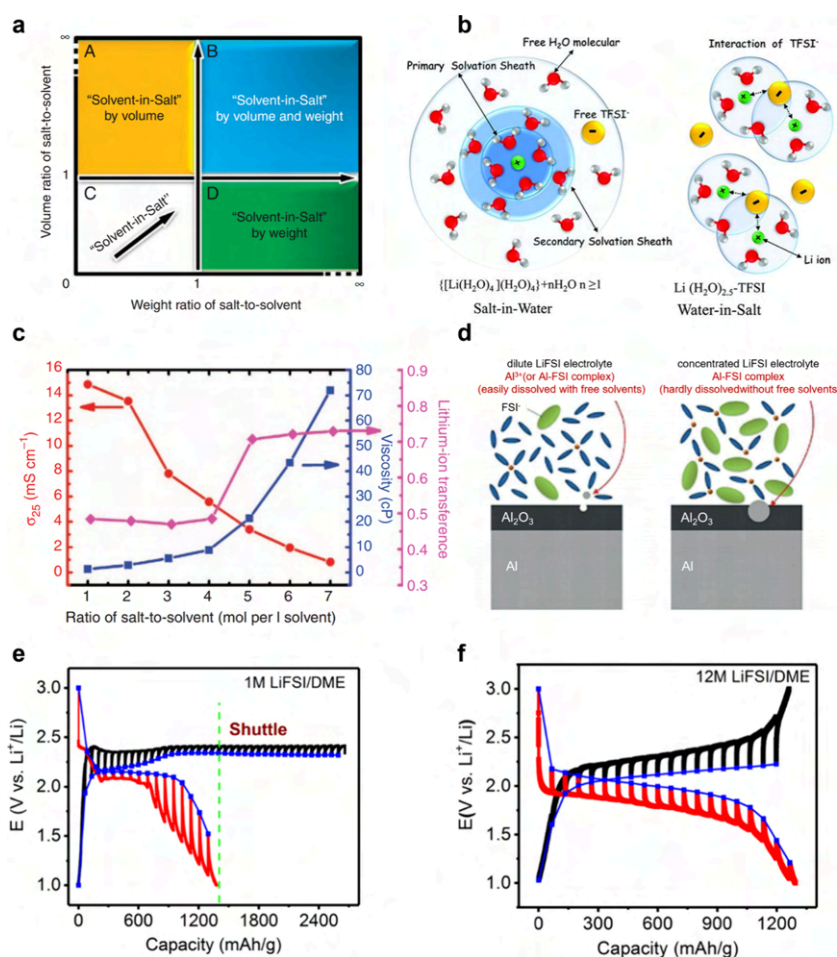
Figure 8. Electrolytes for Li-based batteries with highly concentrated fluorinated salts. (a) Classification of electrolytes according to the volume ratio and weight ratio. Reproduced with permission from ref 132. Copyright 2013 Springer Nature. (b) Schematic diagram of water-in-salt electrolyte. Reproduced with permission from ref 135. Copyright 2015 American Association for the Advancement of Science. (c) Viscosity, ionic conductivity, and Li-ion transference number at room temperature for the various electrolytes. Reproduced with permission from ref 132. Copyright 2013 Springer Nature. (d) Schematic illustrations of the behavior of Al current collectors in a dilute LiFSI/acetonitrile (AN) electrolyte (left) and a highly concentrated LiFSI/AN electrolyte (right) with little free solvent molecules and free FSI⁻ anions. Reproduced with permission from ref 136. Copyright 2015 Wiley-VCH. GITT curves (e) in 1 M LiFSI/DME electrolyte and (f) in 12 M LiFSI/DME electrolyte. Reproduced with permission from ref 137. Copyright 2018 Elsevier.

conductive Li salt (usually $LiPF_6$) and an organic solvent mixture of cyclic and linear organic carbonates. The salt−solvent−additive combination determines the overall performance of rechargeable Li batteries, such as conductivity, thermal stability, and electrochemical stability. However, demand for higher voltage Li batteries has forced researchers to look for new electrolyte formulations, including solid electrolytes, as current liquid electrolytes are unstable at potentials higher than 4.5 V and exhibit safety concerns. Power batteries typically contain high-energy active electrode materials, which tend to easily react with other elements, rendering the combination unusable. The fluoridation of electrolyte components is a key strategy for advanced electrolyte engineering, which can enhance the electrode reaction reversibility, extend the battery life, and reduce the electrolyte flammability.

2.2.1. Fluorinated Salts. Li salts act as the conductor of Li ions in the electrolyte, and the nature of the Li salts is often determined by the structure of the anions. As shown in Figure 7a, F substitution is widely applied in Li salts for LIBs and LMBs. The presence of fluorine atoms and the delocalized charge of the anions make such F-containing Li salts highly

soluble in dipolar aprotic solvents.[125] For battery applications, Li salts need to possess characteristics such as a low molecular weight, low toxicity, stability over a wide electrochemical stability window (ESW), as well as electrolyteIelectrode interphase formation ability. Among the F-substituted Li salts, $LiPF_6$ and Li sulfonate salts are the most widely used. $LiPF_6$ salt exhibits the advantages of high ionic conductivity, good passivation ability for Al collectors, and high oxidation stability, etc. However, the $LiPF_6$ salt has a serious disadvantage of high sensitivity to water, which is easily decomposed to produce HF and cause serious corrosion to the electrodes and the whole battery.[126] For comparison, benefiting from the presence of strong perfluoroalkyl electron-absorbing groups and conjugated structures leading to the delocalization of negative charges, the anion of Li sulfonate salts is relatively stable. Thus, Li sulfonate salts show the advantages of good thermal stability, high solubility, insensitivity to moisture, high dissociation constants, etc. However, severe Al foil dissolution occurs when charged to high voltage.[127] Furthermore, it is crucial to note that Li sulfonate salts, which contain −CF_2− and/or −CF_3 functional
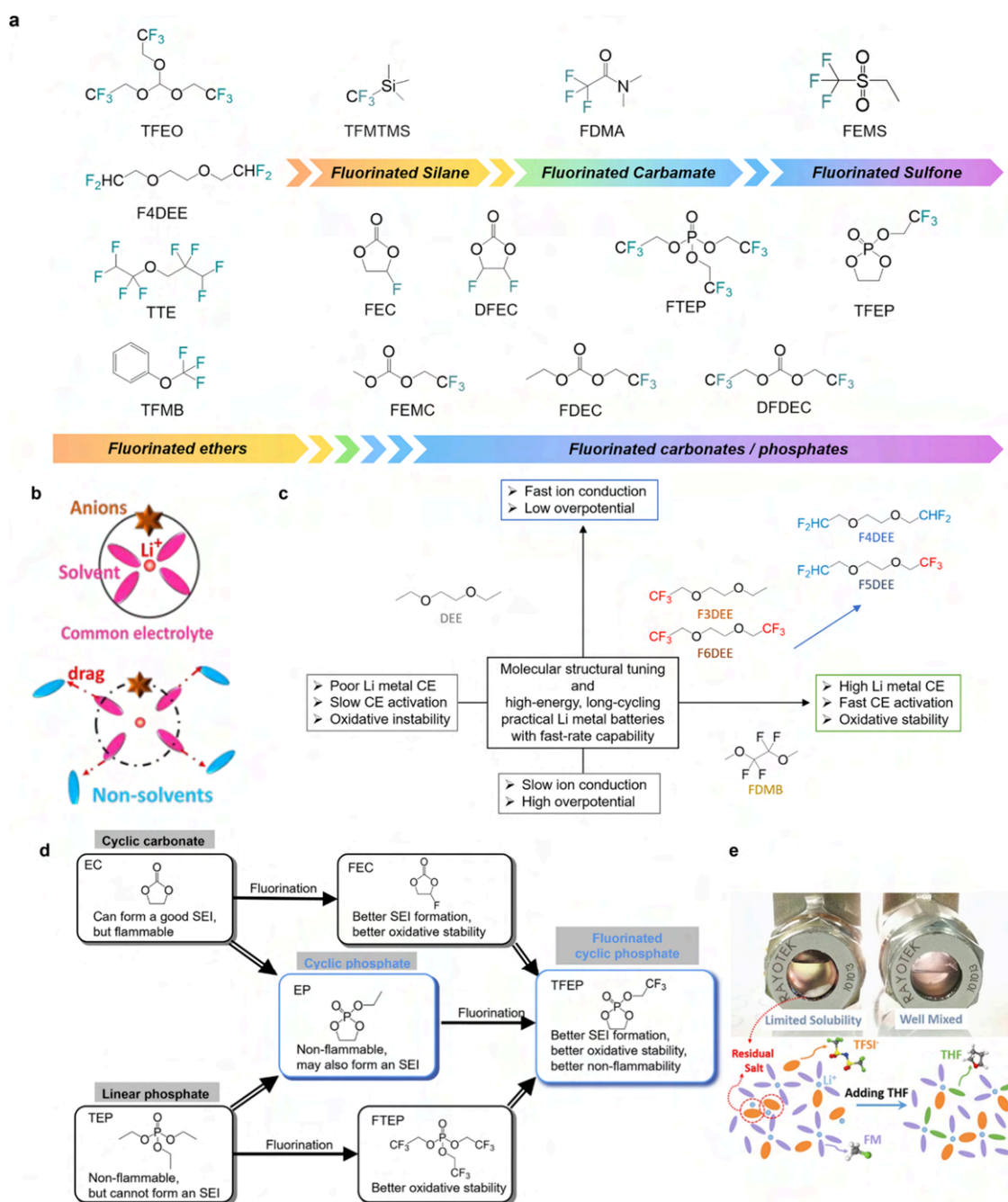
Figure 9. Fluorinated solvents and cosolvents. (a) Molecular structures of representative fluorinated solvents. (b) Established solvation structures of common diluent electrolyte, localized high-concentration electrolyte (LHCE), and nonsolvent-added electrolyte and their desolvation processes. Reproduced with permission from ref 149. Copyright 2023 Royal Society of Chemistry. (c) Optimization of ether electrolytes toward fast ion conduction, low overpotential, high Li metal efficiency, fast CE activation, and high oxidative stability. Reproduced with permission from ref 150. Copyright 2022 Springer Nature. (d) Design of the fluorinated cyclic phosphate solvent to achieve better SEI formation, better oxidation stability, and better nonflammability. Reproduced with permission from ref 151. Copyright 2020 Wiley-VCH. (e) Photographs of solubility tests in window cells of 0.1 M LiTFSI in FM (left) and 0.3 M LiTFSI and 0.3 M THF in FM (right). Reproduced with permission from ref 152. Copyright 2019 Elsevier.

groups, potentially pose environmental risks during production and utilization. Thus, strategies to mitigate these impacts should be developed before the evolution to more eco-friendly alternatives.[128] In addition to the commonly used F-substituted Li salts mentioned above, researchers synthesized new Li salts through asymmetric molecular structure design. For example, Liu et al. reported a new salt under the premise of retaining the strong electron-withdrawing group.[129] An ether

skeleton was introduced to enable F-substituted salt electron-donating ability to capture the migrated Li⁺. The molecule had a large molecular dipole moment, which led to a high donor number (DN) and high Li⁺ transference number. Meanwhile, the quality of interphase film formation largely affects the compatibility with cathodes and anodes, thus determining the cycling stability of the entire battery. Gallant et al. discussed the interplays between CE and generic fluorine content across

a wide range of electrolytes.[24] Figure 7b shows a positive correlation between CE and fluoride levels. Increasing the F concentration through "beneficial" fluorination appears to be a reliable strategy to achieve a high CE of Li plating/stripping, while further understanding of the chemistry and decomposition kinetics of the F source remains. Moreover, apart from the type of Li salts, their purity also has a significant impact on CE.[130] Enhancing the purity of $LiBF_4$ from 99.9% to 99.99% would result in a flatter morphology of the SEI, as depicted in Figure 7c. The purity of the conducting salt directly influences the morphology, composition, and possibly the quality of the formed protective layer. The formation of a more robust interphase that inhibits the growth of high surface area Li directly improves the cycling stability of cells containing fluorine-based conducting salts. To conclude, although $LiPF_6$ is not prominent in ionic conductivity, chemical stability, and thermal stability, it is still dominant in the commercial market of LIBs due to the ability to provide well-balanced properties. Selective fluorination of the anions of Li salts will decrease their interactions with Li^+ cations, thereby increasing the dissociation of the salts in the electrolyte solution and lifting the ionic conductivity. To achieve better performance, two or more F-containing salts are synergistically used to supplement their native deficiencies.

The properties of the electrolyte can be altered by adjusting the concentration of the Li salt. Conventional dilute electrolytes typically operate within a salt concentration range of 1−2 M, which strikes a balance between ionic conductivity, viscosity, and salt solubility. Thus, most of the studies use electrolytes in region C in Figure 8a. However, by carefully selecting appropriate salts and solvents, electrolytes can be relocated in regions A, B, and D, as depicted in Figure 8a, leading to some unexpected properties.[132] Aqueous electrolytes possess a narrow ESW of 1.23 V, which is insufficient to support most electrochemical couples in LIBs. Besides, hydrogen evolution at the anode side is another serious challenge as it occurs at a potential (2.21−3.04 V vs Li/Li+, depending on pH value) far higher than the operating voltage of most LIBs. Consequently, the maximum voltage achieved in aqueous LIBs was limited to 1.5 V.[133,134] Xu et al. developed a "water-in-salt" electrolyte by dissolving lithium bis-(trifluoromethane sulfonyl) imide (LiTFSI) at extremely high concentrations (molality > 20 m) in water, leading to an anion-rich Li^+ solvation sheath and an expanded ESW (∼3.0 V),[135] as exhibited in Figure 8b. This remarkable shift resulted from the formation of a dense interphase on the anode surface, primarily caused by the reduction of salt anions. The $LiMn_2O_4$‖Mo_6S_8 cells using "water-in-salt" electrolyte demonstrated an open-circuit voltage (OCV) of 2.3 V, and the CE was nearly 100% for up to 1000 cycles.

Research on nonaqueous electrolytes offers countless variations in aprotic solvents, Li salts, and their mixing ratios. For a given electrolyte with fixed salt and solvent, ionic conductivity depends on both the viscosity and the Li-ion mobility.[132] For 1 M LiTFSI-1,2-dimethoxyethane (DME)/1,3-dioxolane (DOL) (1:1 by volume), as is concluded in Figure 8c, when the salt concentration is increased, more and more Li−solvent pairs form due to the incomplete Li^+ solvation shell, and the viscosity at room temperature increases obviously. At the same time, the Li-ion transference number rises to a much higher value (t_{Li}^+ = 0.73) than that of dilute salt-in-solvent electrolytes (0.2−0.4).[138] For such electrolytes, Li ions are mostly coordinated with solvent in the first

solvation shell, leading to a large number of free anions and lower mobility of solvated Li cations. In the highly concentrated electrolyte system, more anions come into the first solvation shell and form more contact ion pairs (CIPs) and aggregates (AGGs), thus leading to a higher Li-ion transference number and lower ion conductivity.[139] Apart from these changes in physical properties, the concentrated electrolyte demonstrates unusual electrochemical properties that are remarkably distinct from a conventional dilute electrolyte. In 2003, Ogumi et al. reported that highly concentrated propylene carbonate (PC) electrolytes have shown dramatic changes in the behavior of graphite electrodes.[140,141] Further in 2008, the reversibility of Li metal deposition/stripping was notably improved in highly concentrated PC electrolytes.[142] From 2010 onward, Yamada et al. extended this method to a wide range of nonaqueous solvents of reversible graphite electrodes with EC-free solvent.[143−145] After this path-breaking work, the highly reversible Li metal electrodes with excellent cycling stability were reported by Xu et al.[132] in 2013 and Qian et al.[146] in 2015. These changes can be attributed to the reduction of free solvent in the solution, altering the solvation structure and shifting the energy level of the LUMO toward the salts, resulting in the reduction of the salts at a lower voltage.[144] For LiTFSI/lithium bis(fluoro sulfonyl) imide (LiFSI)-containing electrolyte, Al dissolution is suppressed at high voltage.[147] The presence of fewer free solvents and anions in the electrolyte leads to less dissolution of the Al current collectors, as shown in Figure 8d. For Li−S batteries, the high-concentration electrolytes can inhibit self-discharge caused by polysulfide shuttle (Figure 8e), which significantly improves the reversibility of the batteries (Figure 8f).[137] However, the application of such highly concentrated electrolytes is limited by the high cost and high viscosity due to the extensive use of Li salts.

2.2.2. Fluorinated Solvents and Cosolvents. Introducing fluorine into the molecular structures of electrolyte solvents and cosolvents imparts unique physicochemical properties, such as nonflammability, robust LiF-enriched SEI, high resistance against electrochemical oxidation, and an expanded operating temperature window, etc. These advantages make fluorinated electrolytes highly attractive for advanced battery applications. Representative fluorinated solvents and cosolvents are shown in Figure 9a, showing the dielectric constant increasing from left to right. These fluorinated solvents and cosolvents exhibit unique physicochemical properties because of the very high electronegativity and high ionic potential of the fluorine atom.[148] Partially fluorinated organic solvents possess relatively high polarity compared to perfluorinated organic solvents. This property allows partially fluorinated solvents to be used as functionalized solvents, while perfluorinated solvents are primarily employed as antisolvents due to their poor dissolving ability with Li salts. As shown in Figure 9b, Xie et al. proposed the dipole−dipole interactions model to enhance the compatibility of various electrolytes with graphite anode, thereby suppressing Li^+−solvent cointercalation, preserving the graphite lattice and improving the electrochemical reversibility.[149] After introducing fluorobenzene (FB) into the LiFSI−3DME system (LiFSI−3DME/7FB), the cointercalation of the solvent was suppressed, leading to a high initial CE of 86% and stable cycling performance over 200 cycles with a capacity retention of up to 94%. The nonsolvents were kept out of the Li^+ solvation shell while exerting considerable dipole−dipole interactions toward
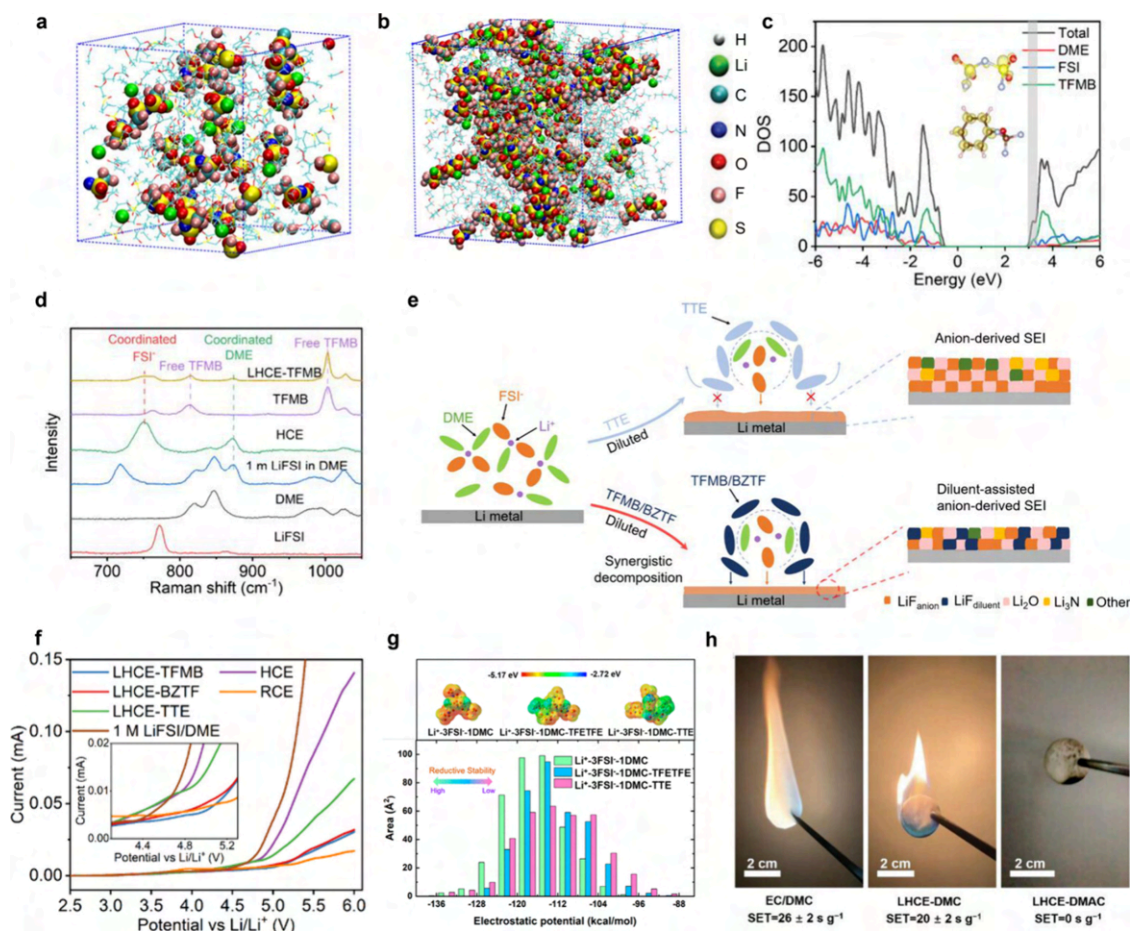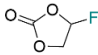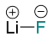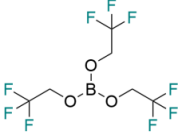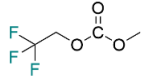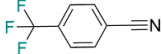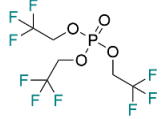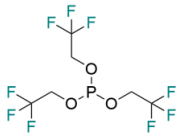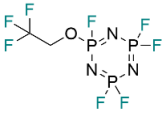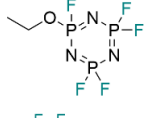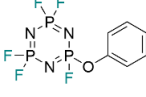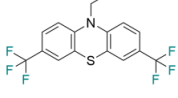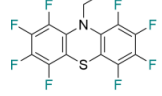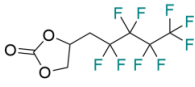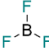
Figure 10. Functions of fluorinated cosolvents of LHCEs. MD simulation results of (a) dilute electrolyte and (b) LHCE. Reproduced with permission from ref 158. Copyright 2021 Wiley-VCH. (c) DOS obtained in quantum mechanical DFT-ab initio molecular dynamics (AIMD) simulations of LHCE with TFMB. Reproduced with permission from ref 160. Copyright 2022 American Chemical Society. (d) Raman spectra of various solvents, diluents, and electrolytes. (e) Schematic diagram of the electrolyte structure and the correspondingly formed SEI in different LHCEs. (f) Oxidation stability of various electrolytes in Li‖Al half-cells characterized by LSV at a scan rate of 0.5 mV s^{-1} from 2.5 to 6.0 V. Reproduced with permission from ref 158. Copyright 2022 American Chemical Society. (g) Electrostatic potential mapping of Li$^+$ solvation structures and the surface area in each ESP range on the van der Waals (vdW) surface of the FSI$^-$ anion part. Reproduced with permission from ref 161. Copyright 2022 American Chemical Society. (h) Flame-retarding testing of EC/DMC, LHCE−DMC, and LHCE−dimethylacetamide (DMAC). Reproduced with permission from ref 165. Copyright 2022 Wiley-VCH.

polar solvents, thus weakening the Coulombic attractions between Li$^+$ and solvents. Rational design by partial fluorination on ethers, e.g., locally polar −CHF$_2$, is identified as the optimal group compared with fully fluorinated −CF$_3$ in popular designs. Such weak solvents could achieve a balance between fast ion conduction and electrode stability through fine tuning the solvation ability (Figure 9c).[150] These developed electrolytes simultaneously endowed high conductivity, a low and stable overpotential, high CE (>99.5%), and fast activation (CE > 99.3% within two cycles). Furthermore, some Li-unfriendly solvents can be optimized by fluorination. For instance, by introducing a fluorinated moiety into the nonflammable phosphate, the five-membered fluorinated cyclic phosphate solvent 2-(2,2,2-trifluoroethoxy)-1,3,2-dioxaphospholane 2-oxide (TFEP) was designed and synthesized, as shown in Figure 9d.[151] Such fluorinated phosphate solvent not only had effective nonflammability but also exhibited excellent electrode compatibility. Besides, fluorine substitution can broaden the range of liquid electrolytes. In 2019, Meng et al. proposed liquified gas electrolytes, which showed high CE with a Li metal anode

(Figure 9e).[152] The 0.5 M LiTFSI and 0.5 M tetrahydrofuran (THF) in fluoromethane (FM) electrolyte exhibited a maximum conductivity of 3.9 mS·cm^{-1} at 20 °C. And, the impressive low-temperature conductivity at −60 °C was 2.8 mS·cm^{-1}, which was competitive among state-of-the-art low-temperature electrolytes.[153,154] Such enhanced liquefied gas electrolytes demonstrated average CEs of 99.6%, 99.4%, and 98.1% (±0.3%) at capacities of 0.5, 1, and 3 mAh cm^{-2}, respectively, during long-term cycling performance.

As mentioned above, per-fluorinated solvents are usually applied as antisolvent or "dilute" in many works to make localized high-concentration electrolytes (LHCEs). Such LHCEs are widely investigated and always show enhanced interphasial stability.[139,155] Compared with HCEs, LHCEs exhibit lower viscosity and wider ESWs. Watanabe et al. used hydrofluoroether (HFE) and 1,1,2,2-tetrafluoroethyl 2,2,3,3-tetrafluoropropyl ether (TTE) to dilute highly concentrated ionic liquid electrolytes.[156] The work indicated that the addition of HFE maintained the solvation structure of the original salt−solvent complexes and effectively reduced the dissolution of Li$_2$S$_n$, which greatly enhanced the power density

Table 2. Fluorinated Additives for Li-Based Batteries[168,170−183]

additive	structural formula	original electrolyte component	main function	ref
5 wt.% FEC		1 M LiPF$_6$-EC/ethyl methyl carbonate (EMC) (1:1 by vol.)	SEI formation	168
0.5 wt.% LiF		1 M LiPF$_6$-EC/EMC	SEI formation	170
2 wt.% tris(2,2,2-trifluoroethyl) borate		1 M LiPF$_6$-EC/DMC (1:2 by vol.)	SEI formation	171
5 wt.% methyl (2,2,2-trifluoroethyl) carbonate		1 M LiPF$_6$-EC/EMC (1:1 by vol.)	CEI formation	172
0.5 wt.% 4-(trifluoromethyl) benzonitrile		1 M LiPF$_6$-EC/EMC/DMC (1:1:1 by vol.)	CEI formation	173
5 wt.% tris(trifluoroethyl)phosphate		1 M LiPF$_6$-EC/EMC (3:7 by vol.)	thermal stability; stabilize LiPF$_6$	174
0.1-1.0 wt.% tris(2,2,2-trifluoroethyl) phosphite		1.2 M LiPF$_6$-C/EC/EMC (3:3:4 by wt.)	thermal stability; stabilize LiPF$_6$	175
5 wt.% (trifluoroethoxy)pentafluorocyclotriphosp-hazene		1 M LiPF$_6$-EC/DMC (3:7 by vol.)	flame retardancy; CEI formation	176
5 wt.% (ethoxy)pentafluorocyclotriphosphazene		1 M LiPF$_6$-EC/EMC/DMC (1:1:1 by vol.)	flame retardancy; CEI formation	177
2 vol.% phenoxy pentafluorocyclotriphosphazene		1 M LiPF$_6$-EC/DMC (1:1 by vol.)	flame retardancy; CEI formation	178
3 mM N-ethyl-3,7-bis(trifluoromethyl)phenothiazine		1.2 M LiPF$_6$-EC/EMC (3:7 by wt.)	overcharge protection	179
0.08 M N-ethyl-1,2,3,4,6,7,8,9-octafluorophenothiazine		1.2 M LiPF$_6$-EC/EMC (3:7 by wt.)	overcharge protection	180
2 wt.% (4-(2,2,3,3,4,4,5,5,5-nonafluoro-pentyl) -1,3-dioxolan-2-one		1 M LiPF$_6$-EC/EMC (3:7 by vol.)	overcharge protection	181
0.1 M Li$_3$AlF$_6$		1 M LiPF$_6$-EC/DMC (1:1 by vol.)	suppress dendrite growth	182
0.01 M BF$_3$		1 M LiPF$_6$-EC/DMC (1:1 by vol.)	enhance the rate capability	183

of the Li−S batteries. By performing molecular dynamics (MD) simulation, the solvation structure can be shown pictorially. Zhang et al. introduced the concept of LHCEs, which consisted of 1.2 M LiFSI in a dimethyl carbonate (DMC)/bis(2,2,2-trifluoroethyl) ether (BTFE) (1:2 by mol)

mixture, exhibiting low concentration, low viscosity, and good wettability that facilitated practical applications of LMBs. The dilution with BTFE slightly weakened the association between Li$^+$ cations and FSI$^−$ anions, promoting FSI$^−$ anion decomposition as the dominant reduction reaction, which

formed a robust FSI-derived SEI layer. The average CE of the electrolyte was greatly increased to ∼99.7%. After that, LHCEs have been extensively applied in LIBs, LMBs, and other electrochemical systems.[157] The dilution with BTFE slightly weakened the association between Li^+ cations and FSI^- anions, which led to more FSI^- anion decomposition as the dominant reduction reaction, forming a robust FSI-derived SEI layer. The average CE of the electrolyte was largely increased to ∼99.7%. After that, LHCEs were widely applied in LIBs, LMBs, and other electrochemical systems. As shown in Figure 10a and 10b, Zhao et al.[158] introduced HFE into initial HCE and simulated the solvation structure. The bulk phase structure of local HCE electrolyte did not greatly change with the addition of HFE diluent. Thus, the salt usage was reduced, and the viscosity of the electrolyte became lower. As a result, the electrolyte has a better wettability with electrodes. Although the ionic conductivity usually increases with the decrease of the viscosity, the addition of diluent has a negative effect on the conductivity of LHCE.[135] The reason is probably the discontinuous Li conducting network separated by the diluent medium. To achieve a balance, the content of diluent should be restricted during the preparation of LHCE. Fluorinated ether diluents typically exhibit lower LUMO and HOMO energy levels. As a result, they may participate in the formation of electrolytelelectrolyte interphase. Wu et al. reported the HFE cosolvent decomposition and metal anode dissolution phenomenon in ether-based LHCE systems.[159] Such light decomposition behavior comes from diluents synergistically decomposed with anions on the Li metal anode. Figure 10c shows the density of states (DOS) of LHCE−trifluoromethoxybenzene (TFMB). In LHCE−TFMB, the LUMO is located at either TFMB or FSI^- with nearly equal probability, indicating that both the FSI^- anions and the TFMB molecules contribute to the SEI formation.[160] Besides, the existence of fluorinated ether antisolvent is also attributed to anion decomposition. The solvation structures in LHCE−TFMB were validated by Raman spectroscopy (Figure 10d). Upon coordination of DME with Li^+, the corresponding peaks of both DME and FSI^- shifted to longer wavenumbers. For the 5.0 M LiFSI/ DME electrolyte, only the peak of Li^+-coordinated DME was observed, indicating that few free DME molecules were present in HCE. In LHCE−TFMB, the peak positions were nearly the same as those in HCE plus the vibration bands of free TFMB. Unlike TTE, which decomposed little at the anode side, the TFMB/benzotrifluoride (BZTF) diluents were partially decomposed along with the FSI^- anions and participated in forming the SEI on the Li metal anode (Figure 10e). This synergistic effect through anion−diluent pairing was expected to be of significant importance to the optimized electrochemical performance. Linear sweep voltammetry (LSV) was conducted on an Al electrode to unveil the electrochemical oxidation stability of these electrolytes (Figure 10f). The oxidation stability of LHCE−TFMB/BZTF was significantly improved, and no exponential increase in oxidation current was observed until 5.0 V. He et al. reported that the surface area in different electrostatic potential (ESP) ranges (Figure 10g) helped quantitatively analyze the characteristics of the molecular surface charge.[161] The reduced relative abundance of the ESP distribution on anions suggested that the reduction stability of FSI^- was reduced in the presence of antisolvents. In previous reports, the LHCE−TTE electrolytes demonstrated better cycling performance of Li‖Cu cells (98.9% and 99.6%) than LHCE−TFETFE (98.2% and 99.4%).[162] However, the

intensified inductive effect caused by antisolvents reduced the binding energy of the Li−solvent interactions and changed with different antisolvents. The binding energies of the Li− solvent and Li−anion interactions were decreased with the addition of antisolvent compared with the HCEs, indicating the capability of antisolvents to help lower the desolvation energy and facilitate interphase kinetics in the electrochemical reaction.[163,164] The addition of fluorine also led to a decrease in the flammability of the electrolyte, as shown in Figure 10h.[165] Hereby, $F^•$ radicals were formed, which could scavenge the $H^•$ radicals. Owing to this approach, the free-radical reaction was quenched, and the flame propagation was suppressed. However, ether-based electrolytes are highly volatile and flammable, and flame retardancy cannot be achieved by adding fluorinated solvents/cosolvent alone. Aurbach et al. reported a synergy of fluorinated cosolvent and gelation treatment by a butenoxycyclotriphosphazene (BCPN) monomer, which facilitated the use of ether-based electrolyte for high-energy Li metal batteries.[166] The safety risks of fire and electrolyte leakage were eliminated by the fluorinated cosolvent and fireproof polymeric matrices.

2.2.3. Fluorinated Additives. Electrolyte additives are usually defined as the functional compounds added into the bulk electrolyte in a low amount (0.1−5%, either by weight or volume) by which electrolyte can be regulated economically and efficiently.[130] Compared to their nonfluorinated counterparts, fluorinated additives exhibit decreased cathodic stability, increased anodic stability, reduced flammability, etc., which endow fluorinated additives with tremendous application potential in (i) SEI/CEI formation, (ii) flame retardancy, (iii) overcharge protection, (iv) Li salt stability regulation, (v) electrolyte wettability adjustment, and (vi) electrolyte conductivity improvement.[167] Table 2 summarizes the components and functions of different fluorinated additives used in Li-based batteries. As the most widely reported organic additive, FEC is believed to be capable of improving the interphasial stability of the anode by the formation of LiF-rich SEI layers. Substitution of a hydrogen atom in EC by a fluorine atom sharply reduces the LUMO energy level from −0.38 to −0.87 eV, which makes it easier to be reduced on the anode side and form a SEI.[168] The C−F bond in FEC breaks first during the reduction process, eventually leading to the formation of a stable, compact SEI rich in LiF and poly(vinyl carbonate) (poly(VC)).[168] The combination of LiF and poly(VC) remarkably inhibits continuous electrolyte decomposition and facilitates uniform Li deposition, which exhibits an even better passivation effect than the VC-containing electrolyte.[169] Apart from the FEC, Archer and co-workers demonstrated that the direct use of 0.5 wt % LiF to a conventional electrolyte could enable high surface stability and fast surface diffusion of Li ions over the layer rich in LiF crystals,[170] further confirming the vital role of LiF in stabilizing the SEI. Yin and co-workers adopted a fluoride boron-based anion receptor, tris(2,2,2-trifluoroethyl) borate (TTFEB), as a bifunctional electrolyte additive to improve the performance of LMBs.[171] With 2 wt % TTFEB, uniform Li deposition without uncontrollable Li dendrites can be realized due to the LiF-rich SEI layer. Moreover, the electron-deficient boron-center atoms acted as anion receptors to tether the PF_6^- anions in the electrolyte, causing the increased Li-ion transference number.

In addition to the Li anode, the stability of the cathode is also crucial for the development of high energy density Li-based batteries. However, the CEI chemistry is even more
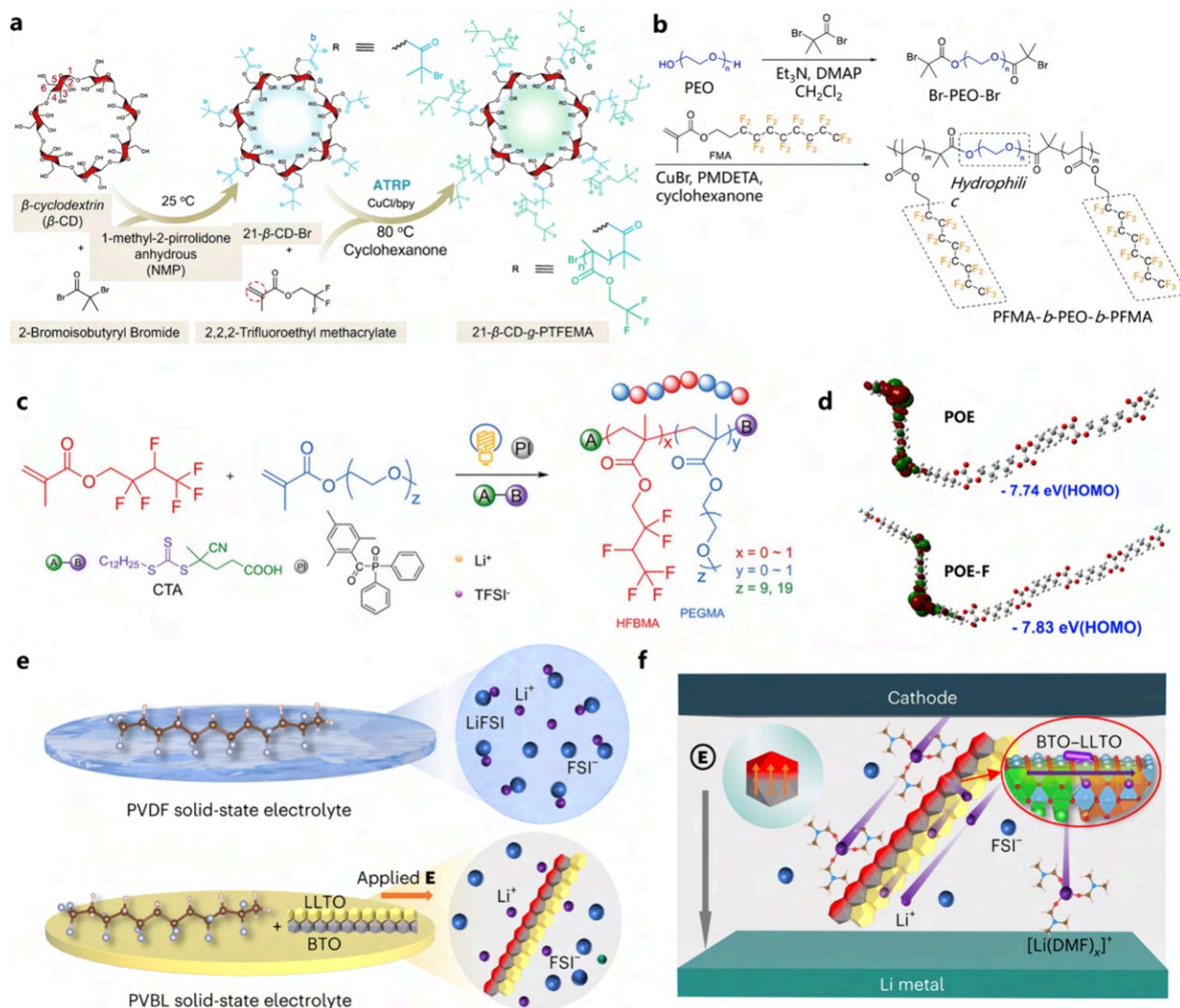
Figure 11. Fluorinated solid-state/quasi-solid-state polymer electrolytes. (a) Detailed synthetic scheme of 21-arm fluoropolymers. Reproduced with permission from ref 195. Copyright 2022 Springer Nature. (b) Synthesis paths of FBCPs. Reproduced with permission from ref 196. Copyright 2021 Elsevier. (c) Schematic of synthesizing FB-SPE by visible-light-driven photocontrolled radical polymerization (photo-CRP). Reproduced with permission from ref 197. Copyright 2021 Wiley-VCH. (d) Simulated HOMO energy level of POE (upper panel) and POE-F (lower panel). Reproduced with permission from ref 198. Copyright 2021 Wiley-VCH. Illustration of (e) the Li salt state in the PVDF and PVBL electrolytes and (f) the Li salt dissociation and Li+ transport by the coupled BTO−LLTO in the PVBL electrolyte. Reproduced with permission from ref 199. Copyright 2023 Springer Nature.

complex, and the electrochemical performance of the cathode has been plagued by some challenges, including severe oxidative decomposition of the electrolyte, gas evolution, transition metal dissolution, cracking of primary/secondary particles, etc., especially for layered transition metal oxide cathodes under a high cutoff voltage.[184] The design of novel fluorinated additives such as fluorocarbonates, fluoronitriles, and fluoroborates can improve the oxidation stability after fluorination due to the ability to in situ form an F-containing CEI layer, which offers a promising solution for the aforementioned challenges.[185] Song and co-workers reported a fluorinated linear carbonate, methyl (2,2,2-trifluoroethyl) carbonate (FEMC), as a new electrolyte additive to achieve the performance improvement of commercial carbonate electrolyte at a 4.6 V cutoff voltage, far beyond the oxidation limit (4.3 V vs Li/Li+) of conventional carbonate electrolyte.[172] FEMC played a crucial role in generating a passivating layer rich in

metal fluorides and C−F-containing species, which effectively delayed the cathode degradation and capacity fade.

The practical application of batteries may encounter different abuse conditions such as thermal abuse, electronic abuse, and mechanical abuse, which trigger a series of exothermic reactions and thermal runaway of batteries.[186] Generally, fluorinated phosphates and fluorinated phosphites such as tris(trifluoroethyl)phosphate (TFP)[174] and tris(2,2,2-trifluoroethyl) phosphite (TTFP)[175] exhibit superior flame retardance over nonfluorinated counterparts. When heated, F• radicals can scavenge the hydrogen radicals and quench the free-radical reaction and flame propagation.[187] Addition of fluorinated phosphates or fluorinated phosphites in the organic electrolyte can remarkably promote the thermal stability and suppress the thermal decomposition of LiPF6.[188] However, to achieve nonflammable electrolyte formulation, the amount of fluorinated phosphates or fluorinated phosphites is usually required to be greater than 5%.[130] Phosphazene derivatives

rich in F, N, and P elements are considered as more outstanding flame-retardant additives than phosphates and phosphites. Feng and co-workers synthesized a novel (trifluoroethoxy)pentafluorocyclotriphosphazene (TFPN) and deployed a flame test, which revealed that only 5 wt % TFPN addition can enable electrolyte nonflammability.[176] Moreover, the preferential oxidative decomposition of fluorinated phosphazene derivatives also produced a multiphase CEI layer consisting of linear/multiring polymers, such as Li_3N, LiF, etc., which suppressed decomposition of the electrolyte and achieved a high reversible capacity and better capacity retention.[177,178] As a typical electronic abuse, overcharge can cause premature electrode and electrolyte failure and catastrophic safety issues. Overcharge protection additives with an oxidation potential slightly higher than the delithiated potential (vs Li/Li^+) can exert a preferential redox reaction, resulting in circuit break or a microshort circuit inside the batteries.[189,190] An electron-withdrawing substituent with F or CF_3 groups provides a promising method to increase the oxidation potential of the overcharge protection additives for use as redox shuttles in high-voltage Li-based batteries. Odom and co-workers synthesized a series of F-substituted phenothiazine derivatives such as N-ethyl-3,7-bis-(trifluoromethyl)phenothiazine (BCF3EPT) for a $LiFePO_4$ cathode[179] and N-ethyl-1,2,3,4,6,7,8,9-octafluorophenothiazine (OFEPT) for a high-voltage $LiNi_{0.8}Co_{0.15}Al_{0.05}O_2$ cathode,[180] which acted as reversible redox shuttles to protect batteries from overcharge. All in all, although numerous fluorinated additives have been explored, the physicochemical properties of fluorinated additives do not show a simple monotonous correlation with the content of fluorine substitution.[191] Moreover, the decisive influence of the fluoride substitution position on the performance of additives still needs further investigation.

2.2.4. Fluorinated Solid/Quasi-Solid-State Electrolytes. Exploration of highly affordable batteries with enhanced safety is crucial for achieving electric devices with energy densities of 400 Wh kg^{-1}. To address this need, the development of all-solid-state batteries has emerged as a promising pathway. Traditionally, liquid electrolytes select organic solvents with strong polarity, creating a high dielectric constant environment conducive to Li-ion dissociation.[192] This strategy also applies to the selection of all-solid polymer electrolytes. The electrostatic force between ions in SPEs is significantly influenced by the polarity of the polymer. Since the report of ion conduction in poly(ethylene oxide) (PEO) in 1975, it has been considered as an intriguing polymeric matrix for electrolytes due to the excellent chemical and electrochemical stabilities.[193,194] However, the high crystallinity of PEO at room temperature results in low ionic conductivity ($10^{-6}-10^{-8}$ S cm^{-1}); meanwhile, the narrow ESW of PEO-based electrolytes also hinders their widespread application. Efforts to enhance PEO-based solid electrolytes are underway. As an example shown in Figure 11a, Hu et al. proposed a top-down design concept through atom transfer radical polymerization.[195] Through an orthogonal test method, the optimal composition of a F-rich macromolecule containing all-solid-state polymer electrolyte (FMC-ASPE) was determined. This new PEO electrolyte exhibited significantly improved high-voltage stability and transference number (t_{Li^+} = 0.88) to suppress the side reaction at the cathode side and dendrite growth at the Li anode side. Additionally, the as-prepared FMC−ASPE showed improved physical and electrochemical

properties, including higher ionic conductivity, higher toughness (2.7 times higher than PEO−ASPE), and higher thermal stability. Sun et al. synthesized fluorine-containing ABA triblock copolymer electrolytes (FBCPEs) (perfluoroalkyl pendant in the A segment and PEO in the B segment) with a small number of $-CF_2$ repeating units (Figure 11b).[196] Addition of $-CF_2$ decreased the HOMO energy level of the whole electrolyte. Thus, the antioxidant capacity of FBCPEs was improved, resulting in a wider ESW of 4.9 V. Jia et al. proposed a fluorinated bifunctional solid polyelectrolyte, as shown in Figure 11c, in which fluorinated chains were covalently bonded to polyether-based fragments through the controlled radical polymerization.[197] Compared with conventional nonfluorinated polyether-derived solid polyelectrolytes, FB-SPEs were able to provide an electrochemical window of 5 V. In addition to PEO, fluorination plays an essential role in other all-solid-state polymer electrolytes as well. Sun et al. selected polyoxalic (POE) acid as the polymer matrix and found that the HOMO electrons of the POE were located at the terminal unit.[198] When trifluoroacetic acid was applied as the terminal unit (POE-F), the HOMO electrons were transferred to the middle oxalic acid unit, which improved the antioxidant capacity (Figure 11d). Furthermore, the interfacial compatibility between the Li metal and POE-F was also improved by generating a LiF-based SEI, and the stability of Li‖NMC811 full cells was significantly improved, which kept cycling stably over 200 cycles at 1 C.

Apart from all-solid-state polymer electrolytes, quasi-solid-state gel polymer electrolytes (GPEs) can also be optimized by fluorination. One of the extensively studied materials for quasi-solid-state polymer electrolytes is PVDF, first investigated in the 1980s.[200] In 1996, Warren et al. assembled the first LIB based on a PVDF-HFP-based GPE. The copolymer exhibited advantages of a low degree of crystallinity due to the addition of hexafluoropropylene (HFP), high mechanical flexibility, and good compatibility with electrodes.[49,201] Afterward, the number of studies on PVDF-based electrolytes gradually increased, with GPEs being the main focus. He et al. developed a highly conductive and dielectric GPE by compositing PVDF with coupled $BaTiO_3$ (BTO) and $Li_{0.33}La_{0.56}TiO_{3-x}$ (LLTO) (named as PVBL) nanowires, as shown in Figure 11e and 11f.[199] The PVBL effectively restrained the formation of the space charge layer with PVDF, and the coupling effects contributed to an exceptionally high ionic conductivity (8.2×10^{-4} S cm^{-1}) and Li^+ transference number (0.57) of the PVBL at 25 °C. The PVBL also homogenized the interfacial electric field with electrodes. The Li|PVBL| ($LiNi_{0.8}Co_{0.1}Mn_{0.1}O_2$) NCM811 solid-state cells stably cycled 1500 times at a current density of 180 mA g^{-1}, and the pouch cells also exhibited excellent electrochemical performance and good safety. Nevertheless, various tough challenges need to be resolved before the practical application for PVDF-based electrolytes, including the following: (i) the in-depth understanding of interphase degradation mechanisms is still insufficient; (ii) achieving considerable ionic conductivity in solvent-less conditions is of significant importance; (iii) the rate performance should be promoted under high current density; (iv) the solid interface still has natural deficiency compared with liquid electrolytes; (v) to further improve the energy density, the thickness of the polymer electrolyte needs to be thinner up to 10−20 μm; (vi) the polymerized homogeneity of PVDF-based electrolytes in industrial conditions is insufficient, which will lead to uneven
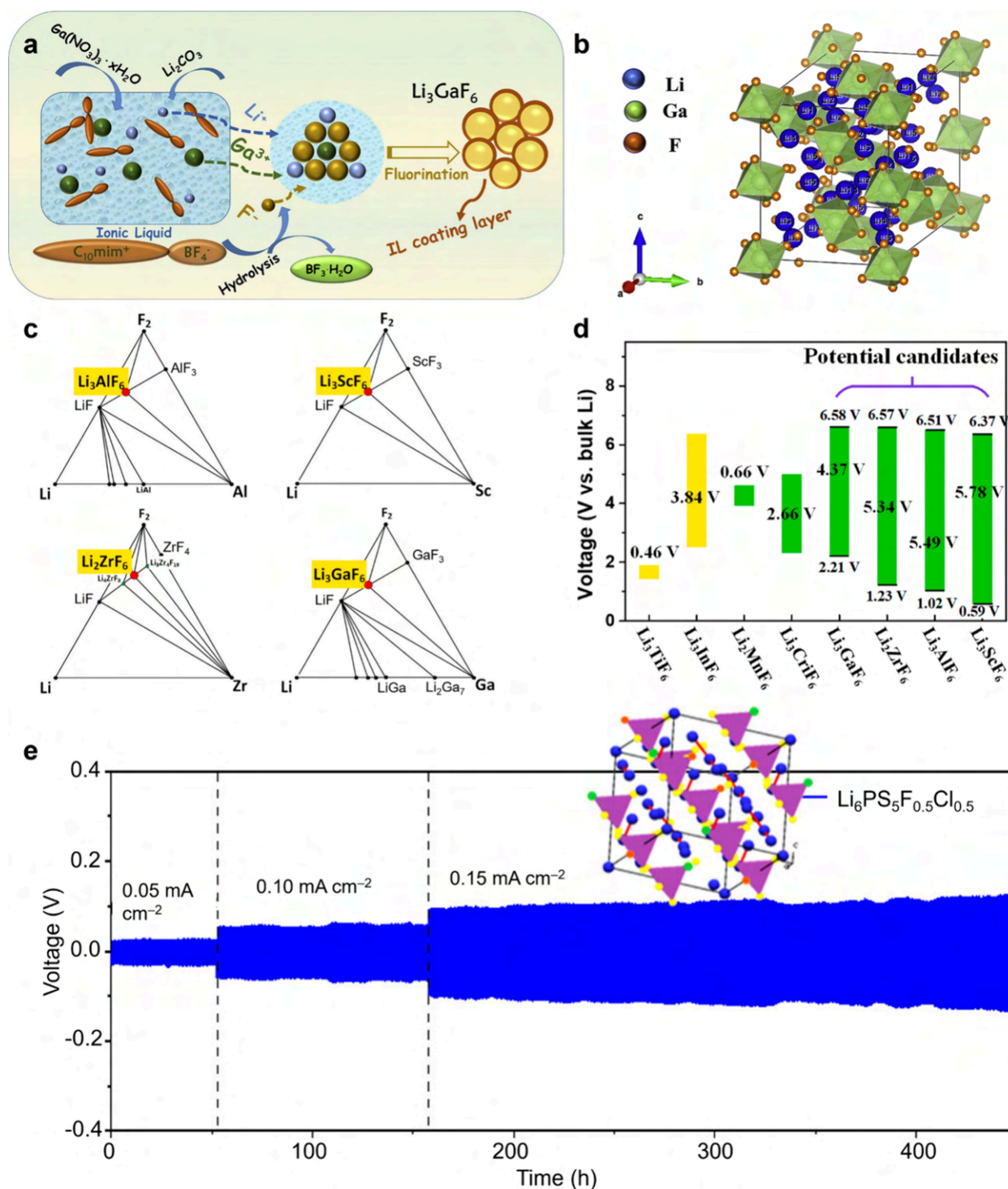
Figure 12. Fluorinated inorganic solid electrolyte. (a) Schematic synthesis of Li_3GaF_6. (b) Crystal structures of β-Li_3GaF_6 viewed along [111]. Reproduced with permission from ref 203. Copyright 2022 Springer Nature. (c) Li−M−F ternary phase diagram assessing the computed stability of Li−M−F compounds. Black solid circles indicate stable phases, while red solid circles show the targeted fluoride materials. (d) Electrochemical stability ranges of Li_xMF_6 fluoride electrolytes. The yellow region reflects the possible extension of the voltage window over which decomposition occurs but without any metallic products. Reproduced with permission from ref 204. Copyright 2021 Elsevier. (e) The crystal structure of $Li_6PS_5F_{0.5}Cl_{0.5}$ and the voltage profile of Li‖Li symmetric cell cycling with $Li_6PS_5F_{0.5}Cl_{0.5}$ under current densities of 0.05, 0.10, and 0.15 mA cm^{-2}. Reproduced with permission from ref 205. Copyright 2022 American Chemical Society.

Li transportation. Understanding the above specific challenges faced by PVDF-based electrolytes will contribute to the development of next-generation all-solid-state batteries.

For inorganic solid-state electrolytes, although fluorination strategies have been successfully applied on oxide, sulfide, and polyanion solid electrolyte systems, Li−fluoride solid electrolytes have yet to be reported.[202] To investigate the structure and corresponding synthesis strategy, Li et al. proposed a novel Li-rich fluoride electrolyte, Li_3GaF_6, with a high ionic conductivity close to 10^{-4} S cm^{-1} at room temperature

(Figure 12a).[203] The synergic effect of open bulk transport and compact interphase transport in Li_3GaF_6 endowed LiFePO$_4$-based solid-state LMBs with an improved cycling performance for at least 150 cycles at 1 C. The crystal structure of the Li_3GaF_6 derivative from the cryolite phase is shown in Figure 12b. The characteristic building units are GaF$_6$ octahedra, and the Li atoms are octahedrally, pentahedrally, or tetrahedrally coordinated by F. To understand the phase stability relative to their corresponding separated phases, including elemental, binary, and ternary ones, Lin et al. used the grand canonical linear programming method (GCLP) to explore the phase diagram of Li−M−F compounds (Figure 12c).[204] The favorable combination was the decomposition of ternary Li_xMF_6 into binary LiF and MF$_3$ or MF$_4$ with the order of decomposition energy ($\Delta E = [E$ (phase equilibrium) $- E(Li_xMF_6)]$ N_{atoms}^{-1}) being as follows: Li_3GaF_6 (52 meV atom^{-1}) > Li_3AlF_6 (38 meV atom^{-1}) > Li_2ZrF_6 (13 meV atom^{-1}) > Li_3ScF_6 (1 meV atom^{-1}). Figure 12d shows the sequence of fluoride materials determined by their ESW: Li_3ScF_6 (5.78 V) > Li_3AlF_6 (5.49 V) > Li_2ZrF_6 (5.34 V) > Li_3GaF_6 (4.37 V). The fluoride materials exhibit a wider ESW compared to that of the sulfides. Li_3AlF_6 exhibits a cathodic (anodic) limit of 0.56 V (6.0 V) versus bulk Li, while Li_3PS_4 operates within a narrow window of 1.6−3.0 V. The electronically insulating and ionically conducting phase LiF is formed at low voltage, which may potentially serve as a passivating interphase that can act as a barrier against further solid electrolyte decomposition.

The Li∥NMC811 cells matched with Li_6PS_5Cl (LPSCl) electrolyte suffer from a fast capacity decay because the sulfide solid electrolyte is not stable to both the Li anode and the NMC811 cathode.[206,207] To solve this problem, Wang et al. added a small amount (0.32 wt %) of CuF$_2$−LiNO$_3$ (CL) into LPSCl electrolyte to in situ form a mixed-conductive−lithiophobic and self-healing LiF−Li$_3$N−Cu SEI. The compatibility of LPSCl−CL electrolyte to single-crystalline NMC811 was further enhanced by adding a small amount (0.02 wt %) of AlF$_3$.[208] Doping F into LPSCl electrolyte largely improved the oxidation stability; thus, the Li∥NCM811 full cell achieved a high capacity retention of 69.4% after 100 cycles at 2.55 mA cm^{-2}/2.55 mAh cm^{-2}. In addition, Wang and co-workers reported F-doped $Li_{5+y}PS_5F_y$ argyrodites with a tunable doping content and dual dopants (F$^-$/Cl$^-$ and F$^-$/Br$^-$) that were synthesized through a solvent-based approach, as shown in Figure 12e.[205] Among all compositions, $Li_6PS_5F_{0.5}Cl_{0.5}$ exhibited the best cycling performance in Li symmetric cells owing to the enhanced interfacial stability against Li metal, which can be attributed to the formation of a stable SEI containing Li$_3$P, LiCl, and LiF. Furthermore, Li∥LiFePO$_4$ (LFP) cells using $Li_6PS_5F_{0.5}Cl_{0.5}$ showed enhanced cycling performance with a specific discharge specific capacity above 105 mAh g^{-1} after 50 cycles. However, F doping also significantly reduced the ionic conductivity of LPSCl due to the high bonding between F and Li.[209] The excessive LiF precursor filled in the boundary/pore of the solid-state electrolytes after fluorine was incorporated into the LPSCl structure. This reduced the electronic conductivity while enhancing the rigidity to suppress the penetration of Li dendrites.

In conclusion, the electrolytes for high-performance Li-based batteries can be tailored by combining the benefits of different partially fluorinated/per-fluorinated electrolytes. Selective fluorination of the anions of Li salts will decrease their interactions with Li$^+$ cations, thereby increasing the dissociation of the salts in the electrolyte solution and lifting the ionic conductivity. Fluorinated solvents can also inhibit the progress of combustion, thus improving the safety of the electrolytes. It is important to achieve a balance between Li salt solubility and interfacial compatibility. Fluorinated additives containing well-tailored functional groups can transform into uniform and thickness controllable SEI/CEI films, which remains a hot field for future research. For the polymer all-solid-state electrolytes, the grafting of F-containing groups/chains on the polymer matrix can widen the electrochemical window and/or facilitate ion conduction; furthermore, F-containing polymers, such as PVDF and PVDF-HFP, have played a significant role in the quasi-solid-state gel polymer electrolytes. The exploration of fluorine chemistry in advanced solid-state battery systems aiming for enhanced performance is also in progress.

2.3. Other Fluorinated Battery Components

2.3.1. Fluorinated Separators. As an essential component in batteries, the separator not only offers transport paths for Li$^+$ migration between two electrodes but also serves as a barrier isolating the cathode from the anode.[210] Despite their critical function, current commercial separators (e.g., polypropylene (PP), polyethylene (PE), and their multilayer composites) suffer from insufficient mechanical strength, inferior liquid electrolyte affinity, low thermal stability, and high flammability. The separator failure/collapse can lead to internal short circuits, potentially triggering thermal runaway, energy release, explosion, and other serious security risks in batteries.[211] Over the past few decades, intensive efforts have been dedicated to overcoming these limitations, among which polymeric separators,[212−223] blends and composites,[224−226] surface coating,[227−229] and surface grafting[230−233] have been mostly the focus. In particular, PVDF and its copolymers (e.g., PVDF−HFP, polyvinylidene-co-chlorotrifluoroethylene (PVDF−CTFE), poly(vinylidene fluoride)−trifluoroethylene (PVDF−TrFE)) have garnered great interest due to their high dielectric constant, strong polarity, and excellent anodic stability, which contribute to their good affinity toward polar electrolytes and their ability to assist in the dissociation of Li salts. For a detailed and specific summary of separators based on PVDF and copolymers, readers are encouraged to consult the excellent review articles.[234,235] It should be noted that the practical applications of PVDF separators are hindered by the low mechanical strength (<10 MPa) caused by their solubility in electrolytes combined with inferior thermal stability due to their low melting point (172 °C).[225] In addition, the formation of LiF and the C═CF bond in the crystallized PVDF, through interactions between F and Li or lithiated graphite, can resist Li$^+$ transport and further deteriorate the rate capability of LIBs.[236,237] Blending two or more polymer solutions has been considered as an effective strategy to achieve complementary properties of each component. In 2014, Liu and co-workers blended PVDF−HFP with polyimide (PI) by cross-electrospinning, arranging the two polymer solutions alternately to construct a PVDF-HFP/PI composite membrane. This composite separator, combining the advantages of both polymers, demonstrated increased porosity, higher thermal dimensional stability, improved electrochemical stability, and higher ionic conductivity compared to the commercial Celgard 2400 separator.[238] Similarly, the poly(m-phenylene isophthalamide) (PMIA), known for its high mechanical strength and high temperature tolerance, was blended with PVDF to
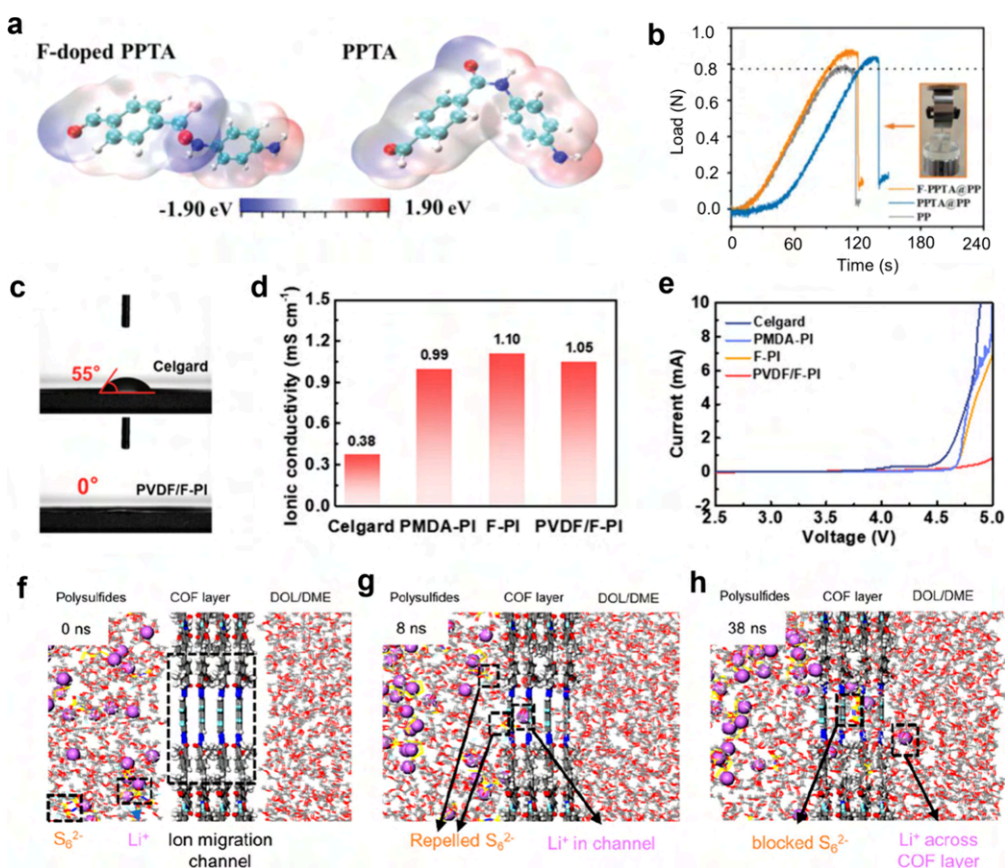
Figure 13. Functions of fluorinated separators in Li-based batteries. (a) Electrostatic potential surface for pristine PPTA and F-PPTA molecules. (b) Puncture strength curves of the PP, PPTA@PP, and F-PPTA@PP separators. Reproduced with permission from ref 243. Copyright 2022 Wiley-VCH. Evaluations of the (c) electrolyte contact angles, (d) ionic conductivity, and (e) LSV for the PVDF/F−PI separator and other separators. Reproduced with permission from ref 244. Copyright 2023 Wiley-VCH. Schematic illustration of the ion transport behavior through the fluorinated COF nanofluidic nanochannels at (f) 0, (g) 8, and (h) 38 ns. MD simulation results show that the fluorinated separator exhibits a higher Li$^+$ migration activity than the anion (TFSI$^-$ and S$_6^{2-}$). Reproduced with permission from ref 245. Copyright 2023 American Chemical Society.

construct a sandwich-structured PVdF/PMIA/PVdF composite membrane. This membrane displayed high ionic conductivity, reinforced tensile strength (13.96 MPa), and excellent thermal stability as well as desirable electrochemical stability/rate performance for the assembled Li||LiCoO$_2$ battery.[225] The enhancement of the mechanical property and thermal stability of the PVDF-based separator was also achieved by blending with polyacrylonitrile (PAN).[237] Nevertheless, blending polymer solutions can increase the fiber diameter size and influence the fiber morphology, generally leading to a nonuniform fiber structure. Besides, the obtained ionic conductivity of the resulting blends needs to be further improved. To address these issues and enhance the separator properties such as electrolyte uptake, thermal stability, and ionic conductivity, nanoscale particles including Al$_2$O$_3$, SiO$_2$, TiO$_2$, and Sb$_2$O$_3$ have been successfully incorporated into the polymer matrix.[239,240]

A variety of modification strategies have also been employed to enhance the physiochemical and electrochemical performance of the separators, among which the surface coating/grafting method has been considered as a promising candidate to address the above-mentioned drawbacks facing the common commercial separator.[226,234] By coating the composite material of graphite fluoride nanosheets (GFNs) and PVDF, the pristine PP separator was modified by Zhang et al. on a large

scale. Attributed to the reaction between GFNs and Li, a concrete-like protective layer with improved mechanical properties was constructed on the Li metal anode, enabling fast Li$^+$ transport, resisting Li dendrite growth and maintaining good integrity as well. In addition, owing to the lithiophilic feature of GFNs, sufficient physical contact between the Li anode and the protective layer was achieved, realizing low interphasial resistance and homogeneous Li deposition layer by layer.[241] As the most electronegative elements that have been known, F is capable of forming the strongest single covalent bond of C−F with a bond energy of 488 kJ mol^{-1}.[242] A F-modified PPTA (poly-p-phenyleneterephthalamide) protective layer on the PP separator (F−PPTA@PP) was developed via coating PPTA nanofibers on a commercial PP membrane and subsequently grafting F-containing groups on the separator. As shown in Figure 13a, an F atom was grafted on the PPTA (F-doped PPTA) via a C−F bond, where the generated electronegativity around the C−F bond endowed a stronger organic affinity to promote the electrolyte wettability. This F−PPTA@PP separator exhibited high thermal stability to suppress thermal shrinkage, excellent physical strength to prevent potential mechanical abuse, and good capability to simultaneously in situ construct a LiF-rich SEI layer to promote the uniform electrodeposition of Li and eliminate Li dendrite risks (Figure 13b). With this separator, the assembled
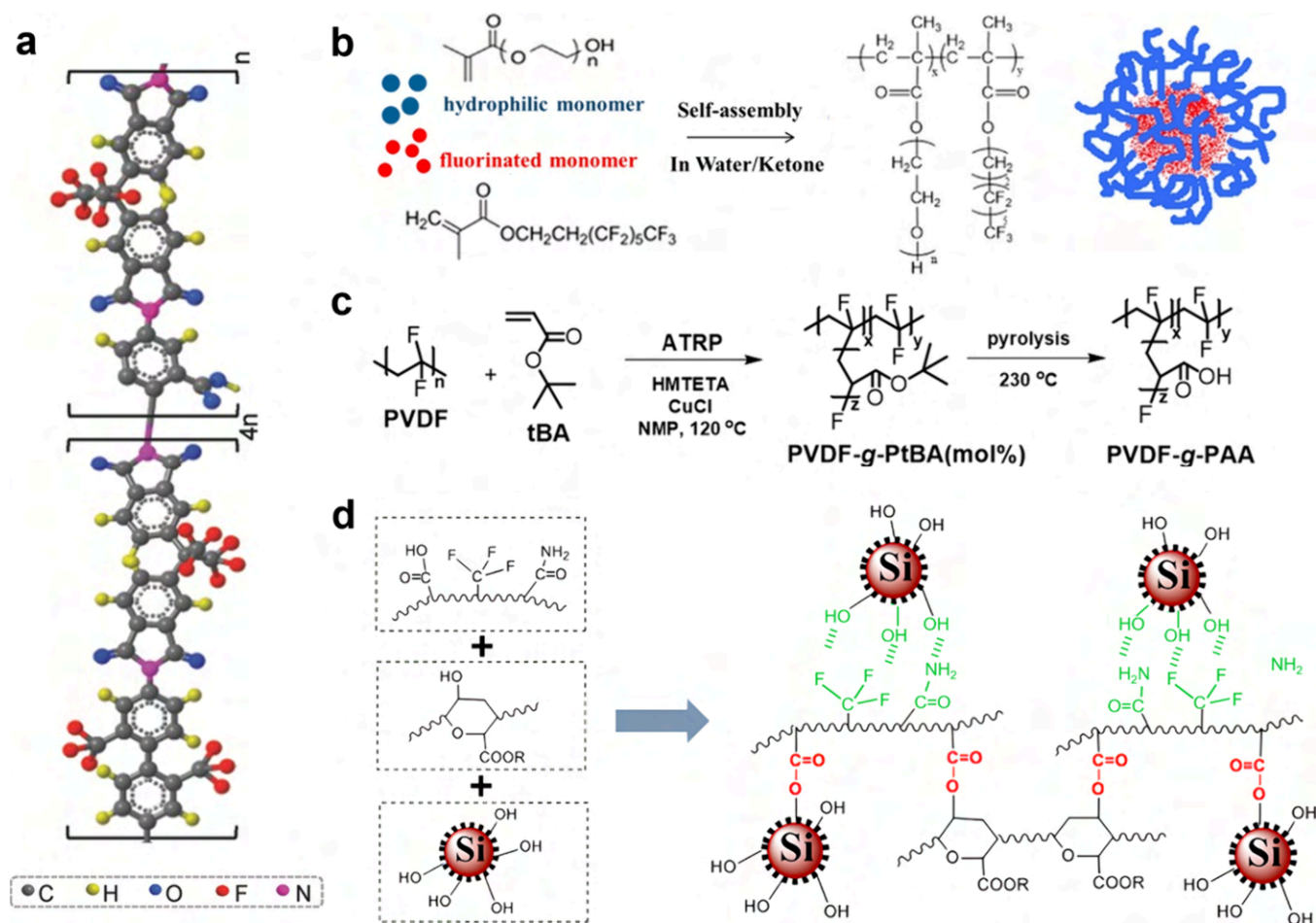
Figure 14. Developments of fluorinated binders for enhancing electrode performance. (a) Molecular structures of synthesized FPI. Reproduced with permission from ref 262. Copyright 2018 Wiley-VCH. (b) Scheme of the preparation for self-assembled fluorinated copolymers. Reproduced with permission from ref 269. Copyright 2018 American Chemical Society. (c) Preparation routes for amphiphilic graft copolymer precursors (PVDF-*g*-PtBA) and pyrolytic transformation to PVDF-*g*-PAA. Reproduced with permission from ref 270. Copyright 2016 Wiley-VCH. (d) Illustration of the dual-cross-linked network combining covalent bonds and hydrogen bonds among the designed fluorinated copolymer, sodium alginate, and the Si surface. Reproduced with permission from ref 271. Copyright 2019 American Chemical Society.

Li‖NCM811 battery featured an initial capacity of 194.1 mAh g^{-1} at 0.5 C and a stable cycling performance for over 1000 cycles. Under various extreme conditions, such as a wide temperature range from −10 to 100 °C, an ultrafast charging/discharging rate of 30 C, and lean electrolyte/high mass loading, the battery exhibited promising electrochemical performance.[243] Very recently, a novel fluorine-functionalized PVDF/fluorinated-PI (FPI) composite nanofibrous separator was developed for wide-temperature LMBs.[244] On one side, the abundant polar −CF$_3$ groups in the F−PI composite provided an electronegative environment for fast Li$^+$ transfer. Besides, the −CF$_3$ group contributed to enhanced thermal stability and fire retardancy for enabling the operation of LMBs in a wide temperature range. On the other side, the incorporation of PVDF enhanced the mechanical properties by increasing physical contacts among the F−PI nanofibers and facilitated the uniform Li deposition via homogenizing the pore size as well. This F-functionalization treatment endowed the separator not only with increased affinity toward organic electrolytes and high value of ionic conductivity but also a wider ESW (Figure 13c−e). Based on this separator, the Li‖Li cell sustained a steady cycling of 2400 h at 1 mA cm^{-2} with an areal capacity of 1 mAh cm^{-2}, which survived for 1000 h with a

low overpotential of 15 mV at 60 °C. Briefly, the fluorination method offers a promising and facial strategy for enhancing the overall properties of the separator, including the electrolyte wettability, ionic conductivity, thermal stability, and electrochemical stability, thus effectively resisting safety risks and improving the electrochemical performance of LMBs.

As one of the most promising high-energy Li-based rechargeable battery systems, the practical Li−S battery has been restricted by the irreversible cathode consumption due to the polysulfide shuttling as well as notorious Li dendrite growth, inducing severe capacity fading during cycling. Introducing modification layers or interlayers on separators has been adopted as a feasible strategy for entrapping negatively charged sulfur species.[246,247] Particularly, to utilize the polar active site of F atoms for immobilizing polysulfides, Dominko et al. synthesized fluorinated reduced graphene oxide (F−rGO) to act as a separator interlayer, which prevented the polysulfide shuttling and achieved improved cycling performance.[248] Unfortunately, the usage of fluorine gas or XeF$_2$ brings safety concerns for practical applications. Via a facile, cost-effective, safe, and scalable approach, fluorinated carbon was successfully constructed on a PP separator. Thanks to the strong chemical bonding ability of the F groups and physical

adsorption of the mesoporous structure, the polysulfide shuttling was suppressed significantly. In addition, the F doping induced a pseudocapacitive effect for fast Li$^+$ diffusion, affording a dense and homogeneous Li deposition during repeated cycling.[249] However, most separator coating layers are unfavorable for the transfer/migration process of Li$^+$.[250,251] Very recently, a fluorinated covalent−organic framework (4F-COF)-based nanofluidic membrane was constructed for regulating the Li−S battery performance. The fluorine functionalities endowed the 4F-COF permselective nanofluidic channels to contain negatively charged sites, allowing Li$^+$ cations to enter the 4F-COF layers while repelling the anion (S$_6^{2-}$) transport (Figure 13f−h). With the fluorinated COF/ PP separator, a highly stable Li metal was achieved with plating/stripping for 2000 h at 1 mA cm^{-2}. Besides, the as-assembled Li−S batteries demonstrated a stable cycling performance for over 1000 times with 82.3% capacity retention at 2 C, a high rate capability with 568.0 mA h g^{-1} at 10 C, as well as an areal capacity of 7.60 mA h cm^{-2} at a high sulfur cathode loading (∼9 mg cm^{-2}).[245]

2.3.2. Fluorinated Binders and Current Collectors. It is commonly known that during battery cycling, the electrodes are vulnerable to mechanical stress (i.e., severe volume changes for conversion- and alloy-type electrodes). Therefore, insufficient binding strength leads to severe pulverization and further capacity degradation. Thus, serving to provide the cathode and anode electrodes with both interconnected structures and mechanical strength for sufficient electron transport and ion migration upon charging/discharging, the polymeric binder is of vital significance to the battery performance.[252] Recently, owing to the high thermal stability, strong adhesive strength, and electrochemical/chemical inert-ness with a symmetrical linear F-bonded carbon skeleton, PVDF has been recognized as the earliest and most popular binder material for commercial LIBs. However, with the increasing versatile requirements of practical battery tech-nologies, the current polymer binders should not only act as a binding reagent but also provide different functionalities, including high ionic/electric conductivity, stable electrode| electrolyte interphase, excellent polysulfide anchoring capa-bility, and improved mechanical strength to buffer the volume change. These features cannot be achieved by the current PVDF binder. Especially at large volume expansion, conven-tional PVDF binder will lose the adhesion as a result of the slippage of the linear chain in the electrode.[253] More specific reviews focusing on different binders and their corresponding developments have been conducted earlier.[254−256] In this section, we will mainly introduce the mechanisms and properties of fluorinated binders on the electrodes and further on the battery performance. The design and application of fluorinated binders in Li-based batteries will provide opportunities to develop advanced binders.

When it comes to layered oxide cathode materials represented by LiCoO$_2$, PVDF has been the most widely used binder in industry. It was found that the crystallinity of PVDF was reduced via embedding maleic anhydride-grated-PVDF (MA-*g*-PVDF) into PVDF, which is favorable for improving electrolyte uptake. As a result, the rate capability and cycle performance of the LiCoO$_2$ cathode were enhanced.[257] However, it was pointed out that the reduced crystallinity of PVDF with a lower molecular weight led to the decreased adhesion strength.[258] Therefore, the crystallinity degree should be carefully optimized and balanced to fulfill the

cathode performance. Unfortunately, it was demonstrated that the PVDF binder can be changed when charging the cathodes to a high voltage above 4.3 V. Due to the weak cohesive force, PVDF is unable to generate a robust layer on the cathode surface and easily causes detachment between cathodes and current collectors, which finally leads to continuous electrolyte decomposition and rapid capacity decay for high-voltage cathodes.[259−261] Therefore, it is necessary to explore electro-chemically inactive binders beyond PVDF. With the obvious advantage of strong adhesion to the electrodes and good thermal stability, PI has been proved to improve the battery performance. By introducing six −CF$_3$ functionalities per unit in the PI backbone (Figure 14a), the fluorinated PI (FPI) showed faster ion transfer, greater resistance to electrochemical oxidation, as well as higher thermal stability. The FPI had excellent binding ability to mitigate the degradation issue of the Li-rich cathode at 4.7 V while functioning as a surface protective layer on the cathode via constructing a robust thin film. The resulting cathode presented improved cycle stability in both half cells and full cells when paired with graphite anodes.[262] Moreover, employing ionic conductive polymers such as poly(ionic liquid)s (PILs) or single-ion conducting polymers (e.g., PEO) as binders has been considered as an effective strategy to improve the ionic conductivity and Li$^+$ diffusion rate for high-performance LIBs.[263−267] Typically, cationic or anionic species are bonded to polymer backbones in the PILs, contributing to the high Li$^+$ ionic conductivity as well as wide ESW.[268] By incorporating the ionic conducting lithiated poly(perfluoroalkylsulfonyl)imide (PFSILi) ionene with PVDF to serve as the binder, the LiFePO$_4$ cathode exhibited increased working voltage, lower electrochemical polarization, and higher reversibility than that with PVDF binder, especially operated at elevated temperatures or high current rates. Besides, a higher reversible capacity and energy density (1.50 and 1.66 times) of the LiFePO$_4$ cathode was enabled compared to the cathode with PVDF binder.[266] Lithiated perfluorosulfonate ionomer (Li−Nafion) was re-ported to demonstrate similar effects as the binder for LiMn$_2$O$_4$ cathodes. The resultant Li−Nafion binder displayed an ionic conductivity of 1.4 × 10^{-4} S cm^{-1}, generating an ion conducting layer on the LiMn$_2$O$_4$ cathodes, which reduced the interphase resistance for high-rate cycling (5−20 C) and stabilized the cathode even at high temperature (60 °C).[267] Zhao et al. prepared an ionic conducting binder by pairing sulfonated polyether ether ketone with pendant lithiated fluorinated sulfonic groups (SPEEK-FSA−Li) in which sulfonated aromatic poly(ether ketone) had good thermal/ mechanical stability; meanwhile, the charge delocalization over the lithiated fluorinated sulfonic side chains exhibited low lithium dissociation energy for improving Li$^+$ conductivity. The SPEEK-FSA−Li binder contributed to a much smaller interphasial and charge transfer resistance, an enhanced discharge plateau voltage, and a higher reversible capacity for the LiFePO$_4$ cathode, in contrast with that using PVDF binder.[265] Recently, the pyrrolidinium-type poly-(diallyldimethylammonium) (PDADMA) with fluorinated anions was used as a cathode binder, wherein the fluorine content (e.g., FSI, TFSI, bis(perfluoroethylsulfonyl) imide (BETI), and nonafluoro-1-butanesulfonate (CFSO)) led to highly delocalized charge density for facilitating Li$^+$ transport. The consequent high-voltage LiNi$_{0.5}$Co$_{0.2}$Mn$_{0.3}$O$_2$ (NCM 523) electrode achieved improved rate capability and stable cycling performance.[268] Introducing ion conducting materials into

polymer binders is considered as another effective strategy to improve the overall electrochemical performance of LIBs. Copolymerizing the hydrophilic 2-(perfluorohexyl) ethyl methacrylate (PFHEMA) and hydrophobic poly(ethylene glycol) methacrylate (PEGMA), Kuo and co-workers designed a Li$^+$ conducting waterborne fluorinated binder (Figure 14b). The fluorinated moiety was expected to improve the electrochemical stability and adhesive properties, while the PEO segments in PEGMA achieved higher ionic conducting ability. The copolymer can self-assemble into a series of spherical nanoparticles (150−220 nm) dispersed in aqueous solution. The results showed that with an optimal ratio of 3:1 (PFHEMA:PEGMA), the LiFePO$_4$ cathode delivered great cyclability over 150 cycles without obvious capacity decay and nearly 100% CE.[269]

Relying on the weak van der Waals force to connect active materials and other components within the electrodes, a conventional PVDF binder is unsuitable for alloy-type anode materials (e.g., Si) with drastic volume changes during battery cycling. In general, the ideal binders for alloy-type anodes should be chemically stabile at elevated temperatures, electrochemically inert to sustain a wide ESW, and mechanically tolerant to withstand extensive stresses while maintaining ionic or electronic conducting ability.[272,273] It has been elucidated that heating a Si electrode containing 8 wt % PVDF at 300 °C contributed to a more uniform distribution of PVDF on the surface of the active materials, which largely enhanced the adhesive strength and viscoelasticity for improved cycle performance with 600 mAh g^{-1} available capacity after 50 cycles.[274] Nevertheless, less than 20% of the theoretical specific capacity of the Si anode was left, which is still far from the requirement of practical application. Thus, combining PVDF with other polymers can be developed to satisfy the needs of high-performance Si-based anode materials. Based on a tether model in which the binder was filled with carbon black, Dahn and co-workers designed an elastomeric binder of terpolymer PVDF fluoride-tetrafluoroethylene ethylene copolymer (PVDF-TFE-P) for the Si$_{0.64}$Sn$_{0.36}$ alloy anode.[275] It was noted that 3-aminopropyltriethoxysilane was added as an adhesion promoter in the electrode, providing −NH$_2$ to bond with the carbon−carbon double bond in the backbone of PVDF-TFE-P. The resulting Si$_{0.64}$Sn$_{0.36}$ anode exhibited a stable reversible capacity of ∼800 mAh g^{-1} with a volume change of 125%. To further improve the PVDF performance in Si-based anode materials, amphiphilic graft copolymer precursors PVDF-*graft*-poly(*tert*-butyl acrylate) (PVDF-*g*-PtBA) have been synthesized, wherein poly(acrylic acid) (PAA) with abundant carboxylic acid (−COOH) groups was generated through in situ pyrolytic transformation of PtBA (Figure 14c). Taking advantage of the synergistic effects from polymeric backbones (PVDF and PAA segments), excellent mechanical properties against volumetric expansion were achieved, enabling high charge and discharge capacities of 2672 and 2958 mAh g^{-1}, respectively, along with a stable cycling performance over 50 cycles with 84% retention at 0.2 C. Moreover, this graft copolymer binder was proved to be effective in fulfilling the capability of both the LiN$_{0.5}$M$_{1.5}$O$_4$ cathode and the natural graphite (NG) anode, contributing to a high energy density of 546 Wh kg^{-1} along with ∼70% capacity retention after 50 cycles at both 0.5 and 1 C (1 C = 145 mA h g^{-1}) for the Si/NG‖ LiN$_{0.5}$M$_{1.5}$O$_4$ full battery.[270] As an alternative choice, owing to the apolar structures and enriched hydrogen-bonding sites, polytetrafluoroethylene

(PTFE) possessing high mechanical strain and tenacity was introduced, forming a PVDF-*b*-PTFE copolymer binder combining the high viscosity of PVDF with the high elasticity of PTFE. Besides, this binder achieved high ionic conductivity and thermal stability. As a consequence, the binder forms cobweb structures to coalesce Si particles, maintaining good electrical contact of the electrode materials during repeated cycles for superior cycle stability (∼1000 mA h g^{-1} capacity retained over 250 cycles).[276]

To strengthen the mechanical properties and further enhance the cycle stability of the Si-based electrodes, three-dimensional (3D) cross-linked binders with strengthened mechanical properties exhibited strong resistance to irreversible deformation of the Si-based electrodes, but they increased the stiffness of the electrode and finally deteriorated the electrochemical performance of the batteries.[276−280] From this point, Zhang et al. designed a fluorinated copolymer with massive polar groups (carboxylic acid, amide, and fluorinated groups) followed by thermal polymerized with sodium alginate (SA) to construct a dual-cross-linked network binder (FP2SA). It was found that esterification reactions among these functional groups formed a chemical cross-linked network; meanwhile, fluorine and nitrogen enhanced the reversible mechanical features during volume changes (Figure 14d). The uniqueness of this FP2SA, relying on both chemical and physical cross-linking, was able to maintain the structural integrity of the Si electrodes, contributing to a high specific capacity of 1557 mAh g^{-1} after 200 cycles at 4 A g^{-1}. More importantly, FP2SA binder also significantly improved the cycling performance of the Si−C electrode and the SiO-C electrodes with specific capacities of 600 mAh g^{-1} after 200 cycles at 0.5 A g^{-1} and 310 mAh g^{-1} after 700 cycles at 1 A g^{-1}, respectively.[271] However, it was revealed that an excessive cross-linked degree and fluorine content of the fluorinated binder could reduce the capacity and cycle stability of the Si-based electrodes, indicating a moderate cross-linking degree should be considered in designing such binders. In addition, lithiated fluorine-containing ionomers have been demonstrated as effective binders to improve the Li$^+$-ion diffusion as well as ionic conductivity, especially cycling at high rates. Wen and co-workers developed a novel fluorine-containing ionic binder (lithiated sulfonated poly(ether−ether−ketone)) with sulfonimide groups and structural flexibility, i.e., SPEEK-PSA-Li. Compared with other binders, the ionic conducting SPEEK-PSI-Li binder exhibited high adhesion properties and significantly decreased overpotential during high-rate cycling. Owing to the combined features of high cohesion capability, low solubility in electrolytes, high adaptability to volume change, and high ionic conductivity, the Si anodes displayed superior electrochemical performance under high-rate cycling, i.e., maintained reversible capacities of 2000 and 500 mAh g^{-1} at current densities of 400 and 2000 mA g^{-1}, respectively, after 50 cycles.[281]

Serving as an indispensable component to support both electrodes and to transport electrons between electrodes and the external circuit, the current collector plays a critical role in guaranteeing the highly efficient operation of LIBs. Since the commercialization of LIBs, Al and Cu foils have been the most widely used current collectors in the cathodes and anodes, respectively.[282] Nevertheless, electrochemical dissolution of Al and Cu current collectors still occurs during cycling, which is induced by the electrolyte decomposition or side reactions between electrolyte components and these current collectors.

As mentioned above, although the LiTFSI salt possesses advantageous properties such as high ionic conductivity, good thermal stability, and chemical inertness toward the active material, water contaminant, as well as other battery components, it fails to repassivate the Al foil by forming a fluorinated interphase. More specifically, the TFSI⁻ readily reacts with Al^{3+}, which is released from the Al_2O_3 passivation film, forming the soluble aluminum bis-(trifluoromethanesulfonyl)imide $(Al(TFSI)_3)$ product. The $Al(TFSI)_3$ then dissolves well in organic carbonate electrolytes and diffuses to the bulk electrolyte, causing severe capacity decay of Li-based batteries.[283] Despite huge attention having been paid to electrode materials engineering to enhance the battery performance, insufficient attention has been focused on this aspect, especially regarding the effects of fluorine chemistry on the current collectors. Since the review conducted by Lota et al. discussed the positive influence of fluorinated species on the Al current collector on the cathode performance, this section will mainly focus on the anode current collectors.[283]

Over the past few decades, intensive efforts have been devoted to achieving the dendrite-free plating/stripping of the Li anode, including SEI reconstruction,[146,168,276,284−292] uniformization of the Li-ion flux,[293,294] and 3D nanostructured scaffolds.[295−300] Among the existing approaches, interphase design and construction have been considered as an effective way to overcome problems toward the anode. Especially, the construction of halogenated interphases (e.g., LiF) is expected to effectively passivate the active Li surfaces, regulate the Li⁺ migration, suppress Li dendrite nucleation/growth, and enhance the interphase mechanical stability.[301−303] A columnar and uniform Li anode was designed by Zhang and co-workers through a LiF-enriched Cu current collector. When directly immersing a Cu foil into an aqueous $LiPF_6$ solution, the in situ hydrolysis of $LiPF_6$ occurred and coated LiF particles on the Cu surface. The LiF (100) was calculated to give a weaker binding energy and higher diffusion energy barrier to Li than that of the Cu surface (Figure 15a), rendering a uniform spatial distribution of Li⁺ and further contributing to the Li deposition with column structures. As a consequence, these ultrathin and columnar Li anodes exhibited highly improved cycle stability in both carbonate- and ether-based electrolytes.[304] As discussed earlier, PVDF has been extensively used as a binder, separator, or polymeric electrolyte in Li-based batteries. It is known that contrary to the nonpolar α phase PVDF with a trans−gauche−trans−gauche conformation, the β phase PVDF presents an all-trans conformation with F and H atoms distributed on the opposite sides of the PVDF backbone, which contributes to a high dielectric constant within 8−13. A thin (∼4 μm) β-PVDF was coated on the Cu current collector, achieving a uniform plating/stripping of Li at high current densities of 5 mA cm⁻², a high plating capacity of up to 4 mAh cm⁻², along with excellent cyclability. It was inferred that the strong interactions between Li⁺ and the polar C−F groups of β-PVDF could redistribute the Li⁺ flux, while the reaction of the PVDF surface and the fresh Li metal might form a stable and protective SEI layer. Besides, as illustrated in Figure 15b, the F alignment not only could promote the interaction between C−F and Li for layer-by-layer Li deposition but also offered preferential diffusion paths for Li⁺ hopping across the coating layer. This work highlights that constructing an electronegative F-rich interphase is favorable for the layer-by-layer Li deposition.[305] Another effective approach to enriching LiF on Cu substrate is
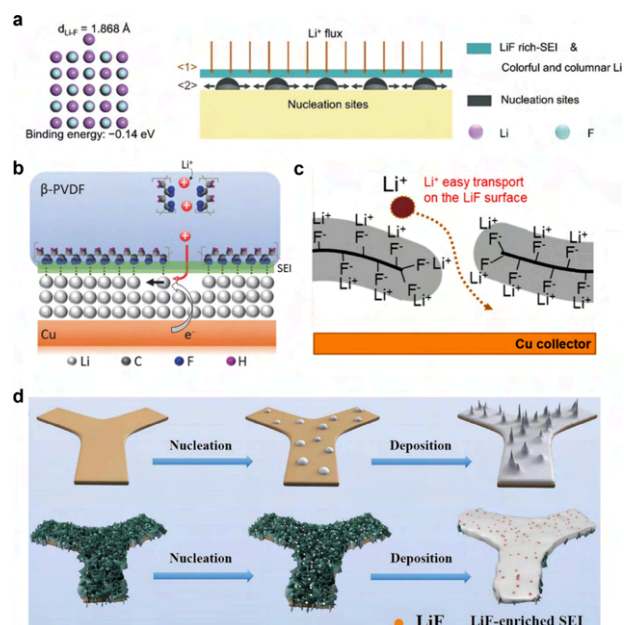
Figure 15. Role of fluorine modification of current collectors on constructing the stable SEI and regulating the Li deposition. (a) Theoretical calculations of the binding energy for Li on the LiF (100) surface, and schematic illustration showing the Li deposition process regulated by LiF (Note: (1) LiF-rich SEI leads to a uniform spatial distribution of Li⁺, (2) uniform and dense nucleation sites are generated on the Cu foil and grow horizontally from these nucleation sites). Reproduced with permission from ref 304. Copyright 2017 Wiley-VCH. (b) Schematics of the layer-by-layer deposition and preferential diffusion pathways for Li⁺. Reproduced with permission from ref 305. Copyright 2018 Wiley-VCH. (c) Mechanism illustration of the SEI growth on the F-ECG surface after Li plating/stripping. Reproduced with permission from ref 309. Copyright 2022 Elsevier. (d) Schematic illustration of the Li nucleation and plating process on the pure Ni foam and the NiF$_x$@NF current collectors. Reproduced with permission from ref 311. Copyright 2020 Elsevier.

employing fluorinated carbon materials such as fluorinated porous carbon materials and fluorinated carbon nano-tubes.[306,307] For instance, Zhi et al. designed a 3D-fluorinated porous carbon as the multifunctional host, which mitigated dendrite growth and was retained for over 300 cycles with an average CE of 99% at 0.5 mA cm⁻² (cycling capacity of 1 mAh cm⁻²). Nevertheless, this host matrix sustained only 70 cycles with fluctuated CE when increasing the current density and cycling capacity to 2 mA cm⁻² and 2 mAh cm⁻², respectively.[308] Based on this work, a novel LiF-rich dual-functional coating layer was designed on a Cu surface by Su and co-workers using fluorinated electrochemically exfoliated graphene (F-ECG) as a modifier. Thanks to the strong interlayer adhesion, the F-ECG layer could prevent volume expansion during plating/stripping cycles. In addition, LiF-enriched SEI film was successfully generated due to the reaction between Li and CF. This suppressed side reactions and facilitated Li⁺ transport across the coating layer for a dendrite-free Li anode with long-term stability (Figure 15c).[309] In another report, a self-assembled monolayer (EAM) of 1,3-benzenedisulfonyl fluoride was introduced on the Cu substrate, where the benzenesulfinate created lithiophilic sites and fluoride generated a LiF nuclei in situ via self-assembly and thiol−Cu reaction. Notably, the EAM-modified Cu displayed a multilayer SEI composed of a LiF-enriched inner layer and an

amorphous outer layer, regulating the Li nucleation and uniform Li growth on the Cu substrate.[310]

Apart from introducing a F-rich coating/modification layer on the Cu current collector, the Li halides (e.g., LiF) can also be formed via the reaction between metal halides and highly active Li, achieving highly enhanced interphasial stability.[312] Through a one-step fluorination treatment, a hybrid NiF_x@NF current collector consisting of vertical lithiophilic NiF_x nanosheets and Ni foam was developed by Huang et al. The NiF_x decreased the Li nucleation barrier and served as even nucleation sites for Li deposition. Besides, a LiF-enriched SEI derived from the reaction between NiF_x and Li during the initial Li plating was constructed, ensuring smooth Li deposition (Figure 15d). Benefiting from this 3D NiF_x@NF current collector, outstanding Li stripping/plating with a CE of ~98% over 450 cycles was obtained (at 1 mA cm^{-2} and 1 mAh cm^{-2}). The Li@NiF_x@NF symmetric cell demonstrated a long cycle life over 1300 h with a low overpotential of ~20 mV (1 mA cm^{-2}, 1 mAh cm^{-2}). Remarkably, the as-prepared Li@NiF_x@NF‖LFP full cell exhibited reasonable cycle performance and rate capability.[311] Recently, using a facile and safe NF_3 plasma fluoridized strategy, the NiF_2 layer was successfully coated on Ni foams (NFF). Following the same way, the Li$^+$ flux preferentially deposited on the NiF_2 sites, which was evenly distributed around the Ni surface. Also, the LiF-rich SEI layer from the NiF_2 reaction toward Li greatly enhanced the interphasial stability. As a result, the NFF@Li anode sustained a long durability over 1600 cycles at 1 mA cm^{-2} and over 2000 cycles at 2 mA cm^{-2}. Moreover, the NFF@Li‖LFP full battery delivered a high-capacity retention of 93% over 250 cycles at 1 C. These works demonstrated that constructing a lithiophilic metal fluoride coating is effective in regulating the Li deposition for a high-performance Li metal anode.[313]

Besides current collector modifications, interphase engineering has been recognized as a crucial strategy to stabilize the Li anodes since most of the knotty issues restricting the performance of Li metal anodes can be attributed to the instability of the Li anode/electrolyte interphase. Among them, constructing fluorinated interphases demonstrates prominent advantages in passivating active Li surfaces, regulating the diffusion and migration of Li$^+$, as well as enhancing the interphase mechanical stability. In particular, LiF has been determined to possess many extreme properties relative to other solids. The large band gap (14.6 eV) and the wide electrochemical stability window (from 0 to 6.4 V vs Li) of LiF contribute to the high electrochemical stability for inhibiting the continuous corrosion of active metallic Li;[314] the high Young's modulus (65 GPa) along with a high shear modulus (49 GPa) effectively enhance the mechanical stability of the SEI to enable long-term cycling;[315] the high interphase energy (γ) can promote a uniform Li distribution and smooth Li deposition behaviors[316] with the negligible solubility of LiF in most electrolytes,[303] etc. A variety of strategies, including physical methods and chemical strategies, have been developed to construct a LiF-rich artificial SEI.[289,317−329] Compared with physical methods, chemical approaches (e.g., gas-, liquid-, and solid-phase reaction methods) via regulating chemical reactions between Li- and F-containing precursors were used to resolve the interphase issues between the artificial layer and the Li metal matrix. As a representative F-containing gas reaction strategy, a LiF coating was developed via treating Li metal in fluorine gas flow. The LiF layer was chemically stable and mechanically strong, significantly suppressing the

corrosion reaction between Li and carbonate electrolytes and thus realizing steady cycling for over 300 times with a high current density of 5.0 mA cm^{-2}.[289] The gas reaction method will not introduce other impurities; however, great attention should be paid to fluorine gas during operation to prevent leakage. In contrast, the LiF-rich interphases constructed via liquid-phase deposition/reaction strategies have been recognized as simpler and more effective strategies. By interposing an oil drop enriched in C−F (perfluoropolyether, PFPE) with low surface energy, a flowable fluorinated interphase was constructed for stabilizing the Li metal and regulating the Li plating. The electron-withdrawing feature of F endows the PFPE with high thermal and oxidative stability, along with good chemical inertness and nonflammability. In addition, the PFPE moieties close to the Li triggered C−F and Li−F species to reinforce the robustness of the SEI and the compactness of the Li plating.[322] Polymeric coating layers generally display superior mechanical deformability and low density, which are promising for constructing LiF-rich interphases. As reported by Goodenough et al., after incorporating graphite fluoride (GF) in molten Li at 250 °C, a LiF layer was produced by the strong reaction between Li metal and the GF, eventually obtaining a GF−LiF protective layer. This as-prepared composite Li metal anode demonstrated high stability in an ambient environment as well as comparable electrochemical performance.[330]

To conclude, fluorine plays a critical role in modifying other components for enhancing the battery performance. Regarding separators, structural modifications and blending with other polymers or inorganic nanoparticles can address limitations such as low mechanical strength, thermal instability, and Li$^+$ transport restrictions of PVDF. Besides, fluorine modification (e.g., surface coating and grafting method) can improve fire retardancy, mechanical abuse resistance, and LiF-rich SEI formation in Li metal batteries. Meanwhile, the abundant polar −CF_3 groups would offer an electronegative environment to promote Li$^+$ transfer. For binders, the fluorine group can be incorporated into polymer binders, enhancing ion transfer, oxidation resistance, and thermal stability, while fluorinated anions combined with ionic conductive polymers improve the binder performance for the cathode. However, excessive fluorine content in binders may compromise the specific capacity and cycle stability of these electrodes. When utilizing to modify current collectors with Li metal anodes, construction of LiF interfaces on Cu current collectors is expected to passivate the active Li surface and regulate the Li$^+$ migration, further suppressing Li dendrite growth.

3. UNDERSTANDING FLUORINATED INTERPHASES IN LI-BASED BATTERIES

3.1. Fluorinated Solid Electrolyte Interphases on Anodes

It is now broadly accepted that the SEI is significant for Li-based battery systems. In 1979, Peled et al. reported a SEI model that was applicable to all alkali metals in nonaqueous battery systems.[331] The SEI layer forms instantaneously upon contact between the anode and the electrolyte solution and consists of insoluble and partially soluble products generated by the reduction of electrolyte components. It exhibits properties similar to a layer of solid electrolyte with high electronic resistivity. As reported in recent years, the SEI played a significant role in determining the safety, power capability, reversibility, and cycle life of Li-based batteries.[332] The SEI must be both mechanically stable and flexible and
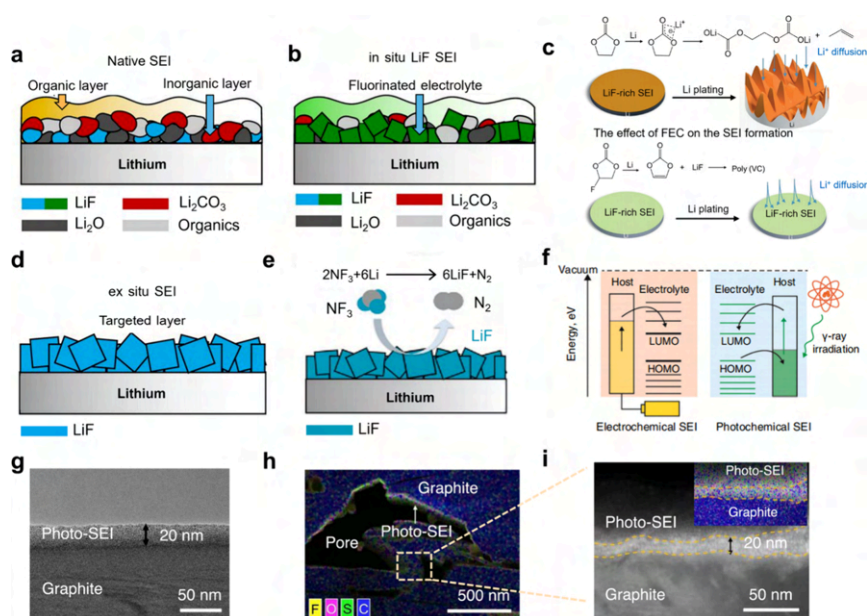
Figure 16. Different formation paths of the fluorinated SEI. (a) Native SEI from conventional carbonate electrolytes without fluoride enrichment. (b) In situ LiF-enriched SEI from fluorine-rich electrolytes. Reproduced with permission from ref 342. Copyright 2020 PNAS. (c) Decomposition mechanism of EC and FEC and the effect on SEI formation at the Li metal anode and Li diffusion near the anode surface. Reproduced with permission from ref 130. Copyright 2019 Wiley-VCH. (d) Ex situ LiF-enriched SEI from nonelectrolyte fluorine sources. (e) Schematic of the Li−NF$_3$ reaction to form LiF layers on Li. Reproduced with permission from ref 342. Copyright 2020 PNAS. (f) Distinct energy schemes in the formation of the SEI using electrochemical and photochemical approaches. (g) Cs-TEM image of the photographite with the photochemically driven SEI layer. (h) Low-magnification energy-dispersive X-ray spectroscopy (EDS) elemental map of the photo-SEI inside the pores of the photographite electrode. (i) High-magnification Cs-TEM image of the photo-SEI image and the corresponding EDS map (inset). Reproduced with permission from ref 343. Copyright 2021 Springer Nature.

should adhere well to the anode, while it is crucial to prevent the dissolution or corrosion of the anode. Therefore, the electrolyte must be designed to contain at least one SEI precursor that reacts rapidly with the anode to form an insoluble and stable SEI.

3.1.1. Components of the SEI. The chemical composition of the SEI on the anode side is highly dependent on the type of conducting salts, solvents, and additives. Although the role of these components in the formation of the SEI has not been fully understood, the presence of species such as LiF, fluoroborates, and fluorophosphates indicates the involvement of fluorinated components in the reduction mechanism of the electrolyte. LiF, in particular, has been identified as a major component of a fluorinated SEI, playing a critical role in regulating the diffusion of Li ions and the strength of the SEI.[289,333,334] Archer and co-workers showed that the presence of halide anions, especially fluorides, significantly increases the surface diffusivity of Li ions at the interphase between the electrolyte and the Li metal anode.[333] The role of LiF in a fluorinated SEI in regulating the nucleation and growth of Li deposition in LMBs was further investigated by a designed model system.[304] The fluorinated SEI facilitated uniform spatial diffusion of Li ions in carbonate- and ether-based electrolytes and guided the deposited Li into an ordered and aligned columnar structure.

Significant efforts have been made to develop artificial fluorinated coatings to enhance SEI performance, including inorganic LiF coatings and LiF-based composite coatings.[320,335,336] While computational simulations have provided insights into the diffusion mechanism of Li ions through fluorinated SEI, the practical SEI in practical battery systems is more complex and needs to be fully understood.[89,337]

Mashayek and co-workers elucidated that Li diffusion in the grain boundaries is generally faster than that in bulk, and the heterogeneous LiF/Li$_2$O grain boundaries demonstrate the fastest Li-ion diffusion rate compared to the homogeneous LiF/LiF and Li$_2$O/Li$_2$O.[89] Further research is needed to comprehend the diffusion mechanism of Li ions through the SEI for practical applications.

3.1.2. Formation of a Fluorinated SEI. The formation of SEI can be generally classified into three modes: the "native" SEI is multicomponent including inorganic and organic phases formed by parasitic reactions between the anode and the electrolyte,[331,338] the "in situ" SEI formed over cycles of cells, and the "ex situ" SEI artificially applied on the anode surface.[339] LiF is a recurring motif found in nearly all functional SEIs (Figure 16a) given that fluorine is commonly present in prevailing electrolyte salts.[340] Among the SEI components, LiF is particularly spotlighted due to its high mechanical strength, low solubility, wide ESW (0−6.4 V vs Li/Li$^+$), and low calculated barriers to Li diffusion. Besides, Wang et al. calculated the interfacial energy of different SEI components, among which LiF exhibited the highest interfacial energy of 73.28 meV Å^{-2}, suggesting significant Li dendrite suppression ability.[323] These properties suggest that LiF may contribute to a homogeneous Li flux and robust SEI, making it a beneficial phase for the SEI on the anode side in recent years.[341]

Multiple studies have indicated that fluorine or fluoride enrichment in the electrolyte results in a LiF-enriched (in situ) SEI, as shown in Figure 16b. F-enriched electrolytes have included additives such as HF[344] and high loadings of LiF salt[333] as well as solvents such as FEC,[168] thus making significant improvements in the cycling stability and high CE
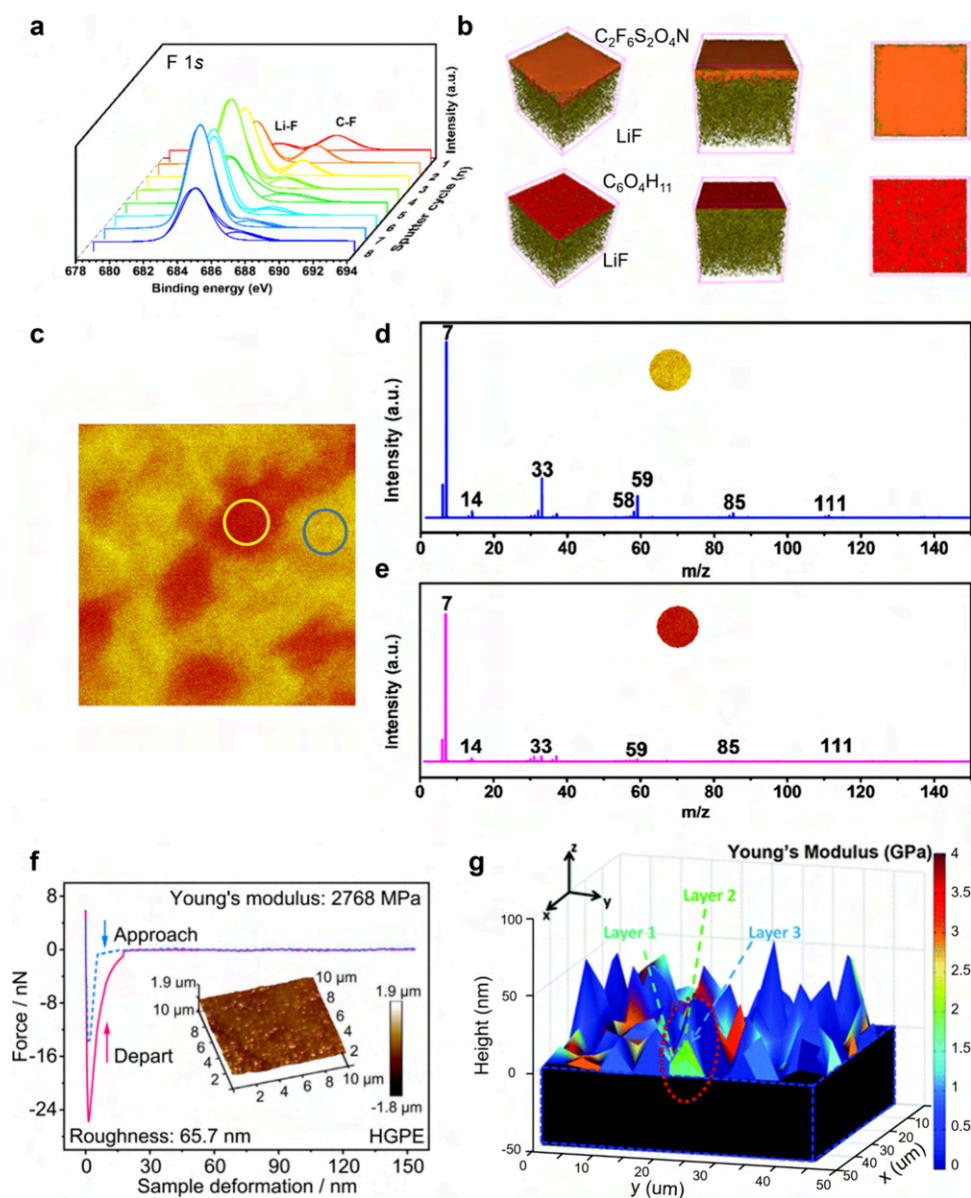
Figure 17. Characterization of fluorinated SEI in Li-based batteries. (a) F 1s XPS depth profile of the Li anode. (b) 3D distribution overlay between LiF and $C_2F_6S_2O_4N$ (upper panel) and between LiF and $C_6O_4H_{11}$ (lower panel). (c) Total mapping distribution and (d, e) related mass spectrum of the SEI on Li-metal anode (1 M LiTFSI−DME/DOL, 1:1 by volume with 2% $LiNO_3$). Reproduced ref 351. Copyright 2022 American Chemical Society. (f) Heteroatom-based gel polymer electrolyte (HGPE)-derived SEI. (Inset) Corresponding 3D-AFM scanning images of SEI layers. Reproduced with permission from ref 353. Copyright 2021 Springer Nature. (g) Cross-section view of 3D plots. Black substrates indicate Li−Si alloys, and the z axis gives the thickness of the SEI films. The color bar of 0−4 GPa shows the Young's modulus for the SEI films. Reproduced with permission from ref 354. Copyright 2014 Royal Society of Chemistry.

(∼89−99%). Postmortem analysis of cycled Li surfaces typically presents high levels of LiF. Figure 16c explains how the FEC molecule affects the mechanisms of SEI formation and the composition.[345] The breaking of C−F bond leads to the formation of LiF and vinyl carbonate (VC),[168] which results in a thinner SEI that prevents further electrolyte decomposition.[346] Such LiF-rich SEI prohibits high surface area lithium growth during Li stripping and plating.[170]

Ex situ fabrication of LiF layers on Li or Cu current collectors has also been widely studied, leading to the formation of an artificial (ex situ) LiF-enriched SEI (Figure 16d). Synthetic methods include hydrolysis of $LiPF_6$ on Cu,[304,347] reactions between Li and fluorinated precursors,[289,319] physical vapor deposition,[348] and atomic layer

deposition (ALD).[318,349] To fabricate ex situ SEI layers, Gallant et al. used nitrogen trifluoride (NF_3) gas to directly grow LiF on the Li foil (Figure 16e).[342] The reduction of NF_3 as a fluorinated gas cathode in Li batteries led to copious amounts of LiF under electrochemical conditions.[350] Additionally, γ-rays can induce an artificial SEI layer with a favorable composition, and the composition of the SEI layer has a substantial effect on the charging rate. Choi et al. reported a γ-ray-driven SEI layer that allowed the battery to be charged to 80% capacity in 10.8 min of 2.6 mAh cm^{-2}. This exceptional charging performance was attributed to the LiF-rich SEI induced by salt-dominant decomposition via γ-ray irradiation.[343] Figure 16f illustrates the electron transfer in both electrochemical and photochemical processes. For the

electrochemical process, electrons were transferred unidirectionally from graphite to the LUMO level of the electrolyte to form the SEI layer, regulating compositions with relatively fewer components of the SEI layer. Besides, γ-ray irradiation could drive radical intermediates, and irradiation with γ-rays could preferentially decompose compounds, which improved the tunability of the SEI composition. The Cs-TEM image of photographite indicates that the photo-SEI layer was uniformly deposited on the graphite surface with a thickness of ~20 nm (Figure 16g). The photo-SEI layer was also observed to exist in the inner pores of the graphite particles (Figure 16h and 16i), implying that γ-ray irradiation was effective even in the interior of the graphite.

3.1.3. Distribution and Impacts of Fluorides on the SEI.

The structure and chemical components of the SEI layer at different depths can be investigated by X-ray photoelectron spectroscopy (XPS) depth profiles. Taking the electrolyte of 1 M LiTFSI in DME/DOL (1:1 by volume) as an example,[351] the main elements of SEI are C, N, O, F, and S, which originated from the reduction reaction between the electrolyte and the Li anode. The depth analysis curves of the SEI are shown in Figure 17a. It can be observed that the signal of the element F increased with increasing sputtering time. The binding energies of 685.0 and 688.3 eV in the F 1s diagram represented Li−F and C−F. The intensity of the C−F signal on the surface was higher than that of Li−F, which indicated that residual LiTFSI salts existed on the surface. The time-of-flight secondary ion mass spectrometry (TOF-SIMS) technique can be applied to further investigate the SEI (Figure 17b). The inorganic phases of LiF-based compounds in 1 M LiTFSI in DME/DOL (1:1 by volume) with 2% $LiNO_3$,[351] such as LiF ($m/z = 26$), LiF_2 ($m/z = 45$), LiF_3 ($m/z = 64$), and Li_2F_3 ($m/z = 71$), were evenly distributed in the inner SEI layer. By overlaying the 3D distribution results of LiF ($m/z = 26$), $C_2F_6S_2O_4N$ ($m/z = 280$), and $C_6O_4H_{11}$ ($m/z = 147$), it was found that the Li salt was evenly distributed at the outermost SEI layer, which completely covered the LiF product. The results indicate that the SEI may not be a dense layer and the liquid electrolyte can be stored between the organic phase and the inorganic phase.[352] As shown in Figure 17c, two circles with equal area were extracted from the mapping image to obtain their mass spectrum. Compared to the light region (Figure 17d), the intensities of the ion fragments with mass charge ratios (m/z) of 14, 33, 59, 85, and 111 decreased in the dark region (Figure 17e). Such fragments may come from the inorganic phase products formed by the strongly electronegative atoms and the Li metal after the decomposition of LiTFSI, such as N, Li_2F, Li_3F_2, Li_4F_3, and $Li_5N_2O_3$.[351] Among them, Li_2F ($m/z = 33$) and Li_3F_2 ($m/z = 59$) exhibited the highest density, which suggested a strong electronegativity of fluorine in LiTFSI. These products were the main components of the inorganic phase of the SEI layer.

The Young's modulus of the SEI layer serves as a crucial metric for assessing the strength of the SEI, since a robust SEI can suppress the repeated rupture−reconstruction of the SEI due to the severe volume changes of the anodes during cycling. Such thin and stable SEI leads to low impedance of the interphase, thus enhancing cycling performance.[166] The Young's modulus of the SEI can be evaluated by 3D atomic force microscopy (3D-AFM) scanning. The proportion of LiF greatly increases the mechanical strength of the SEI (i.e., LiF possesses a shear modulus of 55.1 GPa, almost 11 times higher than that of Li metal (4.9 GPa)), which can significantly

enhance the strength and interphasial energy of the SEI layers.[355] As a result, the SEI consisting of homogeneous LiF makes the anode more robust and uniform (Figure 17f). A 3D Young's modulus plot of discharged silicon electrodes with all force curves in a certain area can be drawn according to Young's moduli at each position at different indentation lengths on the surface of discharged anodes.[354] Some area was not covered by the SEI, and some area was covered by the thick SEI. The soft part of the SEI was always covering the outer layer. This can also be obtained from a cross-section view of the 3D plot, as shown in Figure 17g.[354] The uncovered area and the area with different layered structures with different Young's moduli can be observed clearly. This indicated that the organic species is usually situated on the outside with lower strength, and inorganic species like LiF support the internal SEI strength. It is, therefore, essential to explore the distribution and homogeneity of SEIs.

Despite the phenomenological improvements observed, it remains uncertain whether LiF has a directly beneficial function in the formation of the SEI. Variations among LiF-forming approaches (i.e., in situ vs ex situ) and the electrolytes used would lead to confusion in the understanding. For example, conflicting results about ex situ LiF were found in different works. A standalone layer was found to decrease CE due to inhomogeneous Li deposition,[349] whereas LiF layers on Li were elsewhere reported to improve cycle life in Li‖Li symmetric cells.[289,318] Additionally, LiF is an ionic insulator ($\sim10^{-13}$−10^{-14} S cm^{-1}), and it seems counterintuitive that LiF-enriched SEIs can impart benefits related to Li transport.[356] It remains unclear how such physical properties of LiF can support performance improvements.

3.2. Fluorinated Cathode−Electrolyte Interphases

The presence of a CEI layer was first suggested by Goodenough et al. on the $LiCoO_2$ cathode.[357] Considering that the interphasial reactivity increases at high-voltage cycling, the CEI layer behavior demonstrates an even more complicated response. When the cutoff voltage is increased to 4.5 V, the CEI layer becomes unstable and decomposes, as reported by Cherkashinin et al.[358] Until now, the detailed constituents and electrochemical behavior of the CEI layer have been under debate. However, it is generally accepted that the CEI is extremely sensitive to various factors, such as electrolyte composition, current densities, and cutoff voltage.

Previous studies usually treated the formation of the CEI layer independently. However, recent research results discovered a close relationship between the formation of the CEI on cathodes and the formation of the SEI on anodes.[359−361] A well-known example is the transition metal ion dissolution from cathode materials, which affects the SEI formation on anodes.[362,363] Recently, Xiong et al. verified the interaction between the ternary cathode (i.e., $Li(Ni_{1/3}Mn_{1/3}Co_{1/3})O_2$ and $Li(Ni_{0.42}Mn_{0.42}Co_{0.16})O_2$) and the graphite anodes in batteries operating at high temperature and high voltage.[364] Jung et al. also demonstrated the enhanced cycling performance of the $LiCoO_2$‖graphite full cells by mitigating the coupled side reactions through Al_2O_3 coating on the cathodes.[365] Noting that plenty of studies demonstrated that if the cathode was cycled in the high-voltage range, the effect of repeated formation−decomposition of SEI layers on Li anodes significantly influenced the formation of CEI layers on the cathodes. A deep investigation of the reactions on both the cathode and the Li anode is necessary to collect credible
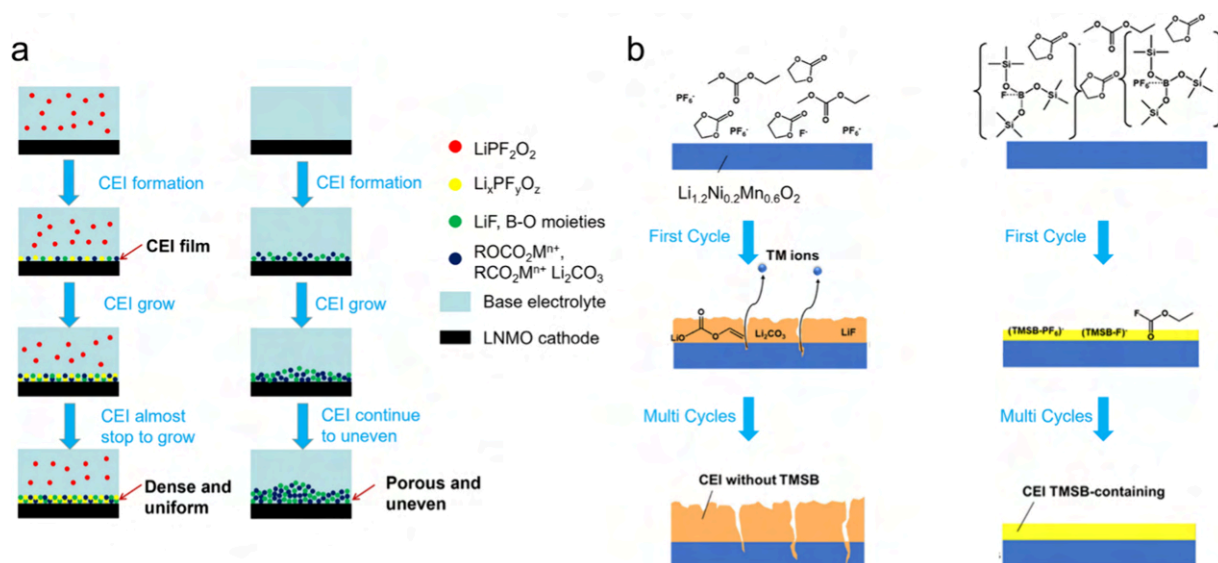
Figure 18. Formation of fluorinated CEI of Li-based batteries. (a) Proposed mechanism of the LiDFP participating in the formation of CEI film. Reproduced with permission from ref 370. Copyright 2019 Elsevier. (b) Schematic of CEI formation during cycling in conventional and TMSB-containing electrolytes. Reproduced ref 371. Copyright 2019 American Chemical Society.

properties of the CEI layer on the cathode and achieve comprehensive understanding of the CEI formation mechanism.

3.2.1. Formation of a Fluorinated CEI. It is widely accepted that the CEI layer contains both inorganic components (e.g., LiF) and organic species (e.g., carbonates and oligomers/polymers).[366−368] In situ neutron scattering further proved that the CEI layer presented dynamic evolution during battery cycling within a low cutoff voltage (4.2 V vs Li/Li$^+$). The thickness of the CEI layer gradually increases upon cycling.[369] Li and co-workers reported the progress of CEI formation with and without electrolyte additives.[370] As shown in Figure 18a, the CEI formed in the base electrolyte of 1 M LiDFOB−ethyl carbonate(EC)/DMC (1:1 by volume) was too loose to prevent direct contact between the electrolyte and the cathode; thereby, the carbonate solvents and salts underwent continuous decomposition reactions at high voltage, and the decomposition products were continuously deposited on the surface of the cathode, which caused continuous growth of the CEI layer. In contrast, for the CEI film formed in the electrolyte with the lithium difluorophosphate (LiDFP) additive, the preferred decomposition of LiDFP promoted the formation of a dense CEI film, effectively preventing the direct contact between the electrolyte and the cathode.

Figure 18b exhibits the mechanism of CEI formation with and without the fluorinated additive tris(trimethylsilyl)borate (TMSB).[371] Generally, the large polarity of EC molecules made them easily diffuse to the cathode surface with anions by a strong electrostatic force during the charge process. Hence, the cathode surface is EC/anion rich before CEI formation, which makes EC easily decompose. However, this effect gets impaired after the addition of TMSB because of the generation of the polyanion group (TMSB−PF$_6$)$^-$ and (TMSB−F)$^-$ with weaker electrostatic force and less electronegativity. As a result, EC decomposition is suppressed effectively. Moreover, TMSB can participate in CEI formation by electrochemical reactions or by directly entering the CEI layer in the form of a polyanion group to optimize the quality of the CEI. The HOMO level

(−6.749 eV)[372] of TMSB is higher than that of the carbonate solvents (−11.905 eV for EC and −11.541 eV for EMC),[373] which offers an opportunity to participate in the formation of a high-quality CEI film before solvent decomposition to protect the active cathode material from erosion of the electrolyte and alleviate the capacity and voltage fading of Li$_{1.2}$Ni$_{0.2}$Mn$_{0.6}$O$_2$.[374]

3.2.2. Impact of the Fluorinated CEI on Battery Performance. Unlike the SEI, CEI formation involves not only the electrolytes but also active components in the cathodes, including transition metal dissolution, H abstraction from the solvents, and the formation of superoxides or peroxides. For unmodified NMC811 or LiCoPO$_4$ (LCP) cathodes (Figures 19a), electrolyte components experience continuous oxidation until a dense and uniform CEI layer forms and blocks the electron transfer from the electrolyte to the cathodes. Compared with EC/DMC- and FEC/DMC-based electrolytes, the extremely high CEs achieved by the all-fluorinated electrolyte on aggressive cathodes should originate from the F-rich CEI that deactivated the catalytic activity of the NMC or LCP cathodes. Quantum chemistry calculations predict that direct oxidation of solvent molecules is energetically unfavorable around 5 V. Instead, solvent oxidation is accompanied by H transfer to another solvent and/or cathode surface. Intermolecular H transfer takes place around 5 V for EC and >5.5 V for FEC, FEMC, and HFE. When the oxidation potential is calculated assuming open-loop EC$^•$ and FEC$^•$ radicals as the products, the oxidation stability decreases to ~4.2 and 4.9 V, respectively. Thus, EC-containing electrolytes are expected to be oxidized from 4.2 V, even in the absence of the active materials. EC is a poor CEI former because the EC$^•$(−H) radical decomposes with a barrier of only 0.91 eV to evolve CO$_2$, leaving only a fraction of EC$^•$(−H) radicals to participate in the second H abstraction, eventually leading to polymerization. The resulting hydrogen-rich polymer is still susceptible to further degradation. Because of the higher barrier (1.28 eV) for the FEC$^•$(−H) ring-opening reaction compared to that of EC$^•$(−H), the FEC$^•$(−H) is a longer lived radical compared to EC$^•$(−H) and will probably react with the formed FEMC$^•$(−H) and 1,1,2,2-tetrafluoroethyl-2′,2′,2′-
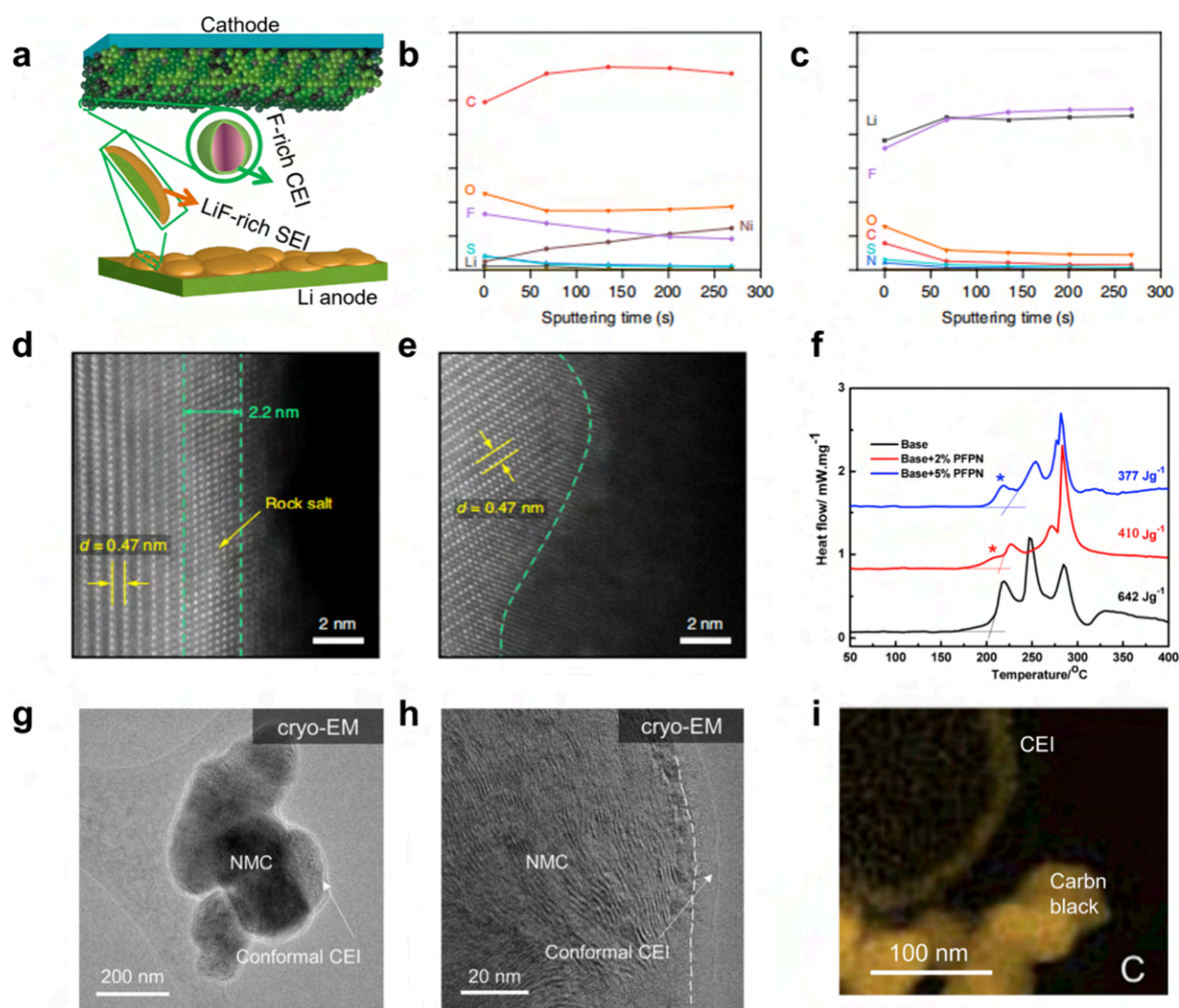
Figure 19. Characterization of fluorinated CEI in Li-based batteries. (a) SEI and CEI chemistries formed in all-fluorinated electrolyte. Reproduced with permission from ref 375. Copyright 2018 Springer Nature. Quantified atomic composition ratios of the CEI obtained by XPS spectra for the NMC811 electrodes collected from cells with (b) 1 M LiFSI−DME and (c) 1 M LiFSI−DME/TFEO electrolyte after 100 cycles. HAADF-STEM of NMC811 electrodes collected from cells with (d) 1 M LiFSI−DME and (e) 1 M LiFSI−DME/TFEO electrolytes after 100 cycles. Reproduced with permission from ref 376. Copyright 2019 Springer Nature. (f) Heat flow profiles of the Li_xCoO_2 charged to 4.5 V after 2 cycles in the absence and presence of PFPN. Reproduced with permission from ref 178. Copyright 2017 Elsevier. (g, h) Cryo-EM images of conformal CEI formed on NMC cathodes. (i) Cryo-STEM EELS mapping of conformal CEI on NMC electrodes (yellow for carbon element). Reproduced with permission from ref 377. Copyright 2021 Elsevier.

trifluoroethyl ether (HFE)•(−H) radicals near the cathode surface, resulting in a fluorine-rich CEI as observed by Fourier-transform infrared spectroscopy. Alternatively, fluorinated radicals also bind to oxygen in $CoPO_4$, preventing the OH formation that facilitates transition metal dissolution. Thus, in all-fluorinated electrolytes, the composition of a protective CEI is inevitably highly fluorinated.[375]

Figure 19b and 19c shows the atomic ratios of the CEI layer formed on the surface of the NMC811 cathode in different electrolytes.[376] An LiF-rich CEI was formed on the cathode surface in the tris(2,2,2-trifluoroethyl)orthoformate (TFEO)-based electrolyte, while in the controlled carbonate and 1 M LiFSI in DME electrolytes, organic-rich CEIs were obtained. Figure 19d and Figure 19e shows the high-angle annular dark-field scanning transmission electron microscopy (HAADF-STEM) imaging results of the cycled NMC811 electrodes.[376] The structure reconstruction appeared in the NMC811

electrode cycled in 1 M LiFSI−DME with a rock salt layer (∼2.2 nm) (Figure 19d). The surface lattice layers of the NMC811 electrode underwent some degree of mixing, with the Li sites partially occupied by antisite Ni ions.[378] In contrast, the electrode surface maintained a layered structure under the same cycling condition in 1 M LiFSI−DME/TFEO (Figure 19e). Such a result indicated the effective suppression of detrimental phase transformation. These beneficial effects can be attributed to the formation of a uniform LiF-rich CEI layer,[379] while the uneven and organic-rich CEI is less protective.

The thermal stability of both the electrolyte and the cathode material at the charged state is of vital importance to battery safety. Differential scanning calorimetry (DSC) was carried out to unravel the thermal stability of the electrolyte and electrode material. Figure 19f shows the DSC curves of the electrolyte with (phenoxy)pentafluorocyclotriphosphazene (PFPN) (red

and blue) and without PFPN (black).[380] It can be clearly seen that the main decomposition peak of the electrolyte shifted toward a higher temperature with the addition of more PFPN, indicating that the thermal stability of the electrolyte had been considerably improved. Several peaks can be identified in the DSC curves, corresponding to the step-by-step decomposition of the charged Li_xCoO_2 material.[380] The electrolyte decomposition/oxidation at the surface of the Li_xCoO_2 electrode usually occurs at around 200 °C.[381] In the presence of 2% PFPN, a new peak (indicated by the red asterisk) at 206 °C from the red DSC curve can be assigned to the thermal−polymerization reaction of PFPN. The calculation results (200−300 °C) demonstrate that the total exothermic heat generated from the Li_xCoO_2 electrode in the presence of PFPN (2% PFPN, 36.1%; 5% PFPN, 41.3%) was less than that from the Li_xCoO_2 electrode in the absence of PFPN (black), indicating that the thermal stability of the charged Li_xCoO_2 electrode was distinctly improved after the addition of electrolyte additive.[178] The layer of the CEI after brief shorting on the positive electrode particle can be observed by cryogenic electron microscopy (cryo-EM) (Figure 19g and 19h). The electrode particle was uniformly coated with a thin layer of mostly amorphous materials, spanning from ∼5 to 10 nm at the edge of the interphase. Furthermore, the conformal CEI and carbon black additives yielded an annular dark-field image along with a C K-edge map (Figures 19i), which indicated the organic polymeric composition of alkyl carbonates.[377]

Fluorinated electrolytes have shown significant potential in achieving improved performance and safety in high-voltage batteries. When hydrogen atoms in the electrolyte are replaced with fluorine atoms, the activation energy is reduced[169] and the HOMO and LUMO energy levels decrease, leading to increased reduction and oxidation potentials.[345,382−384] The decrease in HOMO energy level enhances the cycling performance by promoting the early formation of an effective CEI layer and reducing the overall impedance.[130,384,385] Numerous fluorinated CEI-forming additives have been reported in recent years.[386−388] Future research should focus on understanding the impact of the fluorine atom on the overall performance of Li-based cell chemistry, involving (i) correlating the molecular and (ii) electronic structures of fluorinated electrolyte components, (iii) identifying relevant physicochemical properties and (iv) reactivity, which includes investigating synergistic effects between fluorinated and nonfluorinated electrolyte components, studying the main operation and failure processes in Li-based cells, exploring different plausible reaction pathways, and analyzing the limiting and determining steps that rationalize the results. Systematic research on CEI electrochemistry/chemistry will enable the development of high-performance Li-based batteries with high energy density, energy efficiency, and superior capacity retention.

3.3. Critical Role of Fluorinated Interphases for Extreme Li-Based Batteries

With the continuous upsurge in demand for energy storage, Li-based batteries are increasingly required to survive/operate under extreme conditions, such as a wide temperature range (e.g., ±60 °C), extended charge/discharge cycling life, fast cycling rate (e.g., ≤15 min), and high working voltage (e.g., >4.5 V).[55] For instance, electric vehicles call for battery systems to sustain a stable operation in both hot conditions and cold environments. Some specific applications, including

subsurface exploration, defensive arsenals, space vehicles, etc., require the operation of rechargeable batteries under even more extreme conditions. Apart from these external influences, internal factors also trigger thermal fluctuations in Li-based batteries,[303] significantly raising safety concerns. As an essential region in which electrochemical reactions occur involving Li^+ ions and electrons, the interphase on the electrode plays an essential role in maximizing the electrochemical performance of Li-based batteries. Regarding an ideal interphase, several features should be possessed, including high Li^+-ion conductivity, a compact structure with proper compositions, high chemical/electrochemical stability, and high elastic strength. However, the design of interphases under mild conditions makes it difficult to satisfy the requirements under extreme conditions. When a battery is operated under extreme conditions, the interphase formed on the electrode surface can grow much thicker and lose its protective ability, further causing battery performance decay through various aging mechanisms.[389] Currently, the features and roles of interphases at certain extreme conditions remain significant challenges in the operation of Li-based batteries. Fluorinated interphases have emerged as effective strategies for enhancing battery performance under various operation conditions. In particular, the fluorinated interphase is featured with its main component LiF.[316,375,390] However, the role of LiF for extreme Li-based batteries remains elusive. In the following section, recent in-depth understanding and key progress of the fluorinated interphase at extreme operation conditions of Li-based batteries are summarized, where the SEI formed on the anode will be the focus.

It is generally recognized that the bulk LiF is considered as a favorable SEI component formed via both in situ (derived from electrolyte components) or ex situ (artificial fabrication) approaches. It should be noted that despite the electric/ionic insulation nature of the bulk LiF,[356,391] the LiF-enriched SEI at the nanoscale level can yield a high ionic conductivity, low diffusion energy, and high surface energy, contributing to a uniform and highly stable Li deposition.[333,392] The difference between the macroscopic and the microscopic properties of LiF remains to be elucidated in the future. Moreover, understanding the role of LiF in the electrochemical performance of batteries is inevitably limited by several factors, including the distributions, particle sizes, and formation approaches, requiring great attention to identify the effects of the fluorinated interphase in extreme batteries.

Commercial carbonate electrolytes have largely restricted the battery operation temperature range (from −20 to +50 °C), leading to fast capacity degradation and even battery failure at low temperatures. The successful operation of typical Li-based batteries at low temperature depends on the melting points of the liquid electrolytes. For instance, the commercial electrolytes of Li-ion batteries contain a high proportion of EC solvent that freezes under −20 °C, which results in extremely low ionic conductivity.[393,394] Besides, the thick SEI usually continuously consumes Li, significantly increasing the diffusion energy of Li^+ ions.[394] In addition to the ionic mobility, the low-temperature performance of batteries is dominated by the sluggish kinetics of Li^+ transport across the interphase, which is related to the high charge transfer resistance and poor structure stability of the SEIs.[395] To construct an effective interphase on the surface of both cathodes (e.g., LFP) and anodes (e.g., graphite or Li metal), various additives, such as FEC, $LiPO_2F_2$, and fluorosulfonyl isocyanate (FI), have been introduced to
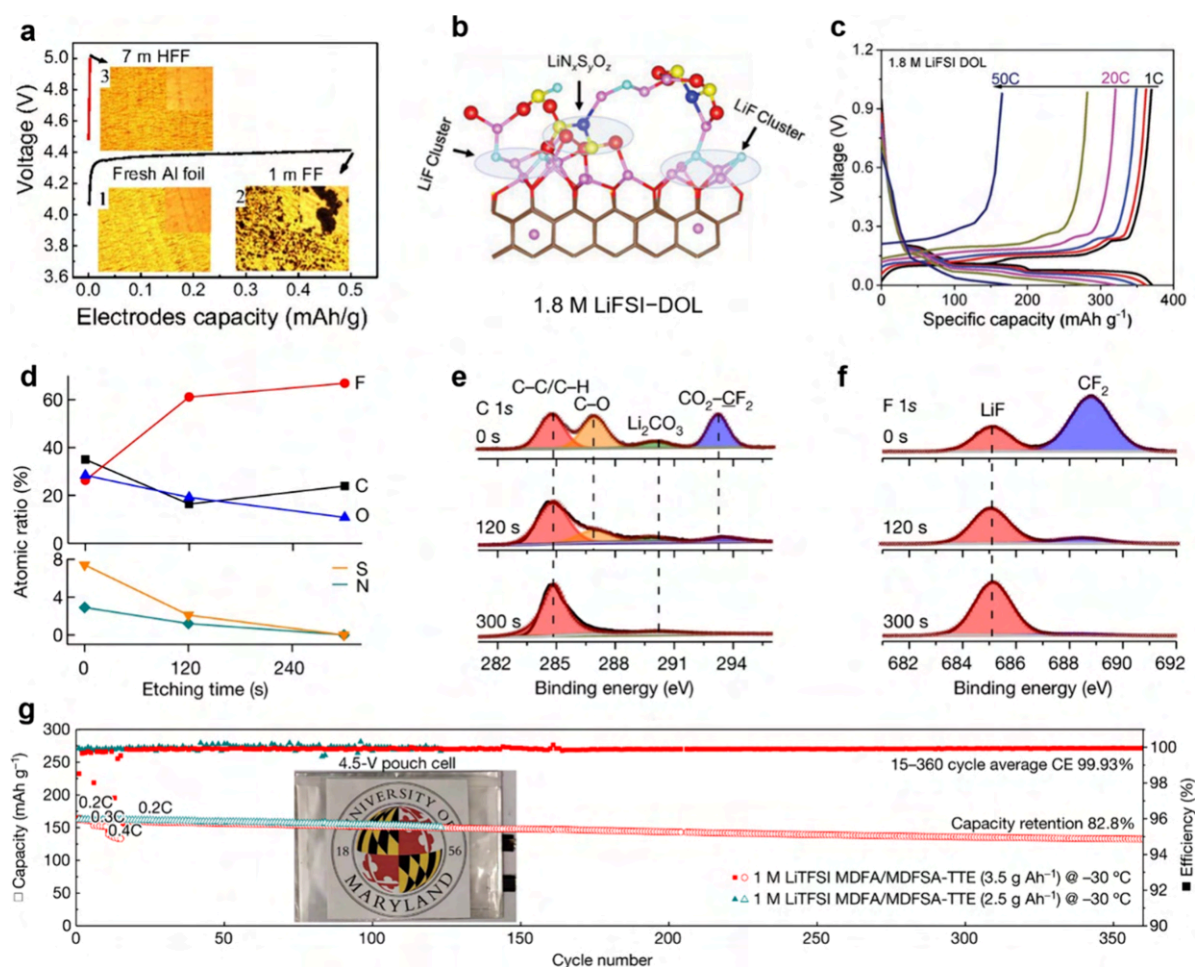
Figure 20. Role of fluorinated interphases for Li-based batteries operated at extreme conditions. (a) Al dissolution in 1 M LiFSI–FEC (1 M FF) and 7 M LiFSI–FEC (7 M HFF) electrolytes when charging to 5 V at 0.5 mA. (Insets) Optical microscopy images of (1) fresh Al foil and Al foil in (2) 1 M FF electrolyte after charging 1 h and (3) 7 M HFF after charging to 5 V. Reproduced with permission from ref 316. Copyright 2018 PNAS. (b) AIMD-simulated atomic SEI structure between the electrolyte and the graphite anode: Li, pink; P, purple; F, cyan; C, brown; O, red; N, blue; S, yellow; graphite, brown wire frame. (c) Charge/discharge curves of graphite‖Li cells with 1.8 M LiFSI DOL at various current rates. Reproduced with permission from ref 411. Copyright 2022 Wiley-VCH. (d–f) XPS results of the SEI on graphite anode in 1 M LiTFSI–MDFA/MDFSA/TTE electrolyte: (d) quantified atomic ratios of the elements, (e) C 1s and (f) F 1s spectra displayed in columns of the corresponding depth profiling results. (g) Graphite‖NCM811 pouch cell performance at −30 °C and 0.2 C rate using 2.5 or 3.5 g Ah^{-1} electrolytes. Rate performance was conducted at various C rates (0.2 C for 5 cycles, 0.3 C for 5 cycles, 0.4 C for 5 cycles, and 0.2 C for 345 cycles) of 3.5 g Ah^{-1} (red color). (Inset) Photo of a 4.5 V pouch cell. Reproduced with permission from ref 55. Copyright 2023 Springer Nature.

optimize the electrolytes.[394,396−398] In addition, fluorinated antifreezing agents have been introduced as electrolyte cosolvent/solvent for low-temperature applications, such as 2,2,2-trifluoroethyl butyrate,[399] isobutyl formate,[400] and 2,2,2-trifluoroethyl *n*-caproate.[401] Recently, He et al. developed a fluorine−sulfur-based electrolyte by applying isobutyl formate (IF) as an antifreezing agent with an ultralow melting point of −132 °C. This electrolyte demonstrated excellent physiochemical and electrochemical properties at ultralow temperature, e.g., forming stable LiF-rich SEI (10.48%) and CEI (17.91%) layers, achieving high Li$^+$ conductivities (1.00×10^{-5} mS cm^{-1} for SEI and 6.65×10^{-5} mS cm^{-1} for CEI) and high diffusion coefficients (1.10×10^{-21} m^2 s^{-1} for SEI and 2.07×10^{-20} m^2 s^{-1} for CEI). It also enabled a stable cycling performance of the Li‖ LiCoO$_2$(LCO) battery at −70 °C with a high retainable capacity of 110 mAh g^{-1} over 170 cycles.[400] Typically, it has been accepted that the LiF-rich SEI formed on anode materials exhibited low interphase impedance and charge transfer resistance as well as high stability, thereby enhancing the Li$^+$

diffusion at low temperatures. These results are consistent with the DFT calculations by Arias et al. They pointed out that the surface diffusivity of Li$^+$ over a layer of LiF crystal was excellent, which also improved the stability of the SEI.[402] However, the role of LiF in the CEI on low-temperature performance is still under debate. Contrary to the desirable effect of a LiF-rich CEI on promoting the rapid Li$^+$ diffusion as a result of the lower energy barrier,[403] Gao et al. observed less LiF content formed in the SEI with the FEC-containing electrolyte than that with the FEC-free electrolyte. They ascribed the smaller interfacial impedances to the less LiF, which would promote the low-temperature performance of the LFP electrode.[404]

Recently, by introducing low-polarity diluents, LHCEs have demonstrated great potential in achieving high Li$^+$ mobility as well as low electrolyte viscosity for low-temperature batteries.[405−407] However, the SEI derived from LiPF$_6$ in LiPF$_6$-based LHCEs generally exhibited high interphase resistance. After adding lithium difluorobis(oxalato) phosphate

(LiDFBOP) as a sacrificial additive, the SEI was regulated to be much thinner, which delivered low interphase impedance due to the decreased Li^+ transport path. It was demonstrated that the addition of LiDFBOP changed the SEI composition, with inorganic LiF and porous organic $Li_n(FOP)_n$-based layers facilitating Li^+ diffusion and LiF along with $Li_2C_2O_4$ increasing the stability of the SEI. Benefiting from this regulated interphase chemistry, the commercial graphite anodes exhibited outstanding low-temperature performance ($\sim$240 mAh g^{-1} at -20 °C with 0.1 C) and high rate performance ($\sim$225 mAh g^{-1} at 2 C).[395]

To satisfy the demand for high energy densities, Li-based batteries are developed to operate at extreme voltages, which are beyond the thermodynamic stability limits of traditional electrolytes. Meanwhile, these electrolytes, mainly consisting of carbonates or ethers, are extremely flammable, causing safety concerns for practical applications. LiF possesses the largest band gap (13.6 eV) and the widest ESW, which is believed to protect the high-voltage cathode.[314] To control the LiF formation, Li et al. designed an all-fluoride electrolyte with a large donatable fluorine concentration, i.e., 7 M LiFSI in FEC, in which both the solvent and the salt donated F. It was revealed that LiF formation on the cathode with a large band gap resulted in a fast-tunneling decay rate, protecting Al from dissolution and suppressing electrolyte oxidation beyond 5 V (Figure 20a). When pairing the 5 V $LiNi_{0.5}Mn_{1.5}O_4$ cathode with the Li metal anode, the full cell (1.4 × excess Li) cycled stably for over 130 times at an industrial loading level of 14.7 mg cm^{-2}, 1.83 mAh cm^{-2} at a current rate of 0.36 C. The promising performance was ascribed to the LiF nanolayer constructed on the surfaces of both the cathode and the anode; therefore, its features, such as a wide band gap, high surface energy, and small Burgers vector, favored the high-voltage stability and also resisted rupture during Li deposition.[316] Unlike using the sole solvent, Wang et al. proposed another all-fluorinated electrolyte consisting of 1 M $LiPF_6$ in a mixture of FEC:FEMC:HFE with a weight ratio of 2:6:2.[375] The high degree of fluorine substitution in each cosolvent rendered a F-rich CEI, where these F-containing species (e.g., CF_x and PO_xF_y) deactivated the catalytic activity of the cathode surface and further resisted unwanted oxidation reactions even charging to 5 V. Besides, the fluorinated cosolvents yielded a robust SEI with an extremely high LiF content ($\sim$90%), promoting Li^+ migration along the interphase and tuning the growth of the deposited Li in parallel to reduce the specific surface area. The resulting batteries exhibited outstanding cyclability with high CEs of 99.2% for Li plating/stripping and $\sim$99.81% for a 5 V $LiCoPO_4$ cathode. Interestingly, the designed electrolyte displayed nonflammability, with F fluorination on the alkyl moiety of each cosolvent inhibiting the propagation of oxygen radicals during combustion.[375] Besides, using the fluorine-containing additives (e.g., FEC, $LiPO_2F_2$, LiDFOB) can also construct more robust SEIs/CEIs that consist of fluorinated species/polymers, which further blocks the continuous side reactions between the electrolyte solvents and the extremely oxidized cathode surface.[408−410] As reported by Ma at al., the perfluorophenylboronic acid (PFPBA) additive was preferentially oxidized on the $LiNi_{0.6}Co_{0.2}Mn_{0.2}O_2$ (NCM622) cathode surface due to the strong coordination with PF_6^-, forming an armor-like CEI with a LiF-rich inner layer and a LiB_xO_y-based outer part. The LiF inner layer in the CEI with high mechanical strength effectively resists the breakdown of the NCM622 cathode during repeated cycling and enhances the Li^+ conductivity. Besides, the outer layer with LiB_xO_y exhibited extremely low solubility in carbonate solvents, maintaining the stability of internal CEI species such as LiF. Consequently, the armor-like CEI prevented unwanted electrolyte decomposition as well as detrimental cathode structural change at high voltage, contributing to an excellent cycle stability with 92.1% capacity retention over 400 cycles at 4.6 V, and it sustained the battery to cycle for 150 times (with 75.67% retention) even at an ultrahigh voltage of 4.8 V.[408] As discussed above, the chemical sources of F were typically confined to negatively charged salt anions or fluorinated solvents/additives in electrolytes, which could not populate the inner Helmholtz layers of the electrode surface (e.g., Li anode) with a high Fermi energy level and thus hindering their participation in the interphasial chemistry. Zhang et al. synthesized a fluorinated cation, 1-methyl-1-propyl-3-fluoropyrrolidinium, and coupled it with an FSI$^-$ anion to form an ionic liquid (PMpyr$_f$FSI).[410] This electrolyte exhibited complete nonflammability and strong antianodic ability up to 5.5 V. More importantly, the fluorine sources on the cation and the anion offered unprecedented interphasial chemistries on both the NMC622 cathode and the Li anode, contributing to excellent battery electrochemical performance. The SEI enriched in SO_2F, C−F, and LiF contributed from the decomposition/defluorination of FSI$^-$ and PMpyr$_f^+$ cations. Stable cycling performance without obvious capacity deterioration after 100 cycles was achieved with a high average CE of 99.9%. This work highlights the importance of exploring fluorinated cations in tailoring highly fluorinated interphases for batteries operated at extreme voltages.

Considerable efforts have been devoted to using FEC-based electrolytes for generating fluorinated SEIs in Li-based batteries, particularly with the graphite anodes or Li metal anodes.[168,412−417] The FEC-derived fluorinated SEI is characteristic of a high LiF amount, which exhibits low electronic conductivity ($\sim$10^{-31} S cm^{-1}) and a high Young's modulus ($\sim$64.9 GPa).[418] Unfortunately, the low Li^+ conductivity of the LiF ($\sim$10^{-12} S cm^{-1}) component largely restricts the fast charging capability especially for Li metal anodes as a result of the blocked transportation ability of Li^+ and further aggravated Li dendrite growth at high current rates (e.g., above 2.0 mAh cm^{-2}).[419−423] Very recently, a dual-anion-regulated electrolyte was designed by Xu's research group via using LiTFSI and LiDFBOP as anion regulators.[424] The TFSI$^-$ anion reduced the desolvation energy of Li^+, while the DFBOP$^-$ anion promoted the formation of highly ion conductive and robust inorganic-rich interphases on both cathodes (less LiF and stronger $Li_xPO_yF_z$) and anodes (large amounts of $Li_xPO_yF_z$ and $Li_2C_2O_4$). These interphase features contributed to an outstanding cyclability (84.6% capacity retention over 150 cycles) in 6.0 Ah pouch cells (Li‖$LiNi_{0.83}Co_{0.11}Mn_{0.06}O_2$, NCM83) along with an ultrahigh rate capability (5 C) in 2.0 Ah pouch cells. More interestingly, a practical Li‖NCM83 pouch cell with an ultralarge capacity of 39.0 Ah realized an ultrahigh energy density of 521.3 Wh kg^{-1}, promoting the practical utilization of high energy density Li-based batteries via a facile electrolyte design. Apart from the beneficial effect of $Li_xPO_yF_z$, other interphase species have also been incorporated in enhancing the battery cycling stability, especially at fast charging rates. Interestingly, there exists another viewpoint believing the LiF-rich SEI is promising for fast kinetics since the wide band gap and high chemical/electrochemical stability of LiF could block the continuous side

reactions.[323,425,354] An extremely fast charging graphite anode as high as 50 C without Li plating was achieved by designing two electrolytes, i.e., low-voltage 1.8 M LiFSI−DOL and high-voltage 1.0 M LiPF$_6$−FEC/AN (7:3 by volume). It was revealed that the LiF formed on the graphite anode (Figure 20b) with high interphase energy and low ionic−electronic significantly suppressed side reactions of electrolytes, thus benefiting fast kinetics. The former electrolyte enabled the graphite anode to deliver a high reversible capacity of 180 mAh g^{-1} even at 50 C (1 C = 370 mAh g^{-1}) (Figure 20c) and endowed the graphite‖LFP full battery to retain a capacity of 60 mAh g^{-1} at an extreme rate of 60 C (representing 1 min for full charge and discharge). The second electrolyte aided the graphite‖NCM811 full battery (cathode loading = 2 mAh cm^{-2}, N/P ratio = 1) in providing a capacity of 170 mAh g^{-1} at 4 C charge and 0.3 C discharge rates.[411,426] Briefly, whether the LiF component in the SEI is sufficiently effective for high stability and fast Li$^+$ transport of Li-based batteries remains unclear, especially under fast charging conditions.

As mentioned above, the most widely used electrolytes based on carbonates fail to simultaneously meet all requirements for supporting extreme Li-based batteries such as higher voltages (≥4.5 V), fast charging (≤15 min), cycling over a wide temperature range (±60 °C), and nonflammability.[12,58,427,428] To tame the high affinity between the solvents and the ions and the high flammability of carbonate-based electrolytes, Wang and co-workers dissolved fluorinated electrolytes into highly fluorinated nonpolar solvents (e.g., tetrafluoro-1-(2,2,2-trifluoroethoxy)ethane (D2)) to obtain an electrolyte formulated with 1.28 M LiFSI−FEC/FEMC/D2. This designed electrolyte yielded both LiF-rich SEI and CEI. The high thermal stability and the excellent Arrhenius behavior of Li$^+$ conductivity for the LiF-rich interphases enhanced the high-temperature performance of both the cathode and the anode. The ionic conductivities of the SEI and CEI at ultralow temperatures were also significantly improved. The Li metal anode achieved high cycling CEs of 99.4%, and the graphite anode achieved high charge/discharge CEs of 99.9%. As for the high-voltage LiNi$_{0.5}$Mn$_{1.5}$O$_4$ (5.0 V) and LiCoMnO$_4$ (5.4 V) cathodes, high CEs of 99.9% and 99% were obtained, respectively. Especially, the Li‖LiNi$_{0.8}$Co$_{0.15}$Al$_{0.05}$O$_2$ battery maintained 56% of its capacity obtained at room temperature, even charging/discharging at −85 °C, along with high cycling stability at 60 °C. In addition to significantly improved wide-temperature performance, this electrolyte design displayed nonflammable characteristics.[429] Furthermore, Wang's group is dedicated to exploring the guiding principle to address the relationships between battery performance, electrolyte solvation structure, and interphase chemistry, especially focusing on extreme operating conditions. Their recent report validated an electrolyte design strategy based on a group of soft solvents with a relatively low DN (less than 10) and high dielectric constant (larger than 5) that stroke a balance between Li$^+$−solvent interactions, sufficient dissociation of Li salts, and satisfactory electrochemistry. As a proof of concept, 1 M LiTFSI-methyl difluoroacetate (MDFA)/methyl 2,2-difluoro-2-(fluorosulfonyl)acetate MDFA (MDFSA)/TTE electrolyte was developed successfully in which MDFSA with a high reduction voltage of 2.2 V was introduced as a cosolvent for further strengthening the LiF-rich SEI and CEI. It was demonstrated that the similar LiF-enriched interphases on the NMC811 cathode and the graphite anode balanced the thermodynamic (capacity) and kinetic (interphase resistance)

matching between the two electrodes at extreme conditions, enabling the 4.5 V graphite‖NMC811 full batteries to keep 75% of RT reversible capacity (0.1 C) at −50 °C (−60 °C) with a practical areal capacity of 2.5 mAh cm^{-2} and the pouch cells with lean electrolyte (2.5 g Ah^{-1}) to stably cycle at −30 °C for over 300 times with an average CE of 99.9% (Figure 20d−g). This work opened a new electrolyte design direction for tuning fluorinated interphases toward practical batteries with high-voltage, fast-charging, and wide-temperature operating features.[55]

For practical Li-based batteries, there is a growing need for their stable operation under all conditions, including high voltage (e.g., ≥4.5 V), fast cycling rate (e.g., ≤15 min), wide temperature range (e.g., ±60 °C), and extended charge/discharge cycling, which are highly related to the interphases. In this case, fluorinated interphases featuring a LiF component demonstrate attractive prospects. LiF exhibits low solubility, high mechanical property, a wide band gap, excellent antioxidation ability, and high interphasial energy against Li metal, contributing to a robust SEI. Moreover, the high shear modulus of LiF suppresses anode pulverization. Unfortunately, the low Li$^+$ conductivity of LiF (∼10^{-12} S cm^{-1}) in the interphase restricts the high-rate performance, particularly toward Li metal anodes. Incorporating fluorinated conducting components (e.g., Li$_x$PO$_y$F$_z$) into the LiF-rich interphase can improve the cycling stability and fast-charging capability. Fluorinated components can also be combined with the organic SEI matrix to accommodate the large volume change of the Li anode. Although a LiF-enriched SEI displays low impedance and high stability to improve Li$^+$ diffusion at low temperatures, controversy remains over the impacts of LiF in the CEI components on the low-temperature performance. Further investigation is needed to unlock the roles and influencing factors of the macroscopic and microscopic properties for LiF, particularly under extreme conditions.

3.4. Techniques To Probe Fluorinated Interphases

As described above, the passivated interphase is electronically insulting but ionic conducting, arising from the decomposition of the electrolyte components on the surface of the electrode, which plays a vital role in determining the capacity, cyclability, rate performance, CE, and safety properties of Li-based batteries. Understanding the morphologies, chemical compositions, and mechanical properties of the CEI/SEI is significant for further designing fluorinated interphases on the active materials, especially on the anodes.[430] Since its first demonstration by Dey et al. in the 1970s, the SEI has attracted significant interest regarding the formation mechanisms, structures, phase, and chemical compositions; however, due to its spatially and temporally dynamic nature, an in-depth comprehensive understanding of the SEI, especially on the atomic scale, remains a huge challenge.[284,389,431−437] Generally, it is difficult to discern the SEI/CEI chemical components from the solvent species, and the SEI/CEI thickness is also hard to quantify with ambiguous boundaries. Besides, the SEI/CEI properties are highly affected by the testing conditions (e.g., electrolytes, operation temperature, current density, voltage range, and electrode materials) and the sample preparation environment (e.g., washing solvent, exposure to air[389] and moisture), which undergoes a dynamic evolution process during the charging and discharging. To provide valuable information on the interphase characteristics, various advanced techniques, including microscopy and spectroscopy,

Table 3. Comparison of the Spatial Resolution, Useful Information (e.g., composition, structure, morphology), as Well as Corresponding Strengths and Limitations of Each Technique for Probing the Interphase

characterization techniques	spatial resolution	composition	structure	morphology	other information	strengths	limitations	ref
cryo-(S)TEM	0.1 nm	yes	yes	yes		preserving the electrochemical state, corresponding structure, and chemical information on the interphase without destruction at cryogenic temperatures	hard to probe organic-enriched SEI derived from solvent decomposition; explaining chemical details in the disordered and amorphous phases remains challenging	444, 445, 447, 492, 493
cryo-FIB/SEM	nm	yes	yes	yes	obtain cross-sectional view of the interphase	obtain spectroscopy imaging from the cross-sectional view at the nanoscale	transfer time even within seconds may not be sufficient for some sensitive samples; requiring optimizing the procedures to eliminate sample exposure	494, 495
EQCM	5×10^{-11} g	yes		yes	gravimetric information	quantify and monitor the real-time interphase evolution and component dissolution during the electrochemical process	lack of exact structural information	450, 496–503
TGC	10^{-7} g	yes				quantify the contribution of the interphase Li^+ and unreacted metallic Li^0 to the capacity decay	requires a nondestructive approach to quantify residual Li during electrochemical cycling	504
XPS	nm	yes	yes			precise in monitoring the electronic structures of interphase compositions	in situ XPS has yet to be fully designed due to ultrahigh vacuum, big challenges with sample preparation, data collection protocols, and data processing that can lead to misleading conclusions	458, 459, 461, 505–507
SIMS	nm	yes	yes			visualize the growth of the interphase micro-structure	creation of secondary products due to the high-energy beam	457, 508–510
NMR	nm	yes	yes		amount and time scale of Li^+ transport through the interphase	noninvasively identify chemical compositions and structures of the interphases	fails to probe the dynamic nature of the interphase	479,480, 487
AFM	nm			yes	mechanical and electrical features	offers high-resolution topographical images; evaluates mechanical evolution of the interphase	fails to unveil chemical information, restricted magnification, and vertical range	462, 511, 512
TERS	nm	yes	yes	yes		provides both topographical and chemical mapping of the interphase with high sensitivity and selectivity	needs to increase the efficiency of motivation and collection to probe the interphase	466, 467, 513–515
NR	nm	yes	yes	yes	interphase evolution	quantitatively determine the interphase properties; detect evolutions of the interphase structure	requires a flat specimen to generate a strong signal; very limited facilities to handle the produced neutrons outside the particle accelerator	437, 473–475, 516
XAS	0.001 nm	yes	yes	yes	local atomic arrangement and electronic structure	high sensitivity to local chemical bonds and solvent environments for interphase investigation	requires a separate kind of electrochemical cell designed for in situ operation	471, 472,517–520
SECM	from 10 nm to 1 μm	yes		yes		monitors the formation and evolution of the interphase; determines electrically insulating feature	probe positioning is complicated by the different faradaic current behavior for conductive and insulating surfaces	483, 484, 521

AK
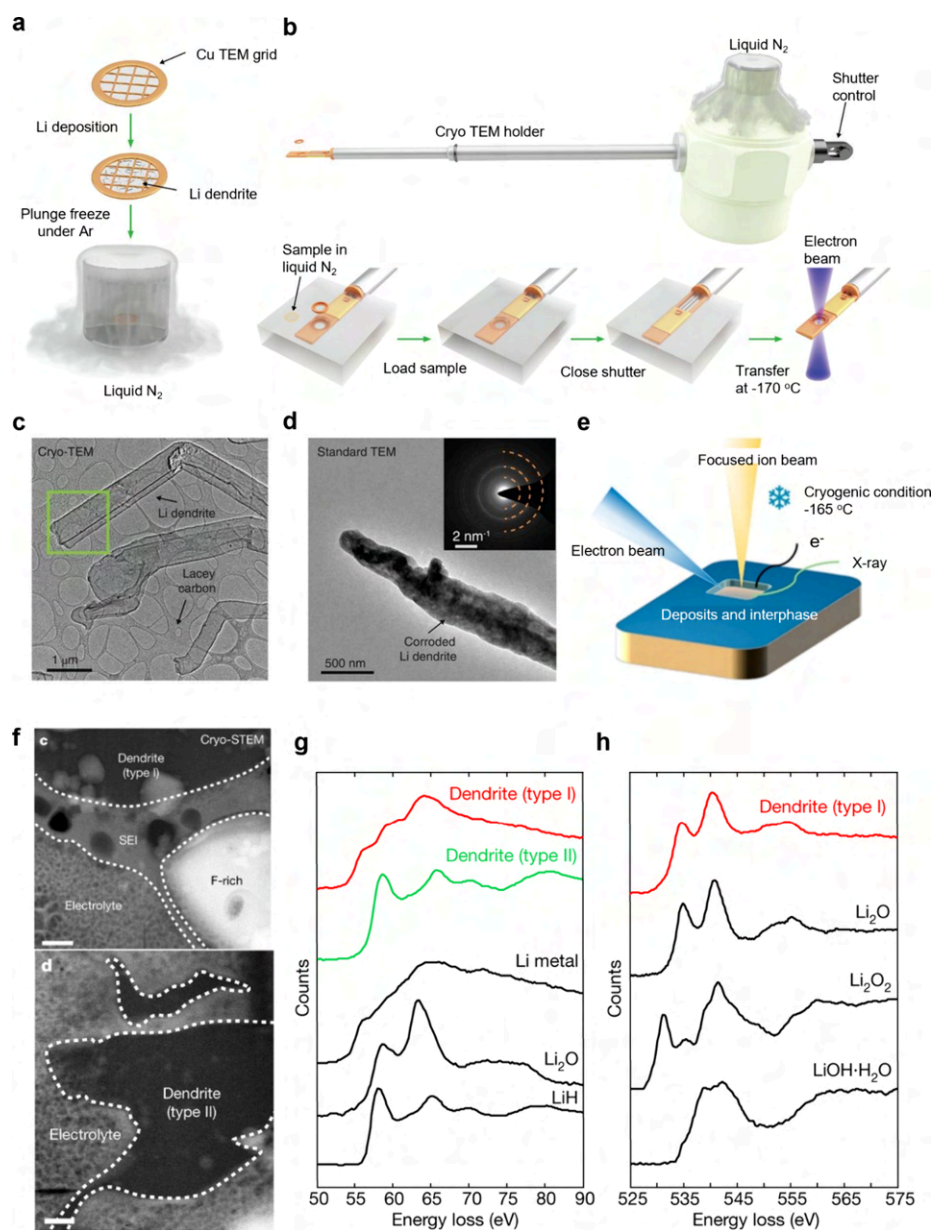
Figure 21. Probing the critical characteristics of sensitive interphases by cryo-EM. (a) Electrochemically depositing Li metal dendrites onto a copper TEM grid followed by plunging into liquid nitrogen after battery disassembly. (b) The specimen is then placed onto the cryo-TEM holder while still maintained in liquid nitrogen and isolated from the environment by a closed shutter. (c) Cryo-TEM image of Li metal dendrites with an electron dose rate < 1 e Å^{-2} s^{-1}. (d) Typical TEM image of a Li metal dendrite after exposing it to air for ∼1 s at room temperature. (Inset) Corresponding SAED pattern. Reproduced with permission from ref 492. Copyright 2017 American Association for the Advancement of Science. (e) Illustration of the cryo-FIB/SEM setup at liquid nitrogen temperature. Reproduced with permission from ref 525. Copyright 2020 American Chemical Society. (f) HAADF cryo-STEM images displaying an extended SEI layer on (upper) type I dendrites but not on (lower) type II dendrites. EELS elemental mapping of SEIs on (g) type I dendrite enriched in O and Li and (h) type II dendrite without carbon. Reproduced with permission from ref 526. Copyright 2018 Springer Nature.

have been applied extensively. Scanning electron microscopy (SEM) and TEM are two powerful and most widely used tools for visualizing and monitoring the interphase directly,[340,438−442] particularly when conducting at cryogenic temperatures for preserving the pristine states of the interphases.[24,352,376,420,443−449] In addition, some properties of the growing interphase can be quantified to establish their correlation with the electrochemical performance of batteries, e.g., developing an electrochemical quartz crystal microbalance (EQCM) for quantifying the interphase dissolution phenomenon.[450] Various interphase analysis techniques, such as

SIMS,[451−457] XPS,[458−461] AFM,[462−467] XAS,[468−472] neutron reflectometry (NR),[473−475] XRD,[476−478] NMR,[479−482] and scanning electrochemical microscopy (SECM),[483−486] have also been widely employed to probe the elemental composition, interphase morphology, and mechanical/electrical properties of the interphase. Notably, due to the elusive and highly dynamic properties, different techniques need to be combined to comprehensively recognize the fluorinated interphases at the atomic level. However, most of these advanced techniques for investigating fluorinated interphases are under ex situ conditions, requiring the disassembling of the

batteries after charging/discharging to various states, which may cause the exposure of the samples to ambient conditions during the transport process for characterization. These processes may change the interphases by affecting the morphology, microstructure, chemical compositions, mechanical properties, etc., which may cause misleading results.[437,473] Therefore, in situ/operando measurements conducted at the operating conditions without disassembling the batteries are more reliable and valuable technologies to provide real-time information about the characteristics and evolution process of fluorinated interphases during battery cycling.

Since several review articles have comprehensively summarized the technical details, research progress, and applications on understanding the SEI using traditional techniques,[430,437,473,487,488] in this section, the focus will be on state-of-the-art developments of updated characterization techniques for fluorinated interphases, elucidating the chemical compositions, morphologies, micro/nanostructures, and other properties. Important features of each technique, including the spatial resolution, useful information, as well as corresponding strengths and limitations for probing the interphase, are compared in Table 3. To capture the moment of the reactions at the interphase, which occurs at the picosecond time scale,[310,489,490] the DFT and MD simulations have been extensively utilized. Besides, theoretical calculations can also help to predict and quantify the correlation between the structure and the properties of the interphases. Therefore, theoretical calculations and simulations are associated with the micro/nanostructure and properties of the SEI, in turn offering guidance in rationally designing and regulating the SEI characteristics for high-performance Li-based batteries. Considerable technical details of the theoretical calculations and simulations for understanding the interphases can be found in previous specialized reviews, which will not be discussed in this section.[437,491]

3.4.1. Cryo-EM. As discussed earlier, SEI layers are sensitive to oxygen and moisture during the transfer process to electron microscopes (e.g., TEM and SEM), causing insufficient resolution for characterizing the micro/nanostructures of the SEI. In addition, under the ultrahigh vacuum of the TEM chamber, Li metal anodes are extremely vulnerable to radiation damage, such as sample ionization and bond breakage, caused by the high electron dose in the incident beam and side chemical reactions induced by free radicals and secondary electrons. Inspired by biological imaging techniques, cryo-EM with a low electron dose and a frozen sample at low temperature has been used to resolve the crystalline atomic lattices of the SEI/CEI while preserving the delicate chemical composition and spatial features, which has demonstrated its advantage in visualizing and elucidating nanostructures and compositions of the beam-sensitive SEI at the atomic level.[24,443]

To preserve the pristine state of chemically reactive and beam-sensitive materials, especially the Li metal anode, Cui and co-workers pioneered cryo-TEM investigation by designing a cryo-transfer method.[492] As illustrated in Figure 21a and e 21b, Li was electrochemically deposited onto a copper grid followed by washing with 1,3-dioxolane to remove Li salts and flash freezing the specimen in liquid nitrogen immediately. Therefore, the electrochemical state as well as the corresponding structure and chemical information on Li dendrites were retained at cryogenic temperatures. Through visualizing individual Li dendrites, they achieved a high atomic resolution

(0.7 Å) image on the spherical aberration-corrected TEM. In contrast to the air-exposed Li dendrites with rough surfaces and darker contrast due to the formation of polycrystalline artifacts, the cryo-transferred Li dendrites preserved their states, which constructed a much smoother and thinner SEI layer on Li metal (Figure 21c and e 21d). Notably, with a standard EC/DEC electrolyte, the formed SEI was composed of small crystalline domains (diameter ≈ 3 nm) embedded randomly in the amorphous matrix. On the contrary, with 10 vol % FEC as the additive, a more ordered multilayer SEI was generated, which was consistent with the structure proposed by Aurbach et al.[522] However, LiF was not observed in the SEI layer, which may be because TEM is sensitive to crystalline phases when probing a small selected surface area.[444,492] In another work, Meng et al. developed a new cell configuration to obtain electrochemically deposited Li (EDLi) for cryo-TEM imaging. A copper grid was placed on the Cu foil and used as a part of the counterpart substrate.[420] After deposition, the cell was disassembled and rinsed with DMC before transferring. Then, the grid was loaded in a covered cryogenic dewar with continuous Ar flow, and the holder was pumped down to 10^{-5} bar and immediately loaded into a vacuum chamber (cooled to 100 K) for transfer. It was revealed that the EDLi is amorphous with uneven SEIs containing amorphous organic species and crystalline LiF. Nevertheless, the crystalline LiF in the SEI layer possessed a low conductivity of $<10^{-12}$ S cm^{-1}, and the amorphous $Li_xPO_yF_z$ species could display a higher ionic conductivity,[523,524] which questioned the favorable effect and the working mechanism of LiF for high CEs. Soon after, using cryo-TEM, Cui and co-workers discovered the fundamental effects of SEI nanostructures (i.e., mosaic and multilayer) on the performance of a Li metal anode, pointing out that fluctuations in the crystalline grain distribution within the SEI played a vital role in differentiating the mosaic structure from the multilayer structure, thus dictating the battery performance.[445] Specifically, a multilayer nanostructure favored uniform Li stripping behavior, while a mosaic nanostructure resulted in fast Li dissolution.

To identify the dominant components and nanostructure of the SEI layer, an effective strategy to minimize Li pulverization was demonstrated by Zhang et al. via a fluorinated orthoformate solvent-based electrolyte. The in situ-formed SEI on the Li anode displayed a monolithic feature with the same composition from the surface to the bottom along with horizontally homogeneous coverage of the SEI observed from cryo-TEM imaging. This unique SEI with enriched inorganics significantly suppressed electrolyte depletion and minimized pulverization for a stable Li anode.[376] Moreover, the evolution of the SEI layer during cycling can be tracked with the aid of cryo-TEM.[446] Cui et al. revealed that the initial SEI generated during the first cycle was thin and amorphous, which evolved into two morphologies upon further cycling, i.e., a compact SEI containing inorganic components that passivated the electrode surface and a large extended SEI without inorganics due to incomplete passivation.[493] The extended SEI growth inevitably consumed massive Li and led to a porosity reduction, which could be prevented by inorganic species in the compact SEI layer. These results via cryo-TEM indicated that the vastly heterogeneous process for SEI growth could be effectively regulated by sufficient passivation of the SEI. Very recently, the same research group further adapted a thin film vitrification approach to preserve the SEI film in its native liquid electrolyte environment, yielding uniform thin films inside the holes of the

Cu grid. Afterward, these samples were probed through cryo-(S)TEM to visualize the intact structure and chemistry of the SEI films. It was demonstrated that the anion-derived SEI enriched with more inorganics contributed to a smaller swelling ratio, preserving its mechanical property and chemical stability for enhancing electrochemical cycling.[352] Encouraged by the successful interphase characterization in liquid electrolytes, cryo-TEM was also utilized to visualize the interphase structure between the anode and the solid polymer electrolytes atomically.[527−533] In 2020, the cryo-TEM results revealed a mosaic interphase between the Li anode and the PEO electrolyte, where various inorganic nanocrystals (Li_2O, $LiOH$, and Li_2CO_3) were randomly distributed inside the amorphous phase. The Li_2S addition favored the decomposition of $N(CF_3SO_2)_2^−$ and thus promoted the enrichment of LiF nanocrystals in the Li/PEO interphase, as verified by both cryo-TEM and simulations. The LiF nanocrystals not only enhanced the Li^+ diffusion kinetics and prevented the chain breaks of C−O but also suppressed side reactions between the Li anode and the PEO electrolyte, thus enabling outstanding electrochemical performance for both half cells and full cells.[447]

Cryo-TEM has been regarded as a powerful tool for confirming and refining SEI models, which have long been hypothesized. Nevertheless, compared to the extensively investigated inorganic components (e.g., LiF) by cryo-TEM, determining the properties of the organic-enriched SEI that are derived from solvent decomposition remains an enormous challenge. Besides, more efforts need to be put in regarding cryo-EM techniques for guiding the optimization of high-performance Li-based batteries, including exploring and explaining the chemical details in the disordered and amorphous phases, revealing more in-depth information from lattice imaging, etc.

Since cryo-TEM requires a thin specimen (<100 nm) on the TEM grids, it is hard to probe the bulk electrode materials. In contrast to previous TEM investigations focusing on the surface structure, the focused ion beam (FIB) technique with milling capability has been applied for preparing TEM samples by lifting out the bulk structure of the electrode materials. Unfortunately, the FIB conducted at room temperature leads to various artifact issues, including surface damage, redeposition of beam-sensitive Li metals, and mechanical deformation related to "cutting" approaches. Therefore, cryo-FIB is necessary to process the electrode samples and interphases at cryogenic temperature (−170 °C).[437,534]

Combining the milling characteristics of FIB at cryogenic temperatures to preserve solid−liquid interphases with the SEM technique to obtain spectroscopy imaging from the cross-sectional view at the nanoscale, the SEI film formed on anode materials can be preciously characterized (Figure 21e).[525] Using cryo-FIB/SEM characterization, Archer et al. reported that a pinhole-free Al_2O_3 coating (with a thickness of 15 nm) served as an artificial solid−electrolyte interphase on the Cu foil, revealing that the deposited Li consisted of both a dense and a porous structure that highly improved the stability of Li deposition.[494] Via conducting imaging and spectroscopic mapping on the cross sections of Li deposits prepared by cryo-FIB milling, Kourkoutis et al. revealed that the intact surface layers and interphase compositions of the exposed reactive materials experienced negligible change, which could be characterized down to the nanoscale.[495] Obviously, a cryogenic sample temperature enabled energy-dispersive EDX

mapping of Li with increased signal over an extended period when coupling the new EDX detectors with the cryo-FIB/SEM technique. However, the rapid transfer time, even within seconds, may not be sufficient for some sensitive samples, requiring further improvements in these techniques to eliminate sample exposure.

It has been recognized that the element distribution and contents of the electrode materials can be determined by EDS and the EELS, offering valuable information about the chemical compositions, especially for some amorphous species.[443] Recent progress in cryo-TEM has been successfully used for beam-sensitive battery materials,[420,448,492,526,535] achieving atomic resolution imaging for SEI layers formed on the Si,[449] carbon,[493] and Li metal anodes.[445,446,536] To restrict the destructive change in structures and interphase chemistry during the cell disassembly and solvent-washing processes before cryo-TEM characterization, cryo-scanning transmission electron microscopy (STEM) combined with the cryo-FIB lift-out procedure was applied for visualizing the SEI layers. Significant work was conducted by Kourkoutis et al. using cryo-STEM, identifying two distinct types of dendrites on the Li anode.[526] According to the HAADF cryo-STEM imaging (Figure 21f), an extended SEI (300−500 nm thick) existed in the type I dendrite, suggesting a typical washing process had removed a large portion of the SEI layer. On the contrary, the type II dendrites with the thickness of hundreds of nanometers are more likely to disconnect with the electrodes due to much smaller contact areas, which could result in dead Li formation and capacity attenuation of batteries. In addition, abundant oxygen and Li in a type I SEI layer without F was observed from EELS elemental maps, while notably, an extended type II SEI was absent with a C-free, Li- and O-enriched type II dendrite (∼20 nm). Based on the fine structures of the Li and O K-edge (Figure 21g and 21h), type I dendrite mainly contained Li metal and partial Li_2O, while type II dendrite was unexpectedly dominated by pure lithium hydride (LiH). More significantly, the fluorinated electrolyte was confirmed to be able to mitigate the LiH dendrite formation and largely altered the Li deposition. The discovery of extended SEI layers as well as LiH dendrites on Li metal was informative to further efforts on overcoming their detrimental effects. Based on this recent progress, it was surprising that the recognized favorable LiF was not observed in the SEI, even using fluorinated electrolytes. Utilizing cryo-STEM and EELS techniques, Cui and his group elucidated that instead of participating in the compact SEI (15 nm) directly, LiF precipitated as large nanoparticles (100−400 nm) across the electrode surface, extending outside of the compact SEI for the indirect SEI regime. In other words, LiF cannot play a dominant role in passivating Li metal or promoting Li^+ transport through the compact SEI. This report refined the traditional SEI structure across multiple length scales and nuanced the effects of the SEI species on the anode stability.[537] Besides the SEI formed on Li metal, the structural and chemical evolution of SEI layers on Si anodes were unveiled in three dimensions via combing sensitive elemental tomography with cryo-STEM. Owing to the continuous void growth and the condensation during the delithiation process, the unstable SEI on the Si anode grew toward the interior, which formed the core−shell structure in the initial cycle and further evolved to a "plum-pudding" structure comprising abundant voids and dead Si upon longer cycling. As a consequence, the engulfing of Si domains by the SEI was revealed, causing the disruption of electron transport
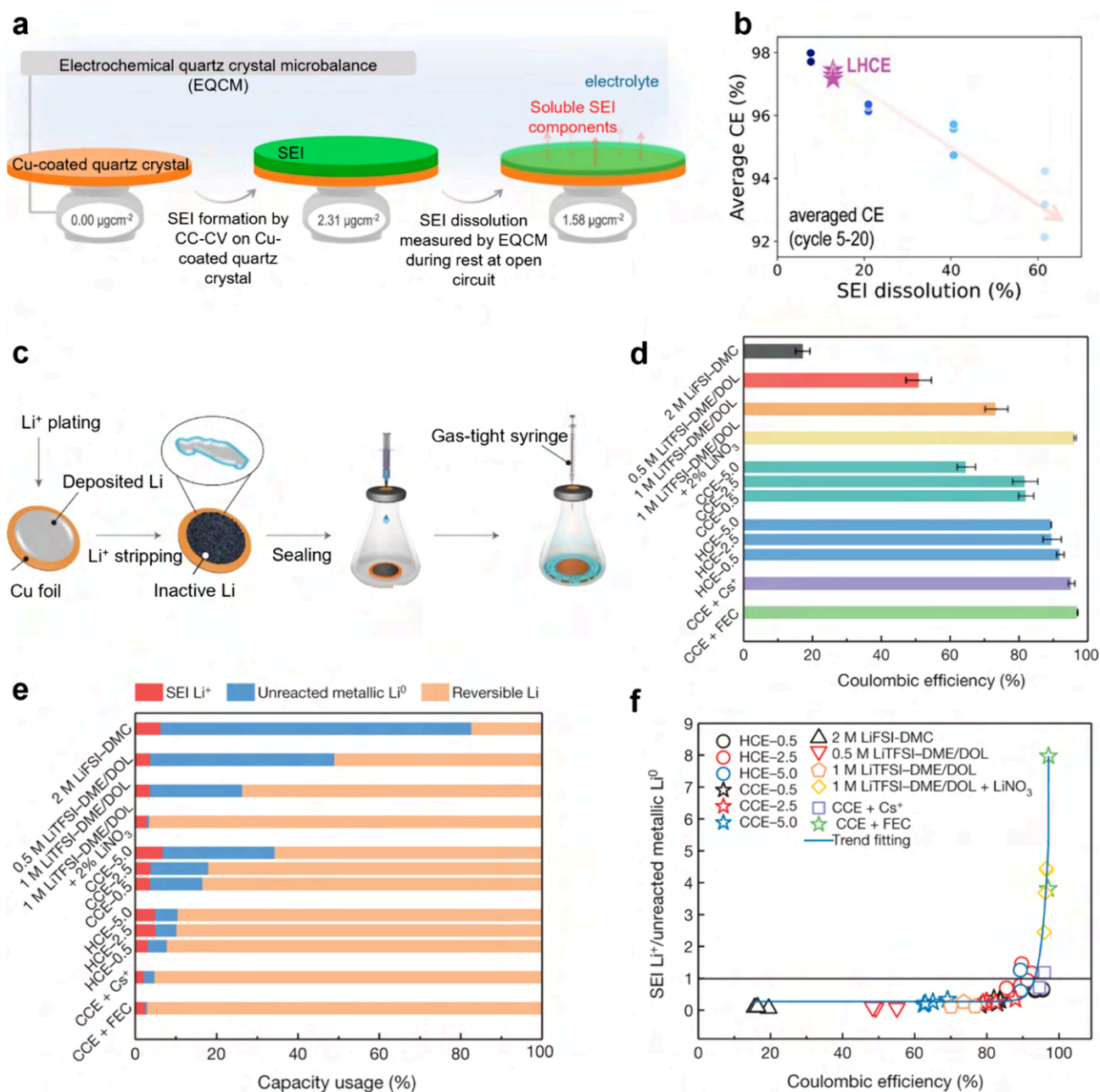
Figure 22. Quantifying the correlation between interfacial chemistry and electrochemical performance by EQCM and TGC methods. (a) The procedure for analyzing the SEI formation and dissolution with the EQCM technique. (b) Relationship between the average CE of the Li‖Cu half-cell, and SEI dissolution results from EQCM. Reproduced with permission from ref 450. Copyright 2023 American Chemical Society. (c) Schematic illustration of the working principle of the TGC technique. (d) The average first CE of Li‖Cu cells with various testing conditions. Eight electrolytes (HCE, CCE, 2 M LiFSI−DMC, 0.5 M LiTFSI−DME/DOL, 1 M LiTFSI−DME/DOL, 1 M LiTFSI−DME/DOL + 2% LiNO$_3$, CCE + Cs$^+$, and CCE + FEC) and three stripping rates (0.5, 2.5, and 5.0 mA cm^{-2} to 1 V) are used. (e) The TGC method for analyzing the capacity usage (SEI Li$^+$, unreacted metallic Li^0, and reversible Li) with various testing conditions. (f) The ratio of SEI Li$^+$ to unreacted metallic Li^0 calculated by TGC (blue line refers to exponential fitting results). Reproduced with permission from ref 504. Copyright 2019 Springer Nature.

pathways and generation of dead Si, which further depleted the electrolyte and deteriorated the battery performance.[437]

3.4.2. Quantifying Techniques. Based on the piezo-electric effect, where the mechanical shear stress is induced in the crystal as a function of the applied voltage, EQCM has been regarded as an extremely sensitive mass monitoring approach to studying electrochemical reactions.[499−503] The electrode is generally deposited on an oscillating sensor (made of quartz crystal), which exhibits a linear relationship between the resonance frequency and its mass based on the Sauerbrey

equation in the ideal case of a homogeneous and rigid layer adhered to the sensor surface. Then, through probing the shift in resonance frequency, the mass change of the electrode can be obtained quantitatively. Therefore, the EQCM technique allows monitoring the real-time SEI evolution and component dissolution phenomenon as a function of applied voltage.[450,498] Through in situ EQCM measurement, Pan et al. revealed that LiF and Li alkylcarbonates comprised the main SEI components on graphite anodes (1 M LiPF$_6$−EC/DMC electrolyte) at various voltages. LiF was formed at 1.5 V, and
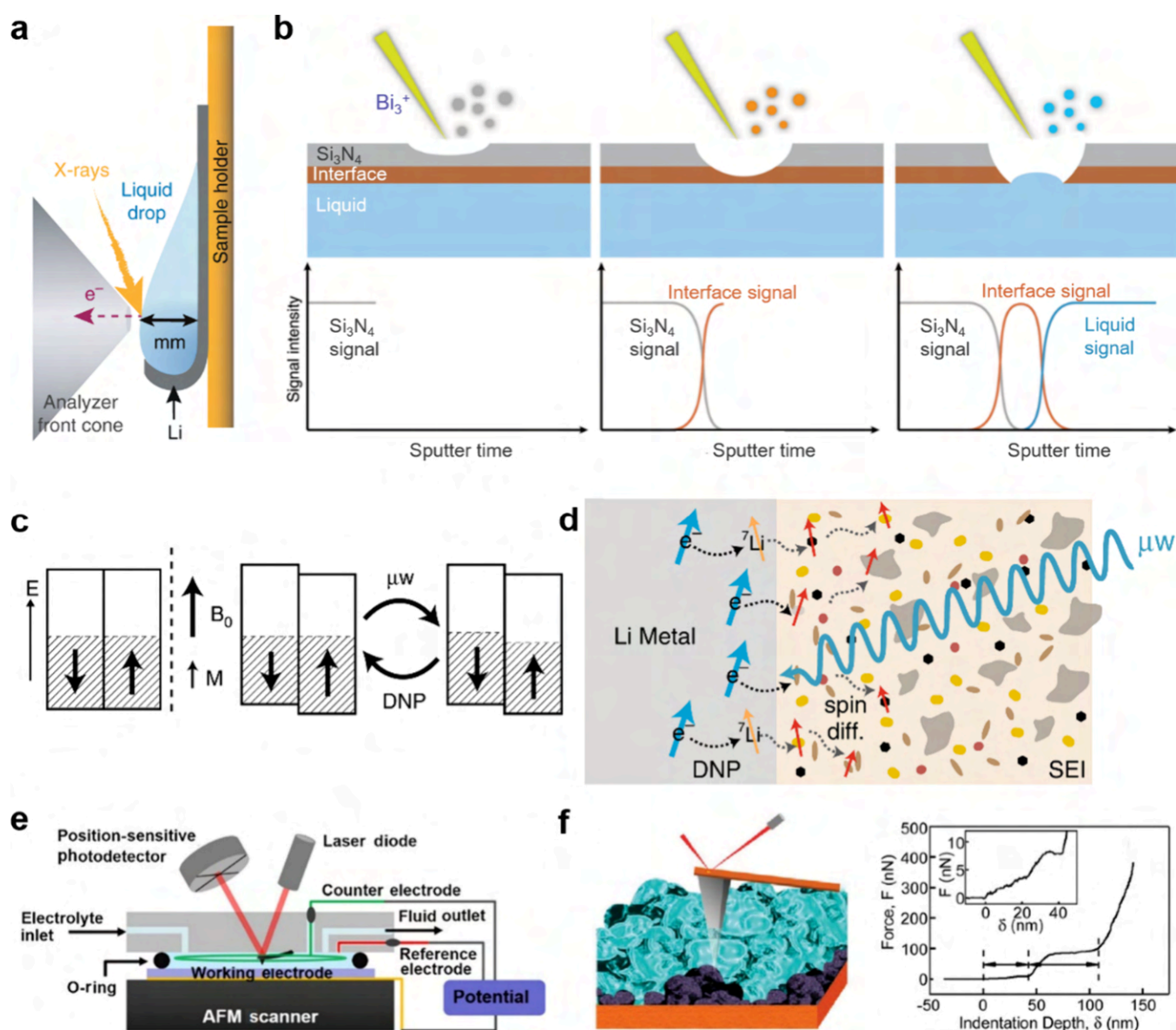
Figure 23. Advanced characterization for analyzing chemical compositions, morphologies, structural information, mechanical properties, etc., for interphases. (a) Schematic illustration of liquid droplets on the Li substrate for APPES measurements. Reproduced with permission from ref 459. Copyright 2019 Springer Nature. (b) Schematic illustration of the developed in situ liquid-SIMS technique for SEI characterization. Reproduced with permission from ref 509. Copyright 2020 Springer Nature. (c, d) The mechanism of Li metal DNP. (c) The conduction electron spin bands of a metal plotted against energy (E): in the absence of a magnetic field (left); (middle) in an applied magnetic field (B_0), leading to a Pauli paramagnetic moment (M); and after microwave (μw) irradiation at the CESR frequency (right). Note: the arrows for each spin band denote the electron magnetic moment. (d) Schematic for hyperpolarization of Li metal on application of microwaves (DNP, black dashed arrows) and subsequent spin diffusion in the heterogeneous mixed organic/inorganic SEI (gray dashed arrows). Reproduced with permission from ref 556. Copyright 2020 Springer Nature. (e) Cross-sectional schematic diagram of an electrochemical AFM cell. Reproduced with permission from ref 511. Copyright 2015 Elsevier. (f) Schematic illustration of the AFM force spectroscopy measurements. (Inset) Indentation curve. Reproduced with permission from ref 462. Copyright 2012 American Chemical Society.

EC was initially reduced at 0.74 V. Moreover, it was very interesting to observe that the nascent interphase could be partially reoxidized during the very first delithiation cycle, which could be the reason for the reported metastability of the SEI ingredients in the nascent form.[538] In recent years, EQCM has been well developed, in which the energy dissipation of the resonating sensor is additionally considered. Introducing the SEI shear viscosity coefficient, SEI shear storage modulus, and electrolyte properties in a multilayered viscoelastic Voigt model, the dissipative properties of a nonrigid SEI and change in electrolyte viscosity are considered.[539] Combining the

EQCM with dissipation monitoring (EQCM-D), gravimetric and viscoelastic changes in $Li_4Ti_5O_{12}$ anodes were assessed during the insertion/extraction of Li^+ and formation/growth of the SEI. These results indicated that the intrinsic viscoelastic properties of the growing SEI layers could be quantified, and the SEI quality (recognized from the EQCM-D data) was improved by optimizing the electrolyte system (e.g., adding vinylene carbonate additive or using LiTFSI salt).[497] Typically, the EQCM-D technique can provide information on the structural change in more realistic nonrigid viscoelastic interphases.[496]

One should note that among all of the SEI properties, the dissolution in the electrolyte can directly influence the formation and growth of the SEI in the subsequent cycles. Generally, additional Li and electrolyte have to be consumed to repair the partially dissolved SEI, which will inevitably increase the SEI thickness,[540,541] resulting in severe capacity loss through the repeated SEI formation and growth process. The EQCM has been applied to quantify the mass loss of the SEI layer (after formation) upon standing at an open circuit. The SEI was found to lose more than one-half of its mass, demonstrating the potential of EQCM to quantify the SEI dissolution and further reveal the mechanisms of SEI formation and growth.[450,542,543] Very recently, utilizing operando EQCM, Cui et al. successfully quantified the SEI mass loss in ether-based electrolytes (Figure 22a and 22b).[450] By establishing the correlation among solubility, passivity, and cyclability, it was concluded that SEI dissolution was a major factor influencing the subsequent SEI formation and growth. In addition, it was elucidated that the calendar life of Li-based batteries can be extended by reducing the SEI dissolution, highlighting the significance of regulating the dissolution phenomenon for mitigating the SEI degradation.

Utilizing advanced characterization techniques, it has been recognized that establishing the correlation between interfacial chemistry and electrochemical performances is significant for resolving issues related to Li metal anode. Recently, using an analytical technique of titration gas chromatography (TGC), Meng et al. quantified the contribution of Li^+ in the SEI components (e.g., LiF, Li_2CO_3, Li_2O) and unreacted metallic Li^0 to the total amount of inactive Li, respectively, which was critical for understanding the real mechanisms causing rapid capacity deterioration.[504] The critical difference exploited between the SEI Li^+ species and metallic Li^0 is their chemical reactivity, where only the metallic Li^0 reacted with protic solvents. For instance, Li^0 reacts with H_2O to create H_2 gas ($2Li + 2H_2O \rightarrow 2LiOH + H_2\uparrow$). The H_2O titration (all metallic Li^0 is reacted) was paired with a gas chromatography facility (quantify generated H_2 in the reaction) to a single analytical tool (TGC), exactly quantifying the amount of unreacted metallic Li^0 (Figure 22c). Then, a high resolution of 10^{-7} g was obtained for analyzing metallic Li^0, after combining with an advanced barrier ionization H_2 detector. Using this TGC methodology, the relationship between the amount of inactive Li with the CEs of Li‖Cu cells in different electrolytes was correlated (Figure 22d). By quantifying the amount of metallic Li^0 directly by the TGC, the content of SEI Li^+ was calculated accordingly. Interestingly, as shown in Figure 22e, the content of Li^+ components in SEI remained constant at a low level, whereas the amount of unreacted metallic Li^0 increased significantly as the CE decreased. In addition, the ratio of Li^+ components in SEI and unreacted metallic Li^0 elucidated the CE below 95%. It was the unreacted metallic Li^0 rather than SEI formation that dictated the amount of inactive Li, further causing the capacity loss (Figure 22f). The SEI formation only dominated at very high CEs. This work provided interesting insights for advancing LMBs. Nevertheless, a nondestructive approach to quantify residual Li upon cycling without disassembling the cell is still urgently required.

3.4.3. Composition Analysis Techniques.
To examine the surface chemistry of the interphases, various analysis approaches such as XPS, SIMS, and NMR have been extensively employed in recent research.[517,544−550] By utilizing the photons in the X-ray range that lead to the emission of the core electrons from the specimen, XPS has been widely used for detecting all elements in the periodic table except H and He. Therefore, XPS is an ideal technology for monitoring the electronic structures of SEI compositions, such as LiF, Li_2CO_3, organics, and other species.[505−507] In 1985, based on a $LiBF_4$-containing electrolyte, the existence of LiF in SEI components was proved for the first time by Takehara et al. using XPS.[434] Nevertheless, the ex situ XPS fails to disclose the natural state and properties of the interphases, making it necessary to develop in situ XPS to capture the real-time state of interphases during the battery cycling. Unfortunately, as a surface-sensitive technique with microscale in-plane spatial resolution, in situ XPS has yet to be fully designed due to the ultrahigh vacuum condition.[458]

To solve this challenge, in situ spectroscopies, such as ambient pressure photoelectron spectroscopy (APPES), were employed by Hahlin et al. (Figure 23a), providing insights for future operando measurements on the dynamic chemical evolution of SEI.[459] Although liquid electrolytes could be used in this investigation, the electrochemical cycling tests were not applied, making this technique fail to reflect the real-time state of SEI in batteries. Despite the extensive application in analyzing the SEI chemical compositions,[460,488,551−555] XPS still exhibited some big challenges related to the sample preparation and data collection protocols, which can lead to misleading conclusions. Recently, an informative and significant work was conducted by Bent et al., identifying some key factors to be carefully considered to avoid erroneous interpretations of XPS for SEI investigation, including the spatial location of the sample, periods of sample inactivity under the ultrahigh vacuum in XPS chamber, and Ar^+ sputtering conditions.[461] Especially, the poorly rinsed sample introduced artifacts to the SEI components, with a 40% variation across the $x−y$ plane for atomic percentage. It was also pointed out that SEI experienced obvious changes in chemical components with the ultrahigh vacuum condition or Ar^+ sputtering. This report offered rigorous guidelines to circumvent issues existing in XPS analysis, which will provide valuable guidelines in SEI understanding with accurate chemical characterization.

Through analyzing the ratio of gravimetric mass to surface charge (m/z) for specific elements, TOF-SIMS has been applied to obtain the chemical compositions of SEIs quantitatively. Generally, when interacting with a surface, the energetic primary ion beam emits secondary ions. These secondary ions pass through a flight tube, and then they are continuously analyzed, with the corresponding intensities being recorded over time. The ion intensities are proportional to element contents, thus forming a semiquantitative concentration-depth image for probing the chemical composition of the SEI layers.[451,557−559] Peled et al. were pioneers in applying SIMS for investigating the mechanism of SEI formation on the basal plane and cross-sectional edge of graphite. Since then, depth profiling by SIMS has been utilized widely to probe the SEIs generated on Cu,[452,560] graphite,[426,453,454,518,561−563] Si,[452,455,564−567] Li metal,[351,452,456,568−571] etc., demonstrating its ability to analyze the dynamic properties of SEI layers with high sensitivity. Especially, the speculated SEI chemical composition can be confirmed via SIMS by profiling their distribution in depths in the SEI layer. For instance, Wang et al. developed a Li-11 wt % Sr alloy anode to form a SrF_2-rich interphase in fluorine-containing electrolyte.[325] With the aid of TOF-SIMS, the

thickness of the SrF$_2$-enriched SEI on the alloy anode was determined. After immersing in 2 M LiFSI for 12 h, the anode surface was investigated by beam over a 5 μm × μm area. Strong signals of both F and Sr were observed with the thickness of the interphase determined to be 250 nm, which is consistent with the XPS results. In another report, a crowding dilutant (1,2-difluorobenzene) modified ionic liquid electrolyte (M-ILE) with energetic kinetics and a superhigh AGG portion was designed for a stable Li metal anode. TOF-SIMS was performed to reveal the distribution of the chemical components in the SEI layer with different sputter times. The LiF$_2^-$ intensity was much higher than that for the ILE-induced SEI, confirming that the M-ILE electrolyte contributed to a LiF-enriched SEI. Besides, the 3D reconstruction of the LiF$_2^-$ distribution map demonstrated that LiF was uniformly dispersed in the M-ILE-induced SEI. However, LiF only existed in the superficial layer of the ILE-derived SEI.[572] The SEI formation mechanism and the in-depth understanding of the interphasial chemistry and structure are still restricted by the ex situ measurements. Inspired by increasing requirements, real-time SEI formation was monitored by Zhu and co-workers by developing an in situ liquid secondary ion mass spectrometry (liquid-SIMS),[457,508,510] as illustrated in Figure 23b. To be specific, first, a thin Si$_3$N$_4$ membrane was used to separate the liquid from the high vacuum, ensuring only Si$_3$N$_4$-related signals were detected at the initial stage. Then, the interfacial signals could be detected until a Bi^{3+} primary ion beam drilled through the Si$_3$N$_4$ membrane. As soon as the interfacial layer was drilled through by the primary ion beam, the liquid signals were obtained. By bombarding the back of the Cu electrode and creating fragments, liquid-SIMS induced the dynamic chemical mapping of the interfacial components. Liquid-SIMS supported the establishment of an electric double layer before SEI formation. Furthermore, this technique displayed a structured SEI consisting of a dense and inorganic but LiF-depleted inner layer (electronic insulator but Li$^+$ conductor) along with an organic-rich outer layer.[509]

As a nondestructive technique, NMR spectroscopy has been applied to investigate various SEI components (such as inorganics like LiF (^{19}F), Li$_2$CO$_3$ (^{13}C), and organic compounds) via collecting ^{1}H, ^{7}Li, ^{13}C, ^{19}F, as well as ^{31}P signals in a time scale. Combining solution with solid-state NMR (ssNMR), Gray et al. characterized the soluble and insoluble SEI components derived from FEC decomposition.[573] To promote the characterization of organic SEI, ^{13}C-FEC was prepared to conduct ssNMR with enhanced dynamic nuclear polarization (DNP) measurements. Notably, the defluorination reaction of the FEC molecule to soluble vinoxyl species (HCOCH$_2$OR) was detected from the ^{1}H and ^{13}C NMR results. In the following step, they reacted to form both soluble and insoluble branched ethylene-oxide-based polymers, while neither vinoxyl species nor cross-linking units were investigated for the FEC-free electrolyte, suggesting that the generation of cross-linked polymers could be significant for improving the SEI stability on the Si anodes. Besides, Wagemaker et al. accessed the spontaneous Li$^+$ transport via 2D Li ion exchange NMR, disclosing that Li$^+$ interfacial transport through the interphase was the major limitation for the Li$^+$ transport through the Li$_2$S–Li$_6$PS$_5$Br solid-state batteries, which were largely affected by the electrode preparation and battery cycling conditions. For instance, ball-milling treatment was required to enable faster Li-ion exchange through the interphase and enhance the kinetics with regard to

the high utilization of the Li$_2$S cathode. This report exhibited the ability of exchange NMR as a noninvasive measurement to investigate Li$^+$ interfacial transport behaviors, quantifying the amount and time scale of Li$^+$ transport through the interphase in the bulk solid-state batteries.[479] The NMR technique was also applied to determine the cathode-to-anode crossover species that caused the SEI disruption on the Li metal anode and further catalyzed side reactions. It was disclosed that the crossed-over transition metal ions from the Li-Ni$_{0.9}$Mn$_{0.05}$Co$_{0.05}$O$_2$ cathode exerted a minimal impact on the Li metal anode. In contrast, decomposition products such as POF$_2$OH (the doublet of the ^{19}F spectra and the triplet in the ^{31}P spectra) and polycarbonates form reactive Li metals that crossed over to the cathode side, significantly altering the CEI. As a result, this crossover phenomenon accelerated the impedance increase and capacity fading of the cathodes and caused instability of the anodes by dissolving these species into the electrolyte.[480]

Moreover, DNP-enhanced NMR has been recognized as a powerful tool for obtaining useful structural information under magic-angle spinning (MAS), which exploits an ∼10^3 times greater gyromagnetic ratio of paramagnetic electrons to hyperpolarize nuclear spins to increase the signal in NMR measurements.[481] The mechanism of Li metal DNP is illustrated in Figure 23c. Without applying a magnetic field, the partially filled up and down electron spin bands of a metal were degenerated, whereas the energies of these bands were shifted in opposite directions while maintaining a common Fermi level with an applied magnetic field. After irradiating the conduction electron spin resonance (CESR) transition, the populations of the spin bands were (partially) equalized. Based on this theory, Gray et al. reported the hyperpolarization by investigating the interphase between the Li metal and the SEI (Figure 23d).[556] They selectively enhanced the ^{7}Li, ^{1}H, and ^{19}F NMR spectra of the SEI species, which provided the chemical nature and spatial distribution of these species. To exploit the significant enhancement of the ^{7}Li, ^{7}Li → ^{1}H cross-polarization (CP) and ^{7}Li → ^{19}F CP, ^{7}Li rotational echo double-resonance (REDOR) experiments were conducted, successfully identifying some SEI species, such as polymeric compounds, organic carbonates, and LiF. In situ measurements based on this technique will be more informative in identifying the chemical compositions and structures of the interphases in rechargeable batteries. The reduced collection time and enhanced signal-to-noise ratio of ^{13}C to confirm organic species in SEI are among the most prominent advantages of the DNP technique. Unfortunately, it fails to probe the dynamic nature of the interphase, which requires the combination of NMR and cryogenic techniques. Moreover, in situ NMR has been realized for probing the real-time SEI evolution in batteries. The differences in the plating processes and transport properties of the interphase in commercial electrolytes (1 M LiPF$_6$–EC/DMC) without and with FEC additive were investigated via in situ NMR. ^{6,7}Li isotopic labeling was employed to monitor the exchange between the bulk Li metal and the electrolyte via NMR, and a numerical model was developed to describe the process. It was revealed that compared to those of the FEC-free electrolytes, the ^{6}Li/^{7}Li exchange was twice as fast in FEC-containing electrolyte with a much faster SEI formation rate, which could account for a more uniform Li deposition behavior. The authors also used this in situ NMR technology to quantify

some critical SEI parameters for regulating the nature of Li deposition, such as Li^{+} transport and the healing rate of the SEI. Other electrolyte additives or components should be explored via this methodology to optimize SEIs for uniform Li plating/stripping under practical conditions in the future.[482] It should be noted that a strict observation condition should be satisfied to avoid interfering signals when conducting in situ NMR for real-time monitoring of the SEI during cycling.[487]

3.4.4. Functional Feature Analysis Techniques.

Based on the scattering of X-rays, the interference of which produces diffraction patterns from crystalline or partial crystalline structured materials, XRD has been widely employed to investigate the changes in crystal structures as well as phase transformations of electrode materials or the ordering and structures of interphases. For instance, according to the analysis of XRD, Huang and co-workers showed that the byproducts LiOH derived from side reactions between Li and oxygen-containing electrolyte were significantly suppressed via boric acid (BA) additive, suggesting the beneficial role of BA in inhibiting unwanted side reactions for high-performance Li-based batteries.[476] In addition, different SEI formation processes with 0.8 M KPF$_6$—EC/EMC and potassium bis(fluorosulfonyl)imide (KFSI)—EMC (molar ratio of 1:2.5) electrolytes were investigated via operando XRD, revealing that the SEI mainly formed at high voltage in KFSI-based concentrated electrolyte, while the SEI was mainly generated at low voltage in KPF$_6$-based dilute electrolyte.[477] However, as a technique to monitor the bulk information on the electrode, it is difficult for XRD to distinguish specific interactions on the interphases. Recently, synchrotron-based X-ray sources with much higher intensities and larger photon energies than laboratory equipment have been recognized as a powerful technique for in situ/operando investigations of battery systems due to the benefits of a fast period of measurement times, large penetration power, along with improved signal-to-noise ratios.[477] Therefore, the synchrotron-based XRD is able to collect high-quality data for a trace amount of sample without significant radiation damage.[478] In 2021, using synchrotron-based XRD and PDF analysis, Hu et al. identified and differentiated two elusive components, LiH and LiF, in the SEI components of Li metal anodes.[574] As revealed from synchrotron-based XRD, LiH existed as a face-centered-cubic (FCC) phase with a lattice parameter of 4.084 Å, which was further confirmed by the changes in the XRD patterns due to its moisture sensitivity. The origins of LiH not being identified could be attributed to two main factors. First, the typical XRD patterns of LiH and LiF were similar FCC structures with close lattice parameters (4.084 Å for LiH and 4.026 Å for LiF). Besides, owing to the high moisture sensitivity, LiH easily decomposed to make it undetectable. It was also found that the nanocrystalline LiF in the SEI components is clearly different from that in the bulk phase, especially featuring a larger lattice parameter (~4.05 Å) along with a smaller particle size (<3 nm), which enables fast Li^{+} transport for higher CE and improved electrochemical performance. It should be noted that the beam may easily lead to the damage of battery materials during testing.

As a nondestructive imaging approach, in situ AFM can monitor the formation and properties of interphases through high-resolution topographical images, providing intertopography information and mechanical properties. For instance, the elastic and plastic properties of the interphases can be evaluated in a quantitative way by analysis of the force–distance curves.[511] In addition, to investigate the nanomechanics of interphases, AFM-nanoindentation was designed as illustrated in Figure 23f. Through converting the tip deflection into normal force F and analyzing indentation depth δ and the cantilever deflection Δd, the Young's modulus can be obtained as shown in the inset of Figure 23f, successfully quantifying the inhomogeneity of the SEI in both morphological and mechanical properties.[462] Following this work, more systematic investigations of SEI information have been conducted, including the two-layered structure and the thickness of the SEI on graphite anodes,[575] the mechanical properties of the organic—inorganic mixed SEI on the Si anode,[575] the effects of electrolyte components, configurations, and electrode face orientation on the SEI morphology and thickness,[463−465,576] the deformation and mechanical failure mechanism of the SEI,[512] etc. Among these progresses, it is interesting to mention that in situ AFM is powerful enough to distinguish the distributions of inorganic and organic species in the SEI at the nanometer level by probing the SEI in liquid electrolytes.

Unfortunately, the failure to unveil chemical information is a large limitation facing the AFM technique. To satisfy the nanometer spatial resolution required to disclose the correlation between the structure and the function in the interphases, tip-enhanced Raman spectroscopy (TERS) was developed.[466,514,515] Through raster scanning the interphase, the chemical fingerprint of the interphases can be obtained. Besides, TERS offers a spatial resolution at several nanometers or even on a subnanometer scale, which is attributed to the highly confined local electric field.[467] Therefore, TERS has been regarded as an effective technique for understanding the interphase as well as interfacial processes at the nanometer spatial resolution, eventually establishing the relationship between the structure and the performance. Although with a high spatial resolution, the one-point foundation makes inherently weaker signals for the TERS technique compared with surface-enhanced Raman scatting (SERS), making it necessary to increase the efficiency of TERS on motivation and collection when used to probe the interphases. Besides, to monitor the dynamic evolutions of the interphase structures and further quantify the interphase compositions at the nanometer spatial resolution and the molecular level, TERS should be developed into an operando technique.[577]

As a scattering technique, NR measures the specular reflection of neutrons from the surface, which changes with the wave vector transfer perpendicular to the sample surface, following the equation $Q = [4\pi \sin(\theta)]/\lambda$ (where θ represents the angle of incidence of the neutron beam with the sample surface and λ denotes the wavelength of the neutrons).[578,579] The thickness, roughness, as well as the layers' scattering length density (SLD) can be obtained by fitting the reflectivity via layered models, which is informative for determining the layer compositions. Therefore, NR has been increasingly employed for probing the interphasial properties of batteries.[474,516]

Particularly, the SLD depth profile yielded from fitting NR data in the surface normal direction can be used to detect the evolutions of the interphase structure during the charging/discharging process.[473] By using in situ NR and a novel designed electrochemical cell, Schmidt et al. detected the growth of a ~7 nm thick SEI layer during delithiation of the Si electrode.[550] Later, the thickness and chemistry of the SEI on a Si anode were determined as a function of the state of charge

during cycling. Based on the SLD results, the SEI thickness decreased from 25 to 18 nm ($Li_{3.7}Si$) after the delithiation process. Besides, the SEI evolved with more LiF component during lithiation, while more Li−C−O−F-like species was discovered during delithiation. More importantly, the SEI started to grow once the electrolyte was in contact with the Si electrode, even though no electrical bias was applied.[580] An opposite trend in SEI thickness was presented by Veith et al., who investigated the SEI on Si anodes using the electrolyte of 0.1 M LiTFSI in deuterated dimethyl perfluoroglutarate.[581] Based on the corresponding SLD profiles, they observed a decrease in the thickness of the SEI layer from 34 to 14 nm after the lithiation process. Moreover, in situ NR revealed that the SEI formed on tungsten thin film electrodes was composed of a porous outer layer enriched in solvent-derived components and a compact inner layer with abundant inorganic species.[474] Following this work, tungsten oxide (e.g., WO_3) was demonstrated to form a SEI with three layers during the reduction process. An innermost layer (the evolving conversion electrode) was assigned to a mixture of W, Li_2O, and incompletely reacted WO_3 or Li_xWO_3, a layer enriched in protons and/or Li, which tentatively consisted of LiOH or LiH (the inner SEI), and an outermost layer adjacent to the electrolyte consisting of lower SLD species with solution-filled porosity or deuteron-rich species derived from the solvents (the outer and fragile SEI). A reverse of SEI evolution was observed during the oxidation process. These results were generally consistent with previous reports of the SEI using other characterization methods, indicating a bilayer structure of the SEI with more inorganic species in the inner layer and more organic components in the outer layer.[475]

Overall, in situ NR sheds light on the study of the SEI generation mechanism by probing the evolution of the interphase structure during battery operation. Unfortunately, its widespread application is significantly restricted by several factors, such as a long analysis time, an excessive choice of electrolyte solvents to enhance contrast, a flat specimen required to generate a strong signal, and very limited facilities to handle the produced neutrons outside the particle accelerator.[437]

To investigate the various functional and morphological features of the interphases, other characterization methods that can offer complementary information have also been developed. For instance, in contrast to XRD providing information about the overall structure of a material, XAS has been considered as an effective technique to probe the local atomic arrangement and electronic structure of a material. XAS technology is based on X-ray photon-induced electronic excitations from the core level to an empty electronic state for the detected element. Thanks to its element-resolved feature and high sensitivity to the local chemical bonds and solvent environments, the XAS measurement shows great potential for interphase characterization.[468−470,582] Additionally, this technique can be used for determining amorphous phases as well as for small nanoparticles. Owing to the utilization of high-energy synchrotron radiation, the data acquisition process is quite fast, which promotes in situ analysis as well.[583,584] Although XAS has been successfully used for analyzing the SEI composition, in situ XAS probing in a full-cell mode remains a big challenge, which requires a special electrochemical cell design.[471,472,517−520]

SECM is considered a powerful tool that can probe the surface characteristics of the interphases with nanoscale resolution. SECM relies on the stark difference in activities between the electronically conductive electrode surface and the electronically insulating feature of the SEI products.[483,484] The basic setup of SECM consists of four parts: a low-current bipotentiostat, a 3D positioning system, an ultramicroelectrode tip, and a data acquisition system.[485] The cell generally contains four electrodes, including the tip, the reference electrode, the counter electrode, and the working electrode. The SECM tip probes the chemical changes occurring at the interphase and detects spatial information on electrochemical reactions taking place at selected areas.[484] SECM has attracted increasing attention in investigating the formation and evolution of SEI layers by employing the feedback mode.[484] For instance, using the feedback mode of SECM with 2,5-di-tert-butyl-1,4-dimethoxybenzene (DBDMB) as the mediator, Wittstock et al. conducted in situ imaging of the spontaneous spatiotemporal changes for SEI layers formed on the graphite surface. The reduction in the mediator regeneration rate was accompanied by SEI formation. Besides, the currents remained stable in some regions of the SEI-covered electrodes, while the currents in other regions changed drastically with time. These changes could be attributed to the volume evolutions during charging/discharging, dissolution of SEI, or gas formation. In addition, the results show that deposition of metallic Li could take place upon charging and compromise battery safety, requiring the self-healing ability of the SEI with incidental defects. Moreover, the repassivation of damaged regions was detected in situ, which showed that it took several hours before these regions were susceptible to further short-term current fluctuation.[486] Later, operando SECM was adopted by Schuhmann et al., probing the electrically insulating feature of the Si surface during the delithiation/lithiation process. Combined with AFM, the SECM results suggested that there were two types of cracks (i.e., cracks partially covered by the SEI and SEI-free cracks) during the initial cycle. The SEI-free cracks contributed to a discontinuity in the electrically insulating feature of the Si surface, further accelerating electrolyte decomposition in the second cycle. More importantly, operando SECM confirmed the electrically insulating feature of the SEI layer on the Si electrode, and the volume changes during the delithiation/lithiation process were what caused the loss of "protecting" character of the SEI at the Si surface.[585]

In brief, to address fundamental questions regarding the chemical composition, spatial distribution, and structure of fluorinated interphases, nondestructive and in situ/operando techniques are essential for real-time, dynamic, and intuitive analysis of the interphase properties and their correlation with the battery performance. Taking cryo-TEM as an example, the combination of a low electron dose and ultralow temperature for the frozen sample reveals atomic-level crystal details, which preserves the delicate chemical and spatial features of interphases. For high-resolution imaging of interphasial evolution, dynamic in situ cell devices and sophisticated sample preparation techniques (e.g., cryo-FIB) should be equipped. It should be kept in mind that each technique has its unique advantages and significant limitations, requiring the synergistic combination of various techniques, which yields multidimensional or multimodal information for elucidating the structure−property relationships and guiding interphase design.
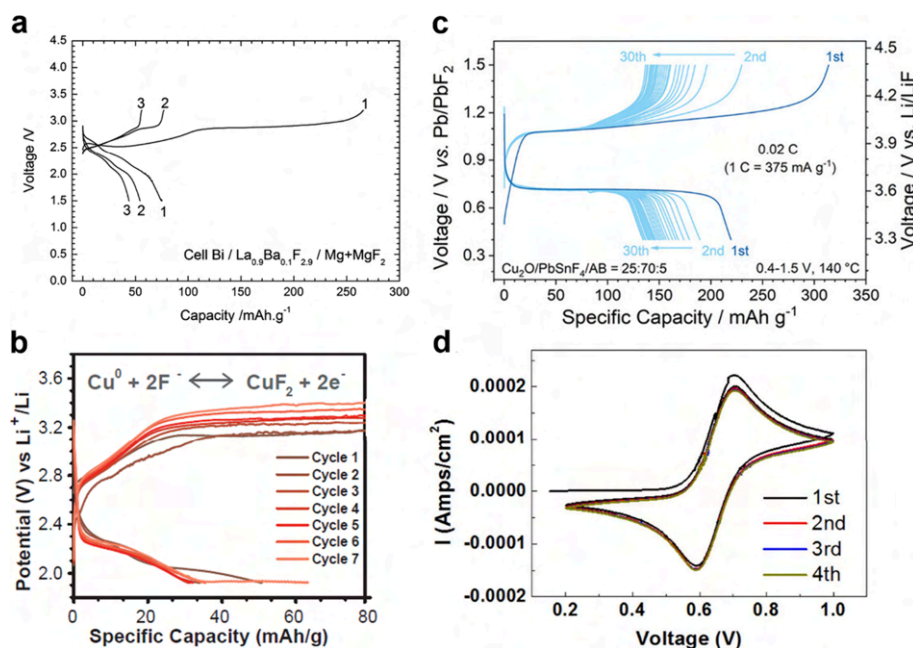
Figure 24. Conversion-type electrode materials for FIBs. (a) Voltage−composition profiles for a FIB with the Bi cathode vs the Mg + MgF$_2$ anode in the three first cycles. The charge/discharge curves were obtained at 150 °C for a current density of ca. ±4 mA g^{-1}. Reproduced with permission from ref 587. Copyright 2014 Royal Society of Chemistry. (b) Electrochemical charge and discharge curves for a three-electrode cell with a Cu@LaF$_3$ cathode in 1 M N,N,N-trimethyl-N-neopentylammonium fluoride (Np$_1$F)−BTFE, cycled at 10 mA. Reproduced with permission from ref 52. Copyright 2018 The American Association for the Advancement of Science. (c) Charge/discharge profiles of Cu$_2$O cathode material for cycles 1−35 at 0.02 C and 140 °C. Reproduced with permission from ref 590. Copyright 2021 Wiley-VCH. (d) CV curves of 4-hydroxy-TEMPO in aqueous 0.8 M NaF electrolyte with glassy carbon as the working electrode, platinum as the counter electrode, and the standard Ag/AgCl electrode as the reference electrode. Reproduced with permission from ref 591. Copyright 2019 IOP Science.

4. FLUORINE CHEMISTRY IN RECHARGEABLE FLUORIDE-ION BATTERIES

4.1. Fluoride Electrode Materials

The electrode material for FIBs can release or absorb F$^-$ ions while obtaining or losing electrons. Depending on the redox potential, the electrode materials for FIBs are utilized as cathodes with relatively high potential or anodes with relatively low potential. Due to the relatively light weight of the electrode materials in FIBs, the theoretical volumetric energy densities of FIBs can reach up to 5000 Wh L^{-1} based on the total volume of the electrode materials,[38] which makes FIBs a promising candidate for next-generation high-energy rechargeable batteries. So far, the mechanism of F$^-$-ion storage of electrodes in FIBs can be mainly classified into conversion type and intercalation type, which are further introduced below.

4.1.1. Conversion-Type Electrode Materials. The fluorination/defluorination process of conversion-type electrode materials (e.g., metal/metal fluorides) is accompanied by continuous breaking or reforming of the metal−fluorine bond. Conversion-type electrode materials for FIBs possess high energy density because they are able to transport more than one F$^-$ ion per redox-active metal species, and the active electrode materials typically possess lower molar masses.

Metal/metal fluorides (M/MF$_x$) are the most extensively studied conversion-type electrode materials for FIBs. The electrons and F$^-$ ions transfer during the fluorination/defluorination between metal and metal fluorides. In 2011, Fichtner and Anji reported the feasibility of a series of metal fluorides (including SnF$_2$, CuF$_2$, KBiF$_2$, and BiF$_3$) as cathode materials in an all-solid-state FIBs system with a F$^-$-ion solid-state electrolyte La$_{1-x}$Ba$_x$F$_{3-x}$ ($0 \leq x \leq 0.15$) at 150 °C.[43]

Cerium (Ce) metal was used as the anode due to the high F$^-$-ion conductivity of its discharge product (cerium fluoride, CeF$_3$).[586] The F$^-$-ion full cell using BiF$_3$ as a cathode successfully realized reversible discharge and charge at 10 μA cm^{-2} with a discharge capacity of 190 mAh g^{-1} and an average voltage of 2.15 V. However, the irreversible volume changes, as a common problem of conversion-type electrode materials, limit the cycling performance of FIBs. Apart from the Ce metal anode, Fichtner and co-workers investigated the application of other potential anode materials such as CaF$_2$, MgF$_2$, and Mg + MgF$_2$ (i.e., the premixed composite of metal and metal fluoride, M + MF$_x$) for all-solid-state FIBs in 2014.[587] When paired with a bismuth (Bi) cathode, the Mg + MgF$_2$ composite anode delivered an initial discharged specific capacity of about 80 mAh g^{-1} at 4 mA g^{-1} and 150 °C (Figure 24a). It revealed that the M + MF$_x$ composite anode can effectively enhance the cycling performance by improving interphase contacts between the reactive phases. In general, the low conductivity of the metal fluorides and the extreme volume change during the fluorination/defluorination process of M + MF$_x$ electrodes cause the massive side reactions[588] together with poor physical contact between active materials,[589] electrolytes, and conductive carbon particles, both of which lead to rapid capacity decay of FIBs.

M/MF$_x$ has also been applied in liquid FIBs. Simon and co-workers reported room-temperature operable FIBs based on organic solvent-based electrolyte in 2018.[52] In this system, a copper−lanthanum trifluoride core−shell cathode was developed, where the F$^-$-ion conductive LaF$_3$ shell not only permitted F$^-$ diffusion but also inhibited the dissolution of the discharge product (CuF$_2$). The Cu@LaF$_3$ cathode achieved
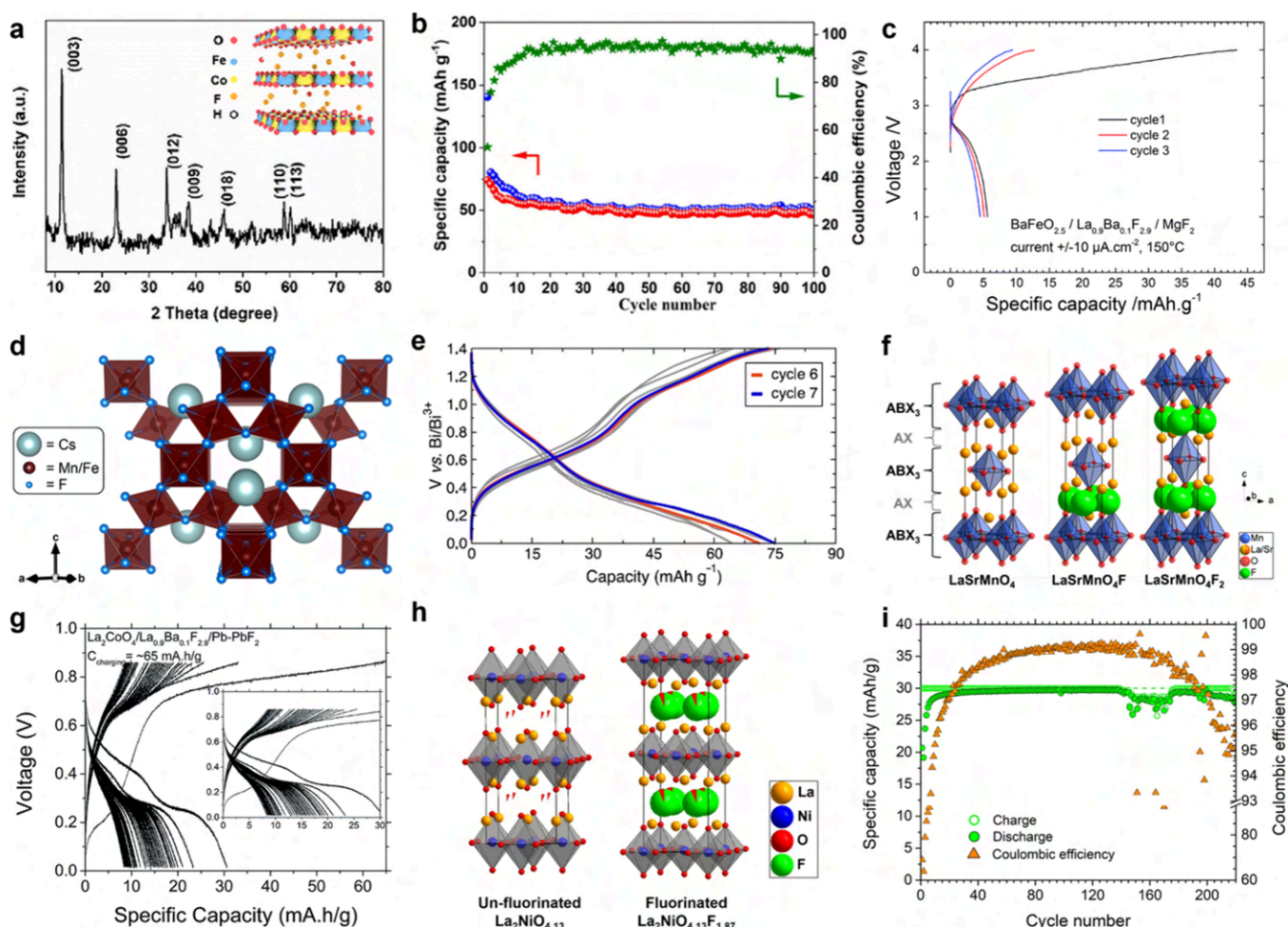
Figure 25. Intercalation-type electrode materials for FIBs. (a) XRD pattern of CoFe-F LDH. (Inset) structural model. (b) Cycling performance and CE for the cell Li||CoFe-F LDH. Reproduced with permission from ref 592. Copyright 2022 Wiley-VCH. (c) Voltage profiles measured during three charge/discharge cycles for the cell $BaFeO_{2.5}|La_{0.9}Ba_{0.1}F_{2.9}|MgF_2$ (current ± 10 μA cm^{-2} at 150 °C). Reproduced with permission from ref 593. Copyright 2014 Royal Society of Chemistry. (d) Crystal structure of the defect fluoride pyrochlore $CsMnFeF_6$ viewed down the [110] direction. (e) Cycles 4−9 from galvanostatic cycling of a F-ion cell with a working electrode of mechanochemically synthesized $CsMnFeF_6$ and a Bi/BiF$_3$ composite counter electrode, cycled at room temperature at a rate of C/20 between 0.0 and 1.4 V vs Bi/BiF$_3$. Cycles six and seven are shown in orange and blue, respectively. Reproduced with permission from ref 594. Copyright 2022 American Chemical Society. (f) K_2NiF_4-type structure of $LaSrMnO_4$ (left) in comparison to partly fluorinated $LaSrMnO_4F$ (middle) and fully fluorinated $LaSrMnO_4F_2$ (right). Reproduced with permission from ref 72. Copyright 2017 American Chemical Society. (g) Electrochemical charging and discharging of La_2CoO_4/La_2CoO_4F at 170 °C; $I_{charging}$ = +10.0 μA, $I_{discharging}$ = −1.0 μA. Reproduced with permission from ref 595. Copyright 2019 Wiley-VCH. (h) Schematic illustrations of the unfluorinated $La_2NiO_{4.13}$ (left) and hypothetical fully fluorinated state $La_2NiO_{4.13}F_{1.87}$ (right). Fractional occupancies are depicted for the interstitial anion site. (i) Charge/discharge capacities and CE against cycle number for the cells with the cutoff capacities of 30 mAh g^{-1} at T = 170 °C, I_{charge} = +24 μA cm^{-2}, $I_{discharge}$ = −12 μA cm^{-2}, and cutoff charge voltage = 2.3 V. Reproduced with permission from ref 596. Copyright 2020 Springer Nature.

seven reversible cycles in liquid FIBs at room temperature in a three-electrode cell (Figure 24b).

Metal oxide-based electrodes have been developed as a new conversion-type electrode material. In 2021, Uchimoto and co-workers reported a cuprous oxide (Cu_2O) cathode with Cu^+/Cu^{2+} redox as a fast fluorination cathode material for all-solid-state FIBs.[590] As shown in Figure 24c, the Pb/PbF$_2$|PbSnF$_4$|Cu_2O cell delivered an initial discharge specific capacity of 220 mAh g^{-1} at 0.02 C (1 C = 375 mA g^{-1}) that remained stable after stabilization of the partially irreversible amorphization phase. The superior rate capability of the Cu_2O cathode (110 mAh g^{-1} at 1 C) surpassed the simple M/MF$_x$ systems, which can be attributed to the fast F$^-$-ion movement on the phase boundary.

An organic compound with radical groups has also been investigated as an electrode material for FIBs. In 2019, Chen and co-workers reported the utilization of 4-hydroxy-2,2,6,6-tetramethylpiperidin-1-oxyl (4-hydroxy-TEMPO) cathode in an aqueous rechargeable FIB.[591] The reaction mechanism of 4-hydroxy-TEMPO is as follows

$$4\text{-hydroxy-TEMPO}^\bullet + F^-$$
$$\leftrightarrow 4\text{-hydroxy-TEMPO} + F^- + e^- \qquad (1)$$
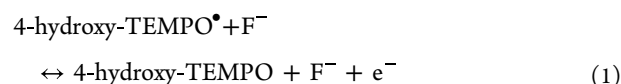
where the electrostatic balance of 4-hydroxy-TEMPO was maintained by the transfer of the fluoride ions and electrons. The redox peak pairs at 0.706 and 0.594 V in the cyclic voltammetry (CV) curves (Figure 24d) can be distributed to the conversion between 4-hydroxy-TEMPO and 4-hydroxy-

$TEMPO^+F^-$. When paired with a BiF_3 anode in a NaF water solution electrolyte and cycled between 0.0 and 1.4 V, this aqueous FIB delivered an initial discharge specific capacity of 145.3 mAh g^{-1} at 1000 mA g^{-1}.

4.1.2. Intercalation-Type Electrode Materials. Different from the conversion-type electrodes, the F^- ion can be reversibly stored in or released from the unoccupied interstitial sites or anion vacancies in the crystal structure of the intercalation-type electrodes for FIBs. Thus, the structural integrity of the intercalation-type electrode can be maintained due to the slight volume charge during the intercalation/deintercalation of the F^- ion, which ensures the highly reversible cycling stability and good rate performance of FIBs.

Recently, a F^--ion-intercalated CoFe-layered double hydroxide (CoFe-F LDH) was reported as a cathode material for FIBs. Zhang and co-workers prepared the CoFe-F LDH through a facile coprecipitation approach combined with an ion-exchange method (Figure 25a) and successfully paired this material as a cathode with a Li metal anode in a CsF-based organic liquid electrolyte.[592] The Li||CoFe-F LDH cell delivered a stable specific capacity of 48.9 mAh g^{-1} during 100 cycles at 10 mA g^{-1} under room temperature (Figure 25b) owing to the unique topochemical transformation property and small volume change (~0.82%) of CoFe-F LDH materials accompanied by electrochemical intercalation/intercalation of F^- ions. Moreover, the good rate performance of CoFe-F LDH indicated that the mitigation of the F^- ion in the layer spacing was facilitated by the weak electrostatic interaction between the anions and the host layers with a low diffusion barrier.

The perovskite-type $BaFeO_2$ was reported as an intercalation-type electrode material for FIBs by Oliver and co-workers in 2014.[593] First, they demonstrated that $BaFeO_{2.5}$ can be directly fluoridated by heating $BaFeO_{2.5}F_{0.5}$ in F_2. The transformation of the monoclinic distorted phase to the cubic perovskite phase in the XRD pattern indicated the successful intercalation of the F^- ion into the subcrystalline vacancies in $BaFeO_{2.5}$. Then, the $MgF_2|La_{0.9}Ba_{0.1}F_{2.9}|BaFeO_{2.5}$ solid-state FIB was assembled and cycled between 3 and 4 V at 150 °C. As shown in Figure 4c, the long charge plateau at the initial cycle was attributed to the formation of a Fe^{4+}-containing phase fraction of a $BaFeO_{2.5}F_y$ compound, where the XRD pattern of electrochemical fluorination was consistent with that of the chemical fluorination result. However, the low reversible capacity in the following cycling suggested that the F^- ions were not fully deintercalated from the $BaFeO_{2.5}F_y$ cathode, which may be caused by the contact problems in the electrodes and side reactions of conductive carbon.

Likewise, $CsMnFeF_6$ was investigated as a cathode material for room-temperature FIBs by Jessica and co-workers in 2022.[594] $CsMnFeF_6$ in a defect pyrochlore structure with suitable particle size and phase purity was obtained through a mechanochemical method. The presence of Frenkel defects was required to endow the F^- ion's diffusion through the network, so the defect pyrochlore $CsMn^{2+}Fe^{3+}F_6$ (Figure 25d) with the disorder in the $MnFeF_6$ substructure and ordered anionic vacancies became a suitable fluoride intercalation host, allowing fast F^--ion transport at room temperature. After combination with an organic liquid electrolyte (1.0 M tetra-n-butylammonium fluoride (TBAF)−THF) and cell activation cycles, the half-cell delivered a reversible capacity of 70 mAh g^{-1} at room temperature with a high CE of 98% (Figure 25e), which almost approached the theoretical capacity for one fluoride-ion transportation. Ex situ XRD and ex situ XAS

revealed that the $CsMnFeF_6$ underwent a topotactic transformation from the original defect pyrochlore structure into a related polytype; meanwhile, the $Fe^{3+/2+}$ and $Mn^{3+/2+}$ redox couples both functioned during the cycling.

Oliver and co-workers reported the investigation of $LaSrMnO_4$ with a K_2NiF_4-type structure as an intercalation-based high-voltage cathode material with high capacity for FIBs in 2017.[72] As shown in Figure 25f, the structure of K_2NiF_4-type compounds (A_2BX_4) can be described as built up by alternating layers of ABX_3 perovskite-type subunits and AX rock salt subunits along the c axis. The large interstitial sites that can store anions existed between the boundary of the rock salt and the perovskite phase layers. The highest F^--ion occupied interstitial sites (Y) per formula unit was 2, which resulted in the composition of $A_2BX_4Y_2$. The Pb−PbF_2 anode was paired with the $LaSrMnO_4F$ cathode with the $La_{0.9}Ba_{0.1}F_{2.9}$ solid-state electrolyte, and the full cell was tested at 10 μA under 200 °C. Combined with the results of the electrochemical data, XRD spectra, and DFT calculations, two charge voltage plateaus at 1 and 2 V were confirmed as the first and the second steps of F^--ion intercalation ($LaSrMnO_4 \rightarrow LaSrMnO_4F$ and $LaSrMnO_4F \rightarrow LaSrMnO_4F_{2-x}$, $x \approx 0.2$). It is worth noting that the side reaction, fluorination of conductive carbon in the cathode, along with the charging process resulted in an overcharge capacity of 800 mAh g^{-1}, which was much higher than the theoretical capacity (155 mAh g^{-1}) of two F^--ion transfers from $LaSrMnO_4 \rightarrow LaSrMnO_4F_2$. Moreover, the fluorination of conductive carbon also deteriorated electron transfer in the cathode, which then led to the low reversible discharge capacity of 20 mAh g^{-1}.

To overcome this side reaction issue, Oliver and co-workers replaced the redox pairs of Mn^{3+}/Mn^{4+} with Co^{2+}/Co^{3+} to reduce the oxidation potentials in the K_2NiF_4-type compounds.[595] The obtained intercalation-type cathode La_2CoO_4 showed a lower F^--ion interaction number of 1.2 per formula in the same battery system with $LaSrMnO_4$. The unwanted side reactions in the cathode were effectively avoided by adjusting the charge cutoff capacity of 65 mAh g^{-1}, which delivered a better discharge capacity of 32 mAh g^{-1} with a capacity retention of ~25% for the initial discharge capacity after 50 cycles (Figure 25g). However, although the side reaction has been suppressed by a cutoff charge voltage of 1 V, the low discharge capacity of $La_2CoO_4F_{1.2}$ indicated that part of the F^- ions was irreversibly fixed in the layered cathode, which was supported by the XRD structural analysis.

Then, Oliver and co-workers developed a high-voltage intercalation-type cathode (La_2NiO_{4+d}) and achieved an all-solid-state FIB with high cycling stability and a CE close to 100%.[596] As shown in Figure 25h, $La_2NiO_{4.13}$ was successfully synthesized by a solid-state method, which delivered a maximum theoretical capacity of 125 mAh g^{-1} after charging into $La_2NiO_{4.13}F_{1.87}$, where all empty interstitial anion sites were filled by F^- ions. When a charge cutoff capacity of 30 mAh g^{-1} was applied, the $Zn/ZnF_2|La_{0.9}Ba_{0.1}F_{2.9}|La_2NiO_{4+d}$ cell reached an average CE of 97.68% over 220 cycles (Figure 25i). As evidenced from the TEM images, automated diffraction tomography (ADT), EDX spectroscopy, and XAS indicated that the interstitial sites the in $La_2NiO_{4.13}$ cathode were nearly fully occupied by F^- ions, leading to the formation of a high fluorine content phase of $La_2NiO_{4.13}F_{1.59}$. However, although the less reactive CNTs were used as conductors in the cathode, the side reaction did not stop in the charge process, as verified by electrochemical impedance spectroscopy
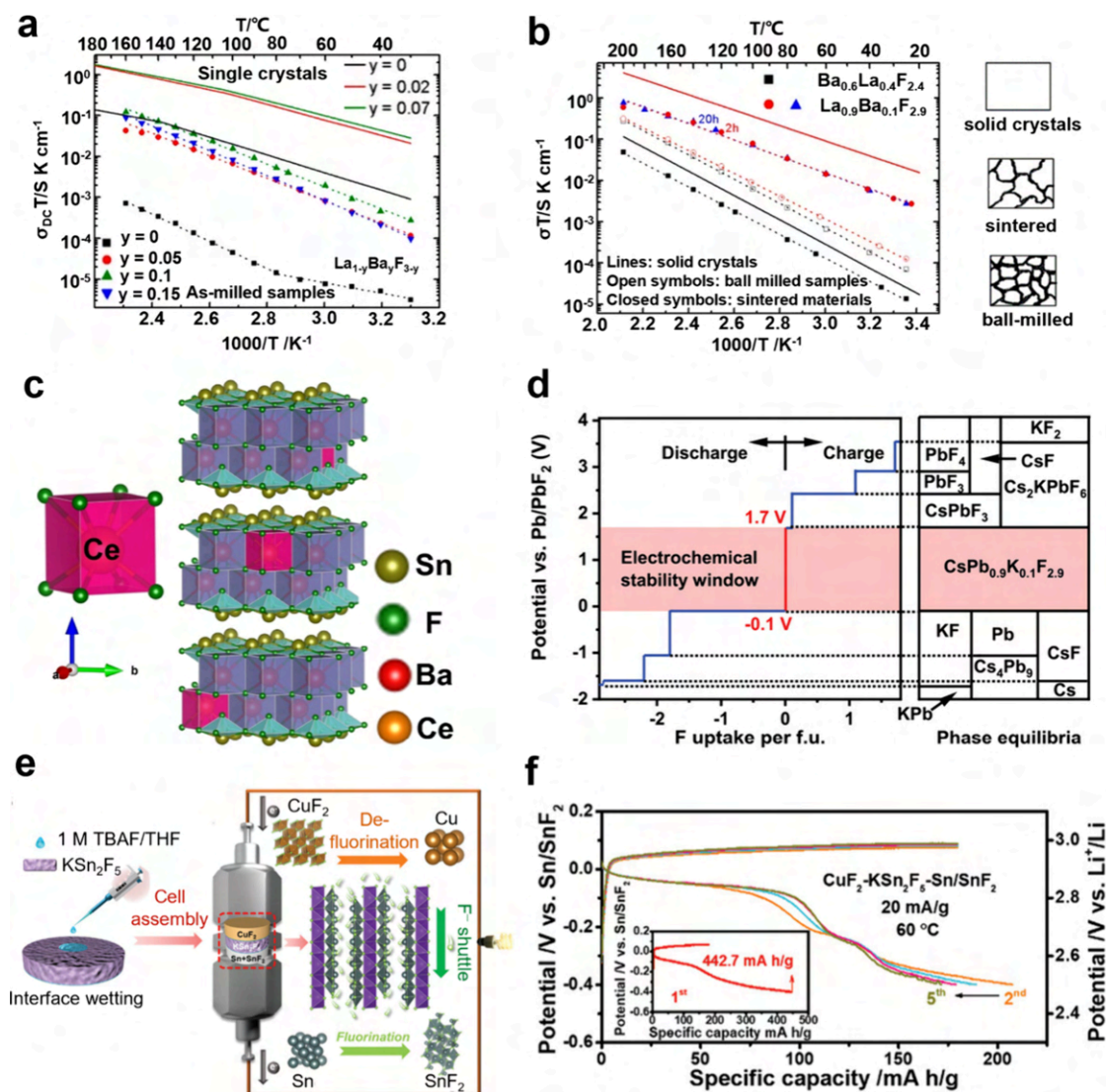
Figure 26. Developments of solid-state electrolytes for FIBs. (a) Arrhenius plot of the ionic conductivity for ball-milled $La_{1-y}Ba_yF_{3-y}$ electrolyte. (b) Arrhenius plots of the ionic conductivities for tysonite-type $La_{0.9}Ba_{0.1}F_{2.9}$ and fluorite-type $Ba_{0.6}La_{0.4}F_{2.4}$ prepared by ball milling and sintering. Reproduced with permission from ref 276. Copyright 2014 American Chemical Society. (c) Crystal structures of the $Ba_{0.95}Ce_{0.05}SnF_{4.05}$ phase. Reproduced with permission from ref 601. Copyright 2022 American Chemical Society. (d) ESW based on the calculated thermodynamic equilibrium voltage profiles and the phase equilibria for the $CsPb_{0.9}K_{0.1}F_{2.9}$ electrolyte. Reproduced with permission from ref 602. Copyright 2022 Wiley-VCH. (e) Illustration of interphase wetting, cell assembly, and predicted reaction processes for Swagelok-cell-type CKC|KSn_2F_5|SSKC FIB. (f) Voltage curves of the initial five cycles for a SSKC|KSn_2F_5|CKC battery. Reproduced with permission from ref 603. Copyright 2023 Wiley-VCH.

(EIS) and XPS testing. Therefore, strategies aiming at improving the stability of the interphase between the active materials and the carbon-based additives in electrode composites (e.g., coating techniques or advanced engineering) should be further developed for development of FIBs.

In general, the conversion-type materials degrade fast due to poor interphase contacts originating from the significant volume change, incomplete conversion reaction, electrode material dissolution, and irreversible generation of oxyfluoride byproducts, while intercalation-type materials are limited by the relatively low capacity and low energy density. Moreover, side reactions between conductive carbons and fluorides in the electrode continuously degrade the performance of FIBs.

4.2. Fluoride Electrolytes

4.2.1. Solid-State Electrolytes.
Since the pioneering work by Fichtner et al., which demonstrated the first rechargeable FIBs employing $La_{0.9}Ba_{0.1}F_{2.9}$ solid electrolyte, there has been

extensive interest in the F^- conducting solid-state electrolytes. Generally, the F^--ion conducting solid electrolytes can be categorized into a tysonite-type structure (rare-earth fluorides MF_3, M = La, Ce, Pr, Nd), fluorite-type structure (alkaline-earth fluorides MF_2, M = Ba, Ca, Sr), and their doped phases, displaying an ionic conductivity of 10^{-4} S cm^{-1} at high temperature (e.g., 150 °C).[43] Thus, insufficient F^- conductivity has been the restricting factor for the operation of solid-state FIBs at low or room temperature.

The F^--ion transport through solid electrolytes is typically facilitated by the Schottky and anti-Frenkel point defects via the vacancy mechanism, interstitial mechanism, and interstitial–substitutional exchange mechanism. Thus, the fast ionic conductivity can be achieved by creating new defects within the solid structure. However, the defect mechanism highly depends on the structure of the solid electrolyte. Given that the F^- interstitial site is relatively smaller (0.84 Å) compared to the

F^- radius (1.19 Å), it is unlikely to be created in tysonite-type $R_{1-x}M_xF_{3-x}$ fluorides (where R denotes the rare-earth element, while M represents the divalent element). In such instances, the formation of F^- vacancies has been demonstrated to be effective in improving the ionic conductivity of RF_3 fluorides.[72,586,597–600] Doping the polycrystalline sintered CeF_3 with various difluorides including CaF_2, SrF_2, and BaF_2 (5 mol %), Takahashi and co-workers revealed that the conductivity of CeF_3 was significantly enhanced up to 1.0×10^{-2} S cm^{-1} at 200 °C (for $Ce_{0.95}Ca_{0.05}F_{2.95}$), which was attributed to the facile movement of vacancies.[276] In addition, the structural features of solid electrolytes have critical impacts on the F^- mobility. In the case of the tysonite $Sm_{1-x}Ca_xF_{3-x}$ solid, as the Ca content increases, the distortion of the F1(Sm, Ca)$_4$ tetrahedral site diminished, leading to an exponentially reduced ionic conductivity and an increase in the activation energy. Consequently, at room temperature, the highest conductivity of 10^{-4} S cm^{-1} was achieved for the lowest Ca content or the smallest fluorine vacancy content in the $Sm_{0.95}Ca_{0.05}F_{2.95}$ tysonite.[599] The F^- conduction mechanism for the tysonite-type structure, however, was drastically different from that for fluorite-type solids. To reveal the conduction mechanism, Fichtner and co-workers prepared a series of $La_{1-y}Ba_yF_{3-y}$ ($0 \leq y \leq 0.15$) solid compounds using the ball-mill method, revealing that grain boundaries exert a detrimental effect on the F^- conduction of tysonite-type solids (Figure 26a and 26b). Sintering the compounds to reduce grain boundaries and improve grain growth contributed to higher ionic conductivities. Unfortunately, extending the sintering time beyond a certain threshold (20 h) did not further increase the ionic conductivity (compared to samples sintered for 2 h) due to the blocking effect of additional grain boundaries induced by oxides, silicates, or fluorite-type phase.[276]

The above-mentioned two mainstream fluorides have achieved substantial progress, yet they generally realize an ionic conductivity of 10^{-4} S cm^{-1} at high temperatures around 150 °C.[604] Their practical applications are still plagued by insufficient RT conductivity, prompting researchers to explore novel fluoride structures with faster transport of F ions at low temperature.[43,605–607] Sn(II)-based fluorides such as $BaSnF_4$ compound are anticipated to deliver high F^- conductivity since the polarizable lone pair of electrons on Sn^{2+} can reorient during moving, enabling the mobile F^- between the Sn–Sn and the Sn–Ba layers to take part in the ionic conduction process.[608–610] Unfortunately, the strong electrostatic interaction between Ba and F in the Ba–Ba layer considerably impedes the F-ion migration. To eliminate this shielding effect, the introduction of point defects within $BaSnF_4$ solids has been adopted for realizing efficient F^- shuttling. By partially substituting Ba^{2+} by Ce^{3+}, which has a similar atomic radius, point defects can be built in the tetragonal $BaSnF_4$ crystal (Figure 26c). Accordingly, the Ba–Ba 3D barrier was disrupted, broadening the pathways for F^- transport. $Ba_{0.95}Ce_{0.05}SnF_{4.05}$ displayed an enhanced RT conductivity of 5.2×10^{-4} S cm^{-1} and a reduced activation energy of 0.15 eV compared to 1.49×10^{-4} S cm^{-1} and 0.15 eV for $BaSnF_4$ solid electrolyte, respectively. The assembled all-solid-state BiF_3|$Ba_{0.95}Ce_{0.05}SnF_{4.05}$|Sn FIB realized a high reversible specific capacity of 170.9 mA h g^{-1} and a stable cyclability over 30 cycles at RT.[601] Clearly, constructing point defects in F^- conducting solid electrolytes is promising for efficient shuttling of F ions. Although $BaSnF_4$ delivered high RT ionic

conductivities comparable to those for solid electrolytes in LIBs,[611] its narrow ESW restricted the selection of cathode and anode materials, which led to a low average discharge voltage (usually less than 0.5 V).[609,612,613] To fulfill the requirements of high conductivity (e.g., 10^{-4} S cm^{-1}) at RT and an adequately broad ESW simultaneously, a solid electrolyte with the chemical formula of $CsPb_{0.9}K_{0.1}F_{2.9}$ was designed. It was revealed that introducing F vacancies greatly facilitated the ionic transport of $CsPb_{1-x}K_xF_{3-x}$, with the F^- conductivity reaching the maximum of 1.23×10^{-3} S cm^{-1} when x was increased to 0.1. Moreover, the redox reaction was found to proceed through the valence change of Pb rather than Sn, as indicated by the calculation result. The reduction of Pb occurred at -0.1 V (vs Pb/PbF$_2$), while the oxidation to obtain high-valent Pb took place at 1.7 V, contributing to a wide ESW of 1.8 V for the $CsPb_{0.9}K_{0.1}F_{2.9}$ electrolyte (Figure 26d). This result agreed well with LSV measurements, which showed a distinct oxidation started at 1.92 V and a reduction started at 0.11 V. Owing to these desirable features, a Pb/PbF$_2$|$CsPb_{0.9}K_{0.1}F_{2.9}$|Ag battery with high discharge voltage was constructed, maintaining high and stable specific capacity ($\sim$140 mAh g^{-1}) after 72 cycles (4581 h) at a current density of 5.2 mA g^{-1}.[602] Most recently, Li et al. introduced a new class of layered Sn(II)-based fluoride conductor (i.e., KSn_2F_5) where F^- acted as charge carrier. The KSn_2F_5 solid electrolyte exhibited a higher ionic conductivity (10^{-4} S cm^{-1} at 60 °C) compared to typical tysonite-type and fluorite-type fluorides, mainly due to the increased charge carrier concentration and more frequent jumping process. Integrating this solid conductor with a high potential CuF_2 cathode and a low potential Sn anode (Figure 26e), a high initial specific discharge capacity of 442 mAh g^{-1} was achieved (Figure 26f), retaining a reversible specific capacity of $\sim$150 mAh g^{-1} for more than 70 cycles at 60 °C. It should be noted that the interphase wetting of the solid electrolyte by the TBAF favors the F^- transfer between the electrode and the electrolyte.[603]

4.2.2. Nonaqueous Liquid Electrolytes. As discussed above, the physicochemical characteristics of F^- conducting solid-state electrolytes have been studied for several decades. Nevertheless, the majority of solid electrolytes necessitate an operation temperature above 150 °C for FIBs due to their low ionic conductivities at lower temperature. In contrast, liquid electrolytes are expected to exhibit superior F^- conductivities to enable RT FIBs. Besides, they demonstrate enhanced interphasial compatibility toward electrode materials, which is crucial for the commercialization of FIBs. Unfortunately, the developments of liquid electrolytes for RT FIBs has been largely constrained by two primary factors, i.e., the low solubility of fluoride salts in the electrochemically stable aprotic organic solvents and the strong chemical reactivity of F^- which is prone to create hydrofluoric acid (HF) in the presence of acidic hydrogen.[9,42] To establish liquid electrolytes for RT FIBs, several requirements should be satisfied, e.g., abundant free fluoride species (F^- or F_2H^-) should exist in the electrolytes to support high ionic conductivity, sufficient electrochemical stability of the electrolytes to prevent decompositions during cycling, and high chemical stability of the electrolyte to prevent the dissolution of electrode active materials.[40] Thus, extensive attempts have been made to explore novel electrolytes for potential RT FIBs. However, initial efforts were disappointing due to the insolubility of most fluoride salts in organic solvents. Among these endeavors, a significant breakthrough was realized in 2018 by Jones et al.,
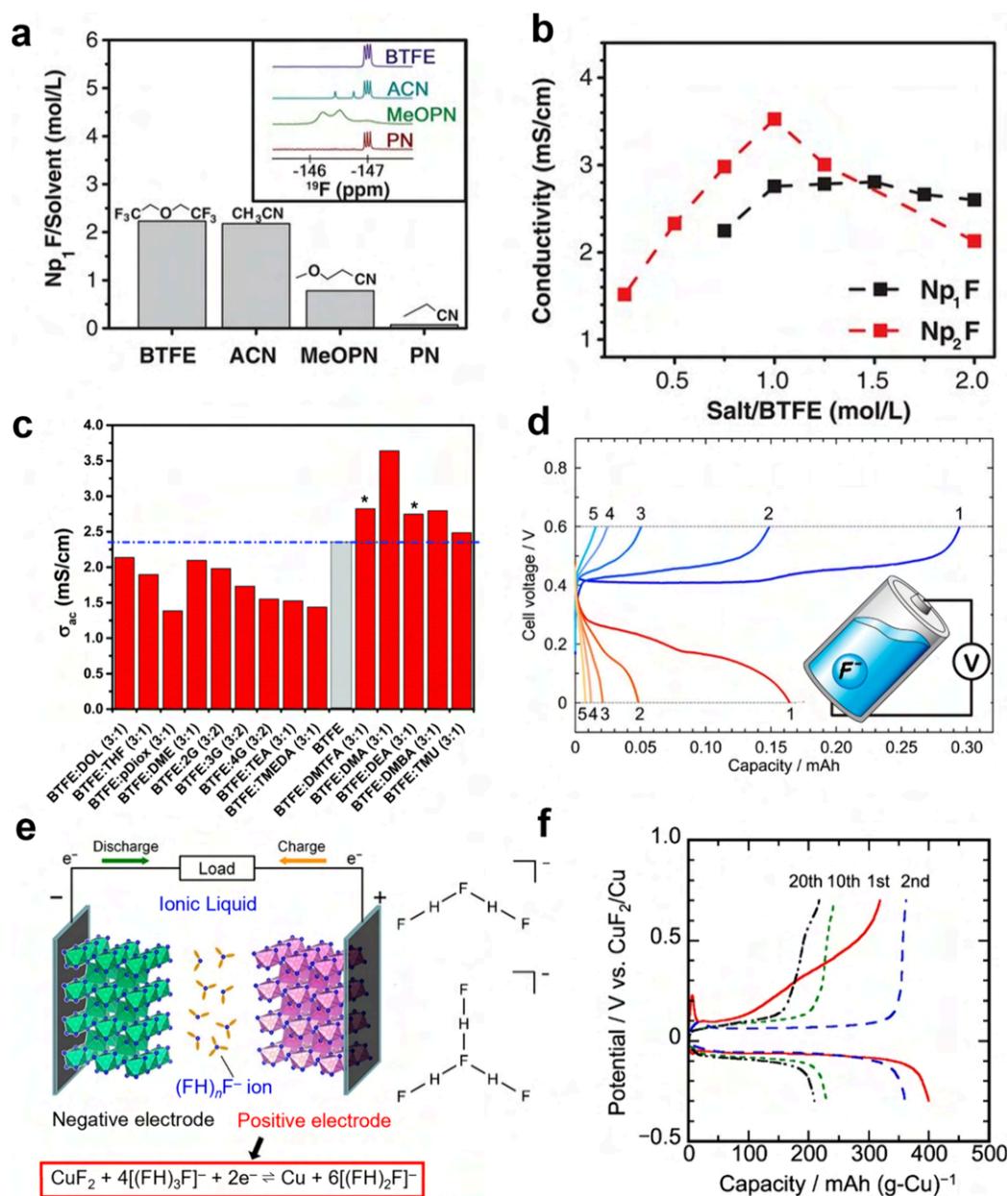
Figure 27. Room-temperature F^- conducting nonaqueous liquid electrolytes for FIBs. (a) Solubility of $N_{p1}F$ salt in BTFE, AN, 3-methoxypropionitrile (MeOPN), and propionitrile (PN) solvents. (Inset) ^{19}F NMR spectra in the bifluoride region for $N_{p1}F$ salt dissolved in each solvent. (b) Ionic conductivity of $N_{p1}F$ and $N_{p2}F$ in BTFE solvent as a function of salt concentration. Reproduced with permission from ref 52. Copyright 2018 American Association for the Advancement of Science. (c) Ionic conductivity of $N_{p1}F$ salt (0.75 M) in a mixture of BTFE and cosolvent. Reproduced with permission from ref 614. Copyright 2019 Royal Society of Chemistry. (d) Charge/discharge curves of the RT FIB based on a Bi cathode and a $PbF_2|Pb$ anode in ~0.35 M MPPF/TMPA−TFSA at 20 μA cm^{-2}. Reproduced with permission from ref 618. Copyright 2017 American Chemical Society. (e) Schematic illustration of a FIB based on a fluorohydrogenate ionic liquid electrolyte, and structures of fluorohydrogenate anions ($[(FH)_nF]^-$ when $n = 2$ and 3). Reproduced with permission from ref 619. Copyright 2019 American Chemical Society. (f) Voltage curves of the Cu electrode in the $[C_2C_1pyrr][(FH)_{2.3}F]$ electrolyte at RT with a current rate of 0.05 C (= 42.2 mA (g-Cu)$^{-1}$). Reproduced with permission from ref 620. Copyright 2021 Elsevier.

who designed RT F^- conducting electrolytes with high ionic conductivity, wide electrochemical stability window, as well as sufficient chemical stability via dissolving tetraalkylammonium fluoride salts (i.e., neopentyl (Np)-substituted alkylammonium fluorides) into ether solvents. The Np salt was chosen because the branched Np chain enhanced salt solubility while the absence of β-hydrogens inhibited HF_2^- generation. Results show that a high NpF salt concentration (>2.2 M) could only be obtained when employing BTFE as the solvent without reacting with F^- (Figure 27a), exhibiting high ionic

conductivity comparable to that of LIB electrolytes (within the range from 10^{-3} to 10^{-2} S cm^{-1}, Figure 27b). It is important to note that the electron-withdrawing groups on the BTFE molecule could strengthen the partial positive charges on α-CH$_2$, guaranteeing adequate F^- solvation. When paired with a Cu@LaF$_3$ core−shell nanostructure cathode, reversible electrochemical cycling with F^- shuttling was achieved at RT.[52] Though the cycle stability was far from satisfactory for practical battery systems, this report represents the pioneering work in exploring high-energy devices beyond that of LIBs. To
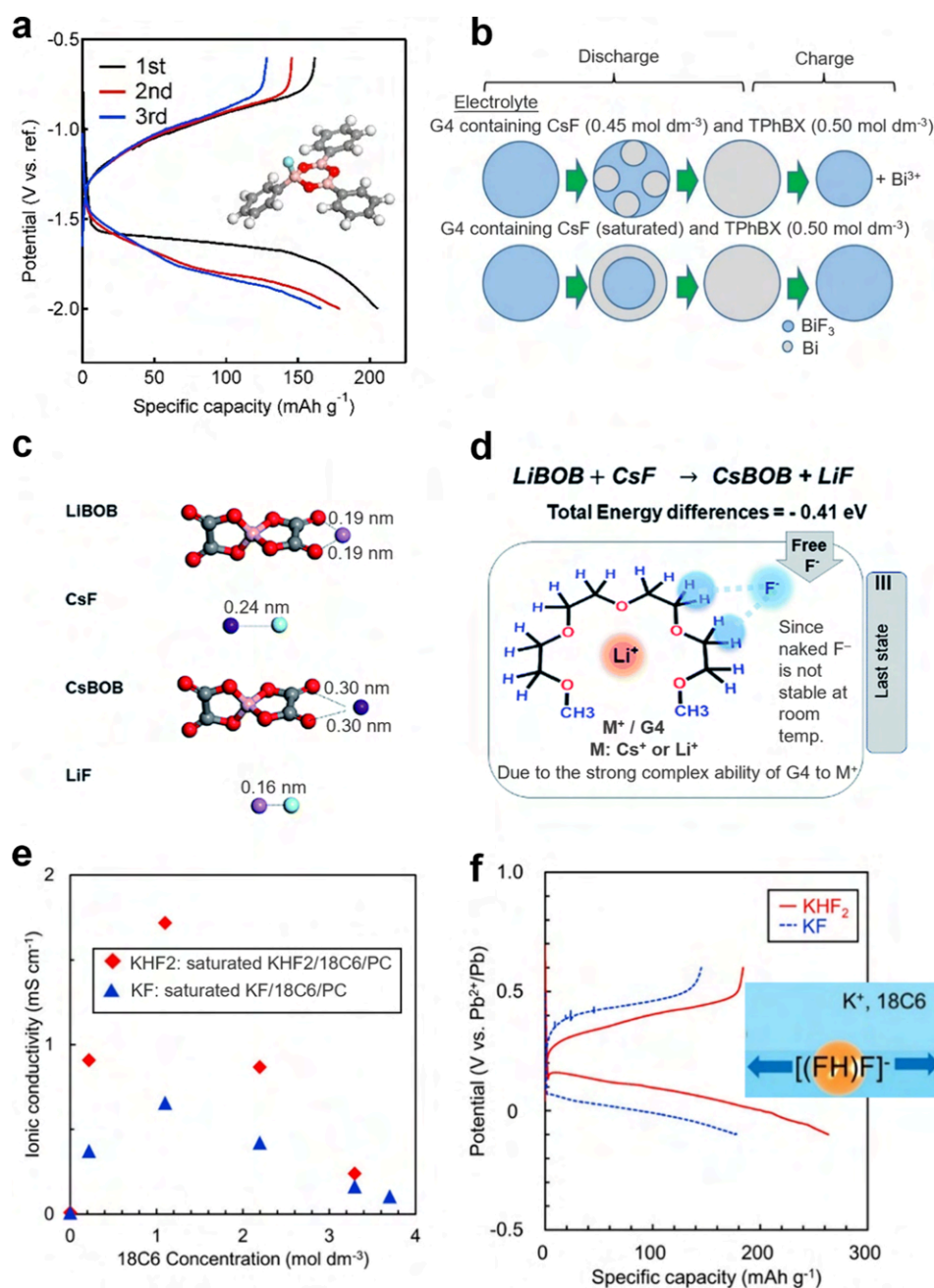
Figure 28. Employing anion acceptors and cation acceptors to improve the F$^-$ conductivity for FIB electrolytes. (a) Discharge/charge curves of the PbF$_2$ (C) electrodes (vs Ag/Ag$^+$) at 0.025 C (1 C = 219 mA g^{-1}). (Inset) Optimized molecular structure of TPhBX-F$^-$. Reproduced with permission from ref 627. Copyright 2019 Elsevier. (b) Scheme illustrating the effects of electrolyte concentrations (CsF: 0.45 mol dm^{-3} or saturated) on the BiF$_3$ dissolution during cycling. Reproduced with permission from ref 636. Copyright 2019 American Chemical Society. (c) The most stable structures of lithium bis(oxalato)borate (LiBOB), CsF, CsBOB, and LiF. (d) Possible interactions in the LiBOB$_{0.25}$/CsF/G4 electrolyte system. Reproduced with permission from ref 637. Copyright 2019 Royal Society of Chemistry. (e) Relationship between the 18C6 concentration and the ionic conductivity. (f) Charge/discharge curve of BiF$_3$ electrodes at 0.02 C (1 C = 302 mA g^{-1}; KHF$_2$ represents the saturated KHF$_2$/18C6/PC electrolyte, KF denotes the saturated KF/18C6/PC electrolyte, while 18C6 concentration is 1.10 M). (Inset) [(FH)F]$^-$ shuttling between two electrodes during charge/discharge. Reproduced with permission from ref 638. Copyright 2022 American Chemical Society.

gain a deep understanding of the factors affecting F ion–solvent properties in liquid FIBs, these authors further investigated various organic solvents in combination with the Np$_1$F salt. They revealed that partially fluorinated solvents possessing partial charge distribution and conformational flexibility achieved the highest level of salt dissolution, with BTFE being particularly prominent for its large Np$_1$F salt dissolution. Besides, introducing amide as a cosolvent promoted the ion dissociation between Np$_1^+$ cations and F$^-$

anions, thus enhancing the electrolyte ionic conductivity (Figure 27c).[614] Apart from organic fluoride salts, inorganic fluoride salts (i.e., CsF, KF, or NaF) have been successfully employed as fluoride sources in the development of RT F$^-$-transporting liquid electrolytes, as demonstrated by the RISING project in Japan.[615−617] They introduced novel lactone (γ-butyrolactone, GBL)-based liquid electrolytes, which consist either of CsF or KF, through a solvent substitution method. Despite of the low F$^-$ concentration of

around 0.05 M, these electrolytes delivered high ionic conductivity of 0.8 mS cm^{-1}, enabling reversible metal/metal–fluoride transformations for a wide range of metal electrodes. Nevertheless, the electrolyte solvent showed poor antireductive stability with the anode, which was promoted by the presence of fluoride ions.[617] In another effort, when 4.5 M LiFSI and 0.45 M CsF salts were dissolved in tetraglyme (G4) solvent as the electrolyte, this project revealed the formation of a SEI on a MgF$_2$ anode, which resulted from the irreversible decomposition of the liquid electrolyte during the reduction process. However, the detected LiF within the SEI could exert a detrimental impact on the FIB performance, given the poor electronic and F$^-$ conductivity of LiF.[615] Consequently, a thorough investigation of the SEI compositions and properties is warranted to optimize the FIB performance in the future.

Owing to their characteristic physicochemical properties, including high ionic conductivities, sufficient thermal and chemical stabilities, low volatilities, high nonflammability, and favorable solubility, RT (ionic liquids) ILs have been utilized for operating liquid FIBs. The first proof-of-principle RT FIB was presented by Darolles et al. in US patent 9166249, reporting an IL electrolyte consisting of tetramethylammonium fluoride (TMAF) in 1-methyl-1-propylpiperidinium bis-(trifluoromethanesulfonyl) imide (MPPTFSI). An ionic conductivity of ~10^{-3} S cm^{-1} at RT and a stable voltage window > 4 V were realized, delivering an initial discharge specific capacity of 103 mAh g^{-1} in a polyaniline (PANI)‖PbF$_2$ battery.[621] Nevertheless, the extent of F$^-$ shuttling contributed to the cyclability was not adequately verified, the possible influence of IL cations on the cycling process remained unsolved, and the redox reactions associated with the PANI cathode were not thoroughly investigated, as noted by Hörmann et al. Despite these shortcomings and the very limited electrochemical performance, this patent remains seminal in the development of RTFIBs.[40] Subsequently, the RISING project in Japan has achieved notable progress in enhancing the ionic conductivity of ILs for the operation of RT FIBs. By dissolving the 1-methyl-1-propylpiperidinium fluoride (MPPF) in an IL, specifically N,N,N-trimethyl-N-propylammonium bis(trifluoromethanesulfonyl)amide (TMPA–TFSA), with a fluoride concentration of ~0.35 M, a high conductivity of 2.5 mS cm^{-1} was realized. When paired with a Bi cathode and a PbF$_2$|Pb anode, the resulting liquid FIB exhibited distinct two-step plateaus in the initial charge/discharge profiles. However, some of the charged products (e.g., BiF$_3$) was electrically detached from the Bi cathode through exfoliation, causing diminished charge–discharge efficiency and poor cycle stability (Figure 27d).[618] Notably, the possible generation of bifluoride ions from organic cations with β-hydrogens due to Hofmann elimination was not discussed in these IL-based electrolytes, presenting a significant challenge for the development of RT FIBs. To eliminate this issue, a novel liquid electrolyte based on fluorohydrogenate ionic liquids (FHILs) was designed by this project (Figure 27e), featuring the fluorohydrogenate anion ((FH)$_n$F$^-$), which possesses high ionic conductivities (e.g., 100 mS cm^{-1} at RT for [C$_2$C$_1$im]-[(FH)$_{2.3}$F] (C$_2$C$_1$im = 1-ethyl-3-methylimidazolium)). When paired with this electrolyte, the CuF$_2$ cathode underwent reversible defluorination/fluorination, achieving 94.7% of the theoretical specific capacity (528 mAh (g-CuF$_2$)$^{-1}$) for the first cycle. However, a drastic capacity decay was observed upon subsequent cycling.[619] Afterward, these authors developed an alternative FHIL, [C$_2$C$_1$pyrr][(FH)$_{2.3}$F] (C$_2$C$_1$pyrr = N-ethyl-

N-methylpyrrolidinium), which, despite delivering reduced initial specific capacities (400 mAh (g-Cu)$^{-1}$), extended the cycle life to 20 cycles while maintaining the specific capacity (Figure 27f). The improved cyclability was attributed to the low CuF$_2$ solubility in [C$_2$C$_1$pyrr][(FH)$_{2.3}$F], which largely inhibits the aggregation of the Cu particles.[620]

Under acidic conditions, β-hydrogen elimination and/or other nucleophilic fluoride attacks toward atoms such as α-H, C=O, ChN, P, Si, etc., take place relatively easily. These reactions can be mitigated by enhancing the solvation of F$^-$ through Lewis acidic solvating agents (i.e., anion acceptors (AAs)) such as organic compounds containing electropositive elements (e.g., B, Si, P, etc.). Among them, boron-based AAs have been proven to be effective in promoting the dissolution of Li salt (e.g., LiF, LiCl, Li$_2$O, Li$_2$O$_2$) by reducing the cation–anion interactions.[622−626] Motivated by these findings, the RISING project in Japan undertook a series of research works to identify boron-containing compounds, including triphenyl-boroxine (TPhBX), triphenylborane (TPhB), fluorobis(2,4,6-trimethylphenyl) borane (FBTMPhB), 4-(4,4,5,5-tetramethyl-1,3,2-dioxaborolan-2-yl)pyridine (DiOB-Py), etc., as AAs to form complexes with anions, thereby providing sufficient F$^-$ conductivity for operating RT FIBs.[627−635] Typically, fluoride salts such as CsF are challenging to dissolve in organic solvent such as G4. Through DFT calculations, the optimized molecular structure of TPhBX-F$^-$ was elucidated, revealing that the boron atom served as the most stable binding site for F$^-$. Besides, the introduction of 0.5 M TPhBX greatly increased the solubility of CsF in G4 solvent from 0.00017 to 0.51 M, experimentally validating the effectiveness of TPhBX as an AA. The resulting PbF$_2$ (mixed with carbon) electrode delivered a high discharge specific capacity approaching the theoretical value (219 mAh g^{-1}), which was sustained after the subsequent three cycles (Figure 28a).[627] While the solubility of CsF in G4 could be enhanced by AAs, it was found that the AA also led to the severe dissolution of the electrode active material, causing fast capacity degradation during cycling.[633] Subsequently, these researchers demonstrated that both the type of AA and the concentration of CsF can be optimized to balance the AA−F$^-$ interaction and the electrode dissolution. It was revealed that though the BiF$_3$ electrode could be discharged/charged normally in both electrolytes, the cycling performance with CsF (saturated)-TPhBX (0.50 M)-G4 electrolyte was higher than that with CsF (0.45 M)−TPhBX (0.50 M)-G4, attributed to the reduced dissolution of BiF$_3$ active material (Figure 28b). Additionally, it was proposed that the CsF/TPhBX ratio would significantly affect the formation state of Bi as well as the electrolyte decomposition products during the discharge process.[636]

Besides the AAs, another type of additive called cation acceptors (CAs) can also improve the conductivity of F$^-$ by promoting the dissolution of F salt in electrolytes. Unlike the AAs discussed above, CAs interact with cations instead of anions from the salts. As an extensively investigated salt additive to mitigate the cathode material dissolution/diffusion in LIBs, lithium bis(oxalato)borate (LiBOB) has exhibited great potential as a CA in liquid FIBs.[637,639−643] This is attributed to the strong interactions between BOB ions and alkali metal ions (such as Na$^+$ and Li$^+$).[644−646] Kucuk et al. found that the optimum BOB$^-$ content to promote CsF dissolution in G4 was 0.25 M. Results revealed that BOB$^-$ addition not only reduced active material loss but also improved the electrolyte electrochemical stability during
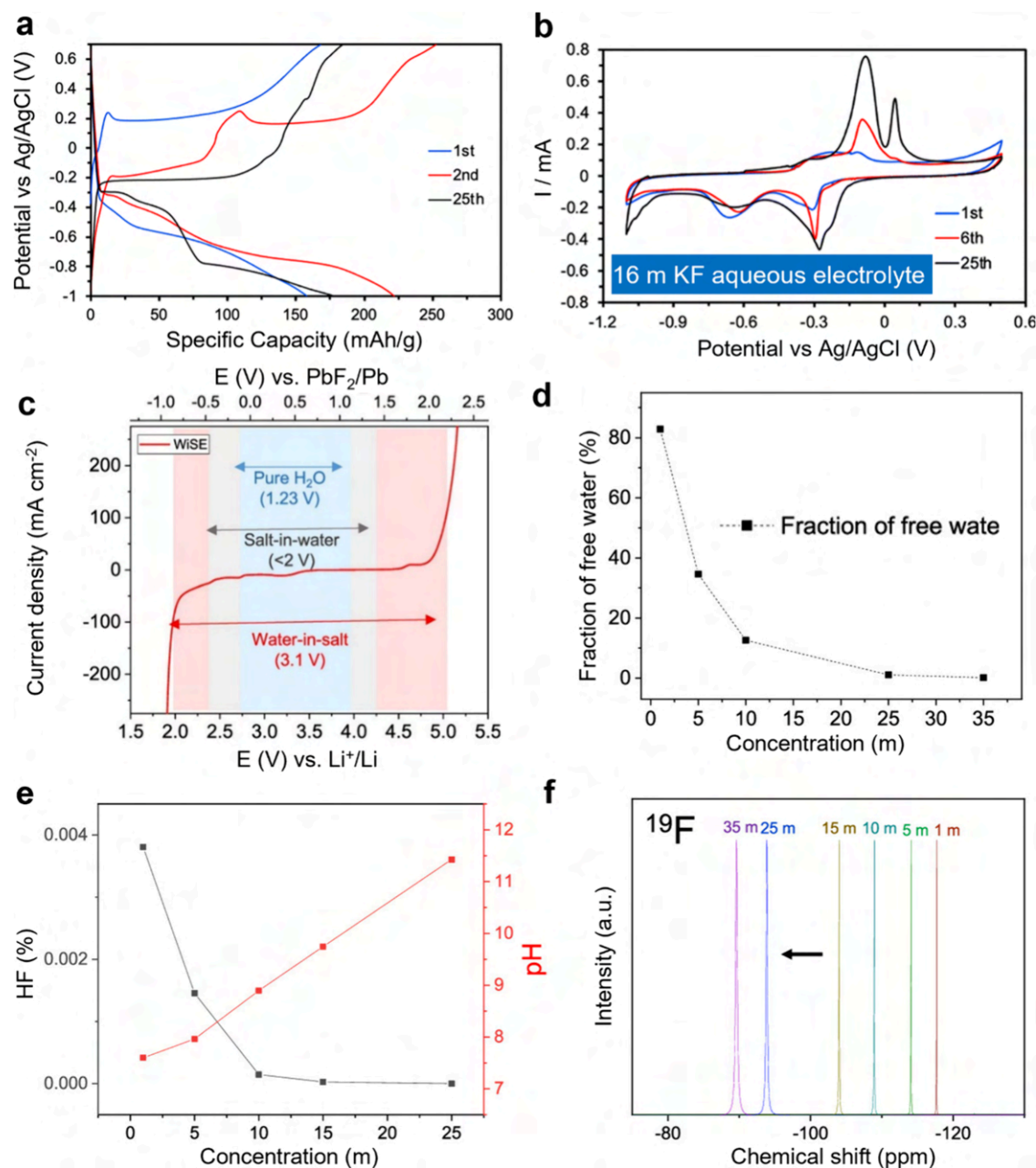
Figure 29. Developments of "water-in-salt" aqueous electrolytes in FIBs. (a) Charge−discharge curves of the Cu electrode in 16 m KF aqueous electrolyte at 500 mA h g^{-1}. (b) CV results for different cycles at a scan rate of 1 mV s^{-1}. Reproduced with permission from ref 647. Copyright 2022 Royal Society of Chemistry. (c) ESW expansion using 25 m CsF aqueous electrolyte compared to pure water and other aqueous electrolytes. (d) The fraction of free water molecules calculated from the MD simulation. Fluoride-ion chemical species and electronic environment: (e) pH as a function of concentration, suggesting a decrease in the HF content, and (f) ^{19}F NMR spectroscopy. Reproduced with permission from ref 649. Copyright 2023 American Chemical Society.

redox reactions via the interactions between BOB$^-$ and Cs$^+$ as well as between fluoride and the CH$_2$ group of G4 solvent (Figure 28c and 28d).[637] More recently, instead of using CsF salt, a widely available potassium salt, potassium bifluoride (KHF$_2$), was employed as the F$^-$ source. To increase the salt disassociation, the 18-crown-6 ether (18C6) was introduced as a CA to interact with potassium ions, significantly boosting the mobility of fluoride ions with an ionic conductivity of 1.72 mS cm^{-1} (Figure 28e). As depicted in Figure 28f, the consequent BiF$_3$ electrode achieved a discharge specific and a charge specific capacity of 263 and 184 mAh g^{-1}, respectively. In contrast, a higher voltage−polarization was observed for the

KF salt-based electrolyte with a reversible specific capacity below 140 mAh g^{-1}. It is interesting to note that the fluoride ions existed in the form of $[(FH)F]^-$, shuttling between the two electrodes during cycling. In addition, the HF generated from the equilibration reactions of $[(FH)F]^-$ was considered to dissolve metal fluorides, further enhancing the fluorination/defluorination reactivity of metal fluorides.[638] Based on these results, the AA (or CA) type as well as fluoride salt/AA (or CA) ratio should be carefully regulated to achieve high mobility of fluoride ions and to suppress the loss of active material. Furthermore, other types of supporting fluoride salts with higher dissociation levels (compared to the common

Table 4. Comparisons of the Electrochemical Performance and Remaining Issues of Liquid Electrolytes for RT FIBs Discussed in This Section[a]

electrolyte	anode‖cathode	ionic conductivity (mS cm⁻¹)	electrolyte stability window (V)	retained capacity (mAh g⁻¹)/cycles	remaining issues	ref
1 M Np₁F-BTFE	Cu@LaF₃ (vs Li⁺/Li)	2–3	4.1	65/7th	poor cycle stability and large electrochemical polarization	52
0.05 M CsF–γ-butyrolactone	Zn‖Ag	0.8		~0.068 mAh cm⁻²/24th	irreversible reductive reactions of the solvent restricted the negative potential to ca. −1.5 V vs SHE	617
6.3 mM KF + 0.5 M DiOB-Py-G4	BiF₃/C (vs REF (0.587 V vs SHE))	1.02 × 10⁻²	~3.2	316/1st	although dissolution of the active material was very low, fast capacity fading still existed	616
TMAF–MPPTFSI	PANI‖PbF₂	~1	>4	103/1st	contribution of F⁻ shuttling to the cyclability was not verified; the possible influence of IL cations on the cycling process remained unclear	621
~0.35 M MPPF–TMPA/TFSA	PbF₂|Pb‖Bi	2.5		<0.01 mAh/5th	some charged products were electrically detached from the cathode by exfoliation, causing poor cycle stability, probably generated bifluoride ions	618
[C₂C₁im][(FH)₂.₃F]	CuF₂ (vs CuF₂/Cu)	100		264 mAh (g-CuF₂)⁻¹/10th	possible chemical dissolution of the CuF₂ produced during charging and its repreciptation on the electrode surface	619
C₂C₁pyrr][(FH)₂.₃F	Cu (vs CuF₂/Cu)			210 mAh (g-Cu)⁻¹/20th	electrochemical dissolution of Cu metal and chemical dissolution of CuF₂ still existed	620
0.51 dm⁻³ CsF–tetraglyme + 0.5 dm⁻³ TPhBX	PbF₂@C (vs Ag/Ag⁺)		4.2	~170/3rd	TPHBX caused severe dissolution of the electrode active material	627
saturated CsF–tetraglyme + 0.5 dm⁻³ TPhBX	BiF₃ (vs REF (0.587 V vs SHE))			~100/3rd	electrochemical reaction mechanism and performance were dependent on the CsF/TPhBX ratio	636
0.5 M CsF–tetraglyme + 0.25 M LiBOB	BiF₃@C (vs REF (0.587 V vs SHE))	~1.6	~2.7	~125/1st	electrochemical polarization was large for redox reactions	637
saturated KHF₂-PC + 18C6	BiF₃ (vs Pb²⁺/Pb)	1.72	3.7	184/1st	fluoride ions of the reactive species bond with protons, probably creating hydrogen during reduction at low potentials	638
0.8 M NaF–H₂O	BiF₃‖TEMPO			89.5/85th	possibility of creating HF or bifluoride in the aqueous electrolyte; the electrolyte compatibility toward electrode materials were unclear	591
16 m KF–H₂O	Cu (vs Ag/Ag⁺)			50/300th	uncontrolled KF precipitation on the electrode surface and the unregulated volumetric changes	647
7.5 M KF + 1.5 M KOH–H₂O	Zn‖Cu		~2.1 V	0.11 mAh cm⁻¹/1600th	low reversible capacity for F⁻ storage reaction	648
25 m CsF–H₂O	symmetric Pb|PbF₂	152	3.1 V	~65/50th	dissolution of active material still existed	649

[a]REF: a silver rod immersed in acetonitrile with 0.1 M silver nitrate and 0.1 M tetraethylammonium perchlorate as reference electrode.
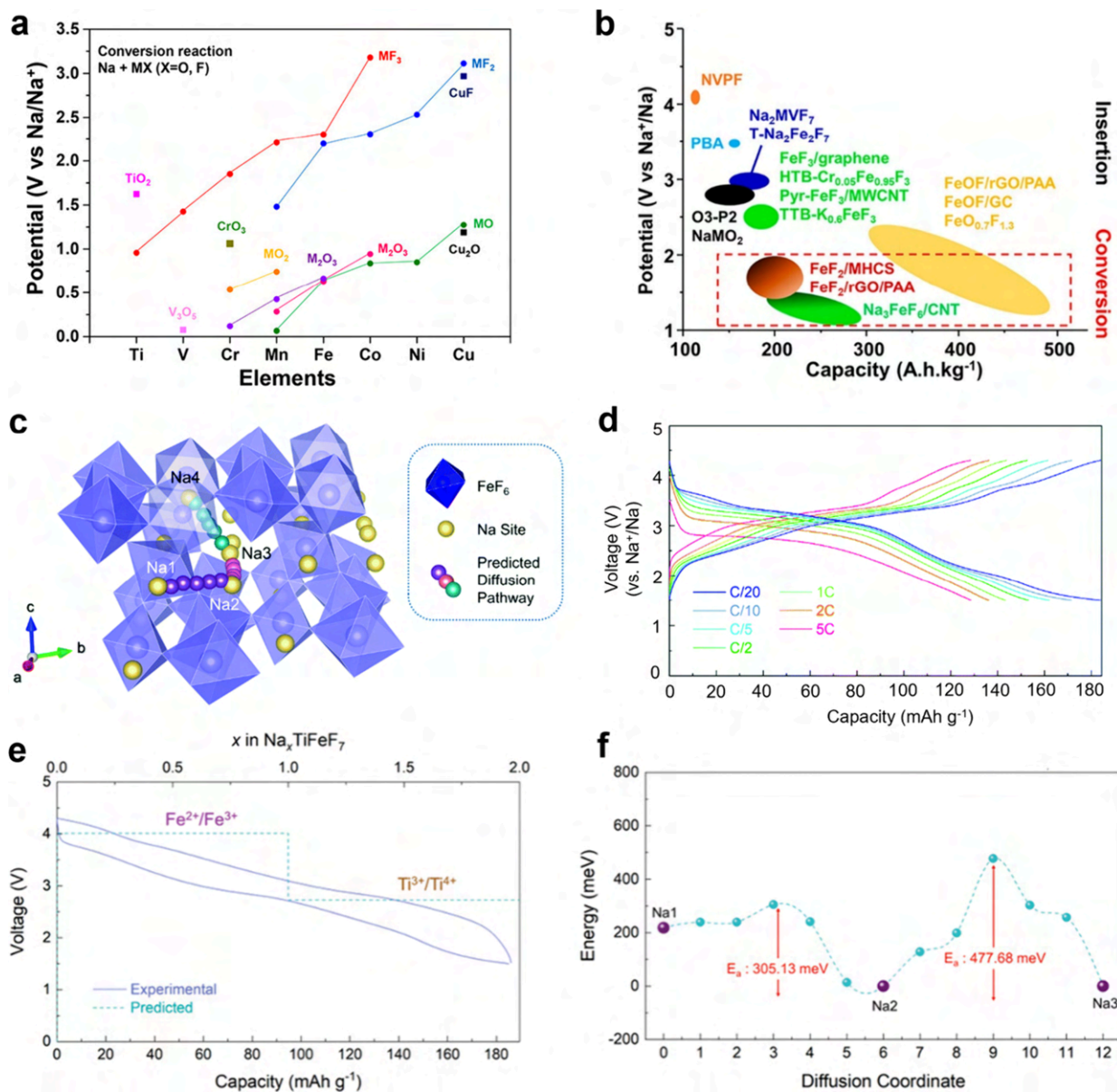
Figure 30. Fluorine-containing electrode materials for SIBs. (a) Calculated potentials for conversion reactions between transition metal oxides or fluorides with Na. (b) Voltage vs capacity of SIB electrode fluorinated materials. Reproduced with permission from ref 655. Copyright 2011 Elsevier. (c) 3D Na^+ migration pathways with the energy landscape predicted by the NEB method in the $Na_xFe_2F_7$ structure. (d) Voltage curves of the $Na_2Fe_2F_7$ cathode within the range of 1.5−4.3 V at a charge current rate of C/20 and various discharge current rates. Reproduced with permission from ref 54. Copyright 2021 Elsevier. (e) Comparison of the predicted redox potential of Na_xTiFeF_7 and its experimentally tested charge/discharge curves. (f) The energy landscape determined by the NEB method in the Na_2TiFeF_7 structure. Reproduced with permission from ref 656. Copyright 2022 Wiley-VCH.

CsF) should be explored. However, it should be noted that ultimately, after enhancing the fluoride-ion solvation, the reactivity of fluoride ions may probably be suppressed due to the high desolvation energy of fluoride ions on the electrode surface, which can affect the electrochemical storage/release of F^- during cycling.

4.2.3. Aqueous Electrolytes. Compared with other electrolyte systems, aqueous solutions typically possess outstanding merits of having high ionic conductivity, having low cost, and being environmentally benign, which have gained attention for developing liquid RT FIBs. In 2019, Chen and co-workers applied an aqueous NaF salt solution to operate a rechargeable FIB based on a TEMPO cathode and a BiF_3 anode. To prevent side effects of insoluble compounds from

both electrodes, an anion exchange membrane was placed to ensure only F^- transported between the cathode and the anode during cycling. This FIB delivered a discharge capacity of 89.5 mAh g^{-1} (based on the mass of BiF_3) after 85 cycles at 1000 mA g^{-1} as well as good rate capability.[591] However, the voltage−polarization was notably larger (~1.0 V) compared to that observed in LIBs. Additionally, the possibility of creating HF or bifluoride in the aqueous electrolyte and the electrolyte compatibility toward electrode materials were not examined. Besides NaF salt, KF, which boasts a high solubility of 16 m in an aqueous solution, has recently attracted much interest for FIBs. As demonstrated by Ji et al., a "water-in-salt" electrolyte of 16 m KF ($KF·3.47H_2O$) facilitated the reversible F^- storage process of commercial Cu powder, mitigating the dissolution

associated with the active material for the reversible conversion between Cu and CuF_2 (the charged product of Cu). Furthermore, the KF solid embedded into the Cu electrode acted as part of the active material, contributing to a higher specific capacity of 222 mA h g^{-1} (based on the Cu mass) in the initial cycle. It was observed that the cathodic peaks shifted to a higher potential to reduce the electrochemical polarization, which aligned with the voltage curves. (Figure 29a and 29b).[647] Soon after, a "water-in-salt" aqueous electrolyte composed of 7.5 M KF and 1.5 M KOH was designed, expanding the electrolyte stability window to ~2.1 V. Taking advantage of this electrolyte, a Zn‖Cu battery based on the F^- shutting was constructed, realizing an improved discharge platform of 1.9 V and a steady operation over 1600 cycles.[648] This finding combined the advantages of the high conversion voltage of metal fluoride and the low-cost, environmental friendliness of Zn‖Cu batteries. Most recently, the ESW of aqueous electrolytes was significantly increased to 3.1 V by dissolving 25 m CsF in water. As reflected in the ^{17}O NMR spectroscopy and MD simulation, the 25 m CsF electrolyte displayed an increased fraction of ion pairs and aggregates in addition to the elimination of free water molecules (compared with 1 m CsF), which confirmed the mechanism behind the expanded ESW (Figure 29c and 29d). More significantly, the chemical stability of fluorides was investigated through ^{19}F NMR coupled with pH measurements, demonstrating that HF formation was almost completely suppressed (Figure 29e and 29f). Therefore, the dissolution of active materials from electrodes such as Pb|PbF_2 and CuF_2 was inhibited, offering improved cycle stabilities.[649]

To conclude, in terms of solid-state electrolytes, the high operating temperature (e.g., >150 °C), low ionic transport capability, and poor interfacial contact remain challenging for most of the fluorite-type and tysonite-type solid-state electrolytes. Novel fluoride structures and modification strategies are urgently needed to promote the development of F^- conducting solid-state electrolytes. Liquid electrolytes permit FIBs to operate at ambient temperature with minimal internal resistance. Nevertheless, several issues persisted, as outlined in Table 4. The majority of fluoride salts exhibit limited solubility in organic solvents, leading to low ionic conductivity. Besides, the narrow ESW strongly constrains the selection of active materials, thus lowering the energy density of FIBs. Dissolution issues related with active material are another main concern that cause unsatisfactory cycle stability. Notably, due to the high chemical reactivity of F^- ions, most liquid electrolytes are corrosive and toxic toward cell components. To achieve high ionic conductivities and simultaneously inhibit nucleophilic β-hydrogen elimination and/or other nucleophilic fluoride attacks, novel fluoride salts (other than the common CsF) and/or suitable solvents should be explored. Besides, suitable anion acceptors acting via forming a complex with the F anion or cation acceptors interacting with cations can be employed for promoting the dissociation of fluoride salts. It should be noted that the anion acceptors may also facilitate the loss of active materials. For a more comprehensive overview of electrolyte advancements in rechargeable FIBs, readers are encouraged to refer to several excellent reviews.[41,276]

5. FLUORINE CHEMISTRY IN OTHER RECHARGEABLE BATTERIES

5.1. Na- and K-Based Batteries

5.1.1. Fluorine-Containing Electrode Materials in Na-Based Batteries.
As mentioned above, fluorine is the most electronegative element with $\chi = 3.98$ compared to 3.44 for oxygen on the Pauling scale, contributing to more ionic M−X bonds in fluorides and thus higher redox potentials of transition metal ions than oxygen ions (Figure 30a and 30b).[54,650] In addition, in contrast to polyanions such as PO_4^{3-} and SO_4^{2-}, the lower molecular weight of F^- is favorable for enhanced specific capacity. Generally, F-based inorganic or organic compounds are more stable against oxidation. Therefore, F-containing compounds ($Na_xM_yF_z$) can combine the benefits of the large gravimetric energy density of layered Na_xMO_2 with the high structural stability of polyanions, which has been proposed as promising cathode materials for SIBs.[54] A summary of the main characteristics of fluorinated materials as the cathode materials of SIBs has been thoroughly reviewed by Maisonneuve et al.;[651] readers are encouraged to refer to this review dedicated solely to fluorinated cathodes based on the material structures and other related reviews focused on transition metal oxyfluorides, transition metal fluorides, etc.[113,652] Here, we mainly discuss some representative cathode materials of SIBs with the best overall performance, especially for 3D materials, analyzing the structure characteristics for further improving highly reversible/stable Na^+ uptake/release.

The metal difluorides (MF_2) synthesized from the decomposition of metal trifluoroacetates were first employed in SIBs in 2014. Different from the direct conversion reaction with Li, FeF_2 reacted with Na by direct conversion at the surface region; then, it reacted heterogeneously with Na to convert to Fe^{3+} and Fe^0.[653] This work proved the disproportionation reaction mechanism in the conversion system, which helped to understand the nanoscale sodiation in metal difluorides. Sun et al. prepared a FeF_2-reduced graphene oxide nanocomposite. When associated with a PAA (poly(acrylic acid)) binder, the reversible capacity of the nanocomposite was greatly improved from 100 to 175 mAh g^{-1} and the high-rate capability was also achieved with a capacity of 78 mAh g^{-1} at 10 A g^{-1}.[654]

To increase the capacity based on conversion reactions, the oxyfluoride FeOF has also been employed in SIBs. FeOF was studied by Deng et al. for insertion−conversion reactions in SIBs, which was prepared through a facial alcohol-assisted solvothermal method. The obtained FeOF nanorods delivered a high reversible capacity of ~250 mAh g^{-1} after 20 cycles at 10 mA g^{-1}.[657] Afterward, $FeO_{0.7}F_{1.3}$/C nanocomposite was synthesized via a solution process for Na storage. This cathode material displayed a high initial discharge capacity of 496 mAh g^{-1}, a reversible capacity of 388 mAh g^{-1} at 50 °C, as well as satisfactory capacity retention of 92.8% after 50 cycles. Furthermore, it was elucidated that the reaction mechanism of $FeO_{0.7}F_{1.3}$/C included a hybridized mechanism of both intercalation and conversion reactions. The initial discharged products were NaF, Fe nanoparticles, and a newly formed rock salt phase ($Na_{1.4}FeO_{1.4}F_{0.6}$). Then, the phase separation was observed during recharging, inducing huge irreversible capacity loss in the first cycle. As the competitive reactions involved the rock salt phase and rutile components could improve the cycling stability of nanosized electrode materials,[658] the

authors then proposed that the phase separation could stabilize the desodation reactions during subsequent cycles.

Apart from the above-mentioned potential high gravimetric energy densities, most $Na_xM_yF_z$ materials exhibit excellent structural stability in the Na-deficient phase compared with layered Na_xMO_2, attributed to their three-dimensional framework. Using a similar solvothermal method for the preparation of $NaFeF_4$ except at elevated temperature (230 °C), NaF was introduced into the one-dimensional (1D) $FeF_3 \cdot 3H_2O$ host to stabilize the lattice structure, obtaining the novel weberite $Na_2Fe_2F_7$ (via the Fe^{2+}/Fe^{3+} redox reaction). A high insertion voltage of 3.25 V vs Na^+/Na was achieved, but the $Na_2Fe_2F_7$ cathode delivered a rather low discharge capacity of 58 mAh g^{-1} and poor cyclability.[659] A more recent report by Kim et al. demonstrated the $Na_xFe_2F_7$ cathode material with the crystal structure composed of point-shared FeF_6 octahedra could deliver a high capacity of 184 mA h g^{-1} at C/20 (1 C = 184 mA g^{-1}), attributed to a single-phase reaction without phase transition and negligible volume change during Na^+ extraction/insertion.. The activation barrier energies for Na^+-ion migration in $Na_xFe_2F_7$ were theoretically predicted by the nudged elastic band (NEB) according to first-principles calculations (Figure 30c), revealing the low activation barrier energies for efficient Na^+ diffusion along 3D pathways. This structure characteristics favor a long-term cycle span of over 1000 cycles at 2 C with ~88% capacity retention and an outstanding rate capability, as shown in Figure 30d.[54] Although $Na_2Fe_2F_7$ had the best reported performance for weberite cathode, the relationships between the structures and the properties remained unclear. To investigate the structure features and electrochemical behavior of the $Na_2Fe_2F_7$ weberite cathode in detail, an experimental–computational approach was adopted by Foley et al.[660] The results showed that $Na_2Fe_2F_7$ was metastable with a mixture of polymorphs (e.g., the orthorhombic (2O), trigonal (3T), and monoclinic (4M) weberite polymorphs). As the $Na_2Fe_2F_7$ phases preferred to transform to the more stable $NaFeF_3$ perovskite, the cathode experienced capacity fading upon cycling. Interestingly, these various polymorphs would not exert a large impact on the Na storage behavior, as indicated from the first-principle investigations. Further comprehensive investigations on regulating the weberite polymorphism and phase stability for advanced SIB cathodes are needed.

Except for $Na_2Fe_2F_7$, the weberite structure contains a large family of materials featuring the chemical formula of $Na_2M^{II}M^{III}F_7$ (e.g., M^{II} = Mg, Fe, Mn, Co, Ni, etc., $M^{II}I$ = Al, Fe, Mn, V, Cr),[661,662] which have not been employed as cathode materials for SIBs. Zhou et al. synthesized three vanadium-based weberite-type fluorides, Na_2MVF_7 (M denotes Mn, Fe, and Co), through a polytetrafluoroethylene-assisted fluorination process. Based on the redox reactions of Fe^{2+}/Fe^{3+} and V^{3+}/V^{4+}, a reversible capacity of 146.5 mA h g^{-1} was obtained for the optimal Na_2FeVF_7 cathode. Furthermore, 95% capacity was retained after 200 cycles owing to the robust crystal structure during repeated Na^+ deintercalation/intercalation.[663] More recently, a novel Fe^{2+}/Ti^{3+}-based fluoride, Na_2TiFeF_7, was prepared as a SIB cathode materials. The Fe^{2+} and Ti^{3+} ions in the Na_2TiFeF_7 structure enabled the full utilization of Ti^{3+}/Ti^{4+} and Fe^{2+}/Fe^{3+} redox couples for a high specific capacity of ~185 mAh g^{-1} at C/20 (1 C = 189 mA g^{-1}). Moreover, the high $Fe^{2+/3+}$ redox potential (~3.75 V vs Na^+/Na) increased the average operating voltage of the cathode to 3.37 V (Figure 30e). Notably, the Na_2TiFeF_7

cathode still delivered a specific capacity of ~136 mAh g^{-1} even at 5 C, which was associated with the low activation energy barriers (~477.68 meV, Figure 30f) and low band-gap energy (~1.83 eV) for high-power SIB applications.[656]

MX_3-type fluorides, in particular FeF_3, have been widely studied for SIBs. Among its three allotropic varieties (ReO_3, hexagonal tungsten bronze (HTB), and pyrochlore), the hydrated $FeF_3 \cdot 0.33H_2O$ HTB has gained visibly increasing interest in recent years due to its high average voltage (~2.74 V vs Na/Na^+), high theoretical specific capacity, nontoxicity, and low cost.[664,665] The presence of cavities could remove water molecules from the [001] hexagonal channels and insert Na^+ ions. In 2013, an HTB-type $FeF_3 \cdot 0.33H_2O$ was synthesized through a solid–solid transformation, where thermally vulnerable channels in $FeF_3 \cdot 3H_2O$ were expanded into more robust ones. At the same time, the microsized precursor underwent particle nanosizing. During this process, the characteristic Fe-based octahedral chains isolated in $FeF_3 \cdot 3H_2O$ precursor were preserved, mainly due to the infiltration and capping of IL (1-butyl-3-methylimidazolium tetrafluoroborate ($BmimBF_4$)), followed by the alleviated release of hydration H_2O from $FeF_3 \cdot 3H_2O$. Beneficial from the well-suited Na-insertable cavities, this HTB-type $FeF_3 \cdot 0.33H_2O$ electrode (wired by 10 wt % single-wall CNT (SWCNTs)) delivered a high discharge capacity of 130 mAh g^{-1} in the first cycle and good capacity retention (74 mAh g^{-1}) after 50 cycles.[666] Despite these advantages, the low electronic and ionic conductivities of $FeF_3 \cdot 0.33H_2O$, induced by the highly ionic character of the Fe–F bond, strongly hinder the practical application of SIBs. To improve the electrochemical performance, the $FeF_3 \cdot 0.33H_2O$ nanoparticles were packaged into 3D ordered mesoporous carbons (3D-OMCs) to serve as a SIB cathode material, where the 3D-OMCs as the carbon source facilitated the electron transfer and shortened the Na^+ diffusion path while improving the structural stability and suppressing nanoparticle aggregation upon the Na^+ deintercalation/intercalation. Besides, 3D-OMCs provided a large surface area for high mass loading as well as increased contact area of the electrode|electrolyte interphase. Consequently, the $FeF_3 \cdot 0.33H_2O$@3D-OMCs nanocomposite exhibited a high first discharge capacity of 386 mAh g^{-1} with a steady capacity of 238.0 mAh g^{-1} over 100 cycles at 20 mA g^{-1}. This nanocomposite cathode also demonstrated remarkable rate performance with a reversible capacity of 201 mAh g^{-1} even at 100 mA g^{-1}.[665] Although the electrochemical properties were enhanced, the intrinsic conductivity of $FeF_3 \cdot 0.33H_2O$ was still the same. Previous studies revealed that the band gap of this material could be decreased through ion doping, thus improving the intrinsic conductivities of $FeF_3 \cdot 0.33H_2O$.[667−670] For instance, with a smaller ionic radius (0.0615 nm) than that of Fe^{3+} (0.0645 nm), Cr^{3+} is easier to enter into the lattice of $FeF_3 \cdot 0.33H_2O$. According to the DFT calculation results, Cr^{3+} doping could redistribute the charge of $FeF_3 \cdot 0.33H_2O$, which reduced the band gap from 0.88 to 0.49 eV to improve its intrinsic conductivity. The optimized $Fe_{0.95}Cr_{0.05}F_3 \cdot 0.33H_2O$ cathode delivered a reversible capacity of 194.02 mAh g^{-1} at 0.1 C, which is much larger than that obtained with the $FeF_3 \cdot 0.33H_2O$ cathode (136.47 mAh g^{-1}). In addition, this doping cathode displayed much lower impedance than that of the $FeF_3 \cdot 0.33H_2O$ cathode, further proving the increased electronic conductivity of the cathode material after Cr^{3+} doping.[671] In brief, these findings suggest that the thermodynamically stable phases of the fluoride-based
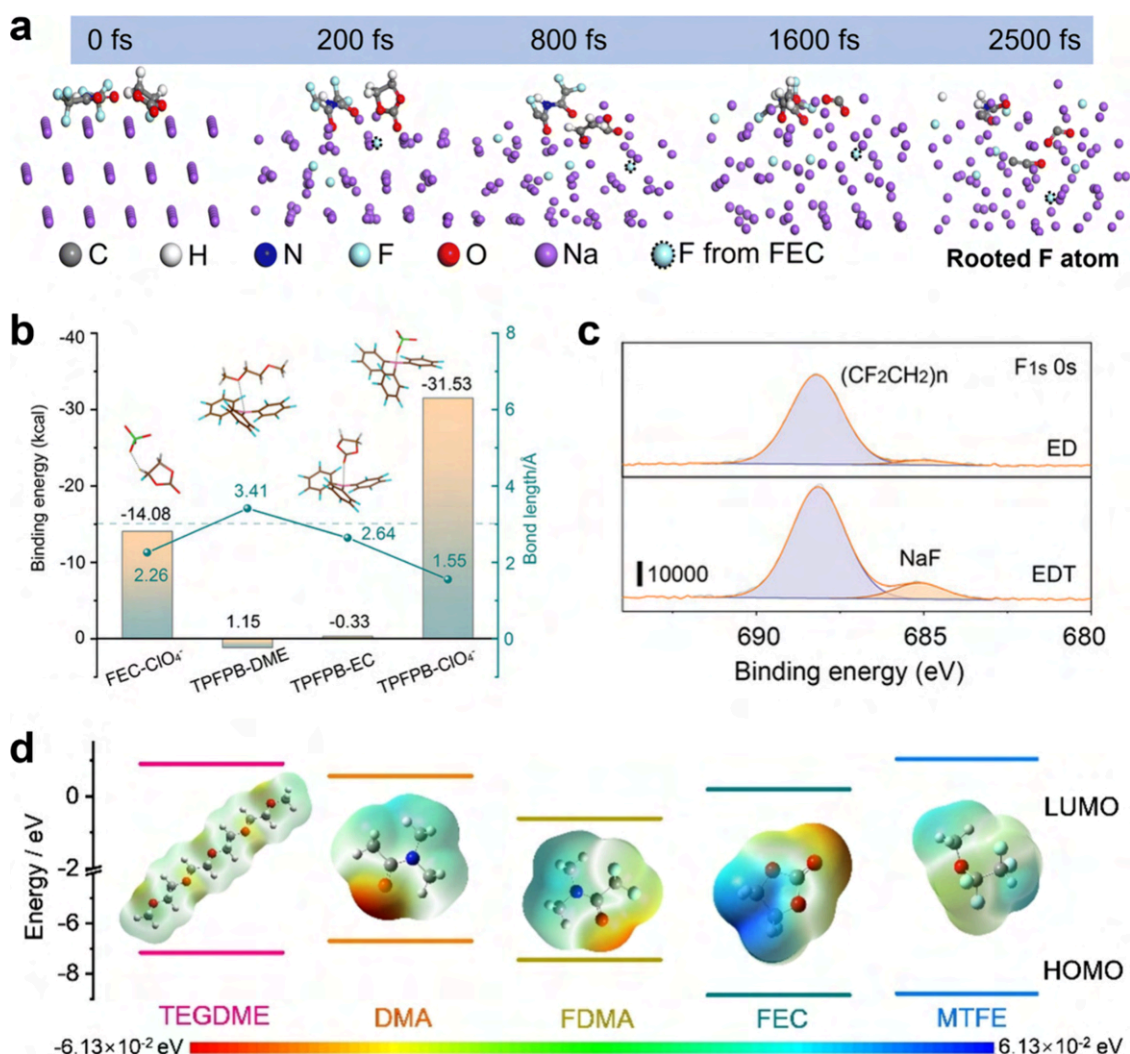
Figure 31. F-containing additives and (co)solvents for stable operation of Na-based batteries. (a) AIMD simulations with ECDA and FEC. Reproduced with permission from ref 680. Copyright 2023 Elsevier. (b) Binding energies and bond lengths of FEC−ClO$_4^-$, TPFPB−DME, TPFPB−EC, and TPFPB-ClO$_4^-$ through H−O, B−O, B−O, and B−O interactions, respectively. (c) XPS spectra of F 1s using electrolytes without and with TPFPB additive. Reproduced with permission from ref 685. Copyright 2023 Wiley-VCH. (d) LUMO and HOMO energy values of electrolyte components. (Inset) Electrostatic potential mapping of these components. Reproduced with permission from ref 686. Copyright 2022 Wiley-VCH.

cathodes are promising to achieve excellent electrochemical performance in SIBs, especially in terms of power capability and cycle durability.

Although great progress has been achieved, fluoride-based cathode materials have been limited to a small number of candidates. In addition, presodiation is required for some of these developed fluoride-based cathodes to utilize their high theoretical capacities. More notably, owing to the large band-gap energies and low electronic conductivities, fluoride-based cathode materials typically suffer from poor electrochemical kinetics, which further causes rapid capacity deterioration, especially at high charging rates, significantly restricting their applications in SIBs.

5.1.2. Fluorinated Electrolytes in Na-Based Batteries.

Similar to Li-based batteries, the battery performance of SIBs is largely determined by the selection of electrolytes,[672−674] especially the stability of the electrolytes toward the high electrochemical polarization of both the cathode and the anode. The ability to form passivation layers on the electrode surfaces must be considered for the stable operation of SIBs.

Encouraged by the positive results obtained from Li-based battery systems, the effect of FEC on the performance of SIBs was first examined in 2011, revealing an improved reversibility insertion/extraction of Na$^+$ ions for the hard carbon (HC) anode and the NaNi$_{1/2}$Mn$_{1/2}$O$_2$ cathode. Besides, FEC benefited the passivation of Na metal anode for suppressing undesirable reactions, thus enhancing the deposition/dissolution of metallic Na with higher reversibility.[675] The favorable role of FEC toward both the anode (e.g., hard carbon, Na metal) and the cathode (e.g., Na$_{0.44}$MnO$_2$) material was further verified by researchers, demonstrating the formation of a desirable passivation layer with FEC for improving the cycle stability and of SIBs.[676−679]

Very recently, a unique SEI was designed via in situ preimplantation of F atoms rooted in Na metal.[680] As a fluorine booster, the soluble functional molecule, amide molecule bis(trifluoroacetamide) (ECDA), can be anchored onto the Na metal. Owing to the strong induction effect and electrostatic repulsion of Na toward ECDA, abundant FEC-decomposed F atoms were driven to penetrate deeply into the

Na metal from the outside inward, which resulted in a desired functional rooted interphase (Figure 31a). Afterward, this interphase promoted the generation of a multilayer, inorganic-rich (e.g., NaF, Na$_x$N, and Na$_2$O) SEI with a concentration gradient, ultimately enabling a high CE of 97.3% with an extended Na plating/stripping lifetime (1700 h) at 1 mA cm^{-2}. In addition, the 4.5 V Prussian Blue‖Na@Cu battery delivered a high capacity retention of 86% over 200 cycles with a limited amount of Na.[680] Unfortunately, these strategies failed to satisfy the wide temperature applications of SIBs. Generally, unwanted electrolyte decomposition on the cathode surface aggravates rapidly with increasing temperature, where the unstable CEI layer is commonly accompanied by continuous electrolyte decomposition, surface reconstruction, and capacity fading.[681−683] In addition, the defects of the uncontrollable CEI would be further aggravated with high-voltage and high-temperature conditions.[684] Recently, Chou and co-workers introduced an anion receptor tris(pentafluorophenyl)borane (TPFPB) containing an electron-deficient B center, which preferentially oxidized for constructing the NaF-rich CEI layer. The strong interactions between the ClO$_4^-$ anion and the TPFPB additive effectively reduced the involvement of ClO$_4^-$ in the first solvation sheath and contributed to facilitated coordination capability between organic solvents and Na$^+$ cations, which greatly enhanced the antioxidative stability (Figure 31b and 31c). With the TPFPB-containing electrolyte, the resulting Na$_3$V$_2$(PO$_4$)$_3$ cathode delivered a capacity retention of 86.9% over 100 cycles, when operated with a high cutoff voltage of 4.2 V (vs Na$^+$/Na) and at a high operating temperature of 60 °C. This electrolyte also exhibited promising performance over a wide temperature range from −30 to 60 °C, highlighting the significance of tailoring the solvation chemistry for high-voltage and high-temperature SIBs.[685]

Learning from the Li-based battery electrolyte systems, fluorinated "inert" diluents have been successfully employed in SIBs for tuning the solvation structure and the related electrochemical behavior. In 2018, Zhang et al. designed a LHCE in SIBs by introducing a hydrofluoroether diluent (i.e., BTFE) to decrease the concentration of NaFSI−DME electrolyte to less than 1.5 M.[687] Taking advantage of the "inert" nature of the fluorinated diluent, the interphasial reaction kinetics and interphasial stability of the Na metal anode were largely improved, which was attributed to the formation of a F-enriched protective SEI layer. Consequently, a dendrite-free Na deposition process along with stable cycling (90.8% capacity retention over 40000 cycles) and fast charging (20 C) were achieved in the Na‖Na$_3$V$_2$(PO$_4$)$_3$ battery. Afterward, the authors reported a nonflammable LHCE composed of NaFSI-triethyl phosphate (TEP)/TTE (1:1.5:2 in molar ratio) for highly reversible SIBs. This electrolyte stabilized the interphases on both the layered Na-Cu$_{1/9}$Ni$_{2/9}$Fe$_{1/3}$Mn$_{1/3}$O$_2$ (Na−NCFM) cathodes and the HC anodes, enabling high CE and long-term cyclability for the HC‖Na−NCFM full cells.[688]

More interestingly, fluorine chemistry has also been utilized in designing novel salts for SIBs. Despite high ionic conductivity, NaPF$_6$ is susceptible to undergoing hydrolysis, leading to toxic species such as HF and POF$_3$ and posing severe safety concerns.[689,690] Meanwhile, alternative Na salts suffer from poor electrochemical performance, severe safety concerns, or high cost. Borate anions with various attractive features have gained interest as electrolyte salts recently,

especially when possessing varying degrees of fluorination for greater ESW. Wright et al. prepared a series of Na borate salts with varying steric and electronic properties, where Na[B-(hfip)$_4$]·DME (hfip = hexafluoroisopropyloxy, O^{i}Pr^F) and Na[B(pp)$_2$] (pp = perfluorinated pinacolato, O$_2$C$_2$(CF$_3$)$_4$) stood out with increased oxidative stability as well as excellent electrochemical performance.[691]

Combining the Na anode with an abundant, nontoxic, and high-capacity (1675 mAh g^{-1}) sulfur cathode, sodium−sulfur (Na−S) batteries have been technologically attractive for grid-scale energy storage. High-temperature Na−S batteries have been commercialized since 2002 with a high efficiency of ∼100% as well as a theoretical energy density of 760 Wh kg^{-1} (based on both the Na anode and the sulfur cathode), the safety concerns and additional maintenance costs brought by the high operating temperature (300−350 °C) still remain unsolved. Besides, the capacity utilization of the sulfur cathode is only ∼1/3 of the theoretical value, which is ascribed to the incomplete sulfur conversion reactions. Motivated by these issues, increasing efforts have been focused on RT Na−S batteries, which operate through a complete sulfur conversion with sodium sulfide (Na$_2$S) as the final discharge product instead of Na polysulfides, improving the theoretical energy density to 1274 W h kg^{-1}. Nevertheless, RT Na−S batteries are strongly restricted by low reversible capacity, serious self-discharge, and insufficient cycle stability, which are mainly attributed to the incompatible electrolyte systems toward the electrodes. By introducing FEC as the electrolyte cosolvent, Wang et al. discovered that the solubility of Na polysulfides in the electrolyte was successfully inhibited due to the low binding energy between FEC and Na polysulfides. Meanwhile, a stable and robust F-rich SEI was generated on the anode, protecting the Na metal from dendrite growth.[692] Recently, their continuous work demonstrated highly reversible long-term Na−S batteries through developing an all-fluorinated electrolyte, consisting of 2,2,2-trifluoro-N,N-dimethylaceta-mide (FDMA) as solvent, 1,1,2,2-tetrafluoroethyl methyl ether (MTFE) as antisolvent, and FEC as additive. The MTFE with a reduced HOMO value would strengthen the electrolyte antioxidative stability. Besides, the decreased negative charge density of the FDMA−MTFE system could suppress the dissolution of polar polysulfide and also lead to weak solvation of Na salts, which contributed to anion-dominated SEI construction (Figure 31d). It was also demonstrated that the FDMA solvent and FEC additive controllably reacted with Na polysulfides to form a NaF- and Na$_3$N-rich CEI, enabling a "quasi-solid-phase" Na−S conversion. As a consequence, the RT Na−S batteries delivered a high reversible capacity of 1114 mAh g^{-1} (based on the mass of sulfur) along with an extended lifespan.[686]

5.1.3. Fluorine-Containing Electrode Materials in K-Based Batteries.
Typically, the larger radius of K$^+$ (1.38 Å) than Li$^+$ (0.76 Å) and Na$^+$ (1.02 Å) causes sluggish intercalation kinetics, which further leads to low storage capacity, unsatisfactory rate capability, and poor cycle stability of PIBs. Thus, exploring appropriate host materials for high-performance PIBs is urgently needed.[693] In PIBs, polyanion compounds possessing 3D open-framework structures have been extensively explored as cathode materials due to the fast K$^+$ diffusion kinetics and high redox voltages, among which fluorophosphates and fluorosulfates have attracted great interest.[694−700] As early as 2012, a family of potassium fluorosulfates, KMSO$_4$F (M = Fe, Co, and Ni), has been
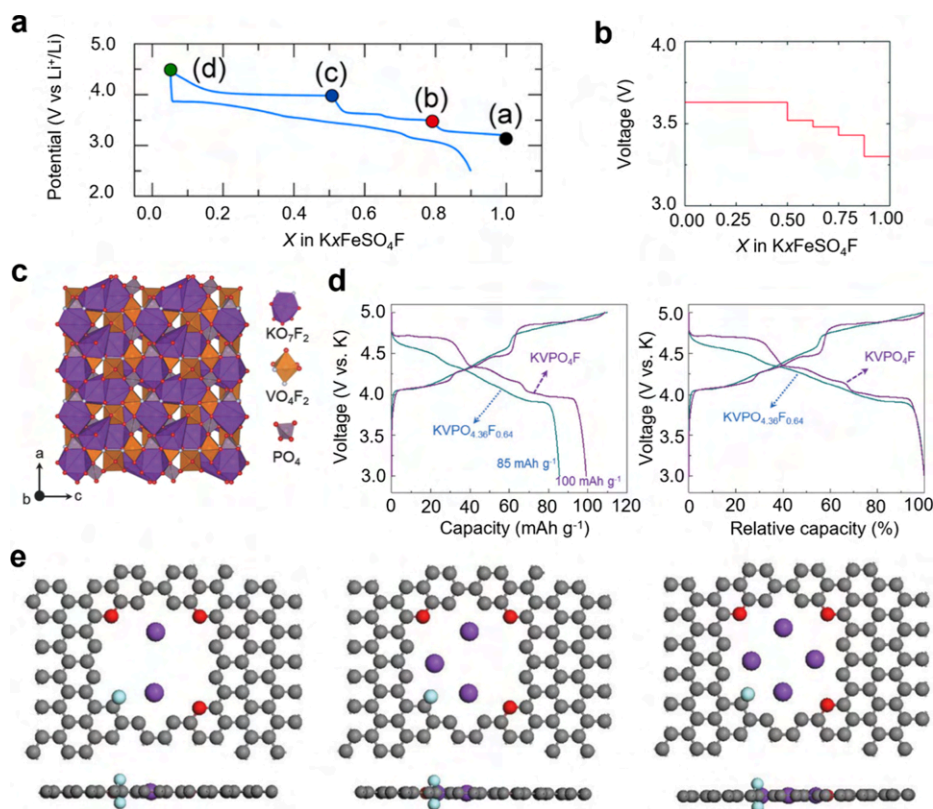
Figure 32. Effect of fluorine on improving the electrochemical performance of polyanion cathode or carbonaceous anode materials in PIBs. (a) Voltage curve of the Li∥KFeSO$_4$F cell starting with the charging process. Reproduced with permission from ref 701. Copyright 2012 American Chemical Society. (b) Voltage curve predicted for the extraction of K$^+$ from KFeSO$_4$F cathode material. Reproduced with permission from ref 702. Copyright 2013 Royal Society of Chemistry. (c) Crystal structure of KVPO$_4$F cathode material. (d) Charge/discharge curves of KVPO$_4$F and KVPO$_{4.36}$F$_{0.64}$ in the second cycle at a current rate of 5 mA g^{-1}. Reproduced with permission from ref 699. Copyright 2018 Wiley-VCH. (e) The optimized mode after absorbing two, three, and four K atoms in the O/F dual-doped carbon (viewed from top and side). Reproduced with permission from ref 71. Copyright 2019 Wiley-VCH.

explored for the insertion/extraction of various alkali ions including Li$^+$, Na$^+$, or K$^+$. KFeSO$_4$F crystallizes in an orthorhombic unit cell (space group $Pna2_1$), and its structure consists of chains of FeO$_4$F$_2$ octahedra linked via F$^-$ ions. With the removal of K$^+$ from KFeSO$_4$F (Figure 32a), no obvious structural change was observed for the K$_{0.55}$MSO$_4$F composition. Further removal of K$^+$ ($x < 0.5$) leads to a new oxidized phase with a formula of "FeSO$_4$F". Notably, this new phase with large and empty channels displayed excellent versatility as reversible hosts for a variety of alkali guests.[701] Afterward, a mechanistic investigation for the K$^+$ removal from the KFeSO$_4$F cathode was conducted. Based on the first-principles calculations, the mechanism that induced this phase transition upon K$^+$ extraction was studied at the atomic scale. It was unveiled that the crystal structure was stable for the phase transition from KFeSO$_4$F to K$_{0.5}$FeSO$_4$F, where only neighboring Fe^{2+}–Fe^{3+} pairs were formed through selective oxidation. The continuous removal of K$^+$ ($x < 0.5$) would cause Fe^{3+}–Fe^{3+} pairs with strong electrostatic repulsion, thus triggering a structure transition to a more ordered "FeSO$_4$F" phase (enlarging the Fe^{3+}–Fe^{3+} distance). Apart from the structural stability, such strong electrostatic repulsion also played a critical role in the voltage curve of the cathode, with multiple voltage plateaus from $x = 1$ to $x = 0.5$ and just a single plateau when $x < 0.5$ (Figure 32b).[702] Nevertheless, the electronic conductivities of these KMSO$_4$F compounds were insufficient for achieving high electrochemical performance. To

tackle this issue, Chen et al. synthesized graphene-decorated KFeSO$_4$F (KFSF@G) submicrometer particles.[700] The ball-milling treatment facilitated a tight wrap of graphene to the KFeSO$_4$F particle for efficient electron and K$^+$ transport while largely reducing the particle size to increase reaction sites. The obtained KFSF@G not only displayed a reversible capacity of 111.5 mAh g^{-1} with a high average operating voltage of 3.55 V but also exhibited excellent rate capability with a discharge capacity of 82.8 mAh g^{-1} at 5 C (1 C = 128 mA h g^{-1}). Unfortunately, all of these efforts have not achieved a satisfactory long-term lifespan of the KFeSO$_4$F-based PIBs.

Compared with the above-mentioned fluorosulfates, V-based polyanion compounds with enhanced cycle stability have attracted great interest in recent years. In 2017, KVPO$_4$F was investigated as a high-voltage cathode material for PIBs, displaying a reversible capacity of 92 mAh g^{-1} and a high average working voltage above 4.0 V (vs K/K$^+$) in 1 M KPF$_6$–EC/PC electrolyte. Notably, the lattice volume of the cathode material shrank only 5.8% after charging to 5 V, which was promising for applying as high-voltage cathodes in PIBs.[695] In these fluorophosphates, F$^-$ could be substituted by some O^{2-} (oxygenation), thus reducing the average working voltage and reversible capacity. To illustrate the effects of the fluorine, a stoichiometric KVPO$_4$F synthesized via a two-step reaction was evaluated by Ceder et al.[699] Such KVPO$_4$F cathode achieved a reversible capacity of ∼105 mAh g^{-1} along with a high average voltage of ∼4.33 V (Figure 32c and 32d),
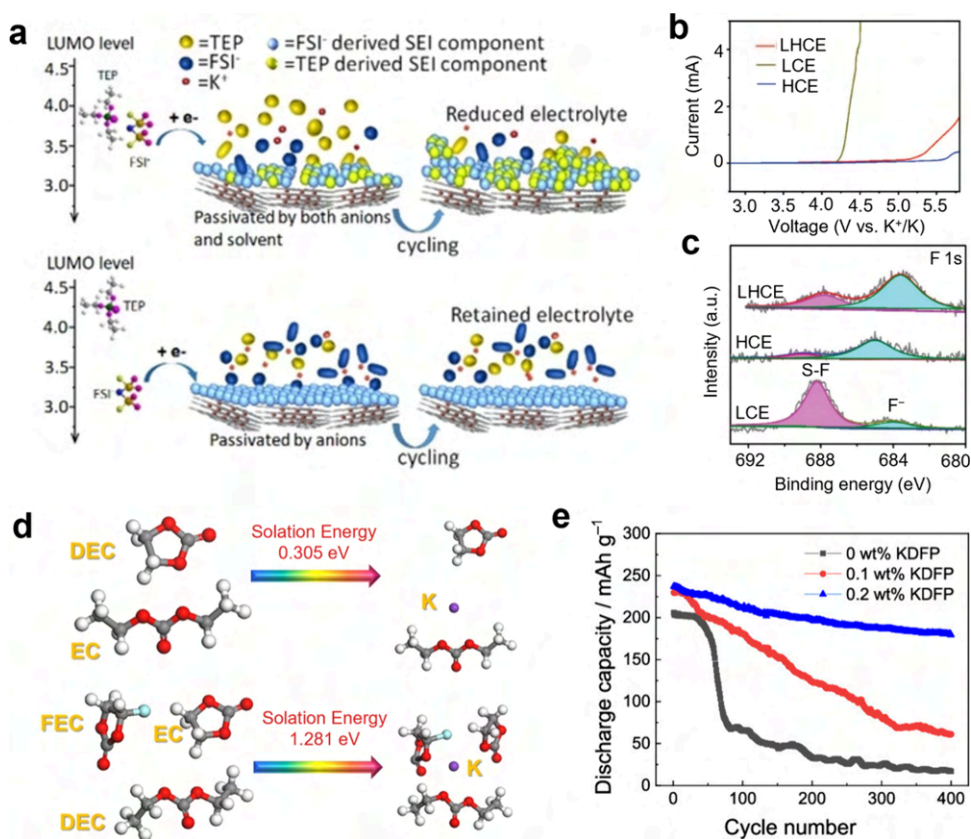
Figure 33. Fluorine-containing salts and electrolyte additives explored in PIBs. (a) Schematic illustration of the SEI constructed with 0.9 M KFSI/TEP and 2 M KFSI/TEP electrolytes. Reproduced with permission from ref 714. Copyright 2020 Wiley-VCH. (b) LSV measurements of low-concentration electrolyte (LCE), HCE, and LHCE. (c) XPS F 1s spectra of the NCP anode with different electrolytes. Reproduced with permission from ref 715. Copyright 2023 Wiley-VCH. (d) DFT calculations for the solvation energies estimated from the binding energy of the clusters. Reproduced with permission from ref 707. Copyright 2018 Elsevier. (e) Cycle stability of the graphite anode in 0.5 M KPF$_6$—EC/DEC electrolyte containing 0, 0.1, and 0.2 wt % of KDFP at 1/3 C (1 C = 279 mA g^{-1}). Reproduced with permission from ref 716. Copyright 2020 American Chemical Society.

corresponding to a promising energy density of ~454 Wh kg^{-1}. In addition, they revealed that intermediate phases at x = 0.75, 0.625, and 0.5 for the K$_x$VPO$_4$F cathode were formed upon cycling. The oxygenation of KVPO$_4$F not only caused a disordered structure to suppress the K$^+$/vacancy formation but also reduced the reversible K$^+$ storage capacity and the operating voltage. To improve the cycle stability of the KVPO$_4$F cathode, Chen et al. prepared KVPO$_4$F through flower-like carbon-coated VPO$_4$ and then enveloped these primary particles in carbon frameworks (KVPO$_4$F/C). The carbon framework enhanced the electronic conductivity and acted as a reducing agent to control the F content in KVPO$_4$F. It was elucidated that with a higher carbon content in the KVPO$_4$F/C material, the oxidation of V and the desorption of F could be suppressed. The optimized KVPO$_4$F/C manifested a reversible capacity of 103 mAh g^{-1} at 20 mA g^{-1} and a stable cycle life of 900 cycles at 1 A g^{-1}. Such cathode also exhibited superior discharging capability with a reversible capacity of 87.6 mAh g^{-1} at 5 A g^{-1}. More promisingly, a full cell based on this KVPO$_4$F/C cathode and a VPO$_4$ anode demonstrated a long lifespan of over 2000 cycles, an excellent capacity retention of 86.8%, and an average CE of 99.5% (at 1 A g^{-1}).[697]

As regards the anode materials, since the first report on the successful electrochemical K$^+$ insertion into graphite by Ji et al. in 2015,[703] carbonaceous materials have become the focus for

PIB anodes because of their low cost, high electronic conductivity, and environmental friendliness. Unfortunately, these carbonaceous anodes such as graphite suffer from a low specific capacity with a theoretical capacity of only 279 mA h g^{-1} with the formation of KC$_8$ after discharging along with poor cycle stability and a huge volume change (61%) upon potassiation. To enhance electrochemical properties of this anode material, heteroatom doping was adopted by Chen et al.[71] The F doping was reported to improve the surface disorder of the carbonaceous material, which could create large amounts of surface defects to facilitate K$^+$ adsorption. In addition, the O doping decreased the inert surface area and generated abundant active sites as well. The codoping of O/F into the porous carbon framework regulated the electronic structure of the carbon atoms and enhanced the adsorption of K$^+$, as suggested by the structural integrity after absorbing a number of K atoms (Figure 32e). Consequently, the O/F-codoped anode material achieved a high reversible capacity of 481 mA h g^{-1} at 0.05 A g^{-1} and excellent cycle performance with 92% capacity retained over 2000 cycles at 1 A g^{-1}. Even at a current density of 10 A g^{-1}, an ultralong lifespan of 5000 cycles can be enabled with a retained capacity of 111 mAh g^{-1}. In brief, structure modification, carbon coating, and heteroatom doping are effective strategies to enhance the overall electrochemical performance of polyanion (e.g., KVPO$_4$F and KFeSO$_4$F) cathode or carbonaceous anode materials.

5.1.4. Fluorinated Electrolytes in K-Based Batteries.

As within LIBs, electrolytes play a critical role in deciding the performance of K-based batteries.[704] With regard to the electrolyte salts, since the electron-withdrawing feature of F atoms favors high solubility in organic aprotic solvents, most K salts contain fluorinated anions.[705] Wu et al. investigated various electrolyte formulations based on KPF_6, potassium bis(trifluoromethylsulfonyl)imide (KTFSI), and KFSI salts, demonstrating that only KFSI/DME electrolyte enabled a reversible/stable plating/stripping behavior for K metal.[706] This result was attributed to the cleavage of weak S−F bonds in FSI^-, forming a stable KF-rich SEI layer. Besides chemical compositions, the choice of electrolyte salts also affects the structure, mechanical properties, and electrical properties of the SEI layer.[707−711] As revealed by Guo et al., a thinner SEI with higher viscoelasticity was formed with the KFSI-based electrolyte instead of the KPF_6-based electrolyte, largely alleviating the stress induced by volume changes during plating/stripping of K metal.[710] Besides, compared with the KPF_6-based electrolyte, the SEI constructed in KFSI-based electrolyte exhibited an improved thermal stability with more thermoduric inorganic species, as evidenced by the decomposition reaction that occurred at ∼117 °C.[712] Afterward, DFT and MD calculations were conducted to reveal the underlining mechanism for different salts. Both the KFSI and the KFSI− solvent complexes exhibited lower LUMO energy levels compared with the corresponding KPF_6 and KPF_6−solvent complexes. The solvation energy of K^+ was higher in KFSI-based electrolyte than that in KPF_6-based electrolyte. These findings suggested that the SEI layer constructed with KFSI electrolytes was salt anion dominated while the layer with KPF_6 was derived from solvent decomposition.[713]

Based on KFSI as the conducting salt and the flame-retardant TEP as the sole solvent, an intrinsically nonflammable electrolyte was demonstrated for K-based batteries.[714] Compared with the requirements of highly concentrated phosphate electrolytes in LIBs and SIBs, a rather dilute electrolyte with a concentration of 0.9 M was sufficient to run the K-based battery system. Further optimizing the concentration of the KFSI−-TEP electrolyte to 2.0 M, a uniform and robust anion-derived SEI layer was constructed along with the synergistic merits of low cost, low viscosity, and high ionic conductivity of the optimized electrolyte (Figure 33a), significantly suppressing the solvent decomposition and allowing a high CE of 99.6% for K-metal plating/stripping without dendrites. This advanced electrolyte was superior to conventional carbonate electrolytes, offering a new avenue for designing nonflammable electrolytes with high safety.

Following the design of LHCEs in LIBs discussed in section 3.2, a low-polarity diluent that does not dissolve K salts was introduced to enhance the performance of LHCEs in K-based batteries. The first attempt adopted the highly fluorinated HFE as a diluent based on the concentrated KFSI−DME electrolyte, forming a LHCE with a molar ratio of 1:1.90:0.95 for the KFSI:DME:HFE components. Such a LHCE displayed higher antioxidation stability, lower flammability, and higher ionic conductivity than the concentrated KFSI−DME electrolyte. In addition, with a durable KF-rich SEI layer constructed on the surface of graphite, the graphite anode with a high mass loading of ∼8 mg cm^{-2} survived for more than 300 cycles with a reversible capacity of 200 mA h g^{-1} along with a high CE of 99.5%.[717] This report employed LHCE to achieve highly reversible graphite anodes. However, the influence of "inert"

diluent molecules on the K^+ solvation structure and the local coordination environment is still ambiguous. Later, a fire-retardant electrolyte was developed by blending concentrated KFSI−TEP electrolyte with TTE as an "inert" diluent. Results revealed that such LHCE retained a relatively weakened anion-coordinated solvation environment and the TTE diluent was nonsolvated. Combining the synergistic effects of the KFI^- anions and the highly fluorinated diluent, a SEI film containing well-balanced inorganic/organic species was tailored in situ on the graphite anode, protecting the graphite anode from continuous side reactions and meanwhile facilitating the K-ion transport. Consequently, the graphite anode retained 92.4% capacity retention after 1400 cycles at 0.1 A g^{-1}.[155] Apart from the effects on graphite anodes, LHCEs were also designed to improve the compatibility between electrolytes and carbon-based anode materials in PIBs. Very recently, a LHCE was designed by introducing the nonsolvent TTE into the concentrated KFSI−DME electrolyte. This LHCE broke the interconnected 3D K^+-solvated shell while maintaining the original individual K^+-solvated structure, thus improving the ionic conductivity and ensuring sufficient oxidation resistance of the electrolyte (Figure 33b). More promisingly, a uniform and durable KF-rich SEI layer was formed on the carbonous (nitrogen-doped carbon spheres, NCP) anode (Figure 33c), delivering a high reversible capacity of 232.5 mAh g^{-1} along with 78.7% capacity retention over 200 cycles.[715] These reports discovered the significance of "inert" diluents combined with salts and solvents for the design of LHCE systems for enhanced K-based batteries.

Besides the fluorine-containing salts, appropriate electrolyte additives can also stabilize the electrode|electrolyte interphase and further enhance the battery performance, which has been widely applied in LIBs and SIBs. Among them, as a widely applied film-forming additive, FEC has demonstrated excellent capability to solve the interfacial incompatibility of electrolytes toward reactive metal anodes. Owing to the antioxidative ability of the F-containing group, FEC additive was adopted to reduce side reactions of the Prussian blue analog (PBA) cathodes in PIBs, thus increasing the CE and cycle stability of the K‖PBA half cell.[718,719] However, the FEC additive sometimes worsened the electrochemical performance of full cells, especially when intercalation-based or alloy-based anode materials were used. This may be related to the excessive reduction of FEC that induces undesirable SEI formation during repeated cycling.[720] Through DFT calculation, Guo et al. verified that the electrolyte with FEC increased the solvation energy from 0.305 to 1.281 eV (Figure 33d), pointing out a larger resistance for the K^+ diffusion and desolvation in the FEC-containing electrolyte, thus leading to poor performance.[707] Similarly, the addition of FEC exerted a negative influence on the electrochemical performance of the Sn_4P_3 anode with fast capacity decay at high current rates. The FEC additive generated more components with carbonyl groups and K−F bonds in an unstable SEI layer that failed to suppress continuous side reactions, resulting in the quick resistance increase and rapid capacity degradation.[708] Later, such excessive SEI layer induced by FEC additive was further observed by Mai et al., displaying a lower initial CE of 58%. In addition, FEC stimulated a large amount of electrolyte decomposition, which inevitably led to an increase in cell resistance and a decrease in capacity.[709] Contrary to the unfavorable role of FEC additive on these anodes, by employing potassium difluorophosphate (KDFP) as additive
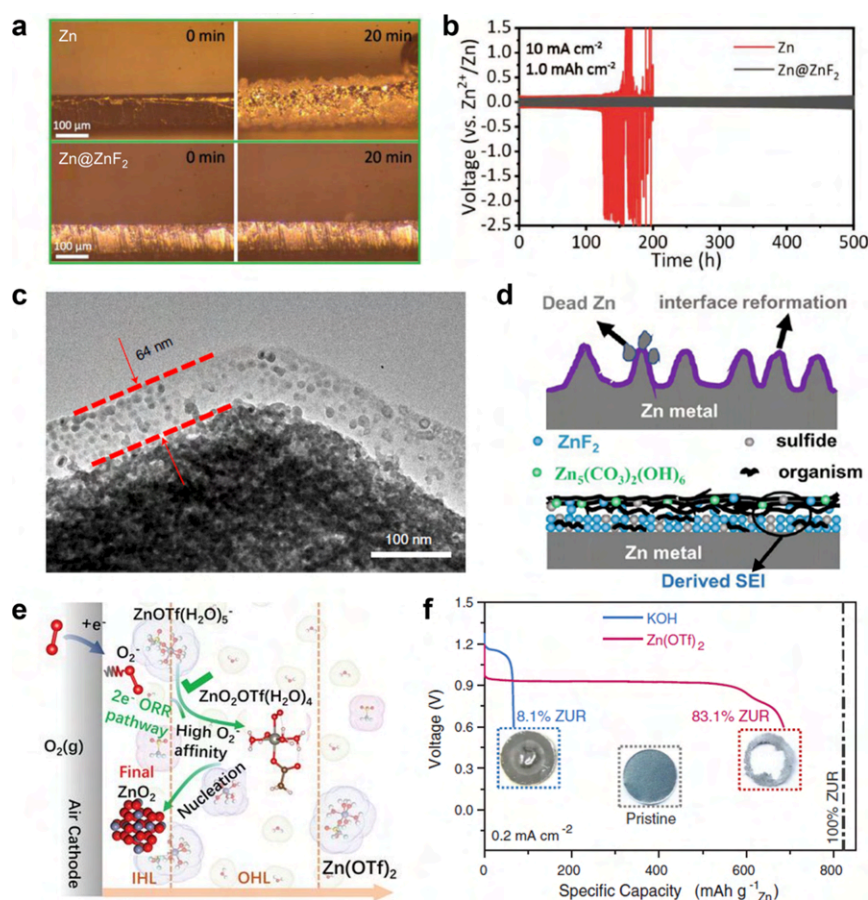
Figure 34. Fluorine chemistry in aqueous multivalent metal-based batteries. (a) Time−voltage curves for Zn‖Zn and Zn@ZnF$_2$‖Zn@ZnF$_2$ symmetrical cells at 10 mA cm^{-1} with a plating/stripping capacity of 1 mAh cm^{-2}. (b) In situ optical observation results of the Zn deposition morphologies on the Zn foil and Zn@ZnF$_2$ electrode at a current density of 10 mA cm^{-2} for 20 min. Reproduced with permission from ref 722. Copyright 2021 Wiley-VCH. (c) TEM images of the cycled Zn anode surface in 4 m Zn(OTf)$_2$ + 0.5 m Me$_3$EtNOTF. Reproduced with permission from ref 723. Copyright 2021 Springer Nature. (d) Illustration of the surface evolution mechanism. (Upper panel) Zn dendrite growth in aqueous electrolytes. The water-passivation-induced porous ZnO layer (purple) constantly breaks and reforms, leading to nonuniform Zn electrodeposition, dendrite formation, and dead Zn during Zn plating/stripping. (Lower panel) Formation mechanism of ZnF$_2$−Zn$_5$(CO$_3$)$_2$(OH)$_6$−organic SEI. The presence of NO$_3^-$ promotes the formation of an electrically and ionically insulating Zn$_5$(OH)$_8$(NO$_3$)$_2$·2H$_2$O layer (red), which subsequently transforms into an electrically insulating but ionically conductive SEI in which the ZnF$_2$−Zn$_5$(CO$_3$)$_2$(OH)$_6$ inner part is coated by the organic outer part. Reproduced with permission from ref 724. Copyright 2021 Wiley-VCH. (e) Galvanostatic discharge profiles of Zn−air cells in KOH (blue) and Zn(OTf)$_2$ (red) electrolytes at 0.2 mA cm^{-2} (cutoff voltage: 0.6 V). The corresponding ZURs are indexed for comparison. (Insets) Photographs of the pristine Zn anode (middle), the Zn anode after discharge in KOH (left), and Zn(OTf)$_2$ (right) electrolytes. (f) Schematic illustration of reaction processes in the inner Helmholtz layer (IHL) and outer Helmholtz layer (OHL) at the surface of the air cathode in Zn(OTf)$_2$ and ZnSO$_4$ electrolytes, respectively. Reproduced with permission from ref 725. Copyright 2021 The American Association for the Advancement of Science.

to the KPF$_6$−EC/DEC electrolyte, Matsumoto et al. successfully constructed a stable K$^+$ conducting SEI (enriched in KF and PO$_x$ species) on the graphite anode, which promoted a highly reversible capacity of 274 mAh g^{-1} with the formation of a suitable potassium−graphite intercalation compound (K−GIC, KC$_8$).[716] The KDFP electrolyte enabled a fast depotassiation/potassiation kinetic process, an increased cyclability with 76.8% capacity retention, and a high average CE of ∼99.9% over 400 cycles (Figure 33e). To briefly summarize, compared with the favorable effects of FEC additive on forming stable and robust SEI layers in LIBs and SIBs, the role of FEC in PIBs remains unclear and needs further investigation. Other effective functional F-containing additives should be explored to avoid undesired reactions between the anode materials and the electrolytes. It is noteworthy that the full cell performance, including both the

cathode and the anode, should be implemented to reveal the real functions of these additives.

Overall, fluorinated electrode materials are of great interest to SIBs, where F$^-$ anions (compared with large polyanions such as PO$_4^{3-}$, SO$_4^{2-}$) can improve the specific capacity and fluorinated compounds are relatively stable against oxidation. The research is currently focusing on 3D fluorinated phases such as cubic perovskite fluorides due to their high-power capability and 3D network stability, but further investigation is needed to regulate polymorphism and phase transition during Na$^+$ storage. Furthermore, establishing structure−performance relationships of these materials can reduce the activation energy barriers and lower the band-gap energy for efficient Na$^+$ diffusion. For PIBs, though 3D open-framework polyanion compounds (e.g., potassium fluorophosphates and fluorosulfates) can enable fast K$^+$ diffusion and high redox potential, the low electronic conductivity of these materials requires surface

modifications. Meanwhile, V-based fluorosulfates offer high working voltages when used as cathodes, but the fluorine to oxygen ratio should be controlled to prevent disordered fluorosulfate structures. Analogous to Li-based batteries, fluorine substitution in cosolvents/solvents and additives can address critical issues in SIBs and PIBs, including interphasial instability, flammability, and capacity decay under fast charging or wide temperature ranges. Notably, strategies from fluorinated electrolytes in Li-based electrolytes cannot be directly applied to SIBs and PIBs, for instance, FEC exhibits a negative influence on certain anodes by stimulating electrolyte decomposition and forming unstable interphases. The current understanding of fluorinated electrolytes and corresponding interphases in SIBs and PIBs is still in the primary stage, and efforts should concentrate on these aspects.

5.2. Multivalent Metal-Based Batteries

5.2.1. Aqueous Multivalent Metal-Based Batteries.
Aqueous multivalent metal-based batteries, such as the aqueous ZIBs, have become a research hotspot owing to the merits of high safety, high specific capacity, low cost, and abundant distribution in the Earth's crust. Zn metal is considered an ideal anode due to its high theoretical specific capacity (820 mAh g^{-1}), low electrode potential (-0.76 V vs standard hydrogen electrode), abundant distribution, and low toxicity. However, when applied in aqueous electrolytes, Zn metal anodes still face serious issues such as corrosion reactions, hydrogen evolution, and uncontrolled dendrite formation.[721] These problems lead to low CE, poor cycle life, continuous electrolyte consumption, and even internal short circuits.

Fluoride plays an important role in constructing highly reversible Zn metal anodes. In 2021, Li et al. devised a novel approach to create durable Zn metal anodes protected by a 3D ZnF$_2$ matrix, effectively preventing dendrite formation and extending the lifespan.[722] In their study, a 3D interconnected ZnF$_2$ matrix was engineered onto the surface of the Zn foil, denoted as Zn@ZnF$_2$, using a rapid and straightforward anodic growth technique. This Zn@ZnF$_2$ electrode served as a versatile protective layer, facilitating the redistribution of Zn^{2+} ions and significantly reducing the desolvation active energy, resulting in stable and efficient Zn deposition. The findings demonstrated that the Zn@ZnF$_2$ electrode effectively suppressed dendrite growth, mitigated hydrogen evolution reactions, and exhibited outstanding plating/stripping of Zn^{2+}/Zn. In addition, the authors used in situ optical microscopy to capture the dynamic Zn plating process within 20 min, revealing the growth of Zn dendrites and large hydrogen bubbles on the pristine Zn electrode. In contrast, the smooth Zn deposition was observed on the surface of the Zn@ZnF$_2$ electrode without dendrites or gas bubbles (Figure 34a). Consequently, the Zn@ZnF$_2$ electrode displayed an impressive cycle life, exceeding 800 h at a current density of 1 mA cm^{-2} in a symmetrical cell test (Figure 34b). This excellent performance was also confirmed in Zn@ZnF$_2$||MnO$_2$ and Zn@ZnF$_2$|| V$_2$O$_5$ full cells. Notably, a hybrid Zn-ion capacitor employing the Zn@ZnF$_2$|| active carbon (AC) configuration demonstrated exceptional durability, maintaining a high capacity retention of 92.8% over 5000 cycles at an ultrahigh current density of approximately 60 mA cm^{-2}.

Fluorine chemistry is widely used in aqueous electrolytes and interface control. Wang et al. reported the development of an aqueous Zn metal battery.[723] They utilized a dilute and acidic aqueous electrolyte containing 4 m zinc trifluoromethanesulfonate (Zn(OTf)$_2$) and an alkylammonium salt (trimethylethylammonium trifluoromethanesulfonate, Me$_3$EtNOTF) as the additive to facilitate the creation of a robust, Zn^{2+} conducting, and waterproof SEI. TEM analysis revealed the presence of a 64 nm thick ZnF$_2$-rich interphase on the deposited Zn surface when Me$_3$EtNOTF was introduced (Figure 34c). This SEI acted as an electron barrier, preventing the reduction of water while allowing the migration of Zn^{2+}. The presence of this SEI led to outstanding performance, including dendrite-free Zn plating and stripping, a remarkable 99.9% CE over 1000 cycles in a Ti||Zn asymmetric cell, stable cycling behavior for 6000 cycles (equivalent to 6000 h) in a Zn||Zn symmetric cell, and impressive energy densities in full cells with limited Zn source (e.g., 136 Wh kg^{-1} in a Zn|| VOPO$_4$ full cell with 88.7% capacity retention over 6000 cycles; 218 Wh kg^{-1} in a Zn||MnO$_2$ full cell with 88.5% capacity retention over 1000 cycles). Furthermore, the electrolyte is conducive to SEI formation, allowing the reversible operation of an anode-free pouch cell. The Ti|| Zn$_x$VOPO$_4$ full cell can be cycled at 100% depth of discharge for 100 cycles, enabling aqueous Zn-based batteries as practical and viable energy storage systems for various applications. Wang et al. also reported the development of a Zn-ion conductive, water-resistant, and ZnF$_2$-rich SEI on the Zn anode.[724] A designed low-concentration aqueous electrolyte composed of fluorine-containing Zn(OTf)$_2$ and Zn(NO$_3$)$_2$ was developed. This electrolyte facilitated the in situ formation of a robust SEI with an inorganic inner layer made of ZnF$_2$ and Zn$_5$(CO$_3$)$_2$(OH)$_6$ to enhance Zn-ion diffusion, and an organic outer layer acted as a barrier against water infiltration. Their research revealed that the initial layer formed on the Zn anode surface was an insulating Zn$_5$(OH)$_8$(NO$_3$)$_2$·2H$_2$O, resulting from a self-terminated chemical reaction involving NO^{3-}, Zn^{2+}, and OH$^-$ generated through the hydrogen evolution reaction (HER). Subsequently, this inorganic layer transformed into Zn-ion conducting Zn$_5$(CO$_3$)$_2$(OH)$_6$, promoting the formation of ZnF$_2$ as the inner layer (Figure 34d). The organic-dominated outer layer was established through the reduction of OTf$^-$. This in situ-formed SEI exhibited remarkable performance, achieving a high CE of 99.8% over 200 h in Ti||Zn half cells and maintaining a high energy density of 168 Wh kg^{-1} in Zn||MnO$_2$ full cells with 96.5% capacity retention after 700 cycles, even with a N/P ratio of 2:1.

Rechargeable Zn−air batteries hold the promise of delivering both high energy density and safety. However, they encounter huge challenges due to the sluggish 4-electron (e$^-$)/oxygen (O$_2$) reaction that relies on water participation. The electrochemical reversibility stems from unwanted side reactions driven by the harsh electrolytes and atmospheric carbon dioxide. In 2021, Winter et al. reported a breakthrough result in the form of Zn−O$_2$/zinc peroxide (ZnO$_2$) chemistry, which was operated via a 2-e$^-$/O$_2$ reaction in nonalkaline aqueous electrolytes.[725] The new reaction mechanism facilitated highly reversible redox reactions for Zn−air batteries. The success of this ZnO$_2$-based chemistry can be attributed to the formation of a water-scarce and Zn^{2+}-rich inner Helmholtz layer (IHZ) on the air cathode, induced by the hydrophobic trifluoromethanesulfonate anions (Figure 34e). In a nonalkaline electrolyte containing 1 mol kg^{-1} Zn(OTf)$_2$, the Zn−air battery exhibited a well-defined discharge plateau at approximately 1.0 V, boasting an areal capacity of 52 mAh cm^{-2}, corresponding to a specific capacity
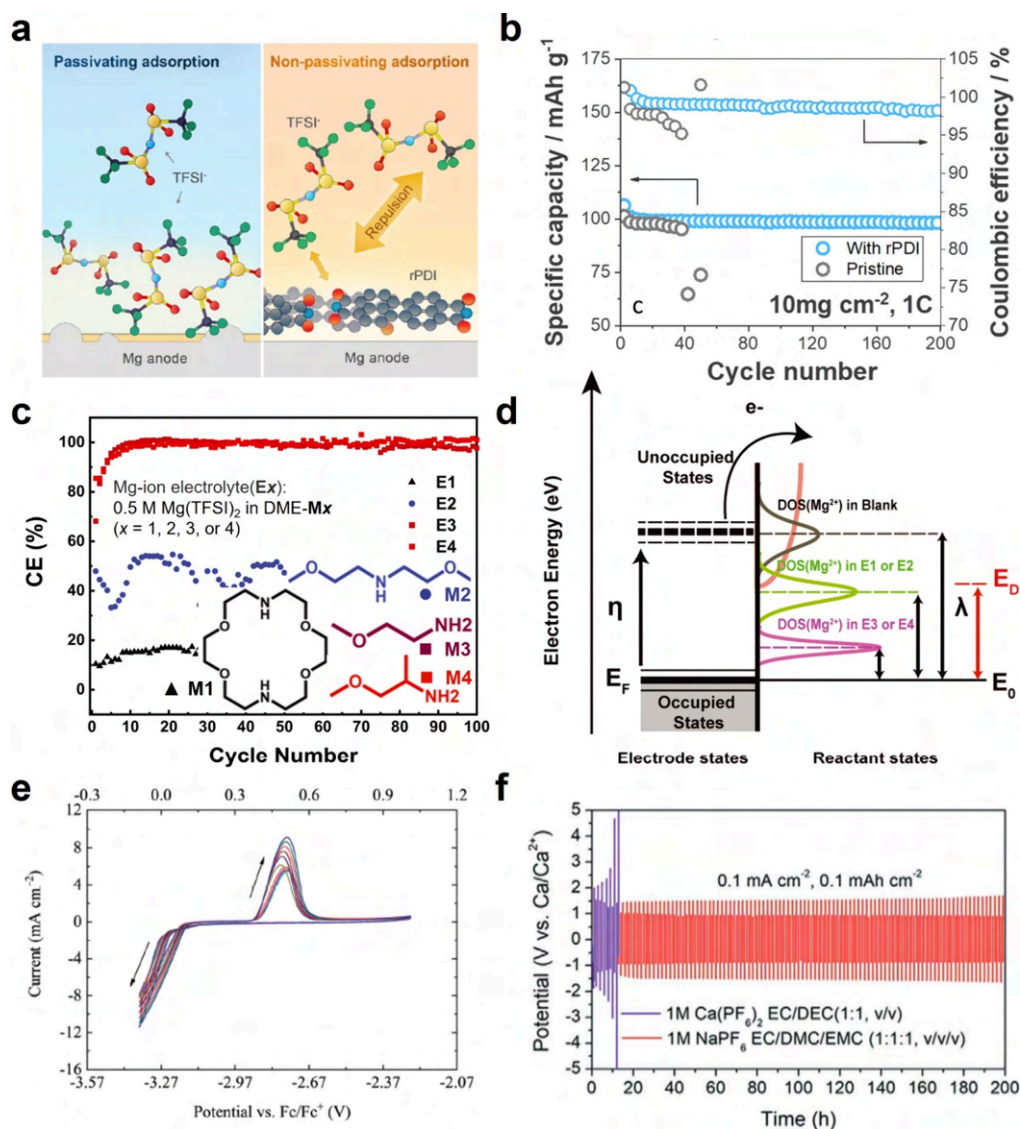
Figure 35. Fluorine chemistry in nonaqueous multivalent metal-based batteries. (a) Schematic illustration of passivating adsorption and nonpassivating adsorption. (Left panel) Passivating anions (TFSI⁻) adsorb on the Mg anode and form the passivation layer. (Right panel) Nonpassivating anions (rPDI) with higher adsorption energy repel TFSI⁻ away to prevent Mg anode passivation. (b) Cycling stability of Mg−PDI full cells with pristine (gray) and rPDI (blue) electrolyte at 15 C under 1 mg cm⁻² (1 C = 128 mA g⁻¹). Reproduced with permission from ref 729. Copyright 2021 American Chemical Society. (c) CEs for Mg plating and stripping in $\mathbf{E}x$ in Mg‖SS cells cycled at 0.1 mA cm⁻². Mg-ion electrolyte ($\mathbf{E}x$): 0.5 M Mg(TFSI)$_2$−DME/$\mathbf{M}x$ (x = 1, 2, 3, or 4). (d) Marcus−Gerischer diagram of electron transfer at the metal electrode‖electrolyte interphase. E_F refers to the Fermi level of the metal electrode, and E_0 refers to the energy level of the electrolyte and electrode at equilibrium. Red, green, and black Gaussians represent the DOS of Mg²⁺ in the electrolyte. The orange curve represents the DOS of other electrolyte components, and E_D refers to the onset potential of the electrolyte decomposition. Reproduced with permission from ref 730. Copyright 2021 The American Association for the Advancement of Science. (e) CVs of Ca plating/stripping in the electrolyte containing Fc as the internal reference with a three-electrode configuration using Pt, Ag, and Ca as the working electrode, reference electrode, and counter electrode, respectively, at a scan rate of 80 mV s⁻¹. Reproduced with permission from ref 731. Copyright 2019 Royal Society of Chemistry. (f) Cycling stability of voltage−time curves with a capacity of ∼0.1 mAh cm⁻² at 0.1 mA cm⁻² of Ca‖Ca symmetrical batteries. Reproduced with permission from ref 732. Copyright 2020 Wiley-VCH.

of 684 mAh g⁻¹ (based on the weight of the Zn anode). Additionally, as shown in Figure 34f, it achieved a remarkable Zn utilization ratio (ZUR) of 83.1%. In contrast, the Zn−air battery with an alkaline electrolyte composed of 6 mol kg⁻¹ KOH only achieved a ZUR of 8.1%. The photographic evidence of pristine and cycled Zn anodes immersed in different electrolytes confirmed the superior ZUR in the Zn(OTf)$_2$ electrolyte, where most of the Zn foil dissolves. As a result, the nonalkaline Zn−air battery not only maintained stable performance in ambient air but also demonstrated

significantly improved reversibility compared to its alkaline counterpart. Similar fluorine chemistry-involved electrolyte engineering strategies can be promisingly extended to other aqueous multivalent-ion systems (e.g., Mg-ion, Ca-ion, and Al-ion batteries).

Moreover, F-containing materials have also been applied as cathodes in aqueous multivalent-ion batteries. In 2021, Gregorio et al. developed a trigonal Na$_5$V(PO$_4$)$_2$F$_2$ as the cathode for Mg-ion batteries.[726] Beneficial from the multi-electron transfer redox couples of V⁴⁺/V³⁺ and V⁵⁺/V⁴⁺, the

Mg|0.5 M magnesium bis(trifluoromethanesulfonyl)imide $(Mg(TFSI)_2)$−DME + 0.4 M H_2O|$Na_5V(PO_4)_2F_2$ cell delivered a reversible specific capacity of 136 mA h g^{-1}, achieving a high energy density of 190 W h kg^{-1} with an average discharge voltage of 1.4 V. It should be noted that the regulation of the F^-/O^{2-} ratio in sodium−vanadium fluorophosphate directly affected the content of V^{3+}/V^{4+} and changed the specific capacity of the cathode materials.

5.2.2. Nonaqueous Multivalent Metal-Based Batteries.

F-related chemistry also plays an important role in the development of nonaqueous multivalent metal-ion batteries (e.g., Mg-ion batteries, Ca-ion batteries, and Al-ion batteries) as promising energy storage systems owing to the high energy densities and low cost. The multielectron redox capability contributes to the high energy density, and the abundant distribution of these multivalent metal ions in the Earth's crust ensures the low manufacturing costs. However, the larger ionic radii and greater charge density of multivalent metal ions bring significant challenges associated with slow ion transport, large polarization, and low reversibility, making them less competitive than Li-based batteries in the race toward ever-rising energy density targets.[727]

A strategy aiming at balancing the protection and passivation effect of the F-containing layer on the anode surface has been widely applied to realize high-performance multivalent metal-ion batteries. For instance, Mg-based batteries often face several challenges, such as low power density and limited cycle life, primarily due to the issue of severe passivation of the Mg anode. Although using nucleophilic electrolytes can effectively stabilize the Mg anode, their high chemical reactivity prevents the use of organic and conversion cathodes. To solve this issue, Lu et al. introduced a nonpassivating anion additive known as reduced perylene diimide-ethylenediamine (rPDI). This additive has been proven effective in facilitating rapid and reversible Mg deposition/dissolution in a straightforward $Mg(TFSI)_2$−$MgCl_2$-based electrolyte with only a minimal addition of 0.2 mM rPDI. The ability of rPDI to selectively adhere to a Mg anode is the key factor for the enhanced performance, thus repelling $TFSI^-$ anions from the surface of the Mg anode. This prevented $TFSI^-$ decomposition and subsequent Mg passivation (Figure 35a). Leveraging rPDI's millimolar-level solubility in the electrolyte, it was employed as an electrolyte additive in both symmetric cells and full cells. With the addition of only 0.2 mM rPDI as the electrolyte additive, Mg symmetric cells with an electrolyte of 0.25 M $Mg(TFSI)_2$−$2MgCl_2$/DME demonstrated impressive results, achieving highly reversible cycling performance for 300 h at 1.0 mA cm^{-2}. More importantly, the protective effect of rPDI persisted even when the electrolyte was exposed to air, which remarkably extended the cycling stability. Furthermore, the researchers showcased the performance of a Mg−organic full cell, demonstrating fast and reversible Mg^{2+} storage at 50 C (6.4 A g^{-1}). This configuration achieved a superior specific power density of 8.78 kW kg^{-1} and a stable cycle life exceeding 1000 cycles at 15 C. Exceptional areal power density (2.0 mW cm^{-2}) and energy density (1.6 mWh cm^{-2}) were attained at 1 C, along with the highest reported areal capacity of 1.0 mAh cm^{-2} and a stable cycle life extending beyond 200 cycles (Figure 35b). In another case, Zhao et al. effectively synthesized magnesium tetrakis(hexafluoroisopropyloxy)-borate, denoted as $Mg[B(hfip)_4]_2$, showcasing its exceptional characteristics as a viable and efficient electrolyte for prospective high-energy Mg-based batteries.[728]

Similar to Mg-based batteries, rechargeable Ca-based batteries show great promise as alternatives to LIBs due to the abundant resource of Ca element in the Earth's crust and the high theoretical specific capacity. However, these batteries face significant challenges related to slow reaction kinetics and unwanted side reactions. Wang et al. developed a significant breakthrough by demonstrating that multidentate methoxyethyl-amine chelates $[-(CH_2OCH_2CH_2N)_n-]$, located in the first solvation sheath of Mg^{2+} and Ca^{2+}, facilitate both highly reversible reactions on Mg and Ca anodes as well as high-voltage layered oxide cathodes.[730] Specifically, 0.5 M Mg-$(TFSI)_2$−DME was selected as the baseline electrolyte. Four types of multidentate chelates (Mx, x = 1, 2, 3, or 4) were added to the baseline electrolyte to form the electrolytes Ex (x = 1, 2, 3, or 4). The overpotentials during the Mg plating and stripping processes were significantly reduced from 2.0 V (blank) to below 0.1 V ($E4$) with a high CE of 99.5% (Figure 35c). Solvation sheath analysis demonstrated that the solvation sheath became less compact and more polarizable, leading to a decrease in solvation sheath reorganization energy (λ) for electron transfer (Figure 35d). This, in turn, lowered the overpotential by preventing electrolyte decomposition and facilitating stable Mg and Ca plating and stripping. Calcium tetrakis(hexafluoroisopropyloxy)borate, known as $Ca[B-(hfip)_4]_2$, was developed as a prospective electrolyte for room-temperature rechargeable Ca batteries, which demonstrated room-temperature reversible Ca plating and stripping (Figure 35e), exceptional oxidative stability up to 4.5 V, and a high ionic conductivity exceeding 8 mS cm^{-1}.[731]

Wang et al. showcased that a hybrid Na/Ca-based SEI surpassed a purely Ca-based SEI in achieving stable Ca plating and stripping processes.[732] In the case of fluorine-based electrolytes like calcium hexafluorophosphate ($Ca(PF_6)_2$) and calcium tetrafluoroborate ($Ca(BF_4)_2$) ethers and esters solutions, Ca metal underwent passivation with a SEI primarily composed of CaF_2 (pure Ca SEI). This CaF_2 layer served as both an ionic and an electronic insulating barrier. Conversely, when using $NaPF_6$ in an electrolyte composed of EC/DMC/EMC in a 1:1:1 ratio by volume, an in situ evolution of a hybrid Na/Ca-based SEI occurred. These hybrid SEIs exhibited excellent ion conductivity for both Ca^{2+} and Na^+ ions, simultaneously preventing anions from deeply penetrating and averting uncontrolled decomposition of the electrolyte upon the freshly deposited Ca. Consequently, long-term Ca plating and stripping (lasting over 1000 h with minimal polarization shift) can be reliably achieved by utilizing Ca metal itself as the current collector (Figure 35f). Furthermore, Ca metal safeguarded by the hybrid Na/Ca-based SEIs also maintains impressive high-voltage stability, extending up to 4.5 V when used in full cells.

Aluminum, the third most abundant element in the Earth's crust with an oxidation state of 3+, endows the construction of cost-effective and high energy density batteries, boosting the high specific capacity in the form of Al metal anodes and enhanced safety due to its air-stable passive surface layer compared to Li metal. In 2017, Masashi et al. reported a fluoropolymer-supported Al^{3+} conducting solid-state electrolyte.[733] By tuning the ratio of PVDF and $AlCl_3$ (F/Al ratio), the optimized Al^{3+} conductivity at room temperature reached 4.4×10^{-4} S cm^{-1} with a F/Al ratio of 8. This Al^{3+} conducting solid-state electrolyte also showed a stable electrochemical window of 0−2.4 V vs Al^{3+}/Al, fulfilling the redox potential of the reported cathode materials of Al-ion batteries. This
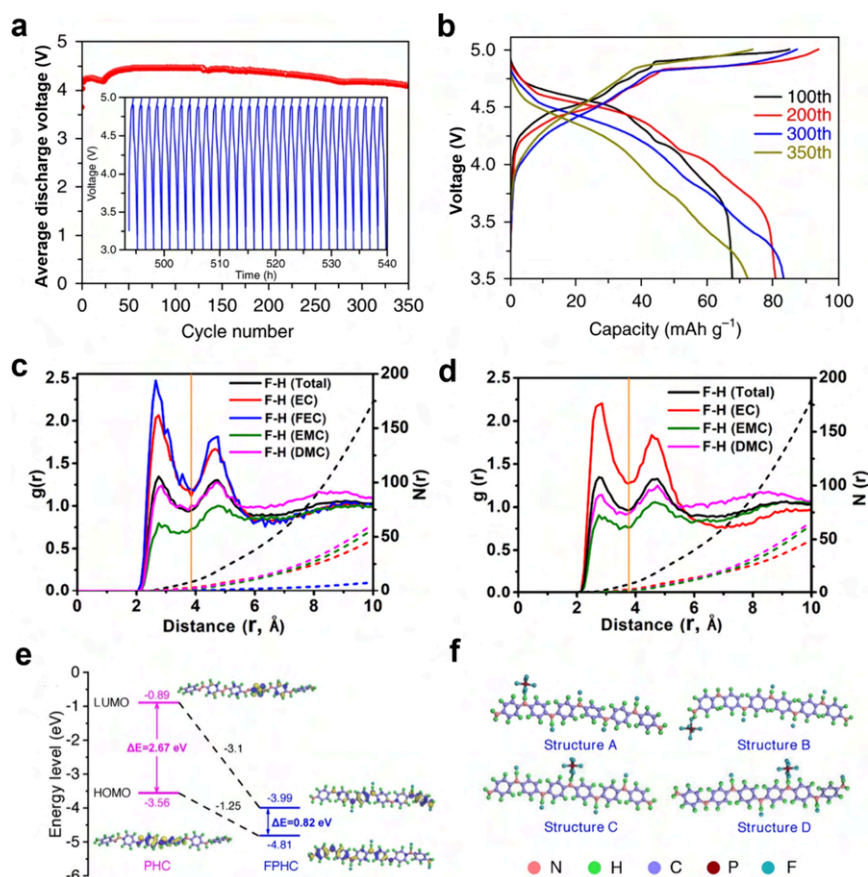
Figure 36. Fluorine-containing electrolytes or electrodes for high-performance DIBs. (a) Average discharge voltage and (b) corresponding charge−discharge profiles of the Ca‖graphite DIB at a current density of 100 mA g^{-1}. (Inset of a) Enlarged curves for the final 30 cycles. Reproduced with permission from ref 739. Copyright 2018 Springer Nature. MD simulation for the RDFs $g(r)$ (solid lines) and coordination number $N(r)$ (dashed lines) of F−H interactions in 1.0 M NaPF$_6$−EC/DMC/EMC (1:1:1 by volume) electrolytes (c) with 10 wt % FEC and (d) without FEC additive. Reproduced with permission from ref 740. Copyright 2021 American Chemical Society. (e) HOMO−LUMO energies and energy gaps of PHC and FPHC molecules. (f) Four optimized models of PF$_6$−FPHC with PF$_6^-$ at the near end group, PF$_6^-$ at the end group, PF$_6^-$ at the middle group, and PF$_6^-$ at the near middle group. Reproduced with permission from ref 741. Copyright 2022 Wiley-VCH.

fluoropolymer-based solid-state electrolyte is promising to eliminate the safety issues such as the leakage of highly corrosive liquid electrolytes in conventional aluminum-ion batteries.

The cathode materials of nonaqueous multivalent metal-based batteries also benefit from fluorine chemistry. In 2021, Xu and colleagues applied a polyanion fluoride (Na$_{1.5}$VPO$_{4.8}$F$_{0.7}$, NVPF) as the cathode material for a nonaqueous Ca-ion battery and achieved a high reversible performance of over 500 cycles with a low capacity fading of 0.02% per cycle.[734] A variety of characterization methods revealed that the volume change relating to the insertion/extraction of Ca^{2+}, the diffusion resistances, and the activation of large Ca^{2+}-ion barriers were successfully suppressed owing to the rigid open framework of VPO$_{4.8}$F$_{0.7}$.

In general, for aqueous multivalent metal-based systems (e.g., ZIBs), the strategy of constructing fluoride-rich anode‖electrolyte interphases can effectively suppress the anode dendrite growth and electrolyte decomposition. Moreover, the sluggish plating kinetics of the anode in nonaqueous multivalent metal-based systems (e.g., Mg-ion and Ca-ion batteries) can be improved by solvation structure modification via the introduction of fluorinated salts, solvents, and additives. All of these fluorine chemistry-involving strategies are

accelerating the real-world application of multivalent metal-based batteries.

5.3. Dual-Ion Batteries and Beyond

In DIBs, anion insertion is considered to be the most important reaction on the cathode side, whereas various inserted anions with F-containing groups were intensively investigated, such as PF$_6^{-}$,[78−81] TFSI^{-},[82,735] FSI^{-},[83−86] FTFSI^{-},[87,88] BF$_4^{-}$,[736] DFOB^{-},[91] CF$_3$SO$_3^{-}$,[92] AlF$_4^{-}$,[93] tris-(pentafluoroethyl) trifluorophosphate [(C$_2$F$_5$)$_3$PF$_3^{-}$],[737] and BETI^{-}.[87] To improve the performance of Al‖graphite DIBs, Tang et al. developed an electrolyte of 7.5 m LiFSI−EC/DMC (1:1 v/v) which not only elongated the cycle stability of the graphite cathode during repeated deintercalation/intercalation of FSI^{-} anions but also enhanced the structural stability of the Al anode via constructing a LiF-rich SEI layer.[738] Motivated by this Al−graphite electrochemistry, Chen et al. developed an EMC/DMC carbonate electrolyte with binary salts of LiPF$_6$ and AlF$_3$. It was revealed that the Al anode was protected from dissolving after adding AlF$_3$ into the electrolyte. More notably, AlF$_4^{-}$ complex anions were formed via combination of the dissolved Al^{3+} and F$^-$ in the electrolyte, which deintercalated/intercalated from/into the graphite during discharging/charging together with PF$_6^{-}$. Based on this electrochemistry, the battery exhibited a high average working voltage of 4.0−4.5

V and a high reversible capacity of ~100 mAh g^{-1} along with a high CE of ~99% over 600 cycles.[93] Besides the Al anode, Ca^{2+}/Ca redox chemistry shows promising prospects for rechargeable batteries due to its low polarization and low reduction potential (−2.87 V vs SHE). Unfortunately, Ca-based batteries experience critical issues, including unsuitable electrode materials for reversible Ca^{2+} storage, low working voltages (<2 V), and poor cycle stability, especially at RT. To tackle these issues, Tang et al. designed a new battery configuration by employing graphite as the cathode material and Sn foil as both the anode material and the current collector. With an electrolyte consisting of 0.8 M Ca(PF$_6$)$_2$ in mixed solvents (EC:PC:DMC:EMC = 2:2:3:3 by volume), highly reversible redox reactions incorporating the deintercalation/intercalation of the PF$_6^-$ anion at the cathode and the dealloying/alloying of Ca^{2+} ions at the metal anode were achieved. The resulting DIBs yielded a high discharge voltage of up to 4.45 V and high cycling stability (95% capacity retention over 350 cycles), as displayed in Figure 36a and 36b.[739]

Apart from the F-containing salts, fluorination treatment of other electrolyte components also endows DIBs with unique features such as wide working windows, a wide temperature range, nonflammability, and enhanced electrode|electrolyte compatibility. Read et al. employed a fluorinated solvent and additive in DIBs. The designed 1.7 M LiPF$_6$−FEC/EMC electrolyte with 5 mM tris(hexafluoroisopropyl) phosphate (HFIP) as the additive supported a graphite∥graphite cell with a charge voltage up to 5.2 V, enabling the accommodation of PF$_6^-$ and Li$^+$ at the graphite cathode and the graphite anode simultaneously with a high CE of 97%.[742] Thereafter, the role of FEC on the anion solvation status and the anion insertion/extraction behaviors in DIBs was carefully evaluated by Yang et al.[740] It was revealed that FEC tuned the solvation structures of both Na$^+$ and PF$_6^-$ by replacing part of the original EMC solvent in the solvation shell (Figure 36c and 36d), inducing the formation of a fluorinated CEI film to resist the electrolyte side reactions at high voltages and suppress the expansion of graphitic layers in the cathodes during long-term cycling. The CEI layer on cathodes can also be modified by different salts as additives, as evidenced by the work conducted by Yu et al.[743] With the addition of ~0.5 wt % LiDFOB (with) in the electrolyte, a less resistive Li$_x$BO$_y$F$_z$-enriched CEI layer was constructed on the cathode surface. The LiDFOB salt has a higher HOMO energy level than that of the baseline solvent (EMC), inducing the preferential decomposition of LiDFOB. This robust and durable CEI enabled fast electrode reaction kinetics and achieved an ultrafast charging capability within 2 min. Later, the authors designed an all-fluorinated electrolyte (1 M LiPF$_6$−FEC/FEMC) that synergistically guaranteed a highly stable operation of the DIB up to 5.2 V by generating robust and ion-conductive passivation films on both electrodes to reduce undesired side reactions. More significantly, this fluorinated electrolyte facilitated the fast reaction kinetics of PF$_6^-$ and Li$^+$ at low temperatures, delivering 97.8% reversible capacity at RT, together with ~100% capacity retention over 3000 cycles at 500 mA g^{-1}.[744] The all-fluorinated electrolyte system endows DIBs as a promising choice for wide-temperature applications. In addition to a wide operational temperature range, safety concerns (e.g., fire, explosion, and leakage of toxic electrolyte components) should be given sufficient consideration. Based on the all-fluorinated electrolyte (1 M LiPF$_6$−FEC/FEMC/THE, 1:6:3 by volume), Wang et al.

prepared a GPE via in situ polymerization of diethyl allyl phosphate (DAP) monomer and pentaerythritol tetraacrylate (PETEA) cross-linker.[353] This GPE with a 3D polymer matrix showcased high safety features (e.g., nonflammability), sufficient ionic conductivity (1.99 mS cm^{-1}), superior stability up to 5.5 V (vs. Li/Li$^+$), and high compatibility toward both electrodes.

To tackle concerns of cost, eco-friendliness, and safety caused by organic electrolytes, aqueous or hybrid aqueous/nonaqueous electrolytes have emerged as a highly interesting alternative for promoting practical applications of DIBs. Particularly, the pioneering work by Xu et al. proposed the concept of "water-in-salt" (WiS) electrolyte, which significantly enlarged the ESW of aqueous electrolytes from 1.23 to ~4.9 V.[135,745] Encouraged by this widely adopted strategy in aqueous metal-ion batteries, especially in LIBs, a WiS electrolyte formulated with 21 M LiTFSI in aqueous electrolyte H$_2$O was combined with 9.25 M LiTFSI−DMC (mass ratio 1:1) nonaqueous electrolyte by Placke et al.[746] This hybrid electrolyte not only guaranteed adequate safety with the nonflammable feature from the WiS aqueous electrolyte but also protected the anode from side reactions by forming a stable SEI with the assistance of the nonaqueous component. Therefore, a stage-2 graphite intercalation compound (GIC) for TFSI$^-$ intercalation was achieved in aqueous-based electrolytes. Afterward, an aqueous WiS consisting of 20 m NaFSI and 0.5 m Zn(TFSI)$_2$ was developed by Placke et al. in a Zn∥graphite DIB.[747] The role of the high-concentration NaFSI salt was to reduce the free water molecules in the WiS electrolyte and to suppress the occurrence of the oxygen evolution reaction (OER). It was interesting to note that instead of the cointercalation of FSI$^-$ and TFSI$^-$, TFSI$^-$ anions were proved to predominantly undergo the intercalation process into the graphite layers, which was associated with its lower intercalation barrier. Benefiting from this advanced electrolyte design, the consequent Zn∥graphite DIB exhibited a high working voltage of ~2.3−2.5 V and a high reversible capacity of ~110 mAh g^{-1} with >80% capacity retention after 200 cycles.

Besides its beneficial effects on electrolyte optimization, the fluorine element can also be introduced to the cathode material to boost and stabilize anion intercalations. It is generally known that with strong electronegativity, a low van der Waals radius, and low polarizability properties, F is considered to have the ability to tune the photoelectric properties of conducting conjugated polymers such as PANI.[741] Based on these merits, a novel fluoridized−polyaniline−H$^+$/CNT composite (FPHC) has been developed as the cathode material for DIBs. The introduction of F effectively reduced the energy gap between the HOMO and the LUMO (Figure 36e), thus enabling highly efficient storage of anions in the FPHC cathode. This result was further reflected by the higher electronic conductivity of 0.162 S cm^{-1} compared with the nonfluorinated PHC cathode (0.138 S cm^{-1}). In addition, the combinative formation of PF$_6^-$ anion in the FPHC cathode was verified, suggesting that F$^-$ of the PF$_6^-$ anion tended to form a stable covalent bond with −NH in FPHC and thus exhibiting a symmetric structure of the whole PF$_6^-$−FPHC molecule, as shown in Figure 36f. This fluoridized treatment guaranteed a stable cycling of 2000 times at 2 A g^{-1} with a retained discharge capacity of 73 mAh g^{-1} along with a high power density of 7720 W kg^{-1} at an energy density of 310 Wh kg^{-1}.[741]
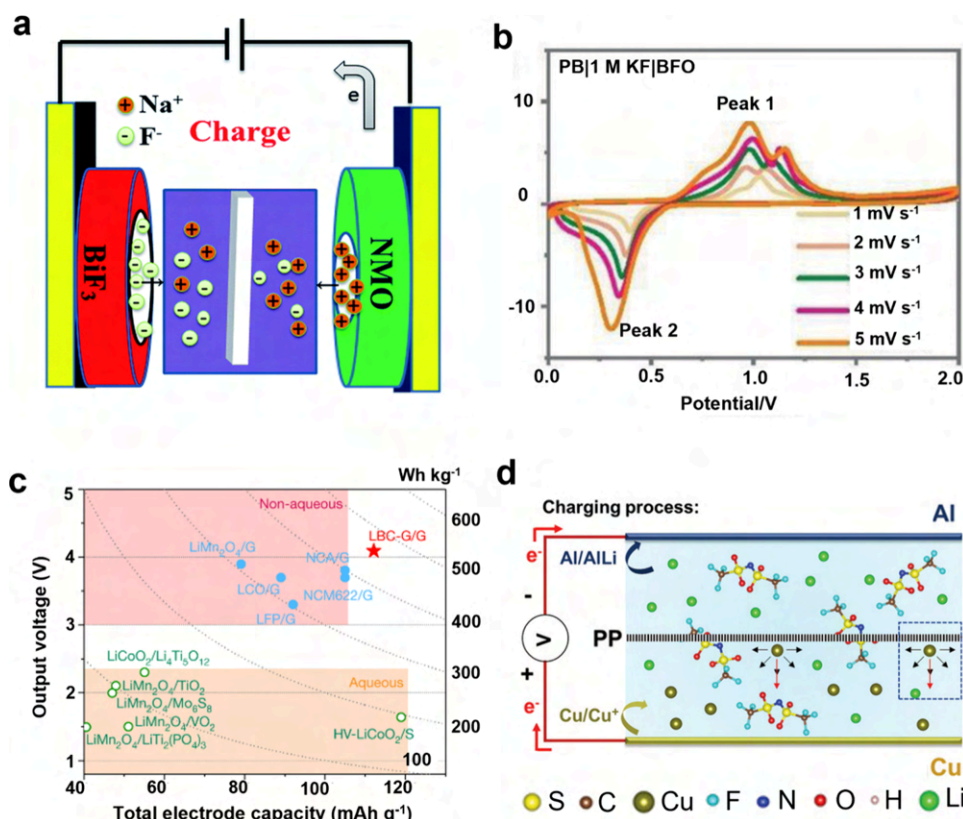
Figure 37. Beneficial effects of fluorine on the RDIB and beyond battery chemistries. (a) Schematics of the aqueous $BiF_3Na_{0.44}$||MnO_2 RDIB based on the F^- anion and Na^+ cation electrochemistry during the charging process. Reproduced with permission from ref 748. Copyright 2018 Royal Society of Chemistry. (b) Voltage curves of the RDIB with BF and modified BFO anode material at 1 A g^{-1}. Reproduced with permission from ref 589. Copyright 2021 Wiley-VCH. (c) Energy density of the highly fluorinated HFE/PEO-protected graphite||$(LiBr)_{0.5}(LiCl)_{0.5}C_{\sim3.7}$ full cell with an aqueous gel electrolyte compared with various state-of-the-art commercial and experimental Li-ion chemistries using nonaqueous (blue circles) and aqueous (green circles) electrolytes. Note: all energy densities were converted using the total weight of the cathode and the anode. Reproduced with permission from ref 749. Copyright 2019 Springer Nature. (d) Schematic diagram of the 3 V Al||Cu battery in 3 M LiTFSI−FEC electrolyte with a PP membrane. Reproduced with permission from ref 750. Copyright 2020 Wiley-VCH.

In addition to the above-mentioned DIBs, another emerging battery system also based on both cations and anions as charge carriers for electrochemical reactions is called RDIBs, except that the sequence of the anion- and cation-storage chemistries is flipped between the cathode and the anodes. To date, the RDIB chemistries have been only realized in aqueous electrolytes. In 2018, Hou et al. developed a novel RDIB relying on F^- anion and Na^+ cation electrochemistry, which was comprised of a 0.8 M NaF aqueous solution as the electrolyte, $Na_{0.44}MnO_2$ as the cathode material, and BiF_3 as the anode material.[748] During the charge process, the BiF_3 anode released F^- ions and the $Na_{0.44}MnO_2$ cathode deintercalated Na^+ ions to the aqueous electrolyte simultaneously. During the discharge process, the F^- ions in the electrolyte were captured by the anode to obtain BiF_3 and the Na^+ ions were intercalated into the cathode material as well (Figure 37a). This RDIB delivered a high discharge capacity of ~123 mAh g^{-1} at a current density of 100 mA g^{-1} based on the mass of BiF_3 anode materials. However, the capacity deteriorated very rapidly to 47.28 mAh g^{-1} over just 40 cycles, which was probably due to the instability of the anode material. An obvious volume change of the anode material was observed during cycling, i.e., 57.3% volume contraction for the phase transition from BiF_3 into Bi and a large volume expansion of 134.0% for the reverse transition from Bi to BiF_3. Therefore, strategies such as structure modifications or surface

coatings should be explored to enhance the cycling stability of the Bi/BiF_3 electrode. Afterward, another RDIB was designed by Li et al. (Figure 37b) utilizing KF aqueous electrolyte, Prussian blue (PB) cathode material, and $BiF_3@Bi_7F_{11}O_5@$ reduced graphene oxide (BFO) anode material.[589] It was elucidated that the low electrolyte concentration improved the cycle stability of the BFO||PB RDIB despite the reduced discharge capacity. The reduction of F^- ions in the dilute electrolytes suppresses the dissolution of Bi^{3+} ions generated upon the discharge process, reducing the deposition of the side products on the electrode surface. In addition, this Bi^{3+} dissolution phenomenon can also be mitigated by the graphene coating on the surface of the BFO anode material. The resulting F/K-based RDIB achieved a high discharge capacity of 218 mAh g^{-1} at 1 A g^{-1} as well as fast rate capability with a capacity retention of 47% at a high current density of 5 A g^{-1}, which were calculated based on the weight of the BFO anode material.

Interestingly, Wang et al. demonstrated a novel conversion−intercalation chemistry based on the sequential intercalation of Br^- and Cl^- into a composite cathode consisting of $(LiBr)_{0.5}(LiCl)_{0.5}C_{\sim3.7}$ (LBC-G) using a highly concentrated "water-in-bisalt" aqueous gel electrolyte. Benefiting from the formed hydrated LiBr/LiCl layer ($LiBr \cdot 0.34H_2O - LiCl \cdot 0.34H_2O$) by extracting water from the electrolyte, the LBC-G surface was separated from the electrolyte accordingly. Upon
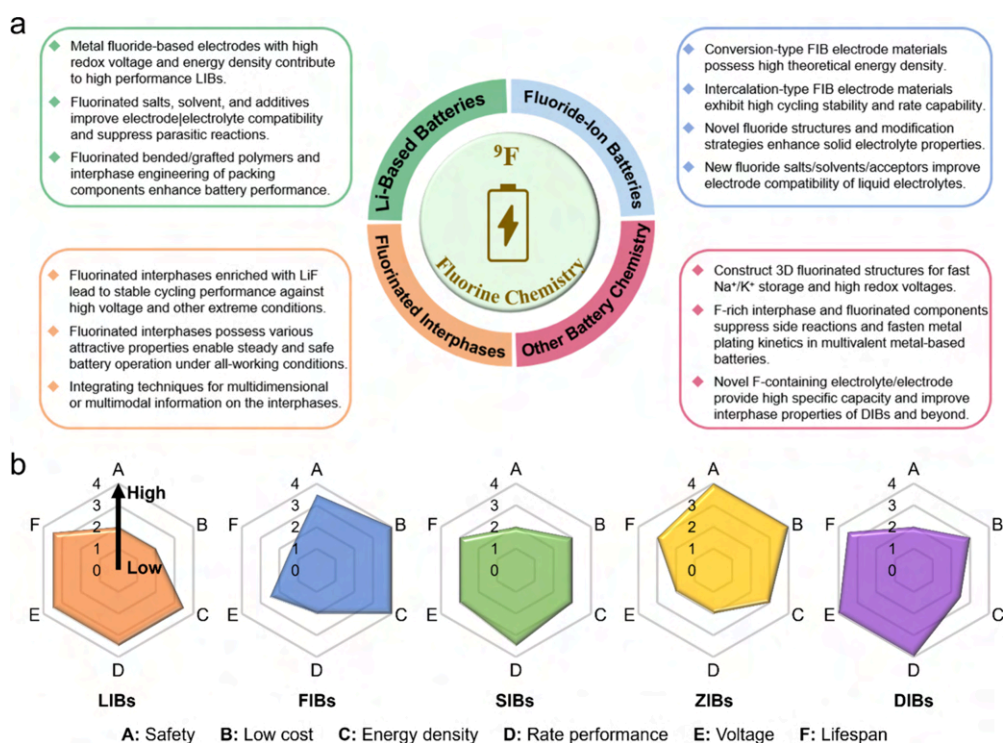
Figure 38. Fluorine chemistry in rechargeable batteries. (a) Strategies and prospects of fluorine chemistry in rechargeable batteries. (b) Radar diagrams of various batteries based on six parameters: (A, safety; B, low cost; C, energy density; D, rate performance; E, voltage; F, lifespan.

charging, the Br^- within the hydration layer was first oxidized to Br_0 and then intercalated into the graphite. As the charging process continued, the oxidation and intercalation of Cl^- occurred, leading to a mixed intercalation compound. This unique mechanism contributed to a stage-1 GIC, which accounted for a high reversible capacity of 243 mAh g^{-1} at a high average voltage of 4.2 V vs Li^+/Li. When coupled with a highly fluorinated ether (i.e., HFE)/PEO-protected graphite anode, the 4 V class full cell achieved a high energy density of 460 Wh kg^{-1} (calculated based on the total weight of the cathode and anode, Figure 37c) along with a CE of ~100%.[749]

It can be reasonably concluded that anion-hosting cathode materials generally provide limited theoretical capacities, requiring the exploration of new cathode chemistry to enhance the energy density of the battery systems.[751] Along this line, Yu et al. proposed a novel metal−metal system that uses Cu and Al metal foils directly as the cathode and anode, respectively.[750] The electrochemical reactions proceed via the stripping/plating of Cu at the cathode and the alloying/dealloying of AlLi at the anode (Figure 37d). However, the Cu^+ ions inevitably shuttled from the cathode to the anode, causing severe self-discharge and low CE during cycling. By utilizing 3 M LiTFSI−FEC electrolyte, they disclosed that Cu^+ ions were bound by FEC and $TFSI^-$ to form the solvation complex, which prevented the Cu^+ ions from transporting through the PP membrane due to high interfacial tension between the FEC molecules and the membrane. The blocking effect by FEC contributed to a stable operation of the 3 V Al‖Cu battery for more than 1000 cycles. For comparison, a Li‖Cu battery was designed by Ji et al. with a different operation mechanism.[751] Upon charging, Cu was oxidized to Cu^{2+} to precipitate as copper(II) bis(trifluoromethane sulfonyl)imide ($Cu(TFSI)_2$) on the cathode; meanwhile, Li^+ was plated on the Li anode. During the discharge process, Cu^{2+} was first reduced to Cu^+ and continuously reduced to Cu, while the anode strips into Li^+. An anion exchange membrane was placed between the two electrodes to prohibit the crossover of cations during charging. Besides, the catholyte//anolyte concentration was regulated to 2 m//6 m for mitigating the negative concentration gradient of $TFSI^-$, therefore utilizing the Cu capacity and suppressing Cu^{2+}/Cu^+ crossover. Although a high reversible capacity of 762 mAh g^{-1} was enabled at an average discharge voltage of 3.2 V vs Li^+/Li, the solubility of charged product $Cu(TFSI)_2$ leads to unsatisfactory reversibility, the heavy $TFSI^-$ as counterions limits the battery energy density, and the usage of AEM increases the cost of the battery system.

Overall, anion insertion with F-containing groups is crucial for DIB/RDIB performance, whereas no existing anion is ideal for satisfying the high energy density, fast charging rate, long lifespan, and low cost simultaneously. Further research should explore novel anions toward higher theoretical specific capacity and energy density of DIBs and RDIBs. Besides, fluorination of the electrolyte components can endow DIBs with broad ESW, wide temperature range, nonflammability, and improved electrode‖electrolyte compatibility. Moreover, though RDIB chemistry can be realized in KF and NaF aqueous electrolytes, the rapid capacity deterioration associated with incompatible electrode materials remains a significant obstacle, requiring further exploration of F-containing salts and novel organic electrolytes to construct protective and robust interphases.

6. CONCLUSIONS AND OUTLOOK

Taking advantage of the extraordinary electronegativity, low atomic weight, small ionic size, natural abundance, and low cost of fluorine, fluorine chemistry has significantly advanced rechargeable battery technology. However, atomic-level insights into fluorine chemistry remain underexplored, especially under extreme conditions, and are not fully understood. This

review summarizes the state-of-the-art research and technical achievements in fluorine-containing materials/interphases for metal ion-batteries, FIBs, DIBs, and beyond (Figure 38a). Specifically, fluorine chemistry can address challenges in various battery materials, including poor intrinsic conductivity and severe structure deterioration during conversion reactions, large volume change and low redox potential during intercalation reactions, safety issues related with anode materials, insufficient chemical/electrochemical stability and/or low ionic conductivity for electrolytes, and performance restrictions of other battery components. This review highlights the pivotal role of fluorinated interphases, material structure−performance relationships, and cutting-edge techniques for probing fluorine chemistry. From a fundamental and practical perspective, the promising research directions to enhance the benefits of fluorine chemistry in rechargeable batteries can be identified as the following five aspects.

6.1. Addressing the Instinctively Low Electrochemical Kinetics of Conversion-Type Metal Fluoride-Based Cathodes

First, systematic studies on the redox mechanisms and structural evolution are essential for a deeper understanding of these cathodes. Theoretical studies on these materials are limited to simple metal fluorides such as FeF_2 and CuF_2. The expanding research of metal fluoride-based cathodes via theoretical simulation and heterometal modification will achieve structurally stable metal fluoride-based cathodes with rapid ion diffusion, which is promising for practical applications. Moreover, the low mass loadings and areal capacities of reported metal fluoride-based cathodes hinder a comprehensive evaluation of their energy density and cycling performance compared to conventional LIB cathodes. Therefore, developing high-loading metal fluoride-based cathodes with increased areal capacities is a priority. In parallel, fluorine chemistry can enhance conventional LIB cathodes such as layered oxides, through F substitution, F doping, and surface fluorination, improving the cycling stability and energy density of the cathodes and providing insights for the development of high-performance LIBs.

6.1.1. Striking a Balance between Electrochemical Performance, Stability, and Environmental Considerations for Optimizing F Substitution/Modification in Battery Components.
The electrolytes for high-performance Li-based batteries can be tailored by combining the benefits of different partially fluorinated/per-fluorinated electrolytes. Future design for Li salts should focus on integrating functional groups with complementary roles for enhanced overall performance. Fluorinated solvents and cosolvents display unique physicochemical properties due to the high electronegativity, high ionic potential, and low polarizability of fluorine. Partial fluorination or optimization of the fluorination positions can be applied to develop single-solvent electrolytes. In parallel, introducing per-fluorinated cosolvent into non-fluorinated solvents for multisolvent electrolytes is also viable.

Fluorine can also be utilized to modify and functionalize battery separators, enhancing fire retardancy, preventing potential mechanical abuse, and also promoting the formation of a LiF-enriched SEI. Regarding battery binders, fluorine groups can be incorporated into polymer backbones, while fluorinated anions can be combined with ionic conductive polymers, enabling higher ion transfer, greater resistance to electrochemical oxidation, and enhanced thermal stability.

Especially, a fluorinated cross-linked network binder should be designed for alloy-type anodes, where massive fluorine groups improve the mechanical features while chemical/physical cross-linking maintains the electrode structures against volume changes. However, excessive fluorine content may lead to a decay in the electrode performance. Furthermore, current collectors can be modified by fluorinated carbon materials, lithiophilic metal fluoride coatings, F-containing interlayers, etc., which regulate Li deposition and enhance interphasial stability. However, the environmental issues brought by F substitution/modification must be taken seriously. Fluorinated compounds in prevalent battery components (e.g., LiTFSI, PVDF, and PTFE), which contain CF_3 or $−CF_2−$ groups, are under consideration for prohibition under European Union regulations. Therefore, optimization of F substitution/modification in battery components should be scrutinized to strike a balance between electrochemical performance, stability, and environmental considerations.[128]

6.2. Tailoring Fluorinated Interphases for Li-Based Batteries at All Working Conditions

The efficient operation of Li-based batteries especially under extreme conditions relies highly on the stability of interphases, including chemical stability, electrochemical stability, mechanical stability, and thermal stability. Interdisciplinary research should be encouraged to reveal the chemical nature of the SEI/CEI. Considering that the low Li^+ conductivity of LiF ($\sim10^{-12}$ S cm^{-1}) restricts the high-rate performance, other fluorinated conducting components (e.g., $Li_xPO_yF_z$) should be incorporated into LiF-rich interphases. A polymer-based organic SEI matrix can also be combined with fluorinated components to accommodate the large volume change of the Li anodes. Besides, a LiF-rich CEI possessing excellent electrochemical stability can effectively protect high-voltage cathodes. Although the LiF-enriched SEI displays low interphase impedance/charge transfer resistance and high stability for facilitating low-temperature operation, the LiF effects on the CEI at low temperatures remain a subject of debate. Further investigation is needed to deeply understand the macroscopic and microscopic properties of LiF, especially the roles and factors (e.g., the distribution, particle size, and formation approach) affecting the performance of Li-based batteries under extreme conditions.

6.2.1. Unlocking Fundamental Issues Regarding Chemical Compositions, Spatial Distributions, and Realistic Structures of the Interphases.
Nondestructive and/or in situ/operando techniques (e.g., cryo-TEM, operando EQCM, in situ XPS, liquid TOF-SIMs, in situ NMR, and synchrotron-based XRD) are imperative for real-time, dynamic, and intuitive investigations of the structural, morphological, and chemical characteristics of interphases and their correlations with the battery performance. Therefore, suitable electrochemical cells for in situ operations should be carefully designed as different cell configurations can cause inconsistent and even misleading results. An integrated approach with complementary techniques is highly desirable for obtaining multidimensional and/or multimodal insights into interphases, facilitating the elucidation of the structure−property relationships and guiding the design of stable interphases.

6.3. Revolution of the Electrode and Electrolyte Materials for High Energy Density and Cycling Stability FIBs

The volume change and polarization issues of conversion-type electrode materials should be solved by reducing the particle size and constructing the conductive network, seeking for high-capacity intercalation-type electrode materials via theoretical screening and experimental verification, and preventing the fluorination of conductive additive through the carbon stabilization process. In parallel, to advance the development of F$^-$ conducting solid-state electrolytes, novel fluoride structures and modification strategies, such as creating point defects, introducing F vacancies, and optimizing synthesis methods, are highly required. For liquid electrolytes, it is essential to explore novel fluoride salts, solvents, and suitable anion/cation acceptors to facilitate the dissociation of fluoride salts. Furthermore, the "water-in-salt" strategy exhibits great prospect in expanding the ESW, suppressing the active material dissolutions, and addressing HF formation in aqueous electrolytes.

6.4. Establishing Fluorinated Material−Function Relationships To Boost SIB/PIB Performance

In SIBs, the development of F-based electrodes is shifted toward 3D fluorinated phases. An in-depth investigation is necessary to regulate the structure and phase transitions to mitigate volume changes and to elucidate the structure−performance correlations, thereby reducing the activation energy barrier and band-gap energy for efficient Na$^+$ diffusion. As for PIBs, surface modifications of potassium fluorophosphate compounds are necessary to improve both the electron and the K$^+$ transport. Besides, the fluorine to oxygen ratio should be carefully controlled to prevent disordered structures of fluorosulfates that suppresses the K$^+$/vacancy formation and decreases the reversible K$^+$ storage capacity. Moreover, F doping can improve the surface disorder of carbonaceous anode materials, creating large amounts of surface defects to facilitate Na$^+$/K$^+$ adsorption. As for electrolyte developments in SIBs/PIBs, strategies from Li-based batteries are not directly applicable due to potential adverse effects (e.g., FEC). Notably, fluorine chemistry facilitates the discovery of novel conducting salts with wide ESW, film-forming ability, and fast ionic transport. However, the molecular structure−function relationships of the fluorinated components remain unclear, necessitating targeted molecular selection. Further efforts should be focused on the challenging aspects of fluorinated interphases to optimize their properties.

6.5. Exploring the Potential of F-Containing Materials for Other Battery Chemistries

Challenges including the insufficient energy density of existing electrodes, the sluggish plating/stripping dynamics kinetics of a metallic anode, and the poor stability of the electrolyte/electrode interphase hinder the utilization of multivalent metal-based batteries with attractive advantages (e.g., low cost and high energy density). Fluorine chemistry is important for seeking suitable F-containing electrode materials as well as providing a deep understanding of the construction of a F-involved SEI film, which could positively or negatively affect the battery performance. As for DIBs/RDIBs, novel anions with smaller sizes and higher antioxidative stability as well as multivalent anions with more charge numbers can potentially provide high theoretical specific capacity and energy density. Though fluorination treatment of the electrolyte components can endow DIBs with enhanced performance, the fundamental

role of these fluorinated components in the anion solvation, the relationship between fluorinated CEI features (e.g., chemical components, micro/nanostructures, mechanical properties), and battery performance remain unclear. Furthermore, other battery chemistries necessitate the exploration of F-containing salts and novel electrolytes to construct protective and robust interphases.

The high-temperature sintering of inorganic materials containing the fluorine element is potentially detrimental to the furnace, impeding its scalability for large-scale synthesis. Thus, alternative soft chemical synthesis methods such as low-temperature solid-phase synthesis, chemical transfer synthesis, and solvent thermal synthesis should be developed for preparing F-containing cathode and solid-state electrolyte materials in the future. Overall, significant breakthrough progress has been achieved by utilizing fluorine chemistry in rechargeable batteries. Although traditional lithium-ion batteries maintain a leading position in overall performance due to decades of research, other alternative battery systems also demonstrate significant advantages in specific aspects (Figure 38b). Thus, expanding fluorine chemistry research into these areas is expected to accelerate the application of these rising battery systems. Nonetheless, the ongoing development of fluorine chemistry is bringing many scientific and technical challenges, leaving substantial investigation room for its future applications. Thus, researchers are highly encouraged to unlock the fundamental role of fluorine chemistry in addressing the obstacles for various types of battery materials, thus promoting the widespread effectuation of fluorine chemistry in rechargeable batteries. More significantly, we hope this review can raise interest and provide key insights into the further development of fluorine chemistry for high-performance rechargeable batteries.

AUTHOR INFORMATION

Corresponding Authors

Baohua Li − *Tsinghua Shenzhen International Graduate School, Tsinghua University, Shenzhen 518055, P. R. China;* orcid.org/0000-0001-5559-5767; Email: libh@sz.tsinghua.edu.cn

Dong Zhou − *Tsinghua Shenzhen International Graduate School, Tsinghua University, Shenzhen 518055, P. R. China;* orcid.org/0000-0002-2578-7124; Email: zhou.d@sz.tsinghua.edu.cn

Chunsheng Wang − *Department of Chemical and Biomolecular Engineering, University of Maryland, College Park, Maryland 20742, United States;* orcid.org/0000-0002-8626-6381; Email: cswang@umd.edu

Guoxiu Wang − *Centre for Clean Energy Technology, School of Mathematical and Physical Sciences, Faculty of Science, University of Technology Sydney, Sydney, New South Wales 2007, Australia;* orcid.org/0000-0003-4295-8578; Email: Guoxiu.Wang@uts.edu.au

Authors

Yao Wang − *Tsinghua Shenzhen International Graduate School, Tsinghua University, Shenzhen 518055, P. R. China*

Xu Yang − *Centre for Clean Energy Technology, School of Mathematical and Physical Sciences, Faculty of Science, University of Technology Sydney, Sydney, New South Wales 2007, Australia*

Yuefeng Meng − *Tsinghua Shenzhen International Graduate School, Tsinghua University, Shenzhen 518055, P. R. China*

Zuxin Wen − *Tsinghua Shenzhen International Graduate School, Tsinghua University, Shenzhen 518055, P. R. China*

Ran Han − *Tsinghua Shenzhen International Graduate School, Tsinghua University, Shenzhen 518055, P. R. China*

Xia Hu − *Tsinghua Shenzhen International Graduate School, Tsinghua University, Shenzhen 518055, P. R. China*

Bing Sun − *Centre for Clean Energy Technology, School of Mathematical and Physical Sciences, Faculty of Science, University of Technology Sydney, Sydney, New South Wales 2007, Australia;* ⦿ orcid.org/0000-0002-4365-486X

Feiyu Kang − *Tsinghua Shenzhen International Graduate School, Tsinghua University, Shenzhen 518055, P. R. China*

Complete contact information is available at:
https://pubs.acs.org/10.1021/acs.chemrev.3c00826

Author Contributions

[†]Y.W., X.Y., and Y.M.: These authors contributed equally. The manuscript was written through contributions of all authors. All authors have given approval to the final version of the manuscript. CRediT: Yao Wang, Xu Yang, and Yuefeng Meng: investigation, mechanisms, writing—original draft. Zuxin Wen, Ran Han, Xia Hu, and Bing Sun: methodology, validation, editing. Baohua Li, Dong Zhou, Chunsheng Wang, and Guoxiu Wang: conceptualization, project administration, supervision, writing—original draft, writing—review and editing.

Notes

The authors declare no competing financial interest.

Biographies

Yao Wang is currently a postdoctoral researcher at Tsinghua Shenzhen International Graduate School, Tsinghua University (China). She received her Ph.D. degree from City University of Hong Kong (CityU) in 2021. Her research mainly focuses on designing electrolyte systems and investigating electrode|electrolyte interphases for high-voltage and low-cost rechargeable batteries.

Xu Yang is currently a Ph.D. student in the Centre for Clean Energy Technology at the University of Technology Sydney (UTS). He received his B.Sc. (2017) and M.Sc. (2019) degrees at the Harbin Institute of Technology. His research interests focus on the development of low-cost rechargeable batteries and all-solid-state lithium-ion batteries.

Yuefeng Meng received her B.Sc. (2018) and M.Sc. (2023) degrees majoring in Materials Science and Engineering at Tsinghua University (China). Her current research interests include safe electrolyte design and interphase chemistry for high-voltage lithium metal batteries.

Zuxin Wen is currently a Ph.D. student at Tsinghua Shenzhen International Graduate School, Tsinghua University (China). He received his B.Sc. (2020) and M.Sc. (2023) degrees at Central South University. His research interests focus on the development of low-cost rechargeable batteries and all-solid-state lithium-ion batteries.

Ran Han received his B.Sc. (2020) degree at Hefei University of Technology and M.Sc. (2023) degree at Shanghai University. His research interests focus on the development of low-temperature rechargeable batteries and aqueous batteries.

Xia Hu is currently a Ph.D. student at Tsinghua Shenzhen International Graduate School, Tsinghua University (China). She obtained her B.Sc. (2015) and M.Sc. (2018) degrees from Central South University. Her research is currently centered on the development of solid-state lithium-based batteries and the associated critical materials.

Bing Sun received his Ph.D. degree in 2012 at the University of Technology Sydney (UTS), Australia. Currently, he is a senior lecturer in the Centre for Clean Energy Technology at the UTS. His research interests focus on the development of next-generation battery materials and technology for lithium-based batteries and sodium-based batteries. He is the recipient of the Australian Research Council (ARC) Discovery Early Career Researcher Award and the ARC Future Fellowship.

Feiyu Kang is a full professor in the Department of Materials Science and Engineering and also a dean in the Graduate School at Shenzhen, Tsinghua University (China). He received his Ph.D. degree from Hong Kong University of Science and Technology (HKUST). His research focuses on nanocarbon materials, graphite, thermal conductive materials, lithium-ion batteries, supercapacitors, electric vehicles, porous carbon and adsorption, indoor air clearing, and water purification. He has published more than 630 refereed journal papers. His publications have attracted over 77 000 citations with an h-index of 143 (Google Scholar). He was ranked as the Global Highly Cited Researchers (top 1% by citation) by Clarivate Analytics in 2018−2023.

Baohua Li is currently a full professor and director of the Division of Energy and Environment at Tsinghua Shenzhen International Graduate School, Tsinghua University (China). He received his Ph.D. degree from the Institute of Coal Chemistry (ICC), Chinese Academy of Sciences (CAS) in 2003. His research interests focus on carbon materials for energy storage, such as electrode materials for supercapacitors and lithium-ion batteries. He has published more than 290 refereed journal papers. His publications have attracted over 38 000 citations with an h-index of 104 (Google Scholar). He was ranked as the World's Top 2% Scientist by Stanford University in 2021. He is also the director of the Advanced Battery and Material Engineering Research Center of Guangdong and a member of the Academic Committee of Guangdong Key Laboratory of Thermal Management Engineering and Materials.

Dong Zhou is currently an assistant professor and Ph.D. supervisor at Tsinghua Shenzhen International Graduate School, Tsinghua University (China). He received his Ph.D. degree from Tsinghua University in 2017 and then worked as a postdoctoral research associate in the University of Technology Sydney, Australia and the University of Tokyo, Japan. His research mainly focuses on the design and synthesis of specialized solid polymer electrolytes and nano-electrode materials for various advanced energy storage devices and investigation of the interfacial mechanisms. As first/corresponding author, his research has resulted in more than 30 refereed journal articles with a total citation of over 7200 (Google Scholar). He is the recipient of the First Prize of Guangdong Natural Science in 2020, the Discovery Early Career Researcher Award (DECRA), and the Japan Society for the Promotion of Science (JSPS) Fellowship.

Chunsheng Wang is a Robert Franklin and Frances Riggs Wright Distinguished Chair Professor in the Chemical & Biomolecular Engineering, Department of Chemistry and Biochemistry, at the University of Maryland. He is an associate editor of *ACS Applied Energy Materials* and UMD Director of the UMD-ARL Center for Research in Extreme Battery. His research focuses on reachable batteries and fuel cells. He has published more than 340 refereed journal papers. His publications have attracted over 70 000 citations with an h-index of 138 (Google Scholar). He was ranked as the Global Highly Cited Researchers (top 1% by citation) by Clarivate Analytics in 2018−2023.

Guoxiu Wang is the Director of the Centre for Clean Energy Technology and a Distinguished Professor at the University of

Technology Sydney (UTS), Australia. Currently, he serves as an associate editor for *Electrochemical Energy Reviews* (Springer-Nature) and *Energy Storage Materials* (Elsevier). His research interests include lithium-ion batteries, lithium−air batteries, sodium-ion batteries, lithium−sulfur batteries, supercapacitors, fuel cells, 2D materials such as graphene and MXenes, and electrocatalysis for hydrogen production. He has published more than 680 refereed journal papers. His publications have attracted over 75 000 citations with an h-index of 150 (Google Scholar). He has been recognized as a highly cited researcher in Chemistry and Materials Science by the Web of Science/Clarivate Analytics. He is an elected fellow of the European Academy of Sciences (EurASc), a fellow of the International Society of Electrochemistry (ISE), and a fellow of the Royal Society of Chemistry (RSC).

REFERENCES

(1) Whittingham, M. S. Lithium Batteries and Cathode Materials. *Chem. Rev.* **2004**, *104*, 4271−4301.

(2) Dunn, B.; Kamath, H.; Tarascon, J. M. Electrical Energy Storage for the Grid: A Battery of Choices. *Science* **2011**, *334*, 928−935.

(3) Schmuch, R.; Wagner, R.; Hörpel, G.; Placke, T.; Winter, M. Performance and Cost of Materials for Lithium-Based Rechargeable Automotive Batteries. *Nat. Energy* **2018**, *3*, 267−278.

(4) Blomgren, G. E. The Development and Future of Lithium Ion Batteries. *J. Electrochem. Soc.* **2017**, *164*, A5019−A5025.

(5) Bigelow, L. A. The Action of Elementary Fluorine upon Organic Compounds. *Chem. Rev.* **1947**, *40*, 51−115.

(6) Groult, H.; Lantelme, F.; Salanne, M.; Simon, C.; Belhomme, C.; Morel, B.; Nicolas, F. Role of Elemental Fluorine in Nuclear Field. *J. Fluor. Chem.* **2007**, *128*, 285−295.

(7) Dolbier, W. R. Fluorine Chemistry at the Millennium. *J. Fluor. Chem.* **2005**, *126*, 157−163.

(8) Gardiner, J. Fluoropolymers: Origin, Production, and Industrial and Commercial Applications. *Aust. J. Chem.* **2015**, *68*, 13.

(9) Xiao, A. W.; Galatolo, G.; Pasta, M. The Case for Fluoride-Ion Batteries. *Joule* **2021**, *5*, 2823−2844.

(10) *CRC Handbook of Chemistry and Physics: A Ready-Reference of Chemical and Physical Data*, 85th ed.; Lide, D. R., Ed. (National Institute of Standards and Technology); CRC Press LLC: Boca Raton, FL, 2004; pp 2712.

(11) *Mineral Commodity Summaries 2021*; U.S. Geological Survey: Reston, VA, 2021, DOI: 10.3133/mcs2021.

(12) Goodenough, J. B.; Kim, Y. Challenges for Rechargeable Li Batteries. *Chem. Mater.* **2010**, *22*, 587−603.

(13) Najib, S.; Erdem, E. Current Progress Achieved in Novel Materials for Supercapacitor Electrodes: Mini Review. *Nanoscale Adv.* **2019**, *1*, 2817−2827.

(14) Ben Yahia, M.; Vergnet, J.; Saubanere, M.; Doublet, M. L. Unified Picture of Anionic Redox in Li/Na-Ion Batteries. *Nat. Mater.* **2019**, *18*, 496−502.

(15) Hu, E.; Yu, X.; Lin, R.; Bi, X.; Lu, J.; Bak, S.; Nam, K.-W.; Xin, H. L.; Jaye, C.; Fischer, D. A.; et al. Evolution of Redox Couples in Li- and Mn-Rich Cathode Materials and Mitigation of Voltage Fade by Reducing Oxygen Release. *Nat. Energy* **2018**, *3*, 690−698.

(16) Yan, P.; Zheng, J.; Liu, J.; Wang, B.; Cheng, X.; Zhang, Y.; Sun, X.; Wang, C.; Zhang, J.-G. Tailoring Grain Boundary Structures and Chemistry of Ni-Rich Layered Cathodes for Enhanced Cycle Stability of Lithium-Ion Batteries. *Nat. Energy* **2018**, *3*, 600−605.

(17) Akhilash, M.; Salini, P. S.; John, B.; Mercy, T. D. A Journey through Layered Cathode Materials for Lithium Ion Cells - from Lithium Cobalt Oxide to Lithium-Rich Transition Metal Oxides. *J. Alloys Compd.* **2021**, *869*, 159239.

(18) Akhilash, M.; Salini, P. S.; Jalaja, K.; John, B.; Mercy, T. D. Synthesis of $Li_{1.5}Ni_{0.25}Mn_{0.75}O_{2.5}$ Cathode Material via Carbonate Co-precipitation Method and Its Electrochemical Properties. *Inorg. Chem. Commun.* **2021**, *126*, 108434.

(19) Kim, T.; Song, W.; Son, D.-Y.; Ono, L. K.; Qi, Y. Lithium-Ion Batteries: Outlook on Present, Future, and Hybridized Technologies. *J. Mater. Chem. A* **2019**, *7*, 2942−2964.

(20) Cheng, X.-B.; Zhao, C.-Z.; Yao, Y.-X.; Liu, H.; Zhang, Q. Recent Advances in Energy Chemistry between Solid-State Electrolyte and Safe Lithium-Metal Anodes. *Chem.* **2019**, *5*, 74−96.

(21) Wang, H.; Yu, D.; Kuang, C.; Cheng, L.; Li, W.; Feng, X.; Zhang, Z.; Zhang, X.; Zhang, Y. Alkali Metal Anodes for Rechargeable Batteries. *Chem.* **2019**, *5*, 313−338.

(22) Zhang, J. G.; Xu, W.; Xiao, J.; Cao, X.; Liu, J. Lithium Metal Anodes with Nonaqueous Electrolytes. *Chem. Rev.* **2020**, *120*, 13312−13348.

(23) Wei, C.; Tan, L.; Tao, Y.; An, Y.; Tian, Y.; Jiang, H.; Feng, J.; Qian, Y. Interfacial Passivation by Room-Temperature Liquid Metal Enabling Stable 5 V-class Lithium-Metal Batteries in Commercial Carbonate-Based Electrolyte. *Energy Storage Mater.* **2021**, *34*, 12−21.

(24) Hobold, G. M.; Lopez, J.; Guo, R.; Minafra, N.; Banerjee, A.; Shirley Meng, Y.; Shao-Horn, Y.; Gallant, B. M. Moving beyond 99.9% Coulombic Efficiency for Lithium Anodes in Liquid Electrolytes. *Nat. Energy* **2021**, *6*, 951−960.

(25) Zou, P.; Sui, Y.; Zhan, H.; Wang, C.; Xin, H. L.; Cheng, H. M.; Kang, F.; Yang, C. Polymorph Evolution Mechanisms and Regulation Strategies of Lithium Metal Anode under Multiphysical Fields. *Chem. Rev.* **2021**, *121*, 5986−6056.

(26) Tan, S. J.; Wang, W. P.; Tian, Y. F.; Xin, S.; Guo, Y. G. Advanced Electrolytes Enabling Safe and Stable Rechargeable Li-Metal Batteries: Progress and Prospects. *Adv. Funct. Mater.* **2021**, *31*, 2105253.

(27) Li, X.; Zhao, R.; Fu, Y.; Manthiram, A. Nitrate Additives for Lithium Batteries: Mechanisms, Applications, and Prospects. *eScience* **2021**, *1*, 108−123.

(28) Ma, H.; Cheng, F.; Chen, J. Y.; Zhao, J. Z.; Li, C. S.; Tao, Z. L.; Liang, J. Nest-like Silicon Nanospheres for High-Capacity Lithium Storage. *Adv. Mater.* **2007**, *19*, 4067−4070.

(29) Peng, B.; Cheng, F.; Tao, Z.; Chen, J. Lithium Transport at Silicon Thin Film: Barrier for High-Rate Capability Anode. *J. Chem. Phys.* **2010**, *133*, 034701.

(30) Huang, A.; Ma, Y.; Peng, J.; Li, L.; Chou, S.-L.; Ramakrishna, S.; Peng, S. Tailoring the Structure of Silicon-Based Materials for Lithium-Ion Batteries via Electrospinning Technology. *eScience* **2021**, *1*, 141−162.

(31) Nayak, P. K.; Yang, L.; Brehm, W.; Adelhelm, P. From Lithium-Ion to Sodium-Ion Batteries: Advantages, Challenges, and Surprises. *Angew. Chem., Int. Ed.* **2018**, *57*, 102−120.

(32) Xu, J.; Dou, Y.; Wei, Z.; Ma, J.; Deng, Y.; Li, Y.; Liu, H.; Dou, S. Recent Progress in Graphite Intercalation Compounds for Rechargeable Metal (Li, Na, K, Al)-Ion Batteries. *Adv. Sci.* **2017**, *4*, 1700146.

(33) Min, X.; Xiao, J.; Fang, M.; Wang, W.; Zhao, Y.; Liu, Y.; Abdelkader, A. M.; Xi, K.; Kumar, R. V.; Huang, Z. Potassium-Ion Batteries: Outlook on Present and Future Technologies. *Energy Environ. Sci.* **2021**, *14*, 2186–2243.

(34) Vaalma, C.; Buchholz, D.; Weil, M.; Passerini, S. A Cost and Resource Analysis of Sodium-Ion Batteries. *Nat. Rev. Mater.* **2018**, *3*, 18013.

(35) Rajagopalan, R.; Tang, Y.; Ji, X.; Jia, C.; Wang, H. Advancements and Challenges in Potassium Ion Batteries: A Comprehensive Review. *Adv. Funct. Mater.* **2020**, *30*, 1909486.

(36) Liang, Y.; Dong, H.; Aurbach, D.; Yao, Y. Current Status and Future Directions of Multivalent Metal-Ion Batteries. *Nat. Energy* **2020**, *5*, 646–656.

(37) Xie, J.; Zhang, Q. Recent Progress in Multivalent Metal (Mg, Zn, Ca, and Al) and Metal-Ion Rechargeable Batteries with Organic Materials as Promising Electrodes. *Small* **2019**, *15*, No. e1805061.

(38) Liu, Q.; Wang, Y.; Yang, X.; Zhou, D.; Wang, X.; Jaumaux, P.; Kang, F.; Li, B.; Ji, X.; Wang, G. Rechargeable Anion-Shuttle Batteries for Low-Cost Energy Storage. *Chem.* **2021**, *7*, 1993–2021.

(39) Sandstrom, S. K.; Chen, X.; Ji, X. A Review of Halide Charge Carriers for Rocking-Chair and Dual-Ion Batteries. *Carbon Energy* **2021**, *3*, 627–653.

(40) Gschwind, F.; Rodriguez-Garcia, G.; Sandbeck, D. J. S.; Gross, A.; Weil, M.; Fichtner, M.; Hörmann, N. Fluoride Ion Batteries: Theoretical Performance, Safety, Toxicity, and a Combinatorial Screening of New Electrodes. *J. Fluor. Chem.* **2016**, *182*, 76–90.

(41) Nowroozi, M. A.; Mohammad, I.; Molaiyan, P.; Wissel, K.; Munnangi, A. R.; Clemens, O. Fluoride Ion Batteries - Past, Present, and Future. *J. Mater. Chem. A* **2021**, *9*, 5980–6012.

(42) Gopinadh, S. V.; Phanendra, P. V. R. L.; John, B.; Mercy, T. D. Fluoride-Ion Batteries: State-of-the-Art and Future Perspectives. *SM&T* **2022**, *32*, No. e00436.

(43) Anji Reddy, M.; Fichtner, M. Batteries Based on Fluoride Shuttle. *J. Mater. Chem.* **2011**, *21*, 17059.

(44) Zhou, M.; Zhao, L.; Doi, T.; Okada, S.; Yamaki, J.-I. Thermal Stability of FeF₃ Cathode for Li-Ion Batteries. *J. Power Sources* **2010**, *195*, 4952–4956.

(45) Zhou, M.; Zhao, L.; Okada, S.; Yamaki, J.-I. Thermal Characteristics of a FeF₃ Cathode via Conversion Reaction in Comparison with LiFePO₄. *J. Power Sources* **2011**, *196*, 8110–8115.

(46) Zhang, L.; Wang, H.; Zhang, X.; Tang, Y. A Review of Emerging Dual-Ion Batteries: Fundamentals and Recent Advances. *Adv. Funct. Mater.* **2021**, *31*, 2010958.

(47) Ou, X.; Gong, D.; Han, C.; Liu, Z.; Tang, Y. Advances and Prospects of Dual-Ion Batteries. *Adv. Energy Mater.* **2021**, *11*, 2102498.

(48) Goodenough, J. B.; Park, K. S. The Li-Ion Rechargeable Battery: A Perspective. *J. Am. Chem. Soc.* **2013**, *135*, 1167–1176.

(49) Tarascon, J. M.; Gozdz, A. S.; Schmutz, C.; Shokoohi, F.; Warren, P. C. Performance of Bellcore's Plastic Rechargeable Li-Ion Batteries. *Solid State Ion.* **1996**, *86–88*, 49–54.

(50) Park, Y. U.; Seo, D. H.; Kim, B.; Hong, K. P.; Kim, H.; Lee, S.; Shakoor, R. A.; Miyasaka, K.; Tarascon, J. M.; Kang, K. Tailoring a Fluorophosphate as a Novel 4 V Cathode for Lithium-Ion Batteries. *Sci. Rep.* **2012**, *2*, 704.

(51) Choi, N.-S.; Yew, K. H.; Lee, K. Y.; Sung, M.; Kim, H.; Kim, S.-S. Effect of Fluoroethylene Carbonate Additive on Interfacial Properties of Silicon Thin-Film Electrode. *J. Power Sources* **2006**, *161*, 1254–1259.

(52) Davis, V. K.; Bates, C. M.; Omichi, K.; Savoie, B. M.; Momcilovic, N.; Xu, Q.; Wolf, W. J.; Webb, M. A.; Billings, K. J.; Chou, N. H.; et al. Room-Temperature Cycling of Metal Fluoride Electrodes: Liquid Electrolytes for High-Energy Fluoride Ion Cells. *Science* **2018**, *362*, 1144–1148.

(53) Huang, Q.; Turcheniuk, K.; Ren, X.; Magasinski, A.; Song, A. Y.; Xiao, Y.; Kim, D.; Yushin, G. Cycle Stability of Conversion-Type Iron Fluoride Lithium Battery Cathode at Elevated Temperatures in Polymer Electrolyte Composites. *Nat. Mater.* **2019**, *18*, 1343–1349.

(54) Park, H.; Lee, Y.; Cho, M.-K.; Kang, J.; Ko, W.; Jung, Y. H.; Jeon, T.-Y.; Hong, J.; Kim, H.; Myung, S.-T.; et al. Na₂Fe₂F₇: a fluoride-based cathode for high power and long life Na-ion batteries. *Energy Environ. Sci.* **2021**, *14*, 1469–1479.

(55) Xu, J.; Zhang, J.; Pollard, T. P.; Li, Q.; Tan, S.; Hou, S.; Wan, H.; Chen, F.; He, H.; Hu, E.; et al. Electrolyte Design for Li-Ion Batteries under Extreme Operating Conditions. *Nature* **2023**, *614*, 694–700.

(56) Shannon, R. D. Revised Effective Ionic Radii and Systematic Studies of Interatomic Distances in Halides and Chalcogenides. *Acta Crystallogr. A* **1976**, *32*, 751–767.

(57) Xu, K. Li-Ion Battery Electrolytes. *Nat. Energy* **2021**, *6*, 763–763.

(58) Winter, M.; Barnett, B.; Xu, K. Before Li Ion Batteries. *Chem. Rev.* **2018**, *118*, 11433–11456.

(59) Reddy, M. V.; Mauger, A.; Julien, C. M.; Paolella, A.; Zaghib, K. Brief History of Early Lithium-Battery Development. *Materials* **2020**, *13*, 1884.

(60) Aurbach, D.; Talyosef, Y.; Markovsky, B.; Markevich, E.; Zinigrad, E.; Asraf, L.; Gnanaraj, J. S.; Kim, H.-J. Design of Electrolyte Solutions for Li and Li-Ion Batteries: A Review. *Electrochim. Acta* **2004**, *50*, 247–254.

(61) Kim, K.; Park, I.; Ha, S.-Y.; Kim, Y.; Woo, M.-H.; Jeong, M.-H.; Shin, W. C.; Ue, M.; Hong, S. Y.; Choi, N.-S. Understanding the Thermal Instability of Fluoroethylene Carbonate in LiPF₆-Based Electrolytes for Lithium-Ion Batteries. *Electrochim. Acta* **2017**, *225*, 358–368.

(62) Su, C.-C.; He, M.; Redfern, P. C.; Curtiss, L. A.; Shkrob, I. A.; Zhang, Z. Oxidatively Stable Fluorinated Sulfone Electrolytes for High Voltage High Energy Lithium-Ion Batteries. *Energy Environ. Sci.* **2017**, *10*, 900–904.

(63) Nambu, N.; Sasaki, Y. Physical and Electrolytic Properties of Monofluorinated Ethyl Acetates and Their Application to Lithium Secondary Batteries. *Open J. Met.* **2015**, *05*, 1–9.

(64) Bolloli, M.; Kalhoff, J.; Alloin, F.; Bresser, D.; Phung Le, M. L.; Langlois, B.; Passerini, S.; Sanchez, J.-Y. Fluorinated Carbamates as Suitable Solvents for LiTFSI-Based Lithium-Ion Electrolytes: Physicochemical Properties and Electrochemical Characterization. *J. Phys. Chem. C* **2015**, *119*, 22404–22414.

(65) Meister, P.; Qi, X.; Kloepsch, R.; Kramer, E.; Streipert, B.; Winter, M.; Placke, T. Anodic Behavior of the Aluminum Current Collector in Imide-Based Electrolytes: Influence of Solvent, Operating Temperature, and Native Oxide-Layer Thickness. *ChemSusChem* **2017**, *10*, 804–814.

(66) He, M.; Hu, L.; Xue, Z.; Su, C. C.; Redfern, P.; Curtiss, L. A.; Polzin, B.; Von Cresce, A.; Xu, K.; Zhang, Z. Fluorinated Electrolytes for 5-V Li-Ion Chemistry: Probing Voltage Stability of Electrolytes with Electrochemical Floating Test. *J. Electrochem. Soc.* **2015**, *162*, A1725–A1729.

(67) Oldiges, K.; Von Aspern, N.; Cekic-Laskovic, I.; Winter, M.; Brunklaus, G. Impact of Trifluoromethylation of Adiponitrile on Aluminum Dissolution Behavior in Dinitrile-Based Electrolytes. *J. Electrochem. Soc.* **2018**, *165*, A3773–A3781.

(68) Tornheim, A.; He, M.; Su, C.-C.; Zhang, Z. The Role of Additives in Improving Performance in High Voltage Lithium-Ion Batteries with Potentiostatic Holds. *J. Electrochem. Soc.* **2017**, *164*, A6366–A6372.

(69) Luo, Y.; Lu, T.; Zhang, Y.; Yan, L.; Xie, J.; Mao, S. S. Enhanced Electrochemical Performance of LiNi₀.₅Mn₁.₅O₄ Cathode Using an Electrolyte with 3-(1,1, 2,2-Tetrafluoroethoxy)-1,1, 2,2-Tetrafluoropropane. *J. Power Sources* **2016**, *323*, 134–141.

(70) Wang, C.; Tang, S.; Zuo, X.; Xiao, X.; Liu, J.; Nan, J. 3-(1,1,2,2-Tetrafluoroethoxy)-1,1,2,2-Tetrafluoropropane as a High Voltage Solvent for LiNi₁/₃Co₁/₃Mn₁/₃O₂/Graphite Cells. *J. Electrochem. Soc.* **2015**, *162*, A1997–A2003.

(71) Lu, J.; Wang, C.; Yu, H.; Gong, S.; Xia, G.; Jiang, P.; Xu, P.; Yang, K.; Chen, Q. Oxygen/Fluorine Dual-Doped Porous Carbon Nanopolyhedra Enabled Ultrafast and Highly Stable Potassium Storage. *Adv. Funct. Mater.* **2019**, *29*, 1906126.

(72) Nowroozi, M. A.; Wissel, K.; Rohrer, J.; Munnangi, A. R.; Clemens, O. LaSrMnO$_4$: Reversible Electrochemical Intercalation of Fluoride Ions in the Context of Fluoride Ion Batteries. *Chem. Mater.* 2017, 29, 3441−3453.

(73) Bhatia, H.; Thieu, D. T.; Pohl, A. H.; Chakravadhanula, V. S. K.; Fawey, M. H.; Kubel, C.; Fichtner, M. Conductivity Optimization of Tysonite-type La$_{1-x}$Ba$_x$F$_{3-x}$ Solid Electrolytes for Advanced Fluoride Ion Battery. *ACS Appl. Mater. Interfaces* 2017, 9, 23707−23715.

(74) Gschwind, F.; Bastien, J. Parametric Investigation of Room-Temperature Fluoride-Ion Batteries: Assessment of Electrolytes, Mg-Based Anodes, and BiF$_3$-Cathodes. *J. Mater. Chem. A* 2015, 3, 5628−5634.

(75) Zhang, L.; Reddy, M. A.; Gao, P.; Diemant, T.; Jürgen Behm, R.; Fichtner, M. Study of All Solid-State Rechargeable Fluoride Ion Batteries Based on Thin-Film Electrolyte. *J. Solid State Electrochem.* 2017, 21, 1243−1251.

(76) Gong, C.; Pu, S. D.; Gao, X.; Yang, S.; Liu, J.; Ning, Z.; Rees, G. J.; Capone, I.; Pi, L.; Liu, B.; et al. Revealing the Role of Fluoride-Rich Battery Electrode Interphases by Operando Transmission Electron Microscopy. *Adv. Energy Mater.* 2021, 11, 2003118.

(77) Seel, J. A.; Dahn, J. R. Electrochemical Intercalation of PF$_6$ into Graphite. *J. Electrochem. Soc.* 2000, 147, 892.

(78) Shi, X.; Zhang, W.; Wang, J.; Zheng, W.; Huang, K.; Zhang, H.; Feng, S.; Chen, H. (EMIm)$^+$(PF$_6$)$^-$ Ionic Liquid Unlocks Optimum Energy/Power Density for Architecture of Nanocarbon-Based Dual-Ion Battery. *Adv. Energy Mater.* 2016, 6, 1601378.

(79) Jiang, H.; Han, X.; Du, X.; Chen, Z.; Lu, C.; Li, X.; Zhang, H.; Zhao, J.; Han, P.; Cui, G. A PF$_6$$^-$-Permselective Polymer Electrolyte with Anion Solvation Regulation Enabling Long-Cycle Dual-Ion Battery. *Adv. Mater.* 2022, 34, No. e2108665.

(80) Yang, H.; Qin, T.; Zhou, X.; Feng, Y.; Wang, Z.; Ge, X.; Yue, N.; Li, D.; Zhang, W.; Zheng, W. Boosting the Kinetics of PF6$^-$ into Graphitic Layers for the Optimal Cathode of Dual-Ion Batteries: The Rehearsal of Pre-intercalating Li$^+$. *J. Energy Chem.* 2022, 71, 392−399.

(81) Placke, T.; Heckmann, A.; Schmuch, R.; Meister, P.; Beltrop, K.; Winter, M. Perspective on Performance, Cost, and Technical Challenges for Practical Dual-Ion Batteries. *Joule* 2018, 2, 2528−2550.

(82) Qi, X.; Blizanac, B.; Dupasquier, A.; Meister, P.; Placke, T.; Oljaca, M.; Li, J.; Winter, M. Investigation of PF$_6$$^-$ and TFSI$^-$ Anion Intercalation into Graphitized Carbon Blacks and Its Influence on High Voltage Lithium-Ion Batteries. *Phys. Chem. Chem. Phys.* 2014, 16, 25306−25313.

(83) Aladinli, S.; Bordet, F.; Ahlbrecht, K.; Tübke, J.; Holzapfel, M. Anion Intercalation into a Graphite Cathode from Various Sodium-Based Electrolyte Mixtures for Dual-Ion Battery Applications. *Electrochim. Acta* 2017, 231, 468−478.

(84) Tan, H.; Zhai, D.; Kang, F.; Zhang, B. Synergistic PF6$^-$ and FSI$^-$ Intercalation Enables Stable Graphite Cathode for Potassium-Based Dual Ion Battery. *Carbon* 2021, 178, 363−370.

(85) Kravchyk, K. V.; Bhauriyal, P.; Piveteau, L.; Guntlin, C. P.; Pathak, B.; Kovalenko, M. V. High-Energy-Density Dual-Ion Battery for Stationary Storage of Electricity Using Concentrated Potassium Fluorosulfonylimide. *Nat. Commun.* 2018, 9, 4469.

(86) Tong, X.; Ou, X.; Wu, N.; Wang, H.; Li, J.; Tang, Y. High Oxidation Potential ≈6.0 V of Concentrated Electrolyte toward High-Performance Dual-Ion Battery. *Adv. Energy Mater.* 2021, 11, 2100151.

(87) Beltrop, K.; Meister, P.; Klein, S.; Heckmann, A.; Grünebaum, M.; Wiemhöfer, H.-D.; Winter, M.; Placke, T. Does Size really Matter? New Insights into the Intercalation Behavior of Anions into a Graphite-Based Positive Electrode for Dual-Ion Batteries. *Electrochim. Acta* 2016, 209, 44−55.

(88) Hao, J.; Li, X.; Song, X.; Guo, Z. Recent Progress and Perspectives on Dual-Ion Batteries. *EnergyChem.* 2019, 1, 100004.

(89) Zhang, Q.; Pan, J.; Lu, P.; Liu, Z.; Verbrugge, M. W.; Sheldon, B. W.; Cheng, Y. T.; Qi, Y.; Xiao, X. Synergetic Effects of Inorganic Components in Solid Electrolyte Interphase on High Cycle Efficiency of Lithium Ion Batteries. *Nano Lett.* 2016, 16, 2011−2016.

(90) Huang, Y.; Wang, H. How Ethylene Carbonate/γ-Butyrolactone Mixtures Affect BF$_4$$^-$ Intercalation into Graphite Electrode. *J. Electrochem. Soc.* 2019, 166, A3838−A3843.

(91) Li, C.; Lao, B.; Li, Z.; Yin, H.; Yang, Z.; Wang, H.; Chen, D.; Zhang, X.; Xu, Y.; Sun, C. Dual-Ion Battery with MoS$_2$ Cathode. *Energy Storage Mater.* 2020, 32, 159−166.

(92) Carlin, R. T.; De Long, H. C.; Fuller, J.; Trulove, P. C. Dual Intercalating Molten Electrolyte Batteries. *J. Electrochem. Soc.* 1994, 141, L73−L76.

(93) Wang, S.; Jiao, S.; Tian, D.; Chen, H. S.; Jiao, H.; Tu, J.; Liu, Y.; Fang, D. N. A Novel Ultrafast Rechargeable Multi-Ions Battery. *Adv. Mater.* 2017, 29, 1606349.

(94) Liu, C.; Neale, Z. G.; Cao, G. Understanding Electrochemical Potentials of Cathode Materials in Rechargeable Batteries. *Mater. Today* 2016, 19, 109−123.

(95) Hu, Q.; Yu, Z.; Tian, L.; Zhao, Y.; Liu, H.; Lai, C.; Yuan, Z. Porous Anhydrous CuF$_2$ with a Micro-Nano-Hierarchical Structure as High-Performance Cathode Material for Li-Ion Battery. *J. Mater. Sci.* 2023, 58, 10120−10130.

(96) Xiao, A. W.; Lee, H. J.; Capone, I.; Robertson, A.; Wi, T. U.; Fawdon, J.; Wheeler, S.; Lee, H. W.; Grobert, N.; Pasta, M. Understanding the conversion mechanism and performance of monodisperse FeF$_2$ nanocrystal cathodes. *Nat. Mater.* 2020, 19, 644−654.

(97) Lee, J.; Kang, B. Superior Electrochemical Performance of N-Doped Nanocrystalline FeF$_3$/C with a Single-Step Solid-State Process. *Chem. Commun.* 2016, 52, 12100−12103.

(98) Villa, C.; Kim, S.; Lu, Y.; Dravid, V. P.; Wu, J. Cu-Substituted NiF$_2$ as a Cathode Material for Li-Ion Batteries. *ACS Appl. Mater. Interfaces* 2019, 11, 647−654.

(99) Wang, X.; Gu, W.; Lee, J. T.; Nitta, N.; Benson, J.; Magasinski, A.; Schauer, M. W.; Yushin, G. Carbon Nanotube-CoF$_2$ Multifunctional Cathode for Lithium Ion Batteries: Effect of Electrolyte on Cycle Stability. *Small* 2015, 11, 5164−5173.

(100) Groult, H.; Neveu, S.; Leclerc, S.; Porras-Gutierrez, A. G.; Julien, C. M.; Tressaud, A.; Durand, E.; Penin, N.; Labrugere, C. Nano-CoF$_3$ prepared by direct fluorination with F$_2$ gas: Application as electrode material in Li-ion battery. *J. Fluor. Chem.* 2017, 196, 117−127.

(101) Rui, K.; Wen, Z.; Lu, Y.; Shen, C.; Jin, J. Anchoring Nanostructured Manganese Fluoride on Few-Layer Graphene Nanosheets as Anode for Enhanced Lithium Storage. *ACS Appl. Mater. Interfaces* 2016, 8, 1819−1826.

(102) Wang, F.; Kim, S. W.; Seo, D. H.; Kang, K.; Wang, L.; Su, D.; Vajo, J. J.; Wang, J.; Graetz, J. Ternary Metal Fluorides as High-Energy Cathodes with Low Cycling Hysteresis. *Nat. Commun.* 2015, 6, 6668.

(103) Cambaz, M. A.; Vinayan, B. P.; Clemens, O.; Munnangi, A. R.; Chakravadhanula, V. S.; Kubel, C.; Fichtner, M. Vanadium Oxy-fluoride/Few-Layer Graphene Composite as a High-Performance Cathode Material for Lithium Batteries. *Inorg. Chem.* 2016, 55, 3789−3796.

(104) Ni, D.; Sun, W.; Xie, L.; Fan, Q.; Wang, Z.; Sun, K. Bismuth Oxyfluoride @ CMK-3 Nanocomposite as Cathode for Lithium Ion Batteries. *J. Power Sources* 2018, 374, 166−174.

(105) Kitajou, A.; Komatsu, H.; Nagano, R.; Okada, S. Synthesis of FeOF Using Roll-Quenching Method and the Cathode Properties for Lithium-Ion Battery. *J. Power Sources* 2013, 243, 494−498.

(106) Louvain, N.; Karkar, Z.; El-Ghozzi, M.; Bonnet, P.; Guérin, K.; Willmann, P. Fluorination of Anatase TiO$_2$ Towards Titanium Oxyfluoride TiOF$_2$: A Novel Synthesis Approach and Proof of the Li-Insertion Mechanism. *J. Mater. Chem. A* 2014, 2, 15308−15315.

(107) Reddy, M. V.; Madhavi, S.; Subba Rao, G. V.; Chowdari, B. V. R. Metal Oxyfluorides TiOF$_2$ and NbO$_2$F as Anodes for Li-Ion Batteries. *J. Power Sources* 2006, 162, 1312−1321.

(108) Hua, X.; Eggeman, A. S.; Castillo-Martinez, E.; Robert, R.; Geddes, H. S.; Lu, Z.; Pickard, C. J.; Meng, W.; Wiaderek, K. M.; Pereira, N.; et al. Revisiting Metal Fluorides as Lithium-Ion Battery Cathodes. *Nat. Mater.* 2021, 20, 841−850.

(109) Liu, L.; Guo, H.; Zhou, M.; Wei, Q.; Yang, Z.; Shu, H.; Yang, X.; Tan, J.; Yan, Z.; Wang, X. A Comparison among $FeF_3\cdot3H_2O$, $FeF_3\cdot0.33H_2O$ and FeF_3 Cathode Materials for Lithium Ion Batteries: Structural, Electrochemical, and Mechanism Studies. *J. Power Sources* **2013**, *238*, 501−515.

(110) Lemoine, K.; Zhang, L.; Dambournet, D.; Grenèche, J.-M.; Hémon-Ribaud, A.; Leblanc, M.; Borkiewicz, O. J.; Tarascon, J.-M.; Maisonneuve, V.; Lhoste, J. Synthesis by Thermal Decomposition of Two Iron Hydroxyfluorides: Structural Effects of Li Insertion. *Chem. Mater.* **2019**, *31*, 4246−4257.

(111) Fan, X.; Hu, E.; Ji, X.; Zhu, Y.; Han, F.; Hwang, S.; Liu, J.; Bak, S.; Ma, Z.; Gao, T.; et al. High Energy-Density and Reversibility of Iron Fluoride Cathode Enabled via an Intercalation-Extrusion Reaction. *Nat. Commun.* **2018**, *9*, 2324.

(112) Jung, S.-K.; Kim, H.; Cho, M. G.; Cho, S.-P.; Lee, B.; Kim, H.; Park, Y.-U.; Hong, J.; Park, K.-Y.; Yoon, G.; et al. Lithium-Free Transition Metal Monoxides for Positive Electrodes in Lithium-Ion Batteries. *Nat. Energy* **2017**, *2*, 16208.

(113) Deng, D. Transition Metal Oxyfluorides for Next-Generation Rechargeable Batteries. *ChemNanoMat* **2017**, *3*, 146−159.

(114) Sorensen, E. M.; Izumi, H. K.; Vaughey, J. T.; Stern, C. L.; Poeppelmeier, K. R. $Ag_4V_2O_6F_2$: An Electrochemically Active and High Silver Density Phase. *J. Am. Chem. Soc.* **2005**, *127*, 6347−6352.

(115) Kim, M.; Lee, S.; Kang, B. Fast-Rate Capable Electrode Material with Higher Energy Density than $LiFePO_4$: 4.2V $LiVPO_4F$ Synthesized by Scalable Single-Step Solid-State Reaction. *Adv. Sci.* **2016**, *3*, 1500366.

(116) Heo, J.; Jung, S.-K.; Hwang, I.; Cho, S.-P.; Eum, D.; Park, H.; Song, J.-H.; Yu, S.; Oh, K.; Kwon, G.; et al. Amorphous Iron Fluorosulfate as a High-Capacity Cathode Utilizing Combined Intercalation and Conversion Reactions with Unexpectedly High Reversibility. *Nat. Energy* **2023**, *8*, 30−39.

(117) Jin, T.; Li, H.; Zhu, K.; Wang, P. F.; Liu, P.; Jiao, L. Polyanion-Type Cathode Materials for Sodium-Ion Batteries. *Chem. Soc. Rev.* **2020**, *49*, 2342−2377.

(118) Recham, N.; Chotard, J. N.; Dupont, L.; Delacourt, C.; Walker, W.; Armand, M.; Tarascon, J. M. A 3.6 V Lithium-Based Fluorosulphate Insertion Positive Electrode for Lithium-Ion Batteries. *Nat. Mater.* **2010**, *9*, 68−74.

(119) Barpanda, P.; Ati, M.; Melot, B. C.; Rousse, G.; Chotard, J. N.; Doublet, M. L.; Sougrati, M. T.; Corr, S. A.; Jumas, J. C.; Tarascon, J. M. A 3.90 V Iron-Based Fluorosulphate Material for Lithium-Ion Batteries Crystallizing in the Triplite Structure. *Nat. Mater.* **2011**, *10*, 772−779.

(120) Andersson, A. M.; Abraham, D. P.; Haasch, R.; Maclaren, S.; Liu, J.; Amine, K. Surface Characterization of Electrodes from High Power Lithium-Ion Batteries. *J. Electrochem. Soc.* **2002**, *149*, A1358.

(121) Rosina, K. J.; Jiang, M.; Zeng, D.; Salager, E.; Best, A. S.; Grey, C. P. Structure of Aluminum Fluoride Coated $Li[Li_{1/9}Ni_{1/3}Mn_{5/9}]O_2$ Cathodes for Secondary Lithium-Ion Batteries. *J. Mater. Chem.* **2012**, *22*, 20602.

(122) Lu, C.; Wu, H.; Zhang, Y.; Liu, H.; Chen, B.; Wu, N.; Wang, S. Cerium Fluoride Coated Layered Oxide $Li_{1.2}Mn_{0.54}Ni_{0.13}Co_{0.13}O_2$ as Cathode Materials with Improved Electrochemical Performance for Lithium-Ion Batteries. *J. Power Sources* **2014**, *267*, 682−691.

(123) Lee, J.; Kitchaev, D. A.; Kwon, D. H.; Lee, C. W.; Papp, J. K.; Liu, Y. S.; Lun, Z.; Clement, R. J.; Shi, T.; Mccloskey, B. D.; et al. Reversible Mn^{2+}/Mn^{4+} Double Redox in Lithium-Excess Cathode Materials. *Nature* **2018**, *556*, 185−190.

(124) Li, L.; Ahn, J.; Yue, Y.; Tong, W.; Chen, G.; Wang, C. Fluorination-Enhanced Surface Stability of Disordered Rocksalt Cathodes. *Adv. Mater.* **2022**, *34*, No. e2106256.

(125) Bieker, P.; Winter, M. Lithium-Ionen-Technologie und Was Danach Kommen Könnte. *Chemie Unserer Zeit* **2016**, *50*, 172−186.

(126) Barlowz, C. G. Reaction of Water with Hexafluorophosphates and with Li Bis(perfluoroethylsulfonyl)imide Salt. *Electrochem. Solid-State Lett.* **1999**, *2*, 362.

(127) Matsumoto, K.; Inoue, K.; Nakahara, K.; Yuge, R.; Noguchi, T.; Utsugi, K. Suppression of Aluminum Corrosion by Using High Concentration LiTFSI Electrolyte. *J. Power Sources* **2013**, *231*, 234−238.

(128) Lohmann, R.; Cousins, I. T.; Dewitt, J. C.; Gluge, J.; Goldenman, G.; Herzke, D.; Lindstrom, A. B.; Miller, M. F.; Ng, C. A.; Patton, S.; et al. Are Fluoropolymers Really of Low Concern for Human and Environmental Health a Separate from Other PFAS? *Environ. Sci. Technol.* **2020**, *54*, 12820−12828.

(129) Xia, Y.; Zhou, P.; Kong, X.; Tian, J.; Zhang, W.; Yan, S.; Hou, W.-H.; Zhou, H.-Y.; Dong, H.; Chen, X.; et al. Designing an Asymmetric Ether-Like Lithium Salt to Enable Fast-Cycling High-Energy Lithium Metal Batteries. *Nat. Energy* **2023**, *8*, 934−945.

(130) Von Aspern, N.; Roschenthaler, G. V.; Winter, M.; Cekic-Laskovic, I. Fluorine and Lithium: Ideal Partners for High-Performance Rechargeable Battery Electrolytes. *Angew. Chem., Int. Ed.* **2019**, *58*, 15978−16000.

(131) Nakajima, T. Fluorine Compounds as Energy Conversion Materials. *J. Fluor. Chem.* **2013**, *149*, 104−111.

(132) Suo, L.; Hu, Y. S.; Li, H.; Armand, M.; Chen, L. A New Class of Solvent-in-Salt Electrolyte for High-Energy Rechargeable Metallic Lithium Batteries. *Nat. Commun.* **2013**, *4*, 1481.

(133) Kim, H.; Hong, J.; Park, K. Y.; Kim, H.; Kim, S. W.; Kang, K. Aqueous Rechargeable Li and Na Ion Batteries. *Chem. Rev.* **2014**, *114*, 11788−11827.

(134) Wang, Y.; Yi, J.; Xia, Y. Recent Progress in Aqueous Lithium-Ion Batteries. *Adv. Energy Mater.* **2012**, *2*, 830−840.

(135) Suo, L.; Borodin, O.; Gao, T.; Olguin, M.; Ho, J.; Fan, X.; Luo, C.; Wang, C.; Xu, K. "Water-in-Salt" Electrolyte Enables High-Voltage Aqueous Lithium-Ion Chemistries. *Science* **2015**, *350*, 938−943.

(136) Yamada, Y.; Chiang, C. H.; Sodeyama, K.; Wang, J.; Tateyama, Y.; Yamada, A. Corrosion Prevention Mechanism of Aluminum Metal in Superconcentrated Electrolytes. *ChemElectroChem* **2015**, *2*, 1687−1694.

(137) Zheng, J.; Fan, X.; Ji, G.; Wang, H.; Hou, S.; Demella, K. C.; Raghavan, S. R.; Wang, J.; Xu, K.; Wang, C. Manipulating Electrolyte and Solid Electrolyte Interphase to Enable Safe and Efficient Li-S Batteries. *Nano Energy* **2018**, *50*, 431−440.

(138) Diederichsen, K. M.; Mcshane, E. J.; Mccloskey, B. D. Promising Routes to a High Li^+ Transference Number Electrolyte for Lithium Ion Batteries. *ACS Energy Lett.* **2017**, *2*, 2563−2575.

(139) Yamada, Y.; Wang, J.; Ko, S.; Watanabe, E.; Yamada, A. Advances and Issues in Developing Salt-Concentrated Battery Electrolytes. *Nat. Energy* **2019**, *4*, 269−280.

(140) Pei, Z.; Gu, J.; Wang, Y.; Tang, Z.; Liu, Z.; Huang, Y.; Huang, Y.; Zhao, J.; Chen, Z.; Zhi, C. Component Matters: Paving the Roadmap toward Enhanced Electrocatalytic Performance of Graphitic C_3N_4-Based Catalysts via Atomic Tuning. *ACS Nano* **2017**, *11*, 6004−6014.

(141) Jeong, S.-K.; Inaba, M.; Iriyama, Y.; Abe, T.; Ogumi, Z. Interfacial Reactions between Graphite Electrodes and Propylene Carbonate-Based Solutions: Electrolyte-Concentration Dependence of Electrochemical Lithium Intercalation Reaction. *J. Power Sources* **2008**, *175*, 540−546.

(142) Jeong, S.-K.; Seo, H.-Y.; Kim, D.-H.; Han, H.-K.; Kim, J.-G.; Lee, Y. B.; Iriyama, Y.; Abe, T.; Ogumi, Z. Suppression of Dendritic Lithium Formation by Using Concentrated Electrolyte Solutions. *Electrochem. commun.* **2008**, *10*, 635−638.

(143) Yamada, Y.; Takazawa, Y.; Miyazaki, K.; Abe, T. Electrochemical Lithium Intercalation into Graphite in Dimethyl Sulfoxide-Based Electrolytes: Effect of Solvation Structure of Lithium Ion. *J. Phys. Chem. C* **2010**, *114*, 11680−11685.

(144) Yamada, Y.; Furukawa, K.; Sodeyama, K.; Kikuchi, K.; Yaegashi, M.; Tateyama, Y.; Yamada, A. Unusual Stability of Acetonitrile-Based Superconcentrated Electrolytes for Fast-Charging Lithium-Ion Batteries. *J. Am. Chem. Soc.* **2014**, *136*, 5039−5046.

(145) Yamada, Y.; Usui, K.; Chiang, C. H.; Kikuchi, K.; Furukawa, K.; Yamada, A. General Observation of Lithium Intercalation into Graphite in Ethylene-Carbonate-Free Superconcentrated Electrolytes. *ACS Appl. Mater. Interfaces* **2014**, *6*, 10892−10899.

(146) Qian, J.; Henderson, W. A.; Xu, W.; Bhattacharya, P.; Engelhard, M.; Borodin, O.; Zhang, J. G. High Rate and Stable Cycling of Lithium Metal Anode. *Nat. Commun.* **2015**, *6*, 6362.

(147) Mcowen, D. W.; Seo, D. M.; Borodin, O.; Vatamanu, J.; Boyle, P. D.; Henderson, W. A. Concentrated Electrolytes: Decrypting Electrolyte Properties and Reassessing Al Corrosion Mechanisms. *Energy Environ. Sci.* **2014**, *7*, 416–426.

(148) Möller, K. C.; Hodal, T.; Appel, W. K.; Winter, M.; Besenhard, J. O. Fluorinated Organic Solvents in Electrolytes for Lithium Ion Cells. *J. Power Sources* **2001**, *97–98*, 595–597.

(149) Qin, M.; Zeng, Z.; Wu, Q.; Yan, H.; Liu, M.; Wu, Y.; Zhang, H.; Lei, S.; Cheng, S.; Xie, J. Dipole-Dipole Interactions for Inhibiting Solvent Co-intercalation into a Graphite Anode to Extend the Horizon of Electrolyte Design. *Energy Environ. Sci.* **2023**, *16*, 546–556.

(150) Yu, Z.; Rudnicki, P. E.; Zhang, Z.; Huang, Z.; Celik, H.; Oyakhire, S. T.; Chen, Y.; Kong, X.; Kim, S. C.; Xiao, X.; et al. Rational Solvent Molecule Tuning for High-Performance Lithium Metal Battery Electrolytes. *Nat. Energy* **2022**, *7*, 94–106.

(151) Lee, S.; Park, K.; Koo, B.; Park, C.; Jang, M.; Lee, H.; Lee, H. Safe, Stable Cycling of Lithium Metal Batteries with Low-Viscosity, Fire-Retardant Locally Concentrated Ionic Liquid Electrolytes. *Adv. Funct. Mater.* **2020**, *30*, 2003132.

(152) Yang, Y.; Davies, D. M.; Yin, Y.; Borodin, O.; Lee, J. Z.; Fang, C.; Olguin, M.; Zhang, Y.; Sablina, E. S.; Wang, X.; et al. High-Efficiency Lithium-Metal Anode Enabled by Liquefied Gas Electrolytes. *Joule* **2019**, *3*, 1986–2000.

(153) Smart, M. C.; Ratnakumar, B. V.; Surampudi, S. Use of Organic Esters as Cosolvents in Electrolytes for Lithium-Ion Batteries with Improved Low Temperature Performance. *J. Electrochem. Soc.* **2002**, *149*, A361.

(154) Dong, X.; Guo, Z.; Guo, Z.; Wang, Y.; Xia, Y. Organic Batteries Operated at −70°C. *Joule* **2018**, *2*, 902–913.

(155) Liang, H. J.; Gu, Z. Y.; Zhao, X. X.; Guo, J. Z.; Yang, J. L.; Li, W. H.; Li, B.; Liu, Z. M.; Sun, Z. H.; Zhang, J. P.; et al. Advanced Flame-Retardant Electrolyte for Highly Stabilized K-ion Storage in Graphite Anode. *Sci. Bull.* **2022**, *67*, 1581–1588.

(156) Dokko, K.; Tachikawa, N.; Yamauchi, K.; Tsuchiya, M.; Yamazaki, A.; Takashima, E.; Park, J.-W.; Ueno, K.; Seki, S.; Serizawa, N.; et al. Solvate Ionic Liquid Electrolyte for Li-S Batteries. *J. Electrochem. Soc.* **2013**, *160*, A1304–A1310.

(157) Chen, S.; Zheng, J.; Mei, D.; Han, K. S.; Engelhard, M. H.; Zhao, W.; Xu, W.; Liu, J.; Zhang, J. G. High-Voltage Lithium-Metal Batteries Enabled by Localized High-Concentration Electrolytes. *Adv. Mater.* **2018**, *30*, No. e1706102.

(158) Lin, S.; Hua, H.; Lai, P.; Zhao, J. A Multifunctional Dual-Salt Localized High-Concentration Electrolyte for Fast Dynamic High-Voltage Lithium Battery in Wide Temperature Range. *Adv. Energy Mater.* **2021**, *11*, 2101775.

(159) Chen, X.; Qin, L.; Sun, J.; Zhang, S.; Xiao, D.; Wu, Y. Phase Transfer-Mediated Degradation of Ether-Based Localized High-Concentration Electrolytes in Alkali Metal Batteries. *Angew. Chem., Int. Ed.* **2022**, *61*, No. e202207018.

(160) Zhu, C.; Sun, C.; Li, R.; Weng, S.; Fan, L.; Wang, X.; Chen, L.; Noked, M.; Fan, X. Anion-Diluent Pairing for Stable High-Energy Li Metal Batteries. *ACS Energy Lett.* **2022**, *7*, 1338–1347.

(161) Wu, Y.; Wang, A.; Hu, Q.; Liang, H.; Xu, H.; Wang, L.; He, X. Significance of Antisolvents on Solvation Structures Enhancing Interfacial Chemistry in Localized High-Concentration Electrolytes. *ACS Cent. Sci.* **2022**, *8*, 1290–1298.

(162) Ding, J. F.; Xu, R.; Yao, N.; Chen, X.; Xiao, Y.; Yao, Y. X.; Yan, C.; Xie, J.; Huang, J. Q. Non-Solvating and Low-Dielectricity Cosolvent for Anion-Derived Solid Electrolyte Interphases in Lithium Metal Batteries. *Angew. Chem., Int. Ed.* **2021**, *60*, 11442–11447.

(163) Kim, S. C.; Kong, X.; Vila, R. A.; Huang, W.; Chen, Y.; Boyle, D. T.; Yu, Z.; Wang, H.; Bao, Z.; Qin, J.; et al. Potentiometric Measurement to Probe Solvation Energy and Its Correlation to Lithium Battery Cyclability. *J. Am. Chem. Soc.* **2021**, *143*, 10301–10308.

(164) Piao, N.; Ji, X.; Xu, H.; Fan, X.; Chen, L.; Liu, S.; Garaga, M. N.; Greenbaum, S. G.; Wang, L.; Wang, C.; et al. Countersolvent Electrolytes for Lithium-Metal Batteries. *Adv. Energy Mater.* **2020**, *10*, 1903568.

(165) Zhang, Q. K.; Zhang, X. Q.; Hou, L. P.; Sun, S. Y.; Zhan, Y. X.; Liang, J. L.; Zhang, F. S.; Feng, X. N.; Li, B. Q.; Huang, J. Q. Regulating Solvation Structure in Nonflammable Amide-Based Electrolytes for Long-Cycling and Safe Lithium Metal Batteries. *Adv. Energy Mater.* **2022**, *12*, 2200139.

(166) Meng, Y.; Zhou, D.; Liu, R.; Tian, Y.; Gao, Y.; Wang, Y.; Sun, B.; Kang, F.; Armand, M.; Li, B.; et al. Designing Phosphazene-Derivative Electrolyte Matrices to Enable High-Voltage Lithium Metal Batteries for Extreme Working Conditions. *Nat. Energy* **2023**, *8*, 1023–1033.

(167) Xu, K. Nonaqueous Liquid Electrolytes for Lithium-Based Rechargeable Batteries. *Chem. Rev.* **2004**, *104*, 4303–4417.

(168) Zhang, X.-Q.; Cheng, X.-B.; Chen, X.; Yan, C.; Zhang, Q. Fluoroethylene Carbonate Additives to Render Uniform Li Deposits in Lithium Metal Batteries. *Adv. Funct. Mater.* **2017**, *27*, 1605989.

(169) Okuno, Y.; Ushirogata, K.; Sodeyama, K.; Tateyama, Y. Decomposition of the Fluoroethylene Carbonate Additive and the Glue Effect of Lithium Fluoride Products for the Solid Electrolyte Interphase: An Ab Initio Study. *Phys. Chem. Chem. Phys.* **2016**, *18*, 8643–8653.

(170) Choudhury, S.; Archer, L. A. Lithium Fluoride Additives for Stable Cycling of Lithium Batteries at High Current Densities. *Adv. Electron. Mater.* **2016**, *2*, 1500246.

(171) Ma, Y.; Zhou, Z.; Li, C.; Wang, L.; Wang, Y.; Cheng, X.; Zuo, P.; Du, C.; Huo, H.; Gao, Y.; et al. Enabling Reliable Lithium Metal Batteries by a Bifunctional Anionic Electrolyte Additive. *Energy Storage Mater.* **2018**, *11*, 197–204.

(172) Lee, Y.-M.; Nam, K.-M.; Hwang, E.-H.; Kwon, Y.-G.; Kang, D.-H.; Kim, S.-S.; Song, S.-W. Interfacial Origin of Performance Improvement and Fade for 4.6 V LiNi$_{0.5}$Co$_{0.2}$Mn$_{0.3}$O$_2$ Battery Cathodes. *J. Phys. Chem. C* **2014**, *118*, 10631–10639.

(173) Wang, X.; Liao, X.; Huang, W.; Xing, L.; Liao, Y.; Huang, Q.; Xu, M.; Li, W. Improved Cyclic Stability of Layered Lithium Cobalt Oxide at High Potential via Cathode Electrolyte Interphase Formed by 4-(Trifluoromethyl) Benzonitrile. *Electrochim. Acta* **2015**, *184*, 94–101.

(174) Doughty, D. H.; Roth, E. P.; Crafts, C. C.; Nagasubramanian, G.; Henriksen, G.; Amine, K. Effects of Additives on Thermal Stability of Li Ion Cells. *J. Power Sources* **2005**, *146*, 116–120.

(175) Zhang, S. S.; Xu, K.; Jow, T. R. Tris(2,2, 2-Trifluoroethyl) Phosphite as a Co-solvent for Nonflammable Electrolytes in Li-Ion Batteries. *J. Power Sources* **2003**, *113*, 166–172.

(176) Li, Y.; An, Y.; Tian, Y.; Fei, H.; Xiong, S.; Qian, Y.; Feng, J. Stable and Safe Lithium Metal Batteries with Ni-Rich Cathodes Enabled by a High Efficiency Flame Retardant Additive. *J. Electrochem. Soc.* **2019**, *166*, A2736–A2740.

(177) Liu, J.; Song, X.; Zhou, L.; Wang, S.; Song, W.; Liu, W.; Long, H.; Zhou, L.; Wu, H.; Feng, C.; et al. Fluorinated Phosphazene Derivative - a Promising Electrolyte Additive for High Voltage Lithium Ion Batteries: From Electrochemical Performance to Corrosion Mechanism. *Nano Energy* **2018**, *46*, 404–414.

(178) Ji, Y.; Zhang, P.; Lin, M.; Zhao, W.; Zhang, Z.; Zhao, Y.; Yang, Y. Toward a Stable Electrochemical Interphase with Enhanced Safety on High-Voltage LiCoO$_2$ Cathode: A Case of Phosphazene Additives. *J. Power Sources* **2017**, *359*, 391–399.

(179) Casselman, M. D.; Kaur, A. P.; Narayana, K. A.; Elliott, C. F.; Risko, C.; Odom, S. A. The Fate of Phenothiazine-Based Redox Shuttles in Lithium-Ion Batteries. *Phys. Chem. Chem. Phys.* **2015**, *17*, 6905–6912.

(180) Kaur, A. P.; Casselman, M. D.; Elliott, C. F.; Parkin, S. R.; Risko, C.; Odom, S. A. Overcharge Protection of Lithium-Ion Batteries above 4 V with a Perfluorinated Phenothiazine Derivative. *J. Mater. Chem. A* **2016**, *4*, 5410–5414.

(181) Beichel, W.; Klose, P.; Blattmann, H.; Hoecker, J.; Kratzert, D.; Krossing, I. Simple Green Synthesis and Electrochemical

Performance of a New Fluorinated Carbonate as Additive for Lithium-Ion Batteries. *ChemElectroChem.* **2018**, *5*, 1415−1420.

(182) Hu, J.; Chen, K.; Li, C. Nanostructured Li-Rich Fluoride Coated by Ionic Liquid as High Ion-Conductivity Solid Electrolyte Additive to Suppress Dendrite Growth at Li Metal Anode. *ACS Appl. Mater. Interfaces* **2018**, *10*, 34322−34331.

(183) Li, Q.; Xue, W.; Sun, X.; Yu, X.; Li, H.; Chen, L. Gaseous Electrolyte Additive BF$_3$ for High-Power Li/CF$_x$ Primary Batteries. *Energy Storage Mater.* **2021**, *38*, 482−488.

(184) Xue, W.; Huang, M.; Li, Y.; Zhu, Y. G.; Gao, R.; Xiao, X.; Zhang, W.; Li, S.; Xu, G.; Yu, Y.; et al. Ultra-High-Voltage Ni-Rich Layered Cathodes in Practical Li Metal Batteries Enabled by a Sulfonamide-Based Electrolyte. *Nat. Energy* **2021**, *6*, 495−505.

(185) Zhao, Q.; Stalin, S.; Archer, L. A. Stabilizing Metal Battery Anodes through the Design of Solid Electrolyte Interphases. *Joule* **2021**, *5*, 1119−1142.

(186) Jiang, F. N.; Cheng, X. B.; Yang, S. J.; Xie, J.; Yuan, H.; Liu, L.; Huang, J. Q.; Zhang, Q. Thermoresponsive Electrolytes for Safe Lithium-Metal Batteries. *Adv. Mater.* **2023**, *35*, No. e2209114.

(187) Xia, L.; Xia, Y.; Liu, Z. A Novel Fluorocyclophosphazene as Bifunctional Additive for Safer Lithium-Ion Batteries. *J. Power Sources* **2015**, *278*, 190−196.

(188) Zhang, S. S.; Xu, K.; Jow, T. R. A Thermal Stabilizer for LiPF$_6$-Based Electrolytes of Li-Ion Cells. *Electrochem. Solid-State Lett.* **2002**, *5*, A206−A208.

(189) Buhrmester, C.; Chen, J.; Moshurchak, L.; Jiang, J.; Wang, R. L.; Dahn, J. R. Studies of Aromatic Redox Shuttle Additives for LiFePO$_4$-Based Li-Ion Cells. *J. Electrochem. Soc.* **2005**, *152*, A2390.

(190) Chen, J.; Buhrmester, C.; Dahn, J. R. Chemical Overcharge and Overdischarge Protection for Lithium-Ion Batteries. *Electrochem. Solid-State Lett.* **2005**, *8*, A59−A62.

(191) Wang, Y.; Li, Z.; Hou, Y.; Hao, Z.; Zhang, Q.; Ni, Y.; Lu, Y.; Yan, Z.; Zhang, K.; Zhao, Q.; et al. Emerging Electrolytes with Fluorinated Solvents for Rechargeable Lithium-Based Batteries. *Chem. Soc. Rev.* **2023**, *52*, 2713−2763.

(192) Hall, D. S.; Self, J.; Dahn, J. R. Dielectric Constants for Quantum Chemistry and Li-Ion Batteries: Solvent Blends of Ethylene Carbonate and Ethyl Methyl Carbonate. *J. Phys. Chem. C* **2015**, *119*, 22322−22330.

(193) Meyer, W. H. Polymer Electrolytes for Lithium-Ion Batteries. *Adv. Mater.* **1998**, *10*, 439−448.

(194) Young, W.-S.; Albert, J. N. L.; Schantz, A. B.; Epps, T. H. Mixed-Salt Effects on the Ionic Conductivity of Lithium-Doped PEO-Containing Block Copolymers. *Macromolecules* **2011**, *44*, 8116−8123.

(195) Su, Y.; Rong, X.; Gao, A.; Liu, Y.; Li, J.; Mao, M.; Qi, X.; Chai, G.; Zhang, Q.; Suo, L.; et al. Rational Design of a Topological Polymeric Solid Electrolyte for High-Performance All-Solid-State Alkali Metal Batteries. *Nat. Commun.* **2022**, *13*, 4181.

(196) Sun, Y.; Zhang, X.; Ma, C.; Guo, N.; Liu, Y.; Liu, J.; Xie, H. Fluorine-Containing Triblock Copolymers as Solid-State Polymer Electrolytes for Lithium Metal Batteries. *J. Power Sources* **2021**, *516*, 230686.

(197) Jia, M.; Wen, P.; Wang, Z.; Zhao, Y.; Liu, Y.; Lin, J.; Chen, M.; Lin, X. Fluorinated Bifunctional Solid Polymer Electrolyte Synthesized under Visible Light for Stable Lithium Deposition and Dendrite-Free All-Solid-State Batteries. *Adv. Funct. Mater.* **2021**, *31*, 2101736.

(198) Sun, H.; Xie, X.; Huang, Q.; Wang, Z.; Chen, K.; Li, X.; Gao, J.; Li, Y.; Li, H.; Qiu, J.; et al. Fluorinated Poly-oxalate Electrolytes Stabilizing both Anode and Cathode Interfaces for All-Solid-State Li/NMC811 Batteries. *Angew. Chem., Int. Ed.* **2021**, *60*, 18335−18343.

(199) Shi, P.; Ma, J.; Liu, M.; Guo, S.; Huang, Y.; Wang, S.; Zhang, L.; Chen, L.; Yang, K.; Liu, X.; et al. A Dielectric Electrolyte Composite with High Lithium-Ion Conductivity for High-Voltage Solid-State Lithium Metal Batteries. *Nat. Nanotechnol.* **2023**, *18*, 602−610.

(200) Tsuchida, E.; Ohno, H.; Tsunemi, K. Conduction of Lithium Ions in Polyvinylidene Fluoride and Its Derivatives−I. *Electrochim. Acta* **1983**, *28*, 591−595.

(201) Jiang, Z.; Carroll, B.; Abraham, K. M. Studies of Some Poly(vinylidene fluoride) Electrolytes. *Electrochim. Acta* **1997**, *42*, 2667−2677.

(202) Feinauer, M.; Euchner, H.; Fichtner, M.; Reddy, M. A. Unlocking the Potential of Fluoride-Based Solid Electrolytes for Solid-State Lithium Batteries. *ACS Appl. Energy Mater.* **2019**, *2*, 7196−7203.

(203) Hu, J.; Yao, Z.; Chen, K.; Li, C. High-Conductivity Open Framework Fluorinated Electrolyte Bonded by Solidified Ionic Liquid Wires for Solid-State Li Metal Batteries. *Energy Storage Mater.* **2020**, *28*, 37−46.

(204) Zhang, B.; Zhong, J.; Zhang, Y.; Yang, L.; Yang, J.; Li, S.; Wang, L.-W.; Pan, F.; Lin, Z. Discovering a New Class of Fluoride Solid-Electrolyte Materials via Screening the Structural Property of Li-Ion Sublattice. *Nano Energy* **2021**, *79*, 105407.

(205) Arnold, W.; Shreyas, V.; Li, Y.; Koralalage, M. K.; Jasinski, J. B.; Thapa, A.; Sumanasekera, G.; Ngo, A. T.; Narayanan, B.; Wang, H. Synthesis of Fluorine-Doped Lithium Argyrodite Solid Electrolytes for Solid-State Lithium Metal Batteries. *ACS Appl. Mater. Interfaces* **2022**, *14*, 11483−11492.

(206) Li, X.; Ren, Z.; Norouzi Banis, M.; Deng, S.; Zhao, Y.; Sun, Q.; Wang, C.; Yang, X.; Li, W.; Liang, J.; et al. Unravelling the Chemistry and Microstructure Evolution of a Cathodic Interface in Sulfide-Based All-Solid-State Li-Ion Batteries. *ACS Energy Lett.* **2019**, *4*, 2480−2488.

(207) Ryu, H.-H.; Namkoong, B.; Kim, J.-H.; Belharouak, I.; Yoon, C. S.; Sun, Y.-K. Capacity Fading Mechanisms in Ni-Rich Single-Crystal NCM Cathodes. *ACS Energy Lett.* **2021**, *6*, 2726−2734.

(208) Wan, H.; Zhang, J.; Xia, J.; Ji, X.; He, X.; Liu, S.; Wang, C. F and N Rich Solid Electrolyte for Stable All-Solid-State Battery. *Adv. Funct. Mater.* **2022**, *32*, 2110876.

(209) Zhao, F.; Sun, Q.; Yu, C.; Zhang, S.; Adair, K.; Wang, S.; Liu, Y.; Zhao, Y.; Liang, J.; Wang, C.; et al. Ultrastable Anode Interface Achieved by Fluorinating Electrolytes for All-Solid-State Li Metal Batteries. *ACS Energy Lett.* **2020**, *5*, 1035−1043.

(210) Liu, J.; Wang, J.; Zhu, L.; Chen, X.; Ma, Q.; Wang, L.; Wang, X.; Yan, W. A High-Safety and Multifunctional MOFs Modified Aramid Nanofiber Separator for Lithium-Sulfur Batteries. *Chem. Eng. J.* **2021**, *411*, 128540.

(211) Feng, X.; Ren, D.; He, X.; Ouyang, M. Mitigating Thermal Runaway of Lithium-Ion Batteries. *Joule* **2020**, *4*, 743−770.

(212) Choi, S.-S.; Lee, Y. S.; Joo, C. W.; Lee, S. G.; Park, J. K.; Han, K.-S. Electrospun PVDF Nanofiber Web as Polymer Electrolyte or Separator. *Electrochim. Acta* **2004**, *50*, 339−343.

(213) Liang, Y.; Lin, Z.; Qiu, Y.; Zhang, X. Fabrication and Characterization of LATP/PAN Composite Fiber-Based Lithium-Ion Battery Separators. *Electrochim. Acta* **2011**, *56*, 6474−6480.

(214) Lee, P.-C.; Han, T.-H.; Hwang, T.; Oh, J.-S.; Kim, S.-J.; Kim, B.-W.; Lee, Y.; Choi, H. R.; Jeoung, S. K.; Yoo, S. E.; et al. Electrochemical Double Layer Capacitor Performance of Electrospun Polymer Fiber-Electrolyte Membrane Fabricated by Solvent-Assisted and Thermally Induced Compression Molding Processes. *J. Membr. Sci.* **2012**, *409−410*, 365−370.

(215) Kim, Y.-J.; Kim, H.-S.; Doh, C.-H.; Kim, S. H.; Lee, S.-M. Technological Potential and Issues of Polyacrylonitrile Based Nanofiber Non-woven Separator for Li-Ion Rechargeable Batteries. *J. Power Sources* **2013**, *244*, 196−206.

(216) Cai, M.; Yuan, D.; Zhang, X.; Pu, Y.; Liu, X.; He, H.; Zhang, L.; Ning, X. Lithium Ion Battery Separator with Improved Performance via Side-by-Side Bicomponent Electrospinning of PVDF-HFP/PI Followed by 3D Thermal Crosslinking. *J. Power Sources* **2020**, *461*, 228123.

(217) Hwang, K.; Kwon, B.; Byun, H. Preparation of PVdF Nanofiber Membranes by Electrospinning and Their Use as Secondary Battery Separators. *J. Membr. Sci.* **2011**, *378*, 111−116.

(218) Orendorff, C. J.; Lambert, T. N.; Chavez, C. A.; Bencomo, M.; Fenton, K. R. Polyester Separators for Lithium-Ion Cells: Improving Thermal Stability and Abuse Tolerance. *Adv. Energy Mater.* **2013**, *3*, 314−320.

(219) Croce, F.; Focarete, M. L.; Hassoun, J.; Meschini, I.; Scrosati, B. A Safe, High-Rate and High-Energy Polymer Lithium-Ion Battery Based on Gelled Membranes Prepared by Electrospinning. *Energy Environ. Sci.* **2011**, *4*, 921–927.

(220) Raghavan, P.; Zhao, X.; Shin, C.; Baek, D.-H.; Choi, J.-W.; Manuel, J.; Heo, M.-Y.; Ahn, J.-H.; Nah, C. Preparation and Electrochemical Characterization of Polymer Electrolytes Based on Electrospun Poly(vinylidene Fluoride-Co-Hexafluoropropylene)/Polyacrylonitrile Blend/Composite Membranes for Lithium Batteries. *J. Power Sources* **2010**, *195*, 6088–6094.

(221) Zhou, X.; Yue, L.; Zhang, J.; Kong, Q.; Liu, Z.; Yao, J.; Cui, G. A Core-Shell Structured Polysulfonamide-Based Composite Nonwoven towards High Power Lithium Ion Battery Separator. *J. Electrochem. Soc.* **2013**, *160*, A1341–A1347.

(222) Zhang, F.; Ma, X.; Cao, C.; Li, J.; Zhu, Y. Poly(vinylidene fluoride)/SiO$_2$ Composite Membranes Prepared by Electrospinning and Their Excellent Properties for Nonwoven Separators for Lithium-Ion Batteries. *J. Power Sources* **2014**, *251*, 423–431.

(223) Hao, J.; Lei, G.; Li, Z.; Wu, L.; Xiao, Q.; Wang, L. A Novel Polyethylene Terephthalate Nonwoven Separator Based on Electrospinning Technique for Lithium Ion Battery. *J. Membr. Sci.* **2013**, *428*, 11–16.

(224) Zhang, C.; Bai, Y.; Sun, Y.; Gu, J.; Xu, Y. Preparation of Hydrophilic HDPE Porous Membranes via Thermally Induced Phase Separation by Blending of Amphiphilic PE-b-PEG Copolymer. *J. Membr. Sci.* **2010**, *365*, 216–224.

(225) Zhai, Y.; Wang, N.; Mao, X.; Si, Y.; Yu, J.; Al-Deyab, S. S.; El-Newehy, M.; Ding, B. Sandwich-Structured PVdF/PMIA/PVdF Nanofibrous Separators with Robust Mechanical Strength and Thermal Stability for Lithium-Ion Batteries. *J. Mater. Chem. A* **2014**, *2*, 14511–14518.

(226) Lee, Y. M.; Kim, J.-W.; Choi, N.-S.; Lee, J. A.; Seol, W.-H.; Park, J.-K. Novel Porous Separator Based on PVdF and PE Nonwoven Matrix for Rechargeable Lithium Batteries. *J. Power Sources* **2005**, *139*, 235–241.

(227) Song, K. W.; Kim, C. K. Coating with Macroporous Polyarylate via a Nonsolvent Induced Phase Separation Process for Enhancement of Polyethylene Separator Thermal Stability. *J. Membr. Sci.* **2010**, *352*, 239–246.

(228) Ryou, M. H.; Lee, Y. M.; Park, J. K.; Choi, J. W. Mussel-Inspired Polydopamine-Treated Polyethylene Separators for High-Power Li-Ion Batteries. *Adv. Mater.* **2011**, *23*, 3066–3070.

(229) Dai, J.; Shi, C.; Li, C.; Shen, X.; Peng, L.; Wu, D.; Sun, D.; Zhang, P.; Zhao, J. A Rational Design of Separator with Substantially Enhanced Thermal Features for Lithium-Ion Batteries by the Polydopamine-Ceramic Composite Modification of Polyolefin Membranes. *Energy Environ. Sci.* **2016**, *9*, 3252–3261.

(230) Yang, C. L.; Li, Z. H.; Li, W. J.; Liu, H. Y.; Xiao, Q. Z.; Lei, G. T.; Ding, Y. H. Batwing-Like Polymer Membrane Consisting of PMMA-Grafted Electrospun PVdF-SiO$_2$ Nanocomposite Fibers for Lithium-Ion Batteries. *J. Membr. Sci.* **2015**, *495*, 341–350.

(231) Li, S.; Gao, K. The Study on Methyl Methacrylate Graft-Copolymerized Composite Separator Prepared by Pre-irradiation Method for Li-Ion Batteries. *Surf. Coat. Technol.* **2010**, *204*, 2822–2828.

(232) Jin, S. Y.; Manuel, J.; Zhao, X.; Park, W. H.; Ahn, J.-H. Surface-Modified Polyethylene Separator via Oxygen Plasma Treatment for Lithium Ion Battery. *J. Ind. Eng. Chem.* **2017**, *45*, 15–21.

(233) Li, X.; He, J.; Wu, D.; Zhang, M.; Meng, J.; Ni, P. Development of Plasma-Treated Polypropylene Nonwoven-Based Composites for High-Performance Lithium-Ion Battery Separators. *Electrochim. Acta* **2015**, *167*, 396–403.

(234) Bicy, K.; Gueye, A. B.; Rouxel, D.; Kalarikkal, N.; Thomas, S. Lithium-Ion Battery Separators Based on Electrospun PVDF: A Review. *Surf. Interfaces* **2022**, *31*, 101977.

(235) Costa, C. M.; Silva, M. M.; Lanceros-Méndez, S. Battery Separators Based on Vinylidene Fluoride (VDF) Polymers and Copolymers for Lithium Ion Battery Applications. *RSC Adv.* **2013**, *3*, 11404.

(236) Abbrent, S.; Plestil, J.; Hlavata, D.; Lindgren, J.; Tegenfeldt, J.; Wendsjö, Å. Crystallinity and Morphology of PVdF-HFP-Based Gel Electrolytes. *Polymer* **2001**, *42*, 1407–1416.

(237) Wu, Q.-Y.; Liang, H.-Q.; Gu, L.; Yu, Y.; Huang, Y.-Q.; Xu, Z.-K. PVDF/PAN Blend Separators via Thermally Induced Phase Separation for Lithium Ion Batteries. *Polymer* **2016**, *107*, 54–60.

(238) Chen, W.; Liu, Y.; Ma, Y.; Liu, J.; Liu, X. Improved Performance of PVdF-HFP/PI Nanofiber Membrane for Lithium-Ion Battery Separator Prepared by a Bicomponent Cross-Electrospinning Method. *Mater. Lett.* **2014**, *133*, 67–70.

(239) Bicy, K.; Mathew, D. E.; Stephen, A. M.; Royaud, I.; Poncot, M.; Godard, O.; Aranda, L.; Rouxel, D.; Kalarikkal, N.; Thomas, S. Sustainable Lithium-Ion Battery Separators Derived from Polyethylene Oxide/Lignocellulose Coated Electrospun P(VDF-TrFE) Nanofibrous Membranes. *Surf. Interfaces* **2022**, *29*, 101716.

(240) K, B.; Paul P, A.; Kalarikkal, N.; Stephen, A. M.; G, G. V.; Rouxel, D.; Thomas, S. Effects of Nanofillers on Morphology and Surface Wetting of Microporous Polypropylene Composite Membranes. *Mater. Chem. Phys.* **2021**, *257*, 123742.

(241) Xiao, J.; Zhai, P.; Wei, Y.; Zhang, X.; Yang, W.; Cui, S.; Jin, C.; Liu, W.; Wang, X.; Jiang, H.; et al. In-Situ Formed Protecting Layer from Organic/Inorganic Concrete for Dendrite-Free Lithium Metal Anodes. *Nano Lett.* **2020**, *20*, 3911–3917.

(242) Jeon, I.-Y.; Ju, M. J.; Xu, J.; Choi, H.-J.; Seo, J.-M.; Kim, M.-J.; Choi, I. T.; Kim, H. M.; Kim, J. C.; Lee, J.-J.; et al. Edge-Fluorinated Graphene Nanoplatelets as High Performance Electrodes for Dye-Sensitized Solar Cells and Lithium Ion Batteries. *Adv. Funct. Mater.* **2015**, *25*, 1170–1179.

(243) Sun, S.; Wang, J.; Chen, X.; Ma, Q.; Wang, Y.; Yang, K.; Yao, X.; Yang, Z.; Liu, J.; Xu, H.; et al. Thermally Stable and Dendrite-Resistant Separators toward Highly Robust Lithium Metal Batteries. *Adv. Energy Mater.* **2022**, *12*, 2202206.

(244) Qian, Y.; Chen, K.; Feng, Z.; Ouyang, Y.; Lan, Q.; Zhang, C.; Feng, W.; Miao, Y.-E.; Liu, T. A Fluorinated-Polyimide-Based Composite Nanofibrous Separator with Homogenized Pore Size for Wide-Temperature Lithium Metal Batteries. *Small Struct.* **2023**, *4*, 2200383.

(245) Zhang, K.; Li, X.; Ma, L.; Chen, F.; Chen, Z.; Yuan, Y.; Zhao, Y.; Yang, J.; Liu, J.; Xie, K.; et al. Fluorinated Covalent Organic Framework-Based Nanofluidic Interface for Robust Lithium-Sulfur Batteries. *ACS Nano* **2023**, *17*, 2901–2911.

(246) Wang, Z.; Zhang, J.; Yang, Y.; Yue, X.; Hao, X.; Sun, W.; Rooney, D.; Sun, K. Flexible Carbon Nanofiber/Polyvinylidene Fluoride Composite Membranes as Interlayers in High-Performance Lithium Sulfur Batteries. *J. Power Sources* **2016**, *329*, 305–313.

(247) Wei, H.; Ma, J.; Li, B.; Zuo, Y.; Xia, D. Enhanced Cycle Performance of Lithium-Sulfur Batteries Using a Separator Modified with a PVDF-C Layer. *ACS Appl. Mater. Interfaces* **2014**, *6*, 20276–20281.

(248) Vizintin, A.; Lozinšek, M.; Chellappan, R. K.; Foix, D.; Krajnc, A.; Mali, G.; Drazic, G.; Genorio, B.; Dedryvère, R.; Dominko, R. Fluorinated Reduced Graphene Oxide as an Interlayer in Li-S Batteries. *Chem. Mater.* **2015**, *27*, 7070–7081.

(249) Xia, S.; Zhang, X.; Yang, G.; Shi, L.; Cai, L.; Xia, Y.; Yang, J.; Zheng, S. Bifunctional Fluorinated Separator Enabling Polysulfide Trapping and Li Deposition for Lithium-Sulfur Batteries. *ACS Appl. Mater. Interfaces* **2021**, *13*, 11920–11929.

(250) Xiong, P.; Zhang, F.; Zhang, X.; Liu, Y.; Wu, Y.; Wang, S.; Safaei, J.; Sun, B.; Ma, R.; Liu, Z.; et al. Atomic-Scale Regulation of Anionic and Cationic Migration in Alkali Metal Batteries. *Nat. Commun.* **2021**, *12*, 4184.

(251) Liu, W.; Zhang, K.; Ma, L.; Ning, R.; Chen, Z.; Li, J.; Yan, Y.; Shang, T.; Lyu, Z.; Li, Z.; et al. An Ion Sieving Conjugated Microporous Thermoset Ultrathin Membrane for High-Performance Li-S Battery. *Energy Storage Mater.* **2022**, *49*, 1–10.

(252) Zou, F.; Manthiram, A. A Review of the Design of Advanced Binders for High-Performance Batteries. *Adv. Energy Mater.* **2020**, *10*, 2002508.

(253) Huang, S.; Ren, J.; Liu, R.; Yue, M.; Huang, Y.; Yuan, G. The Progress of Novel Binder as a Non-ignorable Part to Improve the Performance of Si-Based Anodes for Li-Ion Batteries. *Int. J. Energy Res.* **2018**, *42*, 919−935.

(254) Ai, G.; Dai, Y.; Ye, Y.; Mao, W.; Wang, Z.; Zhao, H.; Chen, Y.; Zhu, J.; Fu, Y.; Battaglia, V.; et al. Investigation of Surface Effects Through the Application of Functional Binders in Lithium-Sulfur Batteries. *Nano Energy* **2015**, *16*, 28−37.

(255) Kwon, T. W.; Choi, J. W.; Coskun, A. The Emerging Era of Supramolecular Polymeric Binders in Silicon Anodes. *Chem. Soc. Rev.* **2018**, *47*, 2145−2164.

(256) Chen, H.; Ling, M.; Hencz, L.; Ling, H. Y.; Li, G.; Lin, Z.; Liu, G.; Zhang, S. Exploring Chemical, Mechanical, and Electrical Functionalities of Binders for Advanced Energy-Storage Devices. *Chem. Rev.* **2018**, *118*, 8936−8982.

(257) Fu, Z.; Feng, H. L.; Xiang, X. D.; Rao, M. M.; Wu, W.; Luo, J. C.; Chen, T. T.; Hu, Q. P.; Feng, A. B.; Li, W. S. A Novel Polymer Composite as Cathode Binder of Lithium-Ion Batteries with Improved Rate Capability and Cyclic Stability. *J. Power Sources* **2014**, *261*, 170−174.

(258) Byun, S.; Choi, J.; Roh, Y.; Song, D.; Ryou, M.-H.; Lee, Y. M. Mechanical Robustness of Composite Electrode for Lithium-Ion Battery: Insight into Entanglement & Crystallinity of Polymeric Binder. *Electrochim. Acta* **2020**, *332*, 135471.

(259) Huang, H.; Li, Z.; Gu, S.; Bian, J.; Li, Y.; Chen, J.; Liao, K.; Gan, Q.; Wang, Y.; Wu, S.; et al. Dextran Sulfate Lithium as Versatile Binder to Stabilize High-Voltage LiCoO₂ to 4.6 V. *Adv. Energy Mater.* **2021**, *11*, 2101864.

(260) Pieczonka, N. P. W.; Borgel, V.; Ziv, B.; Leifer, N.; Dargel, V.; Aurbach, D.; Kim, J.-H.; Liu, Z.; Huang, X.; Krachkovskiy, S. A.; et al. Lithium Polyacrylate (LiPAA) as an Advanced Binder and a Passivating Agent for High-Voltage Li-Ion Batteries. *Adv. Energy Mater.* **2015**, *5*, 1501008.

(261) Liang, J.; Chen, D.; Adair, K.; Sun, Q.; Holmes, N. G.; Zhao, Y.; Sun, Y.; Luo, J.; Li, R.; Zhang, L.; et al. Insight into Prolonged Cycling Life of 4 V All-Solid-State Polymer Batteries by a High-Voltage Stable Binder. *Adv. Energy Mater.* **2021**, *11*, 2002455.

(262) Pham, H. Q.; Kim, G.; Jung, H. M.; Song, S.-W. Fluorinated Polyimide as a Novel High-Voltage Binder for High-Capacity Cathode of Lithium-Ion Batteries. *Adv. Funct. Mater.* **2018**, *28*, 1704690.

(263) Li, J.; Le, D.-B.; Ferguson, P. P.; Dahn, J. R. Lithium Polyacrylate as a Binder for Tin-Cobalt-Carbon Negative Electrodes in Lithium-Ion Batteries. *Electrochim. Acta* **2010**, *55*, 2991−2995.

(264) Tsao, C.-H.; Hsu, C.-H.; Kuo, P.-L. Ionic Conducting and Surface Active Binder of Poly(ethylene oxide)-Block-Poly-(acrylonitrile) for High Power Lithium-Ion Battery. *Electrochim. Acta* **2016**, *196*, 41−47.

(265) Wei, Z.; Xue, L.; Nie, F.; Sheng, J.; Shi, Q.; Zhao, X. Study of Sulfonated Polyether Ether Ketone with Pendant Lithiated Fluorinated Sulfonic Groups as Ion-Conductive Binder in Lithium-Ion Batteries. *J. Power Sources* **2014**, *256*, 28−31.

(266) Shi, Q.; Xue, L.; Wei, Z.; Liu, F.; Du, X.; Desmarteau, D. D. Improvement in LiFePO₄-Li Battery Performance via Poly-(perfluoroalkylsulfonyl)imide (PFSI) Based Ionene Composite Binder. *J. Mater. Chem. A* **2013**, *1*, 15016.

(267) Chiu, K.-F.; Su, S. H.; Leu, H.-J.; Chen, Y. S. Application of Lithiated Perfluorosulfonate Ionomer Binders to Enhance High Rate Capability in LiMn₂O₄ Cathodes for Lithium-Ion Batteries. *Electrochim. Acta* **2014**, *117*, 134−138.

(268) Vauthier, S.; Alvarez-Tirado, M.; Guzmán-González, G.; Tomé, L. C.; Cotte, S.; Castro, L.; Guéguen, A.; Mecerreyes, D.; Casado, N. High-Performance Pyrrolidinium-Based Poly(ionic Liquid) Binders for Li-Ion and Li-Air Batteries. *Mater. Today Chem.* **2023**, *27*, 101293.

(269) Tsao, C.-H.; Wu, E. T.; Lee, W.-H.; Chiu, C.-C.; Kuo, P.-L. Fluorinated Copolymer Functionalized with Ethylene Oxide as Novel Water-Borne Binder for a High-Power Lithium Ion Battery: Synthesis, Mechanism, and Application. *ACS Appl. Energy Mater.* **2018**, *1*, 3999−4008.

(270) Lee, J. I.; Kang, H.; Park, K. H.; Shin, M.; Hong, D.; Cho, H. J.; Kang, N. R.; Lee, J.; Lee, S. M.; Kim, J. Y.; et al. Amphiphilic Graft Copolymers as a Versatile Binder for Various Electrodes of High-Performance Lithium-Ion Batteries. *Small* **2016**, *12*, 3119−3127.

(271) Cai, Y.; Li, Y.; Jin, B.; Ali, A.; Ling, M.; Cheng, D.; Lu, J.; Hou, Y.; He, Q.; Zhan, X.; et al. Dual Cross-Linked Fluorinated Binder Network for High-Performance Silicon and Silicon Oxide Based Anodes in Lithium-Ion Batteries. *ACS Appl. Mater. Interfaces* **2019**, *11*, 46800−46807.

(272) Preman, A. N.; Lee, H.; Yoo, J.; Kim, I. T.; Saito, T.; Ahn, S.-K. Progress of 3D Network Binders in Silicon Anodes for Lithium Ion Batteries. *J. Mater. Chem. A* **2020**, *8*, 25548−25570.

(273) Li, S.; Liu, Y.-M.; Zhang, Y.-C.; Song, Y.; Wang, G.-K.; Liu, Y.-X.; Wu, Z.-G.; Zhong, B.-H.; Zhong, Y.-J.; Guo, X.-D. A Review of Rational Design and Investigation of Binders Applied in Silicon-Based Anodes for Lithium-Ion Batteries. *J. Power Sources* **2021**, *485*, 229331.

(274) Li, J.; Christensen, L.; Obrovac, M. N.; Hewitt, K. C.; Dahn, J. R. Effect of Heat Treatment on Si Electrodes Using Polyvinylidene Fluoride Binder. *J. Electrochem. Soc.* **2008**, *155*, A234.

(275) Chen, Z.; Christensen, L.; Dahn, J. R. Large-Volume-Change Electrodes for Li-Ion Batteries of Amorphous Alloy Particles Held by Elastomeric Tethers. *Electrochem. commun.* **2003**, *5*, 919−923.

(276) Rongeat, C.; Anji Reddy, M.; Witter, R.; Fichtner, M. Solid Electrolytes for Fluoride Ion Batteries: Ionic Conductivity in Polycrystalline Tysonite-Type Fluorides. *ACS Appl. Mater. Interfaces* **2014**, *6*, 2103−2110.

(277) Choi, S.; Kwon, T. W.; Coskun, A.; Choi, J. W. Highly Elastic Binders Integrating Polyrotaxanes for Silicon Microparticle Anodes in Lithium Ion Batteries. *Science* **2017**, *357*, 279−283.

(278) Koo, B.; Kim, H.; Cho, Y.; Lee, K. T.; Choi, N. S.; Cho, J. A Highly Cross-Linked Polymeric Binder for High-Performance Silicon Negative Electrodes in Lithium-Ion Batteries. *Angew. Chem., Int. Ed.* **2012**, *51*, 8762−8767.

(279) Li, C.; Shi, T.; Yoshitake, H.; Wang, H. Improved Performance in Micron-Sized Silicon Anodes by In Situ Polymer-ization of Acrylic Acid-Based Slurry. *J. Mater. Chem. A* **2016**, *4*, 16982−16991.

(280) Song, J.; Zhou, M.; Yi, R.; Xu, T.; Gordin, M. L.; Tang, D.; Yu, Z.; Regula, M.; Wang, D. Interpenetrated Gel Polymer Binder for High-Performance Silicon Anodes in Lithium-ion Batteries. *Adv. Funct. Mater.* **2014**, *24*, 5904−5910.

(281) Qin, D.; Xue, L.; Du, B.; Wang, J.; Nie, F.; Wen, L. Flexible Fluorine-Containing Ionic Binders to Mitigate the Negative Impact Caused by the Drastic Volume Fluctuation from Silicon Nanoparticles in High-Capacity Anodes of Lithium-Ion Batteries. *J. Mater. Chem. A* **2015**, *3*, 10928−10934.

(282) Wang, L.; He, X.; Li, J.; Gao, J.; Fang, M.; Tian, G.; Wang, J.; Fan, S. Graphene-Coated Plastic Film as Current Collector for Lithium/Sulfur Batteries. *J. Power Sources* **2013**, *239*, 623−627.

(283) Gabryelczyk, A.; Ivanov, S.; Bund, A.; Lota, G. Corrosion of aluminium current collector in lithium-ion batteries: A review. *J. Energy Storage* **2021**, *43*, 103226.

(284) Zheng, J.; Engelhard, M. H.; Mei, D.; Jiao, S.; Polzin, B. J.; Zhang, J.-G.; Xu, W. Electrolyte Additive Enabled Fast Charging and Stable Cycling Lithium Metal Batteries. *Nat. Energy* **2017**, *2*, 17012.

(285) Ding, F.; Xu, W.; Graff, G. L.; Zhang, J.; Sushko, M. L.; Chen, X.; Shao, Y.; Engelhard, M. H.; Nie, Z.; Xiao, J.; et al. Dendrite-Free Lithium Deposition via Self-Healing Electrostatic Shield Mechanism. *J. Am. Chem. Soc.* **2013**, *135*, 4450−4456.

(286) Yan, C.; Cheng, X.-B.; Zhao, C.-Z.; Huang, J.-Q.; Yang, S.-T.; Zhang, Q. Lithium Metal Protection Through In-Situ Formed Solid Electrolyte Interphase in Lithium-Sulfur Batteries: The Role of Polysulfides on Lithium Anode. *J. Power Sources* **2016**, *327*, 212−220.

(287) Cheng, X. B.; Zhao, M. Q.; Chen, C.; Pentecost, A.; Maleski, K.; Mathis, T.; Zhang, X. Q.; Zhang, Q.; Jiang, J.; Gogotsi, Y. Nanodiamonds Suppress the Growth of Lithium Dendrites. *Nat. Commun.* **2017**, *8*, 336.

(288) Li, N. W.; Yin, Y. X.; Yang, C. P.; Guo, Y. G. An Artificial Solid Electrolyte Interphase Layer for Stable Lithium Metal Anodes. *Adv. Mater.* **2016**, *28*, 1853−1858.

(289) Zhao, J.; Liao, L.; Shi, F.; Lei, T.; Chen, G.; Pei, A.; Sun, J.; Yan, K.; Zhou, G.; Xie, J.; et al. Surface Fluorination of Reactive Battery Anode Materials for Enhanced Stability. *J. Am. Chem. Soc.* **2017**, *139*, 11550−11558.

(290) Fu, K.; Gong, Y.; Hitz, G. T.; Mcowen, D. W.; Li, Y.; Xu, S.; Wen, Y.; Zhang, L.; Wang, C.; Pastel, G.; et al. Three-Dimensional Bilayer Garnet Solid Electrolyte Based High Energy Density Lithium Metal-Sulfur Batteries. *Energy Environ. Sci.* **2017**, *10*, 1568−1575.

(291) Liu, Y.; Lin, D.; Yuen, P. Y.; Liu, K.; Xie, J.; Dauskardt, R. H.; Cui, Y. An Artificial Solid Electrolyte Interphase with High Li-Ion Conductivity, Mechanical Strength, and Flexibility for Stable Lithium Metal Anodes. *Adv. Mater.* **2017**, *29*, 1605531.

(292) Pang, Q.; Liang, X.; Shyamsunder, A.; Nazar, L. F. An In Vivo Formed Solid Electrolyte Surface Layer Enables Stable Plating of Li Metal. *Joule* **2017**, *1*, 871−886.

(293) Liu, W.; Lin, D.; Pei, A.; Cui, Y. Stabilizing Lithium Metal Anodes by Uniform Li-Ion Flux Distribution in Nanochannel Confinement. *J. Am. Chem. Soc.* **2016**, *138*, 15443−15450.

(294) Cheng, X. B.; Hou, T. Z.; Zhang, R.; Peng, H. J.; Zhao, C. Z.; Huang, J. Q.; Zhang, Q. Dendrite-Free Lithium Deposition Induced by Uniformly Distributed Lithium Ions for Efficient Lithium Metal Batteries. *Adv. Mater.* **2016**, *28*, 2888−2895.

(295) Li, N.; Ye, Q.; Zhang, K.; Yan, H.; Shen, C.; Wei, B.; Xie, K. Normalized Lithium Growth from the Nucleation Stage for Dendrite-Free Lithium Metal Anodes. *Angew. Chem., Int. Ed.* **2019**, *58*, 18246−18251.

(296) Chen, X.; Hou, T.-Z.; Li, B.; Yan, C.; Zhu, L.; Guan, C.; Cheng, X.-B.; Peng, H.-J.; Huang, J.-Q.; Zhang, Q. Towards Stable Lithium-Sulfur Batteries: Mechanistic Insights into Electrolyte Decomposition on Lithium Metal Anode. *Energy Storage Mater.* **2017**, *8*, 194−201.

(297) Zuo, T. T.; Wu, X. W.; Yang, C. P.; Yin, Y. X.; Ye, H.; Li, N. W.; Guo, Y. G. Graphitized Carbon Fibers as Multifunctional 3D Current Collectors for High Areal Capacity Li Anodes. *Adv. Mater.* **2017**, *29*, 1700389.

(298) Zhang, R.; Chen, X. R.; Chen, X.; Cheng, X. B.; Zhang, X. Q.; Yan, C.; Zhang, Q. Lithiophilic Sites in Doped Graphene Guide Uniform Lithium Nucleation for Dendrite-Free Lithium Metal Anodes. *Angew. Chem., Int. Ed.* **2017**, *56*, 7764−7768.

(299) Sun, Y.; Zheng, G.; Seh, Z. W.; Liu, N.; Wang, S.; Sun, J.; Lee, H. R.; Cui, Y. Graphite-Encapsulated Li-Metal Hybrid Anodes for High-Capacity Li Batteries. *Chem.* **2016**, *1*, 287−297.

(300) Liu, L.; Yin, Y.-X.; Li, J.-Y.; Li, N.-W.; Zeng, X.-X.; Ye, H.; Guo, Y.-G.; Wan, L.-J. Free-Standing Hollow Carbon Fibers as High-Capacity Containers for Stable Lithium Metal Anodes. *Joule* **2017**, *1*, 563−575.

(301) Yang, Q.; Li, C. Li Metal Batteries and Solid State Batteries Benefiting from Halogen-Based Strategies. *Energy Storage Mater.* **2018**, *14*, 100−117.

(302) Li, T.; Zhang, X.-Q.; Shi, P.; Zhang, Q. Fluorinated Solid-Electrolyte Interphase in High-Voltage Lithium Metal Batteries. *Joule* **2019**, *3*, 2647−2661.

(303) Wang, Y.; Liang, J.; Song, X.; Jin, Z. Recent Progress in Constructing Halogenated Interfaces for Highly Stable Lithium Metal Anodes. *Energy Storage Mater.* **2023**, *54*, 732−775.

(304) Zhang, X. Q.; Chen, X.; Xu, R.; Cheng, X. B.; Peng, H. J.; Zhang, R.; Huang, J. Q.; Zhang, Q. Columnar Lithium Metal Anodes. *Angew. Chem., Int. Ed.* **2017**, *56*, 14207−14211.

(305) Luo, J.; Fang, C.-C.; Wu, N.-L. High Polarity Poly(vinylidene difluoride) Thin Coating for Dendrite-Free and High-Performance Lithium Metal Anodes. *Adv. Energy Mater.* **2018**, *8*, 1701482.

(306) Cheng, H.; Mao, Y.; Lu, Y.; Zhang, P.; Xie, J.; Zhao, X. Trace Fluorinated-Carbon-Nanotube-Induced Lithium Dendrite Elimination for High-Performance Lithium-Oxygen Cells. *Nanoscale* **2020**, *12*, 3424−3434.

(307) Cui, C.; Yang, C.; Eidson, N.; Chen, J.; Han, F.; Chen, L.; Luo, C.; Wang, P. F.; Fan, X.; Wang, C. A Highly Reversible, Dendrite-Free Lithium Metal Anode Enabled by a Lithium-Fluoride-Enriched Interphase. *Adv. Mater.* **2020**, *32*, No. e1906427.

(308) Li, Z.; Li, X.; Zhou, L.; Xiao, Z.; Zhou, S.; Zhang, X.; Li, L.; Zhi, L. A Synergistic Strategy for Stable Lithium Metal Anodes Using 3D Fluorine-Doped Graphene Shuttle-Implanted Porous Carbon Networks. *Nano Energy* **2018**, *49*, 179−185.

(309) Jamaluddin, A.; Sin, Y.-Y.; Adhitama, E.; Prayogi, A.; Wu, Y.-T.; Chang, J.-K.; Su, C.-Y. Fluorinated Graphene as a Dual-Functional Anode to Achieve Dendrite-Free and High-Performance Lithium Metal Batteries. *Carbon* **2022**, *197*, 141−151.

(310) Gao, Y.; Rojas, T.; Wang, K.; Liu, S.; Wang, D.; Chen, T.; Wang, H.; Ngo, A. T.; Wang, D. Low-Temperature and High-Rate-Charging Lithium Metal Batteries Enabled by an Electrochemically Active Monolayer-Regulated Interface. *Nat. Energy* **2020**, *5*, 534−542.

(311) Huang, G.; Chen, S.; Guo, P.; Tao, R.; Jie, K.; Liu, B.; Zhang, X.; Liang, J.; Cao, Y.-C. In Situ Constructing Lithiophilic NiFx Nanosheets on Ni Foam Current Collector for Stable Lithium Metal Anode via a Succinct Fluorination Strategy. *Chem. Eng. J.* **2020**, *395*, 125122.

(312) Cao, J.; Qian, G.; Lu, X.; Lu, X. Advanced Composite Lithium Metal Anodes with 3D Frameworks: Preloading Strategies, Interfacial Optimization, and Perspectives. *Small* **2023**, *19*, No. e2205653.

(313) Hou, W.; Li, S.; Liang, J.; Yuan, B.; Hu, R. Lithiophilic NiF$_2$ Coating Inducing LiF-Rich Solid Electrolyte Interphase by a Novel NF$_3$ Plasma Treatment for Highly Stable Li Metal Anode. *Electrochim. Acta* **2022**, *402*, 139561.

(314) Richards, W. D.; Miara, L. J.; Wang, Y.; Kim, J. C.; Ceder, G. Interface Stability in Solid-State Batteries. *Chem. Mater.* **2016**, *28*, 266−273.

(315) Mason, W. P.; Mayer, W. G. Physical Acoustics, Principles and Methods. *Phys. Today* **1965**, *18*, 67−67.

(316) Suo, L.; Xue, W.; Gobet, M.; Greenbaum, S. G.; Wang, C.; Chen, Y.; Yang, W.; Li, Y.; Li, J. Fluorine-Donating Electrolytes Enable Highly Reversible 5-V-Class Li Metal Batteries. *Proc. Natl. Acad. Sci. U.S.A.* **2018**, *115*, 1156−1161.

(317) Xu, R.; Zhang, X.-Q.; Cheng, X.-B.; Peng, H.-J.; Zhao, C.-Z.; Yan, C.; Huang, J.-Q. Artificial Soft-Rigid Protective Layer for Dendrite-Free Lithium Metal Anode. *Adv. Funct. Mater.* **2018**, *28*, 1705838.

(318) Chen, L.; Chen, K. S.; Chen, X.; Ramirez, G.; Huang, Z.; Geise, N. R.; Steinruck, H. G.; Fisher, B. L.; Shahbazian-Yassar, R.; Toney, M. F.; et al. Novel ALD Chemistry Enabled Low-Temperature Synthesis of Lithium Fluoride Coatings for Durable Lithium Anodes. *ACS Appl. Mater. Interfaces* **2018**, *10*, 26972−26981.

(319) Lin, D.; Liu, Y.; Chen, W.; Zhou, G.; Liu, K.; Dunn, B.; Cui, Y. Conformal Lithium Fluoride Protection Layer on Three-Dimensional Lithium by Nonhazardous Gaseous Reagent Freon. *Nano Lett.* **2017**, *17*, 3731−3737.

(320) Yan, C.; Cheng, X. B.; Yao, Y. X.; Shen, X.; Li, B. Q.; Li, W. J.; Zhang, R.; Huang, J. Q.; Li, H.; Zhang, Q. An Armored Mixed Conductor Interphase on a Dendrite-Free Lithium-Metal Anode. *Adv. Mater.* **2018**, *30*, No. e1804461.

(321) Pathak, R.; Chen, K.; Gurung, A.; Reza, K. M.; Bahrami, B.; Pokharel, J.; Baniya, A.; He, W.; Wu, F.; Zhou, Y.; et al. Fluorinated Hybrid Solid-Electrolyte-Interphase for Dendrite-Free Lithium Deposition. *Nat. Commun.* **2020**, *11*, 93.

(322) Yang, Q.; Hu, J.; Meng, J.; Li, C. C-F-rich Oil Drop as a Non-expendable Fluid Interface Modifier with Low Surface Energy to Stabilize a Li Metal Anode. *Energy Environ. Sci.* **2021**, *14*, 3621−3631.

(323) Fan, X.; Ji, X.; Han, F.; Yue, J.; Chen, J.; Chen, L.; Deng, T.; Jiang, J.; Wang, C. Fluorinated Solid Electrolyte Interphase Enables Highly Reversible Solid-State Li Metal Battery. *Sci. Adv.* **2018**, *4*, No. eaau9245.

(324) Hu, A.; Chen, W.; Du, X.; Hu, Y.; Lei, T.; Wang, H.; Xue, L.; Li, Y.; Sun, H.; Yan, Y.; et al. An Artificial Hybrid Interphase for an Ultrahigh-Rate and Practical Lithium Metal Anode. *Energy Environ. Sci.* **2021**, *14*, 4115−4124.

(325) Liu, S.; Ji, X.; Yue, J.; Hou, S.; Wang, P.; Cui, C.; Chen, J.; Shao, B.; Li, J.; Han, F.; et al. High Interfacial-Energy Interphase Promoting Safe Lithium Metal Batteries. *J. Am. Chem. Soc.* **2020**, *142*, 2438−2447.

(326) Wang, Y.; Liu, F.; Fan, G.; Qiu, X.; Liu, J.; Yan, Z.; Zhang, K.; Cheng, F.; Chen, J. Electroless Formation of a Fluorinated Li/Na Hybrid Interphase for Robust Lithium Anodes. *J. Am. Chem. Soc.* **2021**, *143*, 2829−2837.

(327) Yan, C.; Cheng, X. B.; Tian, Y.; Chen, X.; Zhang, X. Q.; Li, W. J.; Huang, J. Q.; Zhang, Q. Dual-Layered Film Protected Lithium Metal Anode to Enable Dendrite-Free Lithium Deposition. *Adv. Mater.* **2018**, *30*, No. e1707629.

(328) Liu, S.; Xia, X.; Deng, S.; Xie, D.; Yao, Z.; Zhang, L.; Zhang, S.; Wang, X.; Tu, J. In Situ Solid Electrolyte Interphase from Spray Quenching on Molten Li: A New Way to Construct High-Performance Lithium-Metal Anodes. *Adv. Mater.* **2019**, *31*, No. e1806470.

(329) Gao, Y.; Yan, Z.; Gray, J. L.; He, X.; Wang, D.; Chen, T.; Huang, Q.; Li, Y. C.; Wang, H.; Kim, S. H.; et al. Polymer-Inorganic Solid-Electrolyte Interphase for Stable Lithium Metal Batteries under Lean Electrolyte Conditions. *Nat. Mater.* **2019**, *18*, 384−389.

(330) Shen, X.; Li, Y.; Qian, T.; Liu, J.; Zhou, J.; Yan, C.; Goodenough, J. B. Lithium Anode Stable in Air for Low-Cost Fabrication of a Dendrite-Free Lithium Battery. *Nat. Commun.* **2019**, *10*, 900.

(331) Peled, E. The Electrochemical Behavior of Alkali and Alkaline Earth Metals in Nonaqueous Battery Systems—The Solid Electrolyte Interphase Model. *J. Electrochem. Soc.* **1979**, *126*, 2047−2051.

(332) Peled, E.; Menkin, S. Review—SEI: Past, Present and Future. *J. Electrochem. Soc.* **2017**, *164*, A1703−A1719.

(333) Lu, Y.; Tu, Z.; Archer, L. A. Stable Lithium Electrodeposition in Liquid and Nanoporous Solid Electrolytes. *Nat. Mater.* **2014**, *13*, 961−969.

(334) Ko, J.; Yoon, Y. S. Recent Progress in LiF Materials for Safe Lithium Metal Anode of Rechargeable Batteries: Is LiF the Key to Commercializing Li Metal Batteries? *Ceram. Int.* **2019**, *45*, 30−49.

(335) Yuan, Y.; Wu, F.; Chen, G.; Bai, Y.; Wu, C. Porous LiF Layer Fabricated by a Facile Chemical Method toward Dendrite-Free Lithium Metal Anode. *J. Energy Chem.* **2019**, *37*, 197−203.

(336) Cheng, X.-B.; Yan, C.; Chen, X.; Guan, C.; Huang, J.-Q.; Peng, H.-J.; Zhang, R.; Yang, S.-T.; Zhang, Q. Implantable Solid Electrolyte Interphase in Lithium-Metal Batteries. *Chem.* **2017**, *2*, 258−270.

(337) Breuer, S.; Pregartner, V.; Lunghammer, S.; Wilkening, H. M. R. Dispersed Solid Conductors: Fast Interfacial Li-Ion Dynamics in Nanostructured LiF and LiF:γ-Al$_2$O$_3$ Composites. *J. Phys. Chem. C* **2019**, *123*, 5222−5230.

(338) Zaban, A.; Zinigrad, E.; Aurbach, D. Impedance Spectroscopy of Li Electrodes. 4. A General Simple Model of the Li-Solution Interphase in Polar Aprotic Systems. *J. Phys. Chem.* **1996**, *100*, 3089−3101.

(339) Rehnlund, D.; Ihrfors, C.; Maibach, J.; Nyholm, L. Dendrite-Free Lithium Electrode Cycling via Controlled Nucleation in Low LiPF$_6$ Concentration Electrolytes. *Mater. Today* **2018**, *21*, 1010−1018.

(340) Jurng, S.; Brown, Z. L.; Kim, J.; Lucht, B. L. Effect of Electrolyte on the Nanostructure of the Solid Electrolyte Interphase (SEI) and Performance of Lithium Metal Anodes. *Energy Environ. Sci.* **2018**, *11*, 2600−2608.

(341) Monroe, C.; Newman, J. The Effect of Interfacial Deformation on Electrodeposition Kinetics. *J. Electrochem. Soc.* **2004**, *151*, A880.

(342) He, M.; Guo, R.; Hobold, G. M.; Gao, H.; Gallant, B. M. The Intrinsic Behavior of Lithium Fluoride in Solid Electrolyte Interphases on Lithium. *Proc. Natl. Acad. Sci. U.S.A.* **2020**, *117*, 73−79.

(343) Baek, M.; Kim, J.; Jin, J.; Choi, J. W. Photochemically Driven Solid Electrolyte Interphase for Extremely Fast-Charging Lithium-Ion Batteries. *Nat. Commun.* **2021**, *12*, 6807.

(344) Shiraishi, S.; Kanamura, K.; Takehara, Z. I. Surface Condition Changes in Lithium Metal Deposited in Nonaqueous Electrolyte

Containing HF by Dissolution-Deposition Cycles. *J. Electrochem. Soc.* **1999**, *146*, 1633−1639.

(345) Xia, J.; Petibon, R.; Xiao, A.; Lamanna, W. M.; Dahn, J. R. Some Fluorinated Carbonates as Electrolyte Additives for Li-(Ni$_{0.4}$Mn$_{0.4}$Co$_{0.2}$)O$_2$/Graphite Pouch Cells. *J. Electrochem. Soc.* **2016**, *163*, A1637−A1645.

(346) Wang, J.; Liu, W.; Luo, G.; Li, Z.; Zhao, C.; Zhang, H.; Zhu, M.; Xu, Q.; Wang, X.; Zhao, C.; et al. Synergistic Effect of Well-Defined Dual Sites Boosting the Oxygen Reduction Reaction. *Energy Environ. Sci.* **2018**, *11*, 3375−3379.

(347) Chang, W.; Park, J. H.; Steingart, D. A. Poor Man's Atomic Layer Deposition of LiF for Additive-Free Growth of Lithium Columns. *Nano Lett.* **2018**, *18*, 7066−7074.

(348) Fan, L.; Zhuang, H. L.; Gao, L.; Lu, Y.; Archer, L. A. Regulating Li Deposition at Artificial Solid Electrolyte Interphases. *J. Mater. Chem. A* **2017**, *5*, 3483−3492.

(349) Xie, J.; Liao, L.; Gong, Y.; Li, Y.; Shi, F.; Pei, A.; Sun, J.; Zhang, R.; Kong, B.; Subbaraman, R.; et al. Stitching H-BN by Atomic Layer Deposition of LiF as a Stable Interface for Lithium Metal Anode. *Sci. Adv.* **2017**, *3*, No. eaao3170.

(350) He, M.; Li, Y.; Guo, R.; Gallant, B. M. Electrochemical Conversion of Nitrogen Trifluoride as a Gas-to-Solid Cathode in Li Batteries. *J. Phys. Chem. Lett.* **2018**, *9*, 4700−4706.

(351) Ma, C.; Xu, F.; Song, T. Dual-Layered Interfacial Evolution of Lithium Metal Anode: SEI Analysis via TOF-SIMS Technology. *ACS Appl. Mater. Interfaces* **2022**, *14*, 20197−20207.

(352) Zhang, Z.; Li, Y.; Xu, R.; Zhou, W.; Li, Y.; Oyakhire, S. T.; Wu, Y.; Xu, J.; Wang, H.; Yu, Z.; et al. Capturing the Swelling of Solid-Electrolyte Interphase in Lithium Metal Batteries. *Science* **2022**, *375*, 66−70.

(353) Wu, J.; Wang, X.; Liu, Q.; Wang, S.; Zhou, D.; Kang, F.; Shanmukaraj, D.; Armand, M.; Rojo, T.; Li, B.; et al. A Synergistic Exploitation to Produce High-Voltage Quasi-Solid-State Lithium Metal Batteries. *Nat. Commun.* **2021**, *12*, 5746.

(354) Zheng, J.; Zheng, H.; Wang, R.; Ben, L.; Lu, W.; Chen, L.; Chen, L.; Li, H. 3D Visualization of Inhomogeneous Multi-Layered Structure and Young's Modulus of the Solid Electrolyte Interphase (SEI) on Silicon Anodes for Lithium-Ion Batteries. *Phys. Chem. Chem. Phys.* **2014**, *16*, 13229−13238.

(355) Jaumaux, P.; Wu, J.; Shanmukaraj, D.; Wang, Y.; Zhou, D.; Sun, B.; Kang, F.; Li, B.; Armand, M.; Wang, G. Non-Flammable Liquid and Quasi-Solid Electrolytes toward Highly-Safe Alkali Metal-Based Batteries. *Adv. Funct. Mater.* **2021**, *31*, 2008644.

(356) Yildirim, H.; Kinaci, A.; Chan, M. K.; Greeley, J. P. First-Principles Analysis of Defect Thermodynamics and Ion Transport in Inorganic SEI Compounds: LiF and NaF. *ACS Appl. Mater. Interfaces* **2015**, *7*, 18985−18996.

(357) Thomas, M.; Bruce, P.; Goodenough, J. Lithium Mobility in the Layered Oxide Li$_{1-x}$CoO$_2$. *Solid State Ion.* **1985**, *17*, 13−19.

(358) Cherkashinin, G.; Nikolowski, K.; Ehrenberg, H.; Jacke, S.; Dimesso, L.; Jaegermann, W. The Stability of the SEI Layer, Surface Composition and the Oxidation State of Transition Metals at the Electrolyte-Cathode Interface Impacted by the Electrochemical Cycling: X-ray Photoelectron Spectroscopy Investigation. *Phys. Chem. Chem. Phys.* **2012**, *14*, 12321−12331.

(359) Krueger, S.; Kloepsch, R.; Li, J.; Nowak, S.; Passerini, S.; Winter, M. How Do Reactions at the Anode/Electrolyte Interface Determine the Cathode Performance in Lithium-Ion Batteries? *J. Electrochem. Soc.* **2013**, *160*, A542−A548.

(360) Dedryvère, R.; Foix, D.; Franger, S.; Patoux, S.; Daniel, L.; Gonbeau, D. Electrode/Electrolyte Interface Reactivity in High-Voltage Spinel LiMn$_{1.6}$Ni$_{0.4}$O$_4$/Li$_4$Ti$_5$O$_{12}$ Lithium-Ion Battery. *J. Phys. Chem. C* **2010**, *114*, 10999−11008.

(361) Li, S. R.; Chen, C. H.; Xia, X.; Dahn, J. R. The Impact of Electrolyte Oxidation Products in LiNi$_{0.5}$Mn$_{1.5}$O$_4$/Li$_4$Ti$_5$O$_{12}$ Cells. *J. Electrochem. Soc.* **2013**, *160*, A1524−A1528.

(362) Aurbach, D.; Markovsky, B.; Salitra, G.; Markevich, E.; Talyossef, Y.; Koltypin, M.; Nazar, L.; Ellis, B.; Kovacheva, D. Review

on Electrode-Electrolyte Solution Interactions, Related to Cathode Materials for Li-Ion Batteries. *J. Power Sources* **2007**, *165*, 491−499.

(363) Komaba, S.; Kumagai, N.; Kataoka, Y. Influence of Manganese(II), Cobalt(II), and Nickel(II) Additives in Electrolyte on Performance of Graphite Anode for Lithium-Ion Batteries. *Electrochim. Acta* **2002**, *47*, 1229−1239.

(364) Xiong, D. J.; Petibon, R.; Nie, M.; Ma, L.; Xia, J.; Dahn, J. R. Interactions between Positive and Negative Electrodes in Li-Ion Cells Operated at High Temperature and High Voltage. *J. Electrochem. Soc.* **2016**, *163*, A546−A551.

(365) Jung, Y. S.; Lu, P.; Cavanagh, A. S.; Ban, C.; Kim, G.-H.; Lee, S.-H.; George, S. M.; Harris, S. J.; Dillon, A. C. Unexpected Improved Performance of ALD Coated LiCoO₂/Graphite Li-Ion Batteries. *Adv. Energy Mater.* **2013**, *3*, 213−219.

(366) Xu, K. Electrolytes and Interphases in Li-Ion Batteries and Beyond. *Chem. Rev.* **2014**, *114*, 11503−11618.

(367) Gauthier, M.; Carney, T. J.; Grimaud, A.; Giordano, L.; Pour, N.; Chang, H. H.; Fenning, D. P.; Lux, S. F.; Paschos, O.; Bauer, C.; et al. Electrode-Electrolyte Interface in Li-Ion Batteries: Current Understanding and New Insights. *J. Phys. Chem. Lett.* **2015**, *6*, 4653−4672.

(368) Aurbach, D.; Markovsky, B.; Rodkin, A.; Levi, E.; Cohen, Y. S.; Kim, H. J.; Schmidt, M. On the Capacity Fading of LiCoO₂ Intercalation Electrodes. *Electrochim. Acta* **2002**, *47*, 4291−4306.

(369) Minato, T.; Kawaura, H.; Hirayama, M.; Taminato, S.; Suzuki, K.; Yamada, N. L.; Sugaya, H.; Yamamoto, K.; Nakanishi, K.; Orikasa, Y.; et al. Dynamic Behavior at the Interface between Lithium Cobalt Oxide and an Organic Electrolyte Monitored by Neutron Reflectivity Measurements. *J. Phys. Chem. C* **2016**, *120*, 20082−20088.

(370) Liu, B.; Zhou, H.; Yin, C.; Guan, H.; Li, J. Enhanced Electrochemical Performance of LiNi₀.₅Mn₁.₅O₄ Cathode by Application of LiPF₂O₂ for Lithium Difluoro(oxalate)borate Electrolyte. *Electrochim. Acta* **2019**, *321*, 134690.

(371) Meng, Y.; Chen, G.; Shi, L.; Liu, H.; Zhang, D. Operando Fourier Transform Infrared Investigation of Cathode Electrolyte Interphase Dynamic Reversible Evolution on Li₁.₂Ni₀.₂Mn₀.₆O₂. *ACS Appl. Mater. Interfaces* **2019**, *11*, 45108−45117.

(372) Wang, F.; Lin, Y.; Suo, L.; Fan, X.; Gao, T.; Yang, C.; Han, F.; Qi, Y.; Xu, K.; Wang, C. Stabilizing High Voltage LiCoO₂ Cathode in Aqueous Electrolyte with Interphase-Forming Additive. *Energy Environ. Sci.* **2016**, *9*, 3666−3673.

(373) Song, Y.-M.; Han, J.-G.; Park, S.; Lee, K. T.; Choi, N.-S. A Multifunctional Phosphite-Containing Electrolyte for 5 V-Class LiNi₀.₅Mn₁.₅O₄ Cathodes with Superior Electrochemical Performance. *J. Mater. Chem. A* **2014**, *2*, 9506−9513.

(374) Zhang, H.; Eshetu, G. G.; Judez, X.; Li, C.; Rodriguez-Martinez, L. M.; Armand, M. Electrolyte Additives for Lithium Metal Anodes and Rechargeable Lithium Metal Batteries: Progress and Perspectives. *Angew. Chem., Int. Ed.* **2018**, *57*, 15002−15027.

(375) Fan, X.; Chen, L.; Borodin, O.; Ji, X.; Chen, J.; Hou, S.; Deng, T.; Zheng, J.; Yang, C.; Liou, S. C.; et al. Non-flammable Electrolyte Enables Li-Metal Batteries with Aggressive Cathode Chemistries. *Nat. Nanotechnol.* **2018**, *13*, 715−722.

(376) Cao, X.; Ren, X.; Zou, L.; Engelhard, M. H.; Huang, W.; Wang, H.; Matthews, B. E.; Lee, H.; Niu, C.; Arey, B. W.; et al. Monolithic Solid-Electrolyte Interphases Formed in Fluorinated Orthoformate-Based Electrolytes Minimize Li Depletion and Pulverization. *Nat. Energy* **2019**, *4*, 796−805.

(377) Zhang, Z.; Yang, J.; Huang, W.; Wang, H.; Zhou, W.; Li, Y.; Li, Y.; Xu, J.; Huang, W.; Chiu, W.; et al. Cathode-Electrolyte Interphase in Lithium Batteries Revealed by Cryogenic Electron Microscopy. *Matter* **2021**, *4*, 302−312.

(378) Zou, L.; Liu, Z.; Zhao, W.; Jia, H.; Zheng, J.; Yang, Y.; Wang, G.; Zhang, J.-G.; Wang, C. Solid-Liquid Interfacial Reaction Trigged Propagation of Phase Transition from Surface into Bulk Lattice of Ni-Rich Layered Cathode. *Chem. Mater.* **2018**, *30*, 7016−7026.

(379) Wang, C.; Meng, Y. S.; Xu, K. Perspective—Fluorinating Interphases. *J. Electrochem. Soc.* **2019**, *166*, A5184−A5186.

(380) Macneil, D. D.; Dahn, J. R. The Reactions of Li₀.₅CoO₂ with Nonaqueous Solvents at Elevated Temperatures. *J. Electrochem. Soc.* **2002**, *149*, A912.

(381) Baba, Y. Thermal Stability of LiₓCoO₂ Cathode for Lithium Ion Battery. *Solid State Ion.* **2002**, *148*, 311−316.

(382) Gallus, D. R.; Wagner, R.; Wiemers-Meyer, S.; Winter, M.; Cekic-Laskovic, I. New Insights into the Structure-Property Relationship of High-Voltage Electrolyte Components for Lithium-Ion Batteries Using the pKa Value. *Electrochim. Acta* **2015**, *184*, 410−416.

(383) Wang, F.-M.; Pradanawati, S. A.; Yeh, N.-H.; Chang, S.-C.; Yang, Y.-T.; Huang, S.-H.; Lin, P.-L.; Lee, J.-F.; Sheu, H.-S.; Lu, M.-L.; et al. Robust Benzimidazole-Based Electrolyte Overcomes High-Voltage and High-Temperature Applications in 5 V Class Lithium Ion Batteries. *Chem. Mater.* **2017**, *29*, 5537−5549.

(384) He, M.; Su, C. C.; Peebles, C.; Feng, Z.; Connell, J. G.; Liao, C.; Wang, Y.; Shkrob, I. A.; Zhang, Z. Mechanistic Insight in the Function of Phosphite Additives for Protection of Li-Ni₀.₅Co₀.₂Mn₀.₃O₂ Cathode in High Voltage Li-Ion Cells. *ACS Appl. Mater. Interfaces* **2016**, *8*, 11450−11458.

(385) Mun, J.; Lee, J.; Hwang, T.; Lee, J.; Noh, H.; Choi, W. Lithium Difluoro(oxalate)borate for Robust Passivation of Li-Ni₁.₅Mn₁.₅O₄ in Lithium-Ion Batteries. *J. Electroanal. Chem.* **2015**, *745*, 8−13.

(386) Wang, X. T.; Gu, Z. Y.; Li, W. H.; Zhao, X. X.; Guo, J. Z.; Du, K. D.; Luo, X. X.; Wu, X. L. Regulation of Cathode-Electrolyte Interphase via Electrolyte Additives in Lithium Ion Batteries. *Chem. Asian J.* **2020**, *15*, 2803−2814.

(387) Wölke, C.; Diddens, D.; Heidrich, B.; Winter, M.; Cekic-Laskovic, I. Understanding the Effectiveness of Pholane Electrolyte Additives in Lithium-Ion Batteries under High-Voltage Conditions. *ChemElectroChem* **2021**, *8*, 972−982.

(388) Xu, N.; Shi, J.; Liu, G.; Yang, X.; Zheng, J.; Zhang, Z.; Yang, Y. Research Progress of Fluorine-Containing Electrolyte Additives for Lithium Ion Batteries. *J. Power Sources Adv.* **2021**, *7*, 100043.

(389) Adenusi, H.; Chass, G. A.; Passerini, S.; Tian, K. V.; Chen, G. Lithium Batteries and the Solid Electrolyte Interphase (SEI)—Progress and Outlook. *Adv. Energy Mater.* **2023**, *13*, 2203307.

(390) Lang, J.; Long, Y.; Qu, J.; Luo, X.; Wei, H.; Huang, K.; Zhang, H.; Qi, L.; Zhang, Q.; Li, Z.; et al. One-Pot Solution Coating of High Quality LiF Layer to Stabilize Li Metal Anode. *Energy Storage Mater.* **2019**, *16*, 85−90.

(391) Stoebe, T. G. Influence of OH⁻ Ions on Infrared Absorption and Ionic Conductivity in Lithium Fluoride Crystals. *J. Phys. Chem. Solids* **1967**, *28*, 1375−1382.

(392) Yuan, Y.; Wu, F.; Bai, Y.; Li, Y.; Chen, G.; Wang, Z.; Wu, C. Regulating Li Deposition by Constructing LiF-Rich Host for Dendrite-Free Lithium Metal Anode. *Energy Storage Mater.* **2019**, *16*, 411−418.

(393) Hou, J.; Yang, M.; Wang, D.; Zhang, J. Fundamentals and Challenges of Lithium Ion Batteries at Temperatures between −40 and 60 °C. *Adv. Energy Mater.* **2020**, *10*, 1904152.

(394) Smart, M. C.; Lucht, B. L.; Dalavi, S.; Krause, F. C.; Ratnakumar, B. V. The Effect of Additives upon the Performance of MCMB/LiNiₓCo₁₋ₓO₂ Li-Ion Cells Containing Methyl Butyrate-Based Wide Operating Temperature Range Electrolytes. *J. Electrochem. Soc.* **2012**, *159*, A739−A751.

(395) Song, G.; Yi, Z.; Su, F.; Xie, L.; Wang, Z.; Wei, X.-X.; Xu, G.; Chen, C.-M. Boosting the Low-Temperature Performance for Li-Ion Batteries in LiPF₆-Based Local High-Concentration Electrolyte. *ACS Energy Lett.* **2023**, *8*, 1336−1343.

(396) Li, Q.; Liu, G.; Cheng, H.; Sun, Q.; Zhang, J.; Ming, J. Low-Temperature Electrolyte Design for Lithium-Ion Batteries: Prospect and Challenges. *Chemistry* **2021**, *27*, 15842−15865.

(397) Yang, B.; Zhang, H.; Yu, L.; Fan, W.; Huang, D. Lithium Difluorophosphate as an Additive to Improve the Low Temperature Performance of LiNi₀.₅Co₀.₂Mn₀.₃O₂/graphite Cells. *Electrochim. Acta* **2016**, *221*, 107−114.

(398) Shi, J.; Ehteshami, N.; Ma, J.; Zhang, H.; Liu, H.; Zhang, X.; Li, J.; Paillard, E. Improving the Graphite/Electrolyte Interface in

Lithium-Ion Battery for Fast Charging and Low Temperature Operation: Fluorosulfonyl Isocyanate as Electrolyte Additive. *J. Power Sources* **2019**, *429*, 67−74.

(399) Smith, K. A.; Smart, M. C.; Prakash, G. K. S.; Ratnakumar, B. V. Electrolytes Containing Fluorinated Ester Co-Solvents for Low-Temperature Li-Ion Cells. *ECS Trans.* **2008**, *11*, 91−98.

(400) Liu, J.; Yuan, B.; He, N.; Dong, L.; Chen, D.; Zhong, S.; Ji, Y.; Han, J.; Yang, C.; Liu, Y.; et al. Reconstruction of LiF-Rich Interphases through an Anti-freezing Electrolyte for Ultralow-Temperature $LiCoO_2$ Batteries. *Energy Environ. Sci.* **2023**, *16*, 1024−1034.

(401) Lu, W.; Xie, K.; Chen, Z.; Xiong, S.; Pan, Y.; Zheng, C. A New Co-Solvent for Wide Temperature Lithium-Ion Battery Electrolytes: 2,2,2-Trifluoroethyl n-Caproate. *J. Power Sources* **2015**, *274*, 676−684.

(402) Ozhabes, Y.; Gunceler, D.; Arias, T. Stability and Surface Diffusion at Lithium-Electrolyte Interphases with Connections to Dendrite Suppression. *arXiv* **2015**, 1504.05799.

(403) Yang, T.; Li, S.; Wang, W.; Lu, J.; Fan, W.; Zuo, X.; Nan, J. Nonflammable Functional Electrolytes with All-Fluorinated Solvents Matching Rechargeable High-Voltage Li-Metal Batteries with Ni-Rich Ternary Cathode. *J. Power Sources* **2021**, *505*, 230055.

(404) Liao, L.; Cheng, X.; Ma, Y.; Zuo, P.; Fang, W.; Yin, G.; Gao, Y. Fluoroethylene Carbonate as Electrolyte Additive to Improve Low Temperature Performance of $LiFePO_4$ Electrode. *Electrochim. Acta* **2013**, *87*, 466−472.

(405) Dong, X.; Lin, Y.; Li, P.; Ma, Y.; Huang, J.; Bin, D.; Wang, Y.; Qi, Y.; Xia, Y. High-Energy Rechargeable Metallic Lithium Battery at −70 Degrees C Enabled by a Cosolvent Electrolyte. *Angew. Chem., Int. Ed.* **2019**, *58*, 5623−5627.

(406) Peng, Z.; Cao, X.; Gao, P.; Jia, H.; Ren, X.; Roy, S.; Li, Z.; Zhu, Y.; Xie, W.; Liu, D.; et al. High-Power Lithium Metal Batteries Enabled by High-Concentration Acetonitrile-Based Electrolytes with Vinylene Carbonate Additive. *Adv. Funct. Mater.* **2020**, *30*, 2001285.

(407) Jiang, L. L.; Yan, C.; Yao, Y. X.; Cai, W.; Huang, J. Q.; Zhang, Q. Inhibiting Solvent Co-Intercalation in a Graphite Anode by a Localized High-Concentration Electrolyte in Fast-Charging Batteries. *Angew. Chem., Int. Ed.* **2021**, *60*, 3402−3406.

(408) Yang, Y.; Wang, H.; Zhu, C.; Ma, J. Armor-like Inorganic-rich Cathode Electrolyte Interphase Enabled by the Pentafluorophenyl-boronic Acid Additive for High-voltage Li‖NCM622 Batteries. *Angew. Chem., Int. Ed.* **2023**, *62*, No. e202300057.

(409) Sun, Z.; Li, F.; Ding, J.; Lin, Z.; Xu, M.; Zhu, M.; Liu, J. High-Voltage and High-Temperature $LiCoO^2$ Operation via the Electrolyte Additive of Electron-Defect Boron Compounds. *ACS Energy Lett.* **2023**, *8*, 2478−2487.

(410) Liu, Q.; Jiang, W.; Xu, J.; Xu, Y.; Yang, Z.; Yoo, D. J.; Pupek, K. Z.; Wang, C.; Liu, C.; Xu, K.; et al. A Fluorinated Cation Introduces New Interphasial Chemistries to Enable High-Voltage Lithium Metal Batteries. *Nat. Commun.* **2023**, *14*, 3678.

(411) Sun, C.; Ji, X.; Weng, S.; Li, R.; Huang, X.; Zhu, C.; Xiao, X.; Deng, T.; Fan, L.; Chen, L.; et al. 50C Fast-Charge Li-Ion Batteries using a Graphite Anode. *Adv. Mater.* **2022**, *34*, No. e2206020.

(412) Shin, H.; Park, J.; Sastry, A. M.; Lu, W. Effects of Fluoroethylene Carbonate (FEC) on Anode and Cathode Interfaces at Elevated Temperatures. *J. Electrochem. Soc.* **2015**, *162*, A1683−A1692.

(413) Hu, L.; Zhang, Z.; Amine, K. Fluorinated Electrolytes for Li-Ion Battery: An FEC-Based Electrolyte for High Voltage $LiNi_{0.5}Mn_{1.5}O_4$/Graphite Couple. *Electrochem. commun.* **2013**, *35*, 76−79.

(414) Ehteshami, N.; Ibing, L.; Stolz, L.; Winter, M.; Paillard, E. Ethylene Carbonate-Free Electrolytes for Li-Ion Battery: Study of the Solid Electrolyte Interphases Formed on Graphite Anodes. *J. Power Sources* **2020**, *451*, 227804.

(415) Shen, C.; Hu, G.; Cheong, L. Z.; Huang, S.; Zhang, J. G.; Wang, D. Direct Observation of the Growth of Lithium Dendrites on Graphite Anodes by Operando EC-AFM. *Small Methods* **2018**, *2*, 1700298.

(416) Hwang, J.-Y.; Park, S.-J.; Yoon, C. S.; Sun, Y.-K. Customizing a Li-Metal Battery That Survives Practical Operating Conditions for Electric Vehicle Applications. *Energy Environ. Sci.* **2019**, *12*, 2174−2184.

(417) Markevich, E.; Salitra, G.; Chesneau, F.; Schmidt, M.; Aurbach, D. Very Stable Lithium Metal Stripping-Plating at a High Rate and High Areal Capacity in Fluoroethylene Carbonate-Based Organic Electrolyte Solution. *ACS Energy Lett.* **2017**, *2*, 1321−1326.

(418) Guo, J. C.; Tan, S. J.; Zhang, C. H.; Wang, W. P.; Zhao, Y.; Wang, F.; Zhang, X. S.; Wen, R.; Zhang, Y.; Fan, M.; et al. A Self-Reconfigured, Dual-Layered Artificial Interphase Toward High-Current-Density Quasi-Solid-State Lithium Metal Batteries. *Adv. Mater.* **2023**, *35*, No. e2300350.

(419) Park, S.-J.; Hwang, J.-Y.; Sun, Y.-K. Trimethylsilyl Azide ($C_3H_9N_3Si$): A Highly Efficient Additive for Tailoring Fluoroethylene Carbonate (FEC) Based Electrolytes for Li-Metal Batteries. *J. Mater. Chem. A* **2019**, *7*, 13441−13448.

(420) Wang, X.; Zhang, M.; Alvarado, J.; Wang, S.; Sina, M.; Lu, B.; Bouwer, J.; Xu, W.; Xiao, J.; Zhang, J. G.; et al. New Insights on the Structure of Electrochemically Deposited Lithium Metal and Its Solid Electrolyte Interphases via Cryogenic TEM. *Nano Lett.* **2017**, *17*, 7606−7612.

(421) Guo, L.; Huang, F.; Cai, M.; Zhang, J.; Ma, G.; Xu, S. Organic-Inorganic Hybrid SEI Induced by a New Lithium Salt for High-Performance Metallic Lithium Anodes. *ACS Appl. Mater. Interfaces* **2021**, *13*, 32886−32893.

(422) Guo, Z.; Yang, H.; Wei, Q.; Xu, S.; Hu, G.; Bai, S.; Li, F. Dual-Additives Enable Stable Electrode-Electrolyte Interfaces for Long-Life Li-SPAN Batteries. *Chin. Chem. Lett.* **2024**, *35*, 108622.

(423) Yang, H.-W.; Kang, W. S.; Kim, S.-J. A Significant Enhancement of Cycling Stability at Fast Charging Rate through Incorporation of Li_3N into LiF-Based SEI in SiO Anode for Li-Ion Batteries. *Electrochim. Acta* **2022**, *412*, 140107.

(424) Su, H.; Chen, Z.; Li, M.; Bai, P.; Li, Y.; Ji, X.; Liu, Z.; Sun, J.; Ding, J.; Yang, M.; et al. Achieving Practical High-Energy-Density Lithium-Metal Batteries by a Dual-Anion Regulated Electrolyte. *Adv. Mater.* **2023**, *35*, No. e2301171.

(425) Dong, L.; Liu, Y.; Wen, K.; Chen, D.; Rao, D.; Liu, J.; Yuan, B.; Dong, Y.; Wu, Z.; Liang, Y.; et al. High-Polarity Fluoroalkyl Ether Electrolyte Enables Solvation-Free Li^+ Transfer for High-Rate Lithium Metal Batteries. *Adv. Sci.* **2022**, *9*, No. e2104699.

(426) Yue, X.; Zhang, J.; Dong, Y.; Chen, Y.; Shi, Z.; Xu, X.; Li, X.; Liang, Z. Reversible Li Plating on Graphite Anodes through Electrolyte Engineering for Fast-Charging Batteries. *Angew. Chem., Int. Ed.* **2023**, *62*, No. e202302285.

(427) Rodrigues, M.-T. F.; Babu, G.; Gullapalli, H.; Kalaga, K.; Sayed, F. N.; Kato, K.; Joyner, J.; Ajayan, P. M. A Materials Perspective on Li-Ion Batteries at Extreme Temperatures. *Nat. Energy* **2017**, *2*, 1−14.

(428) Liu, Y.; Zhu, Y.; Cui, Y. Challenges and Opportunities towards Fast-Charging Battery Materials. *Nat. Energy* **2019**, *4*, 540−550.

(429) Fan, X.; Ji, X.; Chen, L.; Chen, J.; Deng, T.; Han, F.; Yue, J.; Piao, N.; Wang, R.; Zhou, X.; et al. All-Temperature Batteries Enabled by Fluorinated Electrolytes with Non-polar Solvents. *Nat. Energy* **2019**, *4*, 882−890.

(430) Liu, W.; Liu, P.; Mitlin, D. Review of Emerging Concepts in SEI Analysis and Artificial SEI Membranes for Lithium, Sodium, and Potassium Metal Battery Anodes. *Adv. Energy Mater.* **2020**, *10*, 2002297.

(431) Dey, A. N. Lithium Anode Film and Organic and Inorganic Electrolyte Batteries. *Thin Solid Films* **1977**, *43*, 131−171.

(432) Nazri, G.; Muller, R. H. Composition of Surface Layers on Li Electrodes in PC, $LiClO_4$ of Very Low Water Content. *J. Electrochem. Soc.* **1985**, *132*, 2050−2054.

(433) Zaban, A.; Aurbach, D. Impedance Spectroscopy of Lithium and Nickel Electrodes in Propylene Carbonate Solutions of Different Lithium Salts a Comparative Study. *J. Power Sources* **1995**, *54*, 289−295.

(434) Kanamura, K.; Tamura, H.; Shiraishi, S.; Takehara, Z. I. XPS Analysis of Lithium Surfaces Following Immersion in Various Solvents Containing LiBF$_4$. *J. Electrochem. Soc.* **1995**, *142*, 340−347.

(435) Peled, E.; Golodnitsky, D.; Ardel, G. Advanced Model for Solid Electrolyte Interphase Electrodes in Liquid and Polymer Electrolytes. *J. Electrochem. Soc.* **1997**, *144*, L208−L210.

(436) Ein-Eli, Y. A New Perspective on the Formation and Structure of the Solid Electrolyte Interface at the Graphite Anode of Li-Ion Cells. *Electrochem. Solid-State Lett.* **1999**, *2*, 212.

(437) Wu, J.; Ihsan-Ul-Haq, M.; Chen, Y.; Kim, J.-K. Understanding Solid Electrolyte Interphases: Advanced Characterization Techniques and Theoretical Simulations. *Nano Energy* **2021**, *89*, 106489.

(438) Kominato, A.; Yasukawa, E.; Sato, N.; Ijuuin, T.; Asahina, H.; Mori, S. Analysis of Surface Films on Lithium in Various Organic Electrolytes. *J. Power Sources* **1997**, *68*, 471−475.

(439) Dollé, M. L.; Sannier, L.; Beaudoin, B.; Trentin, M.; Tarascon, J.-M. Live Scanning Electron Microscope Observations of Dendritic Growth in Lithium/Polymer Cells. *Electrochem. Solid-State Lett.* **2002**, *5*, A286−A289.

(440) Sacci, R. L.; Dudney, N. J.; More, K. L.; Parent, L. R.; Arslan, I.; Browning, N. D.; Unocic, R. R. Direct Visualization of Initial SEI Morphology and Growth Kinetics During Lithium Deposition by In Situ Electrochemical Transmission Electron Microscopy. *Chem. Commun.* **2014**, *50*, 2104−2107.

(441) Sacci, R. L.; Black, J. M.; Balke, N.; Dudney, N. J.; More, K. L.; Unocic, R. R. Nanoscale Imaging of Fundamental Li Battery Chemistry: Solid-Electrolyte Interphase Formation and Preferential Growth of Lithium Metal Nanoclusters. *Nano Lett.* **2015**, *15*, 2011−2018.

(442) Lee, S.-B.; Pyun, S.-I. The Effect of Electrolyte Temperature on the Passivity of Solid Electrolyte Interphase Formed on a Graphite Electrode. *Carbon* **2002**, *40*, 2333−2339.

(443) Li, Y.; Huang, W.; Li, Y.; Chiu, W.; Cui, Y. Opportunities for Cryogenic Electron Microscopy in Materials Science and Nanoscience. *ACS Nano* **2020**, *14*, 9263−9276.

(444) Liu, Q. C.; Xu, J. J.; Yuan, S.; Chang, Z. W.; Xu, D.; Yin, Y. B.; Li, L.; Zhong, H. X.; Jiang, Y. S.; Yan, J. M.; et al. Artificial Protection Film on Lithium Metal Anode toward Long-Cycle-Life Lithium-Oxygen Batteries. *Adv. Mater.* **2015**, *27*, 5241−5247.

(445) Li, Y.; Huang, W.; Li, Y.; Pei, A.; Boyle, D. T.; Cui, Y. Correlating Structure and Function of Battery Interphases at Atomic Resolution Using Cryoelectron Microscopy. *Joule* **2018**, *2*, 2167−2177.

(446) Huang, W.; Boyle, D. T.; Li, Y.; Li, Y.; Pei, A.; Chen, H.; Cui, Y. Nanostructural and Electrochemical Evolution of the Solid-Electrolyte Interphase on CuO Nanowires Revealed by Cryogenic-Electron Microscopy and Impedance Spectroscopy. *ACS Nano* **2019**, *13*, 737−744.

(447) Sheng, O.; Zheng, J.; Ju, Z.; Jin, C.; Wang, Y.; Chen, M.; Nai, J.; Liu, T.; Zhang, W.; Liu, Y.; et al. In Situ Construction of a LiF-Enriched Interface for Stable All-Solid-State Batteries and its Origin Revealed by Cryo-TEM. *Adv. Mater.* **2020**, *32*, No. e2000223.

(448) Li, Y.; Zhou, W.; Li, Y.; Huang, W.; Zhang, Z.; Chen, G.; Wang, H.; Wu, G. H.; Rolston, N.; Vila, R.; et al. Unravelling Atomic Structure and Degradation Mechanisms of Organic-Inorganic Halide Perovskites by Cryo-EM. *Joule* **2019**, *3*, 2854−2866.

(449) Huang, W.; Wang, J.; Braun, M. R.; Zhang, Z.; Li, Y.; Boyle, D. T.; Mcintyre, P. C.; Cui, Y. Dynamic Structure and Chemistry of the Silicon Solid-Electrolyte Interphase Visualized by Cryogenic Electron Microscopy. *Matter* **2019**, *1*, 1232−1245.

(450) Sayavong, P.; Zhang, W.; Oyakhire, S. T.; Boyle, D. T.; Chen, Y.; Kim, S. C.; Vila, R. A.; Holmes, S. E.; Kim, M. S.; Bent, S. F.; et al. Dissolution of the Solid Electrolyte Interphase and Its Effects on Lithium Metal Anode Cyclability. *J. Am. Chem. Soc.* **2023**, *145*, 12342−12350.

(451) Benninghoven, A. Surface Investigation of Solids by the Statical Method of Secondary Ion Mass Spectroscopy (SIMS). *Surf. Sci.* **1973**, *35*, 427−457.

(452) Otto, S. K.; Riegger, L. M.; Fuchs, T.; Kayser, S.; Schweitzer, P.; Burkhardt, S.; Henss, A.; Janek, J. In Situ Investigation of Lithium Metal-Solid Electrolyte Anode Interfaces with ToF-SIMS. *Adv. Mater. Interfaces* **2022**, *9*, 2102387.

(453) Peled, E.; Bar Tow, D.; Merson, A.; Gladkich, A.; Burstein, L.; Golodnitsky, D. Composition, Depth Profiles and Lateral Distribution of Materials in the SEI Built on HOPG-TOF SIMS and XPS Studies. *J. Power Sources* **2001**, *97−98*, 52−57.

(454) Yamagishi, Y.; Morita, H.; Nomura, Y.; Igaki, E. Visualizing Lithiation of Graphite Composite Anodes in All-Solid-State Batteries Using Operando Time-of-Flight Secondary Ion Mass Spectrometry. *J. Phys. Chem. Lett.* **2021**, *12*, 4623−4627.

(455) Pereira-Nabais, C.; Swiatowska, J.; Rosso, M.; Ozanam, F.; Seyeux, A.; Gohier, A.; Tran-Van, P.; Cassir, M.; Marcus, P. Effect of Lithiation Potential and Cycling on Chemical and Morphological Evolution of Si Thin Film Electrode Studied by ToF-SIMS. *ACS Appl. Mater. Interfaces* **2014**, *6*, 13023−13033.

(456) Otto, S.-K.; Moryson, Y.; Krauskopf, T.; Peppler, K.; Sann, J.; Janek, J.; Henss, A. In-Depth Characterization of Lithium-Metal Surfaces with XPS and ToF-SIMS: Toward Better Understanding of the Passivation Layer. *Chem. Mater.* **2021**, *33*, 859−867.

(457) Zhu, Z.; Zhou, Y.; Yan, P.; Vemuri, R. S.; Xu, W.; Zhao, R.; Wang, X.; Thevuthasan, S.; Baer, D. R.; Wang, C. M. In Situ Mass Spectrometric Determination of Molecular Structural Evolution at the Solid Electrolyte Interphase in Lithium-Ion Batteries. *Nano Lett.* **2015**, *15*, 6170−6176.

(458) Papp, C.; Steinrück, H.-P. In Situ High-Resolution X-ray Photoelectron Spectroscopy - Fundamental Insights in Surface Reactions. *Surf. Sci. Rep.* **2013**, *68*, 446−487.

(459) Maibach, J.; Kallquist, I.; Andersson, M.; Urpelainen, S.; Edstrom, K.; Rensmo, H.; Siegbahn, H.; Hahlin, M. Probing a Battery Electrolyte Drop with Ambient Pressure Photoelectron Spectroscopy. *Nat. Commun.* **2019**, *10*, 3080.

(460) Xu, C.; Sun, B.; Gustafsson, T.; Edström, K.; Brandell, D.; Hahlin, M. Interface Layer Formation in Solid Polymer Electrolyte Lithium Batteries: An XPS Study. *J. Mater. Chem. A* **2014**, *2*, 7256−7264.

(461) Oyakhire, S. T.; Gong, H.; Cui, Y.; Bao, Z.; Bent, S. F. An X-ray Photoelectron Spectroscopy Primer for Solid Electrolyte Interphase Characterization in Lithium Metal Anodes. *ACS Energy Lett.* **2022**, *7*, 2540−2546.

(462) Zhang, J.; Wang, R.; Yang, X.; Lu, W.; Wu, X.; Wang, X.; Li, H.; Chen, L. Direct Observation of Inhomogeneous Solid Electrolyte Interphase on MnO Anode with Atomic Force Microscopy and Spectroscopy. *Nano Lett.* **2012**, *12*, 2153−2157.

(463) Shen, C.; Wang, S.; Jin, Y.; Han, W. Q. In Situ AFM Imaging of Solid Electrolyte Interfaces on HOPG with Ethylene Carbonate and Fluoroethylene Carbonate-Based Electrolytes. *ACS Appl. Mater. Interfaces* **2015**, *7*, 25441−25447.

(464) Shi, Y.; Yan, H. J.; Wen, R.; Wan, L. J. Direct Visualization of Nucleation and Growth Processes of Solid Electrolyte Interphase Film Using in Situ Atomic Force Microscopy. *ACS Appl. Mater. Interfaces* **2017**, *9*, 22063−22067.

(465) Liu, R. R.; Deng, X.; Liu, X. R.; Yan, H. J.; Cao, A. M.; Wang, D. Facet-Dependent SEI Formation on the LiNi$_{0.5}$Mn$_{1.5}$O$_4$ Cathode Identified by In Situ Single Particle Atomic Force Microscopy. *Chem. Commun.* **2014**, *50*, 15756−15759.

(466) Anderson, M. S. Locally Enhanced Raman Spectroscopy with an Atomic Force Microscope. *Appl. Phys. Lett.* **2000**, *76*, 3130−3132.

(467) Zhang, R.; Zhang, Y.; Dong, Z. C.; Jiang, S.; Zhang, C.; Chen, L. G.; Zhang, L.; Liao, Y.; Aizpurua, J.; Luo, Y.; et al. Chemical Mapping of a Single Molecule by Plasmon-Enhanced Raman Scattering. *Nature* **2013**, *498*, 82−86.

(468) Hong, L.; Li, L.; Chen-Wiegart, Y. K.; Wang, J.; Xiang, K.; Gan, L.; Li, W.; Meng, F.; Wang, F.; Wang, J.; et al. Two-Dimensional Lithium Diffusion Behavior and Probable Hybrid Phase Transformation Kinetics in Olivine Lithium Iron Phosphate. *Nat. Commun.* **2017**, *8*, 1194.

(469) Wang, J.; Karen Chen-Wiegart, Y. C.; Eng, C.; Shen, Q.; Wang, J. Visualization of Anisotropic-Isotropic Phase Transformation Dynamics in Battery Electrode Particles. *Nat. Commun.* **2016**, *7*, 12372.

(470) Takamatsu, D.; Nakatsutsumi, T.; Mori, S.; Orikasa, Y.; Mogi, M.; Yamashige, H.; Sato, K.; Fujimoto, T.; Takanashi, Y.; Murayama, H.; et al. Nanoscale Observation of the Electronic and Local Structures of LiCoO$_2$ Thin Film Electrode by Depth-Resolved X-ray Absorption Spectroscopy. *J. Phys. Chem. Lett.* **2011**, *2*, 2511–2514.

(471) Jarry, A.; Gottis, S.; Yu, Y. S.; Roque-Rosell, J.; Kim, C.; Cabana, J.; Kerr, J.; Kostecki, R. The Formation Mechanism of Fluorescent Metal Complexes at the Li$_x$Ni$_{0.5}$Mn$_{1.5}$O$_{4-\delta}$)/Carbonate Ester Electrolyte Interface. *J. Am. Chem. Soc.* **2015**, *137*, 3533–3539.

(472) Bleith, P.; Van Beek, W.; Kaiser, H.; Novák, P.; Villevieille, C. Simultaneous in Situ X-ray Absorption Spectroscopy and X-ray Diffraction Studies on Battery Materials: The Case of Fe$_{0.5}$TiOPO$_4$. *J. Phys. Chem. C* **2015**, *119*, 3466–3471.

(473) Liu, D.; Shadike, Z.; Lin, R.; Qian, K.; Li, H.; Li, K.; Wang, S.; Yu, Q.; Liu, M.; Ganapathy, S.; et al. Review of Recent Development of In Situ/Operando Characterization Techniques for Lithium Battery Research. *Adv. Mater.* **2019**, *31*, No. e1806620.

(474) Rus, E. D.; Dura, J. A. In Situ Neutron Reflectometry Study of Solid Electrolyte Interface (SEI) Formation on Tungsten Thin-Film Electrodes. *ACS Appl. Mater. Interfaces* **2019**, *11*, 47553–47563.

(475) Rus, E. D.; Dura, J. A. In Situ Neutron Reflectometry Study of a Tungsten Oxide/Li-Ion Battery Electrolyte Interface. *ACS Appl. Mater. Interfaces* **2023**, *15*, 2832–2842.

(476) Huang, Z.; Ren, J.; Zhang, W.; Xie, M.; Li, Y.; Sun, D.; Shen, Y.; Huang, Y. Protecting the Li-Metal Anode in a Li-O$_2$ Battery by using Boric Acid as an SEI-Forming Additive. *Adv. Mater.* **2018**, *30*, No. e1803270.

(477) Fan, L.; Ma, R.; Zhang, Q.; Jia, X.; Lu, B. Graphite Anode for a Potassium-Ion Battery with Unprecedented Performance. *Angew. Chem., Int. Ed.* **2019**, *58*, 10500–10505.

(478) Sun, Y.; Ren, Y. In Situ Synchrotron X-Ray Techniques for Real-Time Probing of Colloidal Nanoparticle Synthesis. *Part. Par.t Syst. Charact.* **2013**, *30*, 399–419.

(479) Yu, C.; Ganapathy, S.; Eck, E.; Wang, H.; Basak, S.; Li, Z.; Wagemaker, M. Accessing the Bottleneck in All-Solid State Batteries, Lithium-Ion Transport over the Solid-Electrolyte-Electrode Interface. *Nat. Commun.* **2017**, *8*, 1086.

(480) Langdon, J.; Manthiram, A. Crossover Effects in Batteries with High-Nickel Cathodes and Lithium-Metal Anodes. *Adv. Funct. Mater.* **2021**, *31*, 2010267.

(481) Zhu, Y.; Hilty, C.; Savukov, I. Dynamic Nuclear Polarization Enhanced Nuclear Spin Optical Rotation. *Angew. Chem., Int. Ed.* **2021**, *60*, 8823–8826.

(482) Gunnarsdóttir, A. B.; Vema, S.; Menkin, S.; Marbella, L. E.; Grey, C. P. Investigating the Effect of a Fluoroethylene Carbonate Additive on Lithium Deposition and the Solid Electrolyte Interphase in Lithium Metal Batteries Using In Situ NMR Spectroscopy. *J. Mater. Chem. A* **2020**, *8*, 14975–14992.

(483) Kolesov, D. V.; Gorelkin, P. V.; Prelovskaya, A. O.; Erofeev, A. S. Scanning Electrochemical Microscopy for the Study of Energy Accumulators: Principles, Equipment, and Application. *Mosc. Univ. Phys. Bull.* **2022**, *77*, 801–810.

(484) Ventosa, E.; Schuhmann, W. Scanning Electrochemical Microscopy of Li-Ion Batteries. *Phys. Chem. Chem. Phys.* **2015**, *17*, 28441–28450.

(485) Zoski, C. G. Review—Advances in Scanning Electrochemical Microscopy (SECM). *J. Electrochem. Soc.* **2016**, *163*, H3088–H3100.

(486) Bulter, H.; Peters, F.; Schwenzel, J.; Wittstock, G. Spatiotemporal Changes of the Solid Electrolyte Interphase in Lithium-Ion Batteries Detected by Scanning Electrochemical Microscopy. *Angew. Chem., Int. Ed.* **2014**, *53*, 10531–10535.

(487) Shan, X.; Zhong, Y.; Zhang, L.; Zhang, Y.; Xia, X.; Wang, X.; Tu, J. A Brief Review on Solid Electrolyte Interphase Composition Characterization Technology for Lithium Metal Batteries: Challenges and Perspectives. *J. Phys. Chem. C* **2021**, *125*, 19060–19080.

(488) Verma, P.; Maire, P.; Novák, P. A Review of the Features and Analyses of the Solid Electrolyte Interphase in Li-Ion Batteries. *Electrochim. Acta* **2010**, *55*, 6332–6341.

(489) Wang, A.; Kadam, S.; Li, H.; Shi, S.; Qi, Y. Review on Modeling of the Anode Solid Electrolyte Interphase (SEI) for Lithium-Ion Batteries. *Npj Comput. Mater.* **2018**, *4*, 15.

(490) Chen, J.; Li, Q.; Pollard, T. P.; Fan, X.; Borodin, O.; Wang, C. Electrolyte design for Li metal-free Li batteries. *Mater. Today* **2020**, *39*, 118–126.

(491) Yao, N.; Chen, X.; Fu, Z. H.; Zhang, Q. Applying Classical, Ab Initio, and Machine-Learning Molecular Dynamics Simulations to the Liquid Electrolyte for Rechargeable Batteries. *Chem. Rev.* **2022**, *122*, 10970–11021.

(492) Li, Y.; Li, Y.; Pei, A.; Yan, K.; Sun, Y.; Wu, C. L.; Joubert, L. M.; Chin, R.; Koh, A. L.; Yu, Y.; et al. Atomic Structure of Sensitive Battery Materials and Interfaces Revealed by Cryo-Electron Microscopy. *Science* **2017**, *358*, 506–510.

(493) Huang, W.; Attia, P. M.; Wang, H.; Renfrew, S. E.; Jin, N.; Das, S.; Zhang, Z.; Boyle, D. T.; Li, Y.; Bazant, M. Z.; et al. Evolution of the Solid-Electrolyte Interphase on Carbonaceous Anodes Visualized by Atomic-Resolution Cryogenic Electron Microscopy. *Nano Lett.* **2019**, *19*, 5140–5148.

(494) Tu, Z.; Zachman, M. J.; Choudhury, S.; Khan, K. A.; Zhao, Q.; Kourkoutis, L. F.; Archer, L. A. Stabilizing Protic and Aprotic Liquid Electrolytes at High-Bandgap Oxide Interphases. *Chem. Mater.* **2018**, *30*, 5655–5662.

(495) Xiaobing, L.; Holland, J.; Burgess, S.; Bhadare, S.; Yamaguchi, S.; Birtwistle, D.; Statham, P.; Rowlands, N. Detection of Lithium X-rays by EDS. *Microsc. Microanal.* **2013**, *19*, 1136–1137.

(496) Hubaud, A. A.; Yang, Z.; Schroeder, D. J.; Dogan, F.; Trahey, L.; Vaughey, J. T. Interfacial Study of the Role of SiO$_2$ on Si Anodes Using Electrochemical Quartz Crystal Microbalance. *J. Power Sources* **2015**, *282*, 639–644.

(497) Dargel, V.; Shpigel, N.; Sigalov, S.; Nayak, P.; Levi, M. D.; Daikhin, L.; Aurbach, D. In Situ Real-Time Gravimetric and Viscoelastic Probing of Surface Films Formation on Lithium Batteries Electrodes. *Nat. Commun.* **2017**, *8*, 1389.

(498) Levi, M. D.; Shpigel, N.; Sigalov, S.; Dargel, V.; Daikhin, L.; Aurbach, D. In Situ Porous Structure Characterization of Electrodes for Energy Storage and Conversion by EQCM-D: a Review. *Electrochim. Acta* **2017**, *232*, 271–284.

(499) Munoz, R. a. A.; Toma, S. H.; Toma, H. E.; Araki, K.; Angnes, L. Investigation of Interfacial Processes at Tetraruthenated Zinc Porphyrin Films Using Electrochemical Surface Plasmon Resonance and Electrochemical Quartz Crystal Microbalance. *Electrochim. Acta* **2009**, *54*, 2971–2976.

(500) Levi, M. D.; Levy, N.; Sigalov, S.; Salitra, G.; Aurbach, D.; Maier, J. Electrochemical Quartz Crystal Microbalance (EQCM) Studies of Ions and Solvents Insertion into Highly Porous Activated Carbons. *J. Am. Chem. Soc.* **2010**, *132*, 13220–13222.

(501) Griffin, J. M.; Forse, A. C.; Tsai, W. Y.; Taberna, P. L.; Simon, P.; Grey, C. P. In Situ NMR and Electrochemical Quartz Crystal Microbalance Techniques Reveal the Structure of the Electrical Double Layer in Supercapacitors. *Nat. Mater.* **2015**, *14*, 812–819.

(502) Song, X.; Liu, T.; Amine, J.; Duan, Y.; Zheng, J.; Lin, Y.; Pan, F. In-Situ Mass-Electrochemical Study of Surface Redox Potential and Interfacial Chemical Reactions of Li(Na)FePO$_4$ Nanocrystals for Li(Na)-Ion Batteries. *Nano Energy* **2017**, *37*, 90–97.

(503) Shpigel, N.; Levi, M. D.; Sigalov, S.; Girshevitz, O.; Aurbach, D.; Daikhin, L.; Pikma, P.; Marandi, M.; Janes, A.; Lust, E.; et al. In Situ Hydrodynamic Spectroscopy for Structure Characterization of Porous Energy Storage Electrodes. *Nat. Mater.* **2016**, *15*, 570–575.

(504) Fang, C.; Li, J.; Zhang, M.; Zhang, Y.; Yang, F.; Lee, J. Z.; Lee, M. H.; Alvarado, J.; Schroeder, M. A.; Yang, Y.; et al. Quantifying Inactive Lithium in Lithium Metal Batteries. *Nature* **2019**, *572*, 511–515.

(505) Kasahara, S.; Ogose, T.; Ikemiya, N.; Yamamoto, T.; Natsui, K.; Yokota, Y.; Wong, R. A.; Iizuka, S.; Hoshi, N.; Tateyama, Y.; et al.

In Situ Spectroscopic Study on the Surface Hydroxylation of Diamond Electrodes. *Anal. Chem.* **2019**, *91*, 4980−4986.

(506) Sherwood, P. M. A. Photoelectron Spectroscopic Studies of Electrode and Related Surfaces. *Chem. Soc. Rev.* **1985**, *14*, 1.

(507) Bagus, P. S.; Ilton, E. S.; Nelin, C. J. The Interpretation of XPS Spectra: Insights into Materials Properties. *Surf. Sci. Rep.* **2013**, *68*, 273−304.

(508) Wang, J. G.; Zhang, Y.; Yu, X.; Hua, X.; Wang, F.; Long, Y. T.; Zhu, Z. Direct Molecular Evidence of Proton Transfer and Mass Dynamics at the Electrode-Electrolyte Interface. *J. Phys. Chem. Lett.* **2019**, *10*, 251−258.

(509) Zhou, Y.; Su, M.; Yu, X.; Zhang, Y.; Wang, J. G.; Ren, X.; Cao, R.; Xu, W.; Baer, D. R.; Du, Y.; et al. Real-Time Mass Spectrometric Characterization of the Solid-Electrolyte Interphase of a Lithium-Ion Battery. *Nat. Nanotechnol.* **2020**, *15*, 224−230.

(510) Zhang, Y.; Wang, J.-G.; Yu, X.; Baer, D. R.; Zhao, Y.; Mao, L.; Wang, F.; Zhu, Z. Potential-Dynamic Surface Chemistry Controls the Electrocatalytic Processes of Ethanol Oxidation on Gold Surfaces. *ACS Energy Lett.* **2019**, *4*, 215−221.

(511) Liu, X.; Wang, D.; Wan, L. Progress of Electrode/Electrolyte Interfacial Investigation of Li-Ion Batteries via In Situ Scanning Probe Microscopy. *Sci. Bull.* **2015**, *60*, 839−849.

(512) Kumar, R.; Tokranov, A.; Sheldon, B. W.; Xiao, X.; Huang, Z.; Li, C.; Mueller, T. In Situ and Operando Investigations of Failure Mechanisms of the Solid Electrolyte Interphase on Silicon Electrodes. *ACS Energy Lett.* **2016**, *1*, 689−697.

(513) Nanda, J.; Yang, G.; Hou, T.; Voylov, D. N.; Li, X.; Ruther, R. E.; Naguib, M.; Persson, K.; Veith, G. M.; Sokolov, A. P. Unraveling the Nanoscale Heterogeneity of Solid Electrolyte Interphase Using Tip-Enhanced Raman Spectroscopy. *Joule* **2019**, *3*, 2001−2019.

(514) Stöckle, R. M.; Suh, Y. D.; Deckert, V.; Zenobi, R. Nanoscale Chemical Analysis by Tip-Enhanced Raman Spectroscopy. *Chem. Phys. Lett.* **2000**, *318*, 131−136.

(515) Hayazawa, N.; Inouye, Y.; Sekkat, Z.; Kawata, S. Metallized Tip Amplification of Near-Field Raman Scattering. *Opt. Commun.* **2000**, *183*, 333−336.

(516) Steinhauer, M.; Stich, M.; Kurniawan, M.; Seidlhofer, B. K.; Trapp, M.; Bund, A.; Wagner, N.; Friedrich, K. A. In Situ Studies of Solid Electrolyte Interphase (SEI) Formation on Crystalline Carbon Surfaces by Neutron Reflectometry and Atomic Force Microscopy. *ACS Appl. Mater. Interfaces* **2017**, *9*, 35794−35801.

(517) Akai, T.; Ota, H.; Namita, H.; Yamaguchi, S.; Nomura, M. XANES Study on Solid Electrolyte Interface of Li Ion Battery. *Phys. Scr.* **2005**, *2005*, 408.

(518) Ota, H.; Akai, T.; Namita, H.; Yamaguchi, S.; Nomura, M. XAFS and TOF-SIMS Analysis of SEI Layers on Electrodes. *J. Power Sources* **2003**, *119−121*, 567−571.

(519) Ruther, R. E.; Zhou, H.; Dhital, C.; Saravanan, K.; Kercher, A. K.; Chen, G.; Huq, A.; Delnick, F. M.; Nanda, J. Synthesis, Structure, and Electrochemical Performance of High Capacity Li$_2$Cu$_{0.5}$Ni$_{0.5}$O$_2$ Cathodes. *Chem. Mater.* **2015**, *27*, 6746−6754.

(520) Schellenberger, M.; Golnak, R.; Quevedo Garzon, W. G.; Risse, S.; Seidel, R. Accessing the Solid Electrolyte Interphase on Silicon Anodes for Lithium-Ion Batteries In-Situ through Transmission Soft X-ray Absorption Spectroscopy. *Mater. Today Adv.* **2022**, *14*, 100215.

(521) Wei, C.; Bard, A. J. Scanning Electrochemical Microscopy: XXIX. In Situ Monitoring of Thickness Changes of Thin Films on Electrodes. *J. Electrochem. Soc.* **1995**, *142*, 2523−2527.

(522) Aurbach, D.; Ein-Ely, Y.; Zaban, A. The Surface Chemistry of Lithium Electrodes in Alkyl Carbonate Solutions. *J. Electrochem. Soc.* **1994**, *141*, L1−L3.

(523) Geschwind, G. Anion Reduced Ionic Conductivity in LiF. *J. Phys. Chem. Solids* **1969**, *30*, 1631−1635.

(524) Pan, J.; Cheng, Y.-T.; Qi, Y. General Method to Predict Voltage-Dependent Ionic Conduction in a Solid Electrolyte Coating on Electrodes. *Phys. Rev. B* **2015**, *91*, 134116.

(525) Zachman, M. J.; Tu, Z.; Archer, L. A.; Kourkoutis, L. F. Nanoscale Elemental Mapping of Intact Solid-Liquid Interfaces and Reactive Materials in Energy Devices Enabled by Cryo-FIB/SEM. *ACS Energy Lett.* **2020**, *5*, 1224−1232.

(526) Zachman, M. J.; Tu, Z.; Choudhury, S.; Archer, L. A.; Kourkoutis, L. F. Cryo-STEM Mapping of Solid-Liquid Interfaces and Dendrites in Lithium-Metal Batteries. *Nature* **2018**, *560*, 345−349.

(527) Zhang, X.; Su, Q.; Du, G.; Xu, B.; Wang, S.; Chen, Z.; Wang, L.; Huang, W.; Pang, H. Stabilizing Solid-state Lithium Metal Batteries through In Situ Generated Janus-heterarchical LiF-rich SEI in Ionic Liquid Confined 3D MOF/Polymer Membranes. *Angew. Chem., Int. Ed.* **2023**, *62*, No. e202304947.

(528) Han, B.; Zou, Y.; Xu, G.; Hu, S.; Kang, Y.; Qian, Y.; Wu, J.; Ma, X.; Yao, J.; Li, T.; et al. Additive Stabilization of SEI on Graphite Observed Using Cryo-Electron Microscopy. *Energy Environ. Sci.* **2021**, *14*, 4882−4889.

(529) Lu, X.; Cheng, Y.; Li, M.; Zou, Y.; Zhen, C.; Wu, D.; Wei, X.; Li, X.; Yang, X.; Gu, M. A Stable Polymer-based Solid-State Lithium Metal Battery and its Interfacial Characteristics Revealed by Cryogenic Transmission Electron Microscopy. *Adv. Funct. Mater.* **2023**, *33*, 2212847.

(530) Jabbari, V.; Yurkiv, V.; Rasul, M. G.; Phakatkar, A. H.; Mashayek, F.; Shahbazian-Yassar, R. In Situ Formation of Stable Solid Electrolyte Interphase with High Ionic Conductivity for Long Lifespan All-Solid-State Lithium Metal Batteries. *Energy Storage Mater.* **2023**, *57*, 1−13.

(531) Han, B.; Zhang, Z.; Zou, Y.; Xu, K.; Xu, G.; Wang, H.; Meng, H.; Deng, Y.; Li, J.; Gu, M. Poor Stability of Li$_2$CO$_3$ in the Solid Electrolyte Interphase of a Lithium-Metal Anode Revealed by Cryo-Electron Microscopy. *Adv. Mater.* **2021**, *33*, No. e2100404.

(532) Sheng, O.; Jin, C.; Chen, M.; Ju, Z.; Liu, Y.; Wang, Y.; Nai, J.; Liu, T.; Zhang, W.; Tao, X. Platinum Nano-Interlayer Enhanced Interface for Stable All-Solid-State Batteries Observed via Cryo-Transmission Electron Microscopy. *J. Mater. Chem. A* **2020**, *8*, 13541−13547.

(533) Liu, T.; Zheng, J.; Hu, H.; Sheng, O.; Ju, Z.; Lu, G.; Liu, Y.; Nai, J.; Wang, Y.; Zhang, W.; et al. In-Situ Construction of a Mg-Modified Interface to Guide Uniform Lithium Deposition for Stable All-Solid-State Batteries. *J. Energy Chem.* **2021**, *55*, 272−278.

(534) Alvarado, J.; Schroeder, M. A.; Pollard, T. P.; Wang, X.; Lee, J. Z.; Zhang, M.; Wynn, T.; Ding, M.; Borodin, O.; Meng, Y. S.; et al. Bisalt Ether Electrolytes: A Pathway towards Lithium Metal Batteries with Ni-Rich Cathodes. *Energy Environ. Sci.* **2019**, *12*, 780−794.

(535) Li, Y.; Wang, K.; Zhou, W.; Li, Y.; Vila, R.; Huang, W.; Wang, H.; Chen, G.; Wu, G. H.; Tsao, Y.; et al. Cryo-EM Structures of Atomic Surfaces and Host-Guest Chemistry in Metal-Organic Frameworks. *Matter* **2019**, *1*, 428−438.

(536) Wang, J.; Huang, W.; Pei, A.; Li, Y.; Shi, F.; Yu, X.; Cui, Y. Improving Cyclability of Li Metal Batteries at Elevated Temperatures and Its Origin Revealed by Cryo-Electron Microscopy. *Nat. Energy* **2019**, *4*, 664−670.

(537) Huang, W.; Wang, H.; Boyle, D. T.; Li, Y.; Cui, Y. Resolving Nanoscopic and Mesoscopic Heterogeneity of Fluorinated Species in Battery Solid-Electrolyte Interphases by Cryogenic Electron Microscopy. *ACS Energy Lett.* **2020**, *5*, 1128−1135.

(538) Liu, T.; Lin, L.; Bi, X.; Tian, L.; Yang, K.; Liu, J.; Li, M.; Chen, Z.; Lu, J.; Amine, K.; et al. In Situ Quantification of Interphasial Chemistry in Li-Ion Battery. *Nat. Nanotechnol.* **2019**, *14*, 50−56.

(539) Voinova, M. V.; Rodahl, M.; Jonson, M.; Kasemo, B. Viscoelastic Acoustic Response of Layered Polymer Films at Fluid-Solid Interfaces: Continuum Mechanics Approach. *Phys. Scr.* **1999**, *59*, 391−396.

(540) Broussely, M.; Biensan, P.; Bonhomme, F.; Blanchard, P.; Herreyre, S.; Nechev, K.; Staniewicz, R. J. Main Aging Mechanisms in Li Ion Batteries. *J. Power Sources* **2005**, *146*, 90−96.

(541) Heiskanen, S. K.; Kim, J.; Lucht, B. L. Generation and Evolution of the Solid Electrolyte Interphase of Lithium-Ion Batteries. *Joule* **2019**, *3*, 2322−2333.

(542) Tan, J.; Matz, J.; Dong, P.; Shen, J.; Ye, M. A Growing Appreciation for the Role of LiF in the Solid Electrolyte Interphase. *Adv. Energy Mater.* **2021**, *11*, 2100046.

(543) Kitz, P. G.; Lacey, M. J.; Novak, P.; Berg, E. J. Operando EQCM-D with Simultaneous in Situ EIS: New Insights into Interphase Formation in Li Ion Batteries. *Anal. Chem.* **2019**, *91*, 2296–2303.

(544) Edström, K.; Herstedt, M.; Abraham, D. P. A New Look at the Solid Electrolyte Interphase on Graphite Anodes in Li-Ion Batteries. *J. Power Sources* **2006**, *153*, 380–384.

(545) Malmgren, S.; Ciosek, K.; Hahlin, M.; Gustafsson, T.; Gorgoi, M.; Rensmo, H.; Edström, K. Comparing Anode and Cathode Electrode/Electrolyte Interface Composition and Morphology Using Soft and Hard X-ray Photoelectron Spectroscopy. *Electrochim. Acta* **2013**, *97*, 23–32.

(546) Aurbach, D.; Markovsky, B.; Levi, M. D.; Levi, E.; Schechter, A.; Moshkovich, M.; Cohen, Y. New Insights into the Interactions between Electrode Materials and Electrolyte Solutions for Advanced Nonaqueous Batteries. *J. Power Sources* **1999**, *81–82*, 95–111.

(547) Laruelle, S.; Pilard, S.; Guenot, P.; Grugeon, S.; Tarascon, J. M. Identification of Li-Based Electrolyte Degradation Products Through DEI and ESI High-Resolution Mass Spectrometry. *J. Electrochem. Soc.* **2004**, *151*, A1202.

(548) Zhang, Z.; Smith, K.; Jervis, R.; Shearing, P. R.; Miller, T. S.; Brett, D. J. L. Operando Electrochemical Atomic Force Microscopy of Solid-Electrolyte Interphase Formation on Graphite Anodes: The Evolution of SEI Morphology and Mechanical Properties. *ACS Appl. Mater. Interfaces* **2020**, *12*, 35132–35141.

(549) Campana, F. P.; Buqa, H.; Novák, P.; Kötz, R.; Siegenthaler, H. In Situ Atomic Force Microscopy Study of Exfoliation Phenomena on Graphite Basal Planes. *Electrochem. commun.* **2008**, *10*, 1590–1593.

(550) Jerliu, B.; Dorrer, L.; Huger, E.; Borchardt, G.; Steitz, R.; Geckle, U.; Oberst, V.; Bruns, M.; Schneider, O.; Schmidt, H. Neutron Reflectometry Studies on the Lithiation of Amorphous Silicon Electrodes in Lithium-Ion Batteries. *Phys. Chem. Chem. Phys.* **2013**, *15*, 7777–7784.

(551) Schulz, N.; Hausbrand, R.; Wittich, C.; Dimesso, L.; Jaegermann, W. XPS-Surface Analysis of SEI Layers on Li-Ion Cathodes: Part II. SEI-Composition and Formation inside Composite Electrodes. *J. Electrochem. Soc.* **2018**, *165*, A833–A846.

(552) Zhang, H.; Wang, D.; Shen, C. In-Situ EC-AFM and Ex-Situ XPS Characterization to Investigate the Mechanism of SEI Formation in Highly Concentrated Aqueous Electrolyte for Li-Ion Batteries. *Appl. Surf. Sci.* **2020**, *507*, 145059.

(553) Li, J.-T.; Świątowska, J.; Maurice, V.; Seyeux, A.; Huang, L.; Sun, S.-G.; Marcus, P. XPS and ToF-SIMS Study of Electrode Processes on Sn-Ni Alloy Anodes for Li-Ion Batteries. *J. Phys. Chem. C* **2011**, *115*, 7012–7018.

(554) Leroy, S.; Blanchard, F.; Dedryvère, R.; Martinez, H.; Carré, B.; Lemordant, D.; Gonbeau, D. Surface Film Formation on a Graphite Electrode in Li-Ion Batteries: AFM and XPS Study. *Surf. Interface Anal.* **2005**, *37*, 773–781.

(555) Li, J.-T.; Swiatowska, J.; Seyeux, A.; Huang, L.; Maurice, V.; Sun, S.-G.; Marcus, P. XPS and ToF-SIMS Study of Sn-Co Alloy Thin Films as Anode for Lithium Ion Battery. *J. Power Sources* **2010**, *195*, 8251–8257.

(556) Hope, M. A.; Rinkel, B. L. D.; Gunnarsdottir, A. B.; Marker, K.; Menkin, S.; Paul, S.; Sergeyev, I. V.; Grey, C. P. Selective NMR Observation of the SEI-Metal Interface by Dynamic Nuclear Polarisation from Lithium Metal. *Nat. Commun.* **2020**, *11*, 2224.

(557) Benninghoven, A. Die Analyse Monomolekularer Festkörper-oberflächenschichten mit Hilfe der Sekundärionenemission. *Z. anorg. allg. Chem.* **1970**, *230*, 403–417.

(558) Shotyk, W.; Metson, J. B. Secondary Ion Mass Spectrometry (SIMS) and Its Application to Chemical Weathering. *Rev. Geophys.* **1994**, *32*, 197.

(559) Benninghoven, A.; Loebach, E. Analysis of Monomolecular Layers of Solids by the Static Method of Secondary Ion Mass Spectroscopy (SIMS). *J. Radioanal. Chem.* **1972**, *12*, 95–99.

(560) Menkin, S.; O'keefe, C. A.; Gunnarsdottir, A. B.; Dey, S.; Pesci, F. M.; Shen, Z.; Aguadero, A.; Grey, C. P. Toward an Understanding of SEI Formation and Lithium Plating on Copper in Anode-Free Batteries. *J. Phys. Chem. C* **2021**, *125*, 16719–16732.

(561) Xu, H.; Li, Z.; Liu, T.; Han, C.; Guo, C.; Zhao, H.; Li, Q.; Lu, J.; Amine, K.; Qiu, X. Impacts of Dissolved Ni^{2+} on the Solid Electrolyte Interphase on a Graphite Anode. *Angew. Chem., Int. Ed.* **2022**, *61*, No. e202202894.

(562) Ota, H.; Sakata, Y.; Inoue, A.; Yamaguchi, S. Analysis of Vinylene Carbonate Derived SEI Layers on Graphite Anode. *J. Electrochem. Soc.* **2004**, *151*, A1659.

(563) Zhao, D.; Wang, J.; Wang, P.; Liu, H.; Li, S. Regulating the Composition Distribution of Layered SEI Film on Li-Ion Battery Anode by LiDFBOP. *Electrochim. Acta* **2020**, *337*, 135745.

(564) Pereira-Nabais, C.; Świątowska, J.; Chagnes, A.; Ozanam, F.; Gohier, A.; Tran-Van, P.; Cojocaru, C.-S.; Cassir, M.; Marcus, P. Interphase Chemistry of Si Electrodes Used as Anodes in Li-Ion Batteries. *Appl. Surf. Sci.* **2013**, *266*, 5–16.

(565) Bordes, A.; De Vito, E.; Haon, C.; Boulineau, A.; Montani, A.; Marcus, P. Multiscale Investigation of Silicon Anode Li Insertion Mechanisms by Time-of-Flight Secondary Ion Mass Spectrometer Imaging Performed on an In Situ Focused Ion Beam Cross Section. *Chem. Mater.* **2016**, *28*, 1566–1573.

(566) Zhou, L.; Zuo, T.; Li, C.; Zhang, Q.; Janek, J.; Nazar, L. F. $Li_{3-x}Zr_x(Ho/Lu)_{1-x}Cl_6$ Solid Electrolytes Enable Ultrahigh-Loading Solid-State Batteries with a Prelithiated Si Anode. *ACS Energy Lett.* **2023**, *8*, 3102–3111.

(567) Kim, M.; Harvey, S. P.; Huey, Z.; Han, S.-D.; Jiang, C.-S.; Son, S.-B.; Yang, Z.; Bloom, I. A New Mechanism of Stabilizing SEI of Si Anode Driven by Crosstalk Behavior and Its Potential for Developing High Performance Si-Based Batteries. *Energy Storage Mater.* **2023**, *55*, 436–444.

(568) Huo, H.; Chen, Y.; Li, R.; Zhao, N.; Luo, J.; Pereira Da Silva, J. G.; Mücke, R.; Kaghazchi, P.; Guo, X.; Sun, X. Design of a Mixed Conductive Garnet/Li Interface for Dendrite-Free Solid Lithium Metal Batteries. *Energy Environ. Sci.* **2020**, *13*, 127–134.

(569) Paul-Orecchio, A. G.; Weeks, J. A.; Dolocan, A.; Mullins, C. B. High-Stability Lithium Metal Batteries Enabled by a Tetrahydrofuran-Based Electrolyte Mixture. *ACS Appl. Energy Mater.* **2022**, *5*, 9437–9446.

(570) Fang, R.; Xu, B.; Grundish, N. S.; Xia, Y.; Li, Y.; Lu, C.; Liu, Y.; Wu, N.; Goodenough, J. B. Li_2S_6-Integrated PEO-Based Polymer Electrolytes for All-Solid-State Lithium-Metal Batteries. *Angew. Chem., Int. Ed.* **2021**, *60*, 17701–17706.

(571) Sun, H.-H.; Dolocan, A.; Weeks, J. A.; Rodriguez, R.; Heller, A.; Mullins, C. B. In Situ Formation of a Multicomponent Inorganic-Rich SEI Layer Provides a Fast Charging and High Specific Energy Li-Metal Battery. *J. Mater. Chem. A* **2019**, *7*, 17782–17789.

(572) Tu, H.; Li, L.; Wang, Z.; Wang, J.; Lin, H.; Wang, M.; Yan, C.; Liu, M. Tailoring Electrolyte Solvation for LiF-Rich Solid Electrolyte Interphase toward a Stable Li Anode. *ACS Nano* **2022**, *16*, 16898–16908.

(573) Jin, Y.; Kneusels, N. H.; Magusin, P.; Kim, G.; Castillo-Martinez, E.; Marbella, L. E.; Kerber, R. N.; Howe, D. J.; Paul, S.; Liu, T.; et al. Identifying the Structural Basis for the Increased Stability of the Solid Electrolyte Interphase Formed on Silicon with the Additive Fluoroethylene Carbonate. *J. Am. Chem. Soc.* **2017**, *139*, 14992–15004.

(574) Shadike, Z.; Lee, H.; Borodin, O.; Cao, X.; Fan, X.; Wang, X.; Lin, R.; Bak, S. M.; Ghose, S.; Xu, K.; et al. Identification of LiH and Nanocrystalline LiF in the Solid-Electrolyte Interphase of Lithium Metal Anodes. *Nat. Nanotechnol.* **2021**, *16*, 549–554.

(575) Cresce, A. v.; Russell, S. M.; Baker, D. R.; Gaskell, K. J.; Xu, K. In Situ and Quantitative Characterization of Solid Electrolyte Interphases. *Nano Lett.* **2014**, *14*, 1405–1412.

(576) Liu, X. R.; Wang, L.; Wan, L. J.; Wang, D. In Situ Observation of Electrolyte-Concentration-Dependent Solid Electrolyte Interphase on Graphite in Dimethyl Sulfoxide. *ACS Appl. Mater. Interfaces* **2015**, *7*, 9573–9580.

(577) Wang, X.; Huang, S. C.; Huang, T. X.; Su, H. S.; Zhong, J. H.; Zeng, Z. C.; Li, M. H.; Ren, B. Tip-Enhanced Raman Spectroscopy for Surfaces and Interfaces. *Chem. Soc. Rev.* **2017**, *46*, 4020−4041.

(578) Veith, G. M.; Browning, K. L.; Doucet, M.; Browning, J. F. Solid Electrolyte Interphase Architecture Determined through In Situ Neutron Scattering. *J. Electrochem. Soc.* **2021**, *168*, 060523.

(579) Veith, G. M.; Doucet, M.; Sacci, R. L.; Vacaliuc, B.; Baldwin, J. K.; Browning, J. F. Determination of the Solid Electrolyte Interphase Structure Grown on a Silicon Electrode Using a Fluoroethylene Carbonate Additive. *Sci. Rep.* **2017**, *7*, 6326.

(580) Veith, G. M.; Doucet, M.; Baldwin, J. K.; Sacci, R. L.; Fears, T. M.; Wang, Y.; Browning, J. F. Direct Determination of Solid-Electrolyte Interphase Thickness and Composition as a Function of State of Charge on a Silicon Anode. *J. Phys. Chem. C* **2015**, *119*, 20339−20349.

(581) Fears, T. M.; Doucet, M.; Browning, J. F.; Baldwin, J. K.; Winiarz, J. G.; Kaiser, H.; Taub, H.; Sacci, R. L.; Veith, G. M. Evaluating the Solid Electrolyte Interphase Formed on Silicon Electrodes: A Comparison of Ex Situ X-ray Photoelectron Spectroscopy and In Situ Neutron Reflectometry. *Phys. Chem. Chem. Phys.* **2016**, *18*, 13927−13940.

(582) Takamatsu, D.; Orikasa, Y.; Mori, S.; Nakatsutsumi, T.; Yamamoto, K.; Koyama, Y.; Minato, T.; Hirano, T.; Tanida, H.; Arai, H.; et al. Effect of an Electrolyte Additive of Vinylene Carbonate on the Electronic Structure at the Surface of a Lithium Cobalt Oxide Electrode under Battery Operating Conditions. *J. Phys. Chem. C* **2015**, *119*, 9791−9797.

(583) Khalid, S.; Caliebe, W.; Siddons, P.; So, I.; Clay, B.; Lenhard, T.; Hanson, J.; Wang, Q.; Frenkel, A. I.; Marinkovic, N.; et al. Quick Extended X-ray Absorption Fine Structure Instrument with Millisecond Time Scale, Optimized for In Situ Applications. *Rev. Sci. Instrum.* **2010**, *81*, 015105.

(584) Stotzel, J.; Lutzenkirchen-Hecht, D.; Fonda, E.; De Oliveira, N.; Briois, V.; Frahm, R. Novel Angular Encoder for a Quick-Extended X-ray Absorption Fine Structure Monochromator. *Rev. Sci. Instrum.* **2008**, *79*, 083107.

(585) Ventosa, E.; Wilde, P.; Zinn, A. H.; Trautmann, M.; Ludwig, A.; Schuhmann, W. Understanding Surface Reactivity of Si Electrodes in Li-ion Batteries by In Operando Scanning Electrochemical Microscopy. *Chem. Commun.* **2016**, *52*, 6825−6828.

(586) Takahashi, T.; Iwahara, H.; Ishikawa, T. Ionic Conductivity of Doped Cerium Trifluoride. *J. Electrochem. Soc.* **1977**, *124*, 280−284.

(587) Rongeat, C.; Anji Reddy, M.; Diemant, T.; Behm, R. J.; Fichtner, M. Development of New Anode Composite Materials for Fluoride Ion Batteries. *J. Mater. Chem. A* **2014**, *2*, 20861−20872.

(588) Grenier, A.; Porras-Gutierrez, A. G.; Body, M.; Legein, C.; Chrétien, F.; Raymundo-Piñero, E.; Dollé, M.; Groult, H.; Dambournet, D. Solid Fluoride Electrolytes and Their Composite with Carbon: Issues and Challenges for Rechargeable Solid State Fluoride-Ion Batteries. *J. Phys. Chem. C* **2017**, *121*, 24962−24970.

(589) Li, X.; Tang, Y.; Zhu, J.; Lv, H.; Xu, Y.; Wang, W.; Zhi, C.; Li, H. Initiating a Room-Temperature Rechargeable Aqueous Fluoride-Ion Battery with Long Lifespan through a Rational Buffering Phase Design. *Adv. Energy Mater.* **2021**, *11*, 2003714.

(590) Zhang, D.; Yamamoto, K.; Wang, Y.; Gao, S.; Uchiyama, T.; Watanabe, T.; Takami, T.; Matsunaga, T.; Nakanishi, K.; Miki, H.; et al. Reversible and Fast (De)fluorination of High-Capacity Cu_2O Cathode: One Step Toward Practically Applicable All-Solid-State Fluoride-Ion Battery. *Adv. Energy Mater.* **2021**, *11*, 2102285.

(591) Hou, X.; Zhang, Z.; Shen, K.; Cheng, S.; He, Q.; Shi, Y.; Yu, D. Y. W.; Su, C.-Y.; Li, L.-J.; Chen, F. An Aqueous Rechargeable Fluoride Ion Battery with Dual Fluoride Electrodes. *J. Electrochem. Soc.* **2019**, *166*, A2419−A2424.

(592) Zhang, S.; Wang, T.; Zhang, J.; Miao, Y.; Yin, Q.; Wu, Z.; Wu, Y.; Yuan, Q.; Han, J. A Zero-Strain Insertion Cathode Material for Room-Temperature Fluoride-Ion Batteries. *ACS Appl. Mater. Interfaces* **2022**, *14*, 24518−24525.

(593) Clemens, O.; Rongeat, C.; Reddy, M. A.; Giehr, A.; Fichtner, M.; Hahn, H. Electrochemical Fluorination of Perovskite Type $BaFeO_{2.5}$. *Dalton Trans.* **2014**, *43*, 15771−15778.

(594) Andrews, J. L.; Mcclure, E. T.; Jew, K. K.; Preefer, M. B.; Irshad, A.; Lertola, M. J.; Robertson, D. D.; Salamat, C. Z.; Brady, M. J.; Piper, L. F. J.; et al. Room-Temperature Electrochemical Fluoride (De)insertion into $CsMnFeF_6$. *ACS Energy Lett.* **2022**, *7*, 2340−2348.

(595) Nowroozi, M. A.; Ivlev, S.; Rohrer, J.; Clemens, O. La_2CoO_4: A New Intercalation Based Cathode Material for Fluoride Ion Batteries with Improved Cycling Stability. *J. Mater. Chem. A* **2018**, *6*, 4658−4669.

(596) Nowroozi, M. A.; Wissel, K.; Donzelli, M.; Hosseinpourkahvaz, N.; Plana-Ruiz, S.; Kolb, U.; Schoch, R.; Bauer, M.; Malik, A. M.; Rohrer, J.; et al. High Cycle Life All-Solid-State Fluoride Ion Battery with La_2NiO_{4+d} High Voltage Cathode. *Commun. Mater.* **2020**, *1*, 27.

(597) Roos, A.; Vandepol, F.; Keim, R.; Schoonman, J. Ionic Conductivity in Tysonite-Type Solid Solutions $La_{1-x}BaxF_{3-x}$. *Solid State Ion.* **1984**, *13*, 191−203.

(598) Dieudonne, B.; Chable, J.; Body, M.; Legein, C.; Durand, E.; Mauvy, F.; Fourcade, S.; Leblanc, M.; Maisonneuve, V.; Demourgues, A. The Key Role of the Composition and Structural Features in Fluoride Ion Conductivity in Tysonite $Ce_{1-x}Sr_xF_{3-x}$ Solid Solutions. *Dalton Trans.* **2017**, *46*, 3761−3769.

(599) Dieudonné, B.; Chable, J.; Mauvy, F.; Fourcade, S.; Durand, E.; Lebraud, E.; Leblanc, M.; Legein, C.; Body, M.; Maisonneuve, V.; et al. Exploring the $Sm_{1-x}Ca_xF_{3-x}$ Tysonite Solid Solution as a Solid-State Electrolyte: Relationships between Structural Features and F-Ionic Conductivity. *J. Phys. Chem. C* **2015**, *119*, 25170−25179.

(600) Tran, Q. C.; Bui, V. T.; Dao, V. D.; Lee, J. K.; Choi, H. S. Ionic Liquid-Based Polymer Electrolytes via Surfactant-Assisted Polymerization at the Plasma-Liquid Interface. *ACS Appl. Mater. Interfaces* **2016**, *8*, 16125−16135.

(601) Liu, J.; Yi, L.; Zeng, P.; Zou, C.; Chen, X.; Tao, X.; Liu, X.; Yang, L.; Zang, Z.; Chang, B.; et al. Point Defect Engineering Enabled the High Ionic Conductivity of $BaSnF_4$ for Solid-State Fluoride-Ion Batteries at Room Temperature. *Energy Fuels* **2022**, *36*, 15258−15267.

(602) Wang, J.; Hao, J.; Duan, C.; Wang, X.; Wang, K.; Ma, C. A Fluoride-Ion-Conducting Solid Electrolyte with Both High Conductivity and Excellent Electrochemical Stability. *Small* **2022**, *18*, No. e2104508.

(603) Yu, Y.; Lei, M.; Li, D.; Li, C. Near-Room-Temperature Quasi-Solid-State F-Ion Batteries with High Conversion Reversibility Based on Layered Structured Electrolyte. *Adv. Energy Mater.* **2023**, *13*, 2203168.

(604) Rongeat, C.; Reddy, M. A.; Witter, R.; Fichtner, M. Nanostructured Fluorite-Type Fluorides as Electrolytes for Fluoride Ion Batteries. *J. Phys. Chem. C* **2013**, *117*, 4943−4950.

(605) Mori, K.; Mineshige, A.; Emoto, T.; Sugiura, M.; Saito, T.; Namba, K.; Otomo, T.; Abe, T.; Fukunaga, T. Electrochemical, Thermal, and Structural Features of BaF_2-SnF_2 Fluoride-Ion Electrolytes. *J. Phys. Chem. C* **2021**, *125*, 12568−12577.

(606) Murakami, M.; Morita, Y.; Mizuno, M. ^{19}F/^{119}Sn/^{207}Pb NMR Studies on Ion Dynamics in Tetragonal $PbSnF_4$: Spectroscopic Evidence for Defect-Driven Conductivity. *J. Phys. Chem. C* **2017**, *121*, 2627−2634.

(607) Murakami, M.; Morita, Y.; Yonemura, M.; Shimoda, K.; Mori, M.; Koyama, Y.; Kawaguchi, T.; Fukuda, K.; Ishikawa, Y.; Kamiyama, T.; et al. High Anionic Conductive Form of $Pb_xSn_{2-x}F_4$. *Chem. Mater.* **2019**, *31*, 7704−7710.

(608) Denes, G.; Birchall, T.; Sayer, M.; Bell, M. $BaSnF_4$ — a New Fluoride Ionic Conductor with the α-$PbSnF_4$ Structure. *Solid State Ion.* **1984**, *13*, 213−219.

(609) Liu, L.; Yang, L.; Liu, M.; Li, X.; Shao, D.; Luo, K.; Wang, X.; Luo, Z. SnF2-Based Fluoride Ion Electrolytes $MSnF_4$ (M = Ba, Pb) for the Application of Room-Temperature Solid-State Fluoride Ion Batteries. *J. Alloys Compd.* **2020**, *819*, 152983.

(610) Liu, L.; Yang, L.; Shao, D.; Luo, K.; Zou, C.; Luo, Z.; Wang, X. Nd^{3+} Doped BaSnF$_4$ Solid Electrolyte for Advanced Room-Temperature Solid-State Fluoride Ion Batteries. *Ceram. Int.* **2020**, *46*, 20521−20528.

(611) Bachman, J. C.; Muy, S.; Grimaud, A.; Chang, H. H.; Pour, N.; Lux, S. F.; Paschos, O.; Maglia, F.; Lupart, S.; Lamp, P.; et al. Inorganic Solid-State Electrolytes for Lithium Batteries: Mechanisms and Properties Governing Ion Conduction. *Chem. Rev.* **2016**, *116*, 140−162.

(612) Mohammad, I.; Witter, R.; Fichtner, M.; Anji Reddy, M. Room-Temperature, Rechargeable Solid-State Fluoride-Ion Batteries. *ACS Appl. Energy Mater.* **2018**, *1*, 4766−4775.

(613) Mohammad, I.; Witter, R.; Fichtner, M.; Reddy, M. A. Introducing Interlayer Electrolytes: Toward Room-Temperature High-Potential Solid-State Rechargeable Fluoride Ion Batteries. *ACS Appl. Energy Mater.* **2019**, *2*, 1553−1562.

(614) Davis, V. K.; Munoz, S.; Kim, J.; Bates, C. M.; Momčilović, N.; Billings, K. J.; Miller, T. F.; Grubbs, R. H.; Jones, S. C. Fluoride-Ion Solvation in Non-aqueous Electrolyte Solutions. *Mater. Chem. Front.* **2019**, *3*, 2721−2727.

(615) Kobayashi, S.; Nakamoto, H.; Yokoe, D.; Kuwabara, A.; Abe, T.; Ikuhara, Y. Nanoscale Defluorination Mechanism and Solid Electrolyte Interphase of a MgF$_2$ Anode in Fluoride-Shuttle Batteries. *ACS Appl. Energy Mater.* **2021**, *4*, 996−1003.

(616) Celik Kucuk, A.; Yamanaka, T.; Yokoyama, Y.; Abe, T. Low-Cost Fluoride Source for Organic Liquid Electrolyte-Based Fluoride Shuttle Battery. *J. Electrochem. Soc.* **2021**, *168*, 010501.

(617) Kawasaki, M.; Morigaki, K.-I.; Kano, G.; Nakamoto, H.; Takekawa, R.; Kawamura, J.; Minato, T.; Abe, T.; Ogumi, Z. Lactone-Based Liquid Electrolytes for Fluoride Shuttle Batteries. *J. Electrochem. Soc.* **2021**, *168*, 010529.

(618) Okazaki, K.-I.; Uchimoto, Y.; Abe, T.; Ogumi, Z. Charge-Discharge Behavior of Bismuth in a Liquid Electrolyte for Rechargeable Batteries Based on a Fluoride Shuttle. *ACS Energy Lett.* **2017**, *2*, 1460−1464.

(619) Yamamoto, T.; Matsumoto, K.; Hagiwara, R.; Nohira, T. Room-Temperature Fluoride Shuttle Batteries Based on a Fluorohydrogenate Ionic Liquid Electrolyte. *ACS Appl. Energy Mater.* **2019**, *2*, 6153−6157.

(620) Yamamoto, T.; Matsumoto, K.; Hagiwara, R.; Nohira, T. Charge-Discharge Performance of Copper Metal Positive Electrodes in Fluorohydrogenate Ionic Liquids for Fluoride-Shuttle Batteries. *J. Electrochem. Soc.* **2021**, *168*, 040530.

(621) Darolles, I.; Weiss, C. M.; Alam, M. M.; Tiruvannamalai, A.; Jones, S. C. Fluoride Ion Battery Compositions. U.S. Patent US9166249B2, 2015.

(622) Lee, H. S.; Yang, X. Q.; Xiang, C. L.; Mcbreen, J.; Choi, L. S. The Synthesis of a New Family of Boron-Based Anion Receptors and the Study of Their Effect on Ion Pair Dissociation and Conductivity of Lithium Salts in Nonaqueous Solutions. *J. Electrochem. Soc.* **1998**, *145*, 2813−2818.

(623) Lee, H. S.; Sun, X.; Yang, X. Q.; Mcbreen, J. Synthesis and Study of New Cyclic Boronate Additives for Lithium Battery Electrolytes. *J. Electrochem. Soc.* **2002**, *149*, A1460.

(624) Li, L. F.; Lee, H. S.; Li, H.; Yang, X. Q.; Nam, K. W.; Yoon, W. S.; Mcbreen, J.; Huang, X. J. New Electrolytes for Lithium Ion Batteries Using LiF Salt and Boron Based Anion Receptors. *J. Power Sources* **2008**, *184*, 517−521.

(625) Xie, B.; Lee, H. S.; Li, H.; Yang, X. Q.; Mcbreen, J.; Chen, L. Q. New Electrolytes Using Li$_2$O or Li$_2$O$_2$ Oxides and Tris-(pentafluorophenyl) Borane as Boron-Based Anion Receptor for Lithium Batteries. *Electrochem. commun.* **2008**, *10*, 1195−1197.

(626) Chen, Z.; Amine, K. Computational Estimates of Fluoride Affinity of Boron-Based Anion Receptors. *J. Electrochem. Soc.* **2009**, *156*, A672.

(627) Konishi, H.; Minato, T.; Abe, T.; Ogumi, Z. Electrochemical Performance of a Lead Fluoride Electrode Mixed with Carbon in an Electrolyte Containing Triphenylboroxine as an Anion Acceptor for Fluoride Shuttle Batteries. *Mater. Chem. Phys.* **2019**, *226*, 1−5.

(628) Konishi, H.; Minato, T.; Abe, T.; Ogumi, Z. Reversible Electrochemical Reaction of a Fluoride Shuttle Battery with a Bismuth(III) Fluoride Electrode and Electrolyte Containing Triphenylboroxine as an Anion Acceptor. *ChemistrySelect* **2020**, *5*, 6237−6241.

(629) Konishi, H.; Minato, T.; Abe, T.; Ogumi, Z. Triphenylboroxine and Triphenylborane as Anion Acceptors for Electrolyte in Fluoride Shuttle Batteries. *Chem. Lett.* **2018**, *47*, 1346−1349.

(630) Konishi, H.; Takekawa, R.; Minato, T.; Ogumi, Z.; Abe, T. Effect of Anion Acceptor Added to the Electrolyte on the Electrochemical Performance of Bismuth(III) Fluoride in a Fluoride Shuttle Battery. *Chem. Phys. Lett.* **2020**, *755*, 137785.

(631) Konishi, H.; Minato, T.; Abe, T.; Ogumi, Z. Reactivity of the Anion Acceptor in Electrolyte: An Important Factor in Achieving High Electrochemical Performance of a Lead (II) Fluoride Electrode in a Fluoride Shuttle Battery. *J. Electroanal. Chem.* **2020**, *871*, 114103.

(632) Konishi, H.; Minato, T.; Abe, T.; Ogumi, Z. Electrochemical Performance of a Bismuth Fluoride Electrode in a Reserve-Type Fluoride Shuttle Battery. *J. Electrochem. Soc.* **2017**, *164*, A3702−A3708.

(633) Konishi, H.; Minato, T.; Abe, T.; Ogumi, Z. Improvement of Cycling Performance in Bismuth Fluoride Electrodes by Controlling Electrolyte Composition in Fluoride Shuttle Batteries. *J. Appl. Electrochem.* **2018**, *48*, 1205−1211.

(634) Celik Kucuk, A.; Abe, T. Borolan-2-yl Involving Anion Acceptors for Organic Liquid Electrolyte-Based Fluoride Shuttle Batteries. *J. Fluorine Chem.* **2020**, *240*, 109672.

(635) Celik Kucuk, A.; Yamanaka, T.; Abe, T. Using Siloxane-Based Liquid Electrolytes with High Stability for Fluoride Shuttle Batteries. *J. Mater. Chem. A* **2020**, *8*, 22134−22142.

(636) Konishi, H.; Minato, T.; Abe, T.; Ogumi, Z. Influence of Electrolyte Composition on the Electrochemical Reaction Mechanism of Bismuth Fluoride Electrode in Fluoride Shuttle Battery. *J. Phys. Chem. C* **2019**, *123*, 10246−10252.

(637) Celik Kucuk, A.; Minato, T.; Yamanaka, T.; Abe, T. Effects of LiBOB on Salt Solubility and BiF$_3$ Electrode Electrochemical Properties in Fluoride Shuttle Batteries. *J. Mater. Chem. A* **2019**, *7*, 8559−8567.

(638) Kawauchi, S.; Nakamoto, H.; Takekawa, R.; Kobayashi, T.; Abe, T. Electrolytes for Room-Temperature Rechargeable Fluoride Shuttle Batteries. *ACS Appl. Energy Mater.* **2022**, *5*, 2096−2103.

(639) Celik Kucuk, A.; Yamanaka, T.; Minato, T.; Abe, T. Influence of LiBOB as an Electrolyte Additive on the Performance of BiF$_3$/C for Fluoride Shuttle Batteries. *J. Electrochem. Soc.* **2020**, *167*, 120508.

(640) Yamanaka, T.; Kucuk, A. C.; Ogumi, Z.; Abe, T. Evolution of Fluoride Shuttle Battery Reactions of BiF$_3$ Microparticles in a CsF/LiBOB/Tetraglyme Electrolyte: Dependence on Structure, Size, and Shape. *ACS Appl. Energy Mater.* **2020**, *3*, 9390−9400.

(641) Celik Kucuk, A.; Yamanaka, T.; Abe, T. Fluoride Shuttle Batteries: On the Performance of the BiF$_3$ Electrode in Organic Liquid Electrolytes Containing a Mixture of Lithium Bis(oxalato)-borate and Triphenylboroxin. *Solid State Ion.* **2020**, *357*, 115499.

(642) Celik-Kucuk, A.; Abe, T. Electrochemical Behavior of CuF$_2$ as Reversible Cathode in an Organic Liquid Electrolyte for Room-Temperature Fluoride-Shuttle Batteries. *J. Power Sources* **2021**, *496*, 229828.

(643) Celik Kucuk, A.; Abe, T. Influence of Conductive Additives on the Electrochemical Compatibility of Cupper Fluoride Cathode for FSB. *J. Electroanal. Chem.* **2021**, *900*, 115744.

(644) Chen, J.; Huang, Z.; Wang, C.; Porter, S.; Wang, B.; Lie, W.; Liu, H. K. Sodium-Difluoro(oxalato)borate (NaDFOB): A New Electrolyte Salt for Na-Ion Batteries. *Chem. Commun.* **2015**, *51*, 9809−9812.

(645) Zavalij, P. Y.; Yang, S.; Whittingham, M. S. Structures of Potassium, Sodium and Lithium Bis(oxalato)borate Salts from Powder Diffraction Data. *Acta Crystallogr. B* **2003**, *59*, 753−759.

(646) Ge, C.; Wang, L.; Xue, L.; Wu, Z.-S.; Li, H.; Gong, Z.; Zhang, X.-D. Synthesis of Novel Organic-Ligand-Doped Sodium Bis-(oxalate)-Borate Complexes with Tailored Thermal Stability and

Enhanced Ion Conductivity for Sodium Ion Batteries. *J. Power Sources* **2014**, *248*, 77−82.

(647) Gallagher, T. C.; Sandstrom, S. K.; Wu, C. Y.; Stickle, W.; Fulkerson, C. R.; Hagglund, L.; Ji, X. Copper Metal Electrode Reversibly Hosts Fluoride in a 16 *m* KF Aqueous Electrolyte. *Chem. Commun.* **2022**, *58*, 10218−10220.

(648) Fang, Z.; Li, M.; Wang, L.; Duan, X.; Zhao, H. A Long-Life Aqueous Fluoride-Ion Battery Based on Water-in-Salt Electrolyte. *Inorg. Chem. Commun.* **2023**, *148*, 110275.

(649) Alshangiti, O.; Galatolo, G.; Rees, G. J.; Guo, H.; Quirk, J. A.; Dawson, J. A.; Pasta, M. Solvent-in-Salt Electrolytes for Fluoride Ion Batteries. *ACS Energy Lett.* **2023**, *8*, 2668−2673.

(650) Ali, G.; Oh, S. H.; Kim, S. Y.; Kim, J. Y.; Cho, B. W.; Chung, K. Y. An Open-Framework Iron Fluoride and Reduced Graphene Oxide Nanocomposite as a High-Capacity Cathode Material for Na-Ion Batteries. *J. Mater. Chem. A* **2015**, *3*, 10258−10266.

(651) Lemoine, K.; Hemon-Ribaud, A.; Leblanc, M.; Lhoste, J.; Tarascon, J. M.; Maisonneuve, V. Fluorinated Materials as Positive Electrodes for Li- and Na-Ion Batteries. *Chem. Rev.* **2022**, *122*, 14405−14439.

(652) Zhang, N.; Xiao, X.; Pang, H. Transition Metal (Fe, CO, Ni) Fluoride-Based Materials for Electrochemical Energy Storage. *Nanoscale Horiz.* **2019**, *4*, 99−116.

(653) He, K.; Zhou, Y.; Gao, P.; Wang, L.; Pereira, N.; Amatucci, G. G.; Nam, K. W.; Yang, X. Q.; Zhu, Y.; Wang, F.; et al. Sodiation via Heterogeneous Disproportionation in FeF_2 Electrodes for Sodium-Ion Batteries. *ACS Nano* **2014**, *8*, 7251−7259.

(654) Ni, D.; Sun, W.; Lu, C.; Wang, Z.; Qiao, J.; Cai, H.; Liu, C.; Sun, K. Improved Rate and Cycling Performance of FeF_2-rGO Hybrid Cathode with Poly (Acrylic Acid) Binder for Sodium Ion Batteries. *J. Power Sources* **2019**, *413*, 449−458.

(655) Zu, C.-X.; Li, H. Thermodynamic Analysis on Energy Densities of Batteries. *Energy Environ. Sci.* **2011**, *4*, 2614.

(656) Kang, J.; Ahn, J.; Park, H.; Ko, W.; Lee, Y.; Lee, S.; Lee, S.; Jung, S. K.; Kim, J. Highly Stable Fe^{2+}/Ti^{3+}-Based Fluoride Cathode Enabling Low-Cost and High-Performance Na-Ion Batteries. *Adv. Funct. Mater.* **2022**, *32*, 2201816.

(657) Zhu, J.; Deng, D. Wet-Chemical Synthesis of Phase-Pure FeOF Nanorods as High-Capacity Cathodes for Sodium-Ion Batteries. *Angew. Chem., Int. Ed.* **2015**, *54*, 3079−3083.

(658) Zhou, Y.-N.; Sina, M.; Pereira, N.; Yu, X.; Amatucci, G. G.; Yang, X.-Q.; Cosandey, F.; Nam, K.-W. $FeO_{0.7}F_{1.3}$/C Nanocomposite as a High-Capacity Cathode Material for Sodium-Ion Batteries. *Adv. Funct. Mater.* **2015**, *25*, 696−703.

(659) Dey, U. K.; Barman, N.; Ghosh, S.; Sarkar, S.; Peter, S. C.; Senguttuvan, P. Topochemical Bottom-Up Synthesis of 2D- and 3D-Sodium Iron Fluoride Frameworks. *Chem. Mater.* **2019**, *31*, 295−299.

(660) Foley, E. E.; Wu, V. C.; Jin, W.; Cui, W.; Yoshida, E.; Manche, A.; Clement, R. J. Polymorphism in Weberite $Na_2Fe_2F_7$ and its Effects on Electrochemical Properties as a Na-Ion Cathode. *Chem. Mater.* **2023**, *35*, 3614−3627.

(661) Peschel, B.; Molinier, M.; Babel, D. Kristallstrukturbestimmungen an Vier Monoklinen Weberiten $Na_2M^{II}M^{III}F_7$ (M^{II} = Fe, Co; M^{III} = V, Cr). *Z. Physik* **1995**, *621*, 1573−1581.

(662) Peschel, B.; Babel, D. Die Kristallstrukturen der Vanadium-Weberite $Na_2M^{II}V^{III}F_7$ (M^{II} = Mn, Ni, Cu) und von $NaVF_4$. *Z. Physik* **1997**, *623*, 1614−1620.

(663) Liao, J.; Han, J.; Xu, J.; Du, Y.; Sun, Y.; Duan, L.; Zhou, X. Scalable Synthesis of Na_2MVF_7 (M = Mn, Fe, and Co) as High-Performance Cathode Materials for Sodium-Ion Batteries. *Chem. Commun.* **2021**, *57*, 11497−11500.

(664) Leblanc, M.; Ferey, G.; Chevallier, P.; Calage, Y.; De Pape, R. Hexagonal Tungsten Bronze-Type Fe^{III} Fluoride: $(H_2O)_{0.33}FeF_3$; Crystal Structure, Magnetic Properties, Dehydration to a New Form of Iron Trifluoride. *J. Solid State Chem.* **1983**, *47*, 53−58.

(665) Zhang, R.; Wang, X.; Wang, X.; Liu, M.; Wei, S.; Wang, Y.; Hu, H. Iron Fluoride Packaged into 3D Order Mesoporous Carbons as High-Performance Sodium-Ion Battery Cathode Material. *J. Electrochem. Soc.* **2018**, *165*, A89−A96.

(666) Li, C.; Yin, C.; Mu, X.; Maier, J. Top-Down Synthesis of Open Framework Fluoride for Lithium and Sodium Batteries. *Chem. Mater.* **2013**, *25*, 962−969.

(667) Liu, M.; Wang, Q.; Chen, B.; Lei, H.; Liu, L.; Wu, C.; Wang, X.; Yang, Z. Band-Gap Engineering of $FeF_3 \cdot 0.33H_2O$ Nanosphere via Ni Doping as a High-Performance Lithium-Ion Battery Cathode. *ACS Sustain. Chem. Eng.* **2020**, *8*, 15651−15660.

(668) Wei, S.; Wang, X.; Yu, R.; Zhang, R.; Liu, M.; Yang, Z.; Hu, H. Ti-Doped $Fe_{1-x}Ti_xF_3 \cdot 0.33H_2O$/C Nanocomposite as an Ultrahigh Rate Capability Cathode Materials of Lithium Ion Batteries. *J. Alloys Compd.* **2017**, *702*, 372−380.

(669) Yang, Z.; Zhang, Z.; Yuan, Y.; Huang, Y.; Wang, X.; Chen, X.; Wei, S. First-Principles Study of Ti Doping in $FeF_3 \cdot 0.33H_2O$. *Curr. Appl. Phys.* **2016**, *16*, 905−913.

(670) Ding, J.; Zhou, X.; Wang, H.; Yang, J.; Gao, Y.; Tang, J. Mn-Doped $Fe_{1-x}Mn_xF_3 \cdot 0.33H_2O$/C Cathodes for Li-Ion Batteries: First-Principles Calculations and Experimental Study. *ACS Appl. Mater. Interfaces* **2019**, *11*, 3852−3860.

(671) Zhang, C.; Yan, M.; Li, W.; Han, C.; Li, J.; Zhao, H.; Jia, G.; An, S.; Qiu, X. Cr-Doped $Fe_{1-x}Cr_xF_3 \cdot 0.33H_2O$ Nanomaterials as Cathode Materials for Sodium-Ion Batteries. *ACS Appl. Mater. Interfaces* **2021**, *13*, 48653−48660.

(672) Eshetu, G. G.; Elia, G. A.; Armand, M.; Forsyth, M.; Komaba, S.; Rojo, T.; Passerini, S. Electrolytes and Interphases in Sodium-Based Rechargeable Batteries: Recent Advances and Perspectives. *Adv. Energy Mater.* **2020**, *10*, 2000093.

(673) Bommier, C.; Ji, X. Electrolytes, SEI Formation, and Binders: A Review of Nonelectrode Factors for Sodium-Ion Battery Anodes. *Small* **2018**, *14*, No. e1703576.

(674) Lin, Z.; Xia, Q.; Wang, W.; Li, W.; Chou, S. Recent Research Progresses in Ether- and Ester-Based Electrolytes for Sodium-Ion Batteries. *InfoMat* **2019**, *1*, 376−389.

(675) Komaba, S.; Ishikawa, T.; Yabuuchi, N.; Murata, W.; Ito, A.; Ohsawa, Y. Fluorinated Ethylene Carbonate as Electrolyte Additive for Rechargeable Na Batteries. *ACS Appl. Mater. Interfaces* **2011**, *3*, 4165−4168.

(676) Dahbi, M.; Nakano, T.; Yabuuchi, N.; Fujimura, S.; Chihara, K.; Kubota, K.; Son, J.-Y.; Cui, Y.-T.; Oji, H.; Komaba, S. Effect of Hexafluorophosphate and Fluoroethylene Carbonate on Electrochemical Performance and the Surface Layer of Hard Carbon for Sodium-Ion Batteries. *ChemElectroChem.* **2016**, *3*, 1856−1867.

(677) Yi, Q.; Lu, Y.; Sun, X.; Zhang, H.; Yu, H.; Sun, C. Fluorinated Ether Based Electrolyte Enabling Sodium-Metal Batteries with Exceptional Cycling Stability. *ACS Appl. Mater. Interfaces* **2019**, *11*, 46965−46972.

(678) Zheng, X.; Gu, Z.; Liu, X.; Wang, Z.; Wen, J.; Wu, X.; Luo, W.; Huang, Y. Bridging the Immiscibility of an All-Fluoride Fire Extinguishant with Highly-Fluorinated Electrolytes toward Safe Sodium Metal Batteries. *Energy Environ. Sci.* **2020**, *13*, 1788−1798.

(679) Nimkar, A.; Shpigel, N.; Malchik, F.; Bublil, S.; Fan, T.; Penki, T. R.; Tsubery, M. N.; Aurbach, D. Unraveling the Role of Fluorinated Alkyl Carbonate Additives in Improving Cathode Performance in Sodium-Ion Batteries. *ACS Appl. Mater. Interfaces* **2021**, *13*, 46478−46487.

(680) Wang, C.; Sun, Z.; Liu, L.; Ni, H.; Hou, Q.; Fan, J.; Yuan, R.; Zheng, M.; Dong, Q. A Rooted Interphase on Sodium via In Situ Pre-implantation of Fluorine Atoms for High-Performance Sodium Metal Batteries. *Energy Environ. Sci.* **2023**, *16*, 3098−3109.

(681) Guo, X. F.; Yang, Z.; Zhu, Y. F.; Liu, X. H.; He, X. X.; Li, L.; Qiao, Y.; Chou, S. L. High-Voltage, Highly Reversible Sodium Batteries Enabled by Fluorine-Rich Electrode/Electrolyte Interphases. *Small Methods* **2022**, *6*, No. e2200209.

(682) Zou, Y.; Shen, Y.; Wu, Y.; Xue, H.; Guo, Y.; Liu, G.; Wang, L.; Ming, J. A Designed Durable Electrolyte for High-Voltage Lithium-Ion Batteries and Mechanism Analysis. *Chemistry* **2020**, *26*, 7930−7936.

(683) Zheng, X.; Cao, Z.; Gu, Z.; Huang, L.; Sun, Z.; Zhao, T.; Yu, S.; Wu, X.-L.; Luo, W.; Huang, Y. Toward High Temperature Sodium

Metal Batteries via Regulating the Electrolyte/Electrode Interfacial Chemistries. *ACS Energy Lett.* **2022**, 7, 2032−2042.

(684) Feng, Y.; Zhou, L.; Ma, H.; Wu, Z.; Zhao, Q.; Li, H.; Zhang, K.; Chen, J. Challenges and Advances in Wide-Temperature Rechargeable Lithium Batteries. *Energy Environ. Sci.* **2022**, 15, 1711−1759.

(685) Zhou, X.; Chen, X.; Yang, Z.; Liu, X.; Hao, Z.; Jin, S.; Zhang, L.; Wang, R.; Zhang, C.; Li, L.; et al. Anion Receptor Weakens ClO_4^- Solvation for High-Temperature Sodium-Ion Batteries. *Adv. Funct. Mater.* **2024**, 35, 2302281.

(686) Wu, J.; Tian, Y.; Gao, Y.; Gao, Z.; Meng, Y.; Wang, Y.; Wang, X.; Zhou, D.; Kang, F.; Li, B.; et al. Rational Electrolyte Design toward Cyclability Remedy for Room-Temperature Sodium-Sulfur Batteries. *Angew. Chem., Int. Ed.* **2022**, 61, No. e202205416.

(687) Zheng, J.; Chen, S.; Zhao, W.; Song, J.; Engelhard, M. H.; Zhang, J.-G. Extremely Stable Sodium Metal Batteries Enabled by Localized High-Concentration Electrolytes. *ACS Energy Lett.* **2018**, 3, 315−321.

(688) Jin, Y.; Xu, Y.; Le, P. M. L.; Vo, T. D.; Zhou, Q.; Qi, X.; Engelhard, M. H.; Matthews, B. E.; Jia, H.; Nie, Z.; et al. Highly Reversible Sodium Ion Batteries Enabled by Stable Electrolyte-Electrode Interphases. *ACS Energy Lett.* **2020**, 5, 3212−3220.

(689) Barnes, P.; Smith, K.; Parrish, R.; Jones, C.; Skinner, P.; Storch, E.; White, Q.; Deng, C.; Karsann, D.; Lau, M. L.; et al. A Non-aqueous Sodium Hexafluorophosphate-Based Electrolyte Degradation Study: Formation and Mitigation of Hydrofluoric Acid. *J. Power Sources* **2020**, 447, 227363.

(690) Terborg, L.; Nowak, S.; Passerini, S.; Winter, M.; Karst, U.; Haddad, P. R.; Nesterenko, P. N. Ion Chromatographic Determination of Hydrolysis Products of Hexafluorophosphate Salts in Aqueous Solution. *Anal. Chim. Acta* **2012**, 714, 121−126.

(691) Ould, D. M. C.; Menkin, S.; Smith, H. E.; Riesgo-Gonzalez, V.; Jonsson, E.; O'keefe, C. A.; Coowar, F.; Barker, J.; Bond, A. D.; Grey, C. P.; et al. Sodium Borates: Expanding the Electrolyte Selection for Sodium-Ion Batteries. *Angew. Chem., Int. Ed.* **2022**, 61, No. e202202133.

(692) Xu, X.; Zhou, D.; Qin, X.; Lin, K.; Kang, F.; Li, B.; Shanmukaraj, D.; Rojo, T.; Armand, M.; Wang, G. A Room-Temperature Sodium-Sulfur Battery with High Capacity and Stable Cycling Performance. *Nat. Commun.* **2018**, 9, 3870.

(693) Yang, C.; Feng, J.; Lv, F.; Zhou, J.; Lin, C.; Wang, K.; Zhang, Y.; Yang, Y.; Wang, W.; Li, J.; et al. Metallic Graphene-Like VSe_2 Ultrathin Nanosheets: Superior Potassium-Ion Storage and Their Working Mechanism. *Adv. Mater.* **2018**, 30, No. e1800036.

(694) Fan, L.; Hu, Y.; Rao, A. M.; Zhou, J.; Hou, Z.; Wang, C.; Lu, B. Prospects of Electrode Materials and Electrolytes for Practical Potassium-Based Batteries. *Small Methods* **2021**, 5, No. e2101131.

(695) Chihara, K.; Katogi, A.; Kubota, K.; Komaba, S. $KVPO_4F$ and $KVOPO_4$ Toward 4 V-Class Potassium-Ion Batteries. *Chem. Commun.* **2017**, 53, 5208−5211.

(696) Tan, H.; Du, X.; Huang, J. Q.; Zhang, B. $KVPO_4F$ as a Novel Insertion-Type Anode for Potassium Ion Batteries. *Chem. Commun.* **2019**, 55, 11311−11314.

(697) Liao, J.; Hu, Q.; He, X.; Mu, J.; Wang, J.; Chen, C. A long lifespan potassium-ion full battery based on $KVPO_4F$ cathode and VPO_4 anode. *J. Power Sources* **2020**, 451, 227739.

(698) Fedotov, S. S.; Luchinin, N. D.; Aksyonov, D. A.; Morozov, A. V.; Ryazantsev, S. V.; Gaboardi, M.; Plaisier, J. R.; Stevenson, K. J.; Abakumov, A. M.; Antipov, E. V. Titanium-Based Potassium-Ion Battery Positive Electrode with Extraordinarily High Redox Potential. *Nat. Commun.* **2020**, 11, 1484.

(699) Kim, H.; Seo, D. H.; Bianchini, M.; Clément, R. J.; Kim, H.; Kim, J. C.; Tian, Y.; Shi, T.; Yoon, W. S.; Ceder, G. A New Strategy for High-Voltage Cathodes for K-Ion Batteries: Stoichiometric $KVPO_4F$. *Adv. Energy Mater.* **2018**, 8, 1801591.

(700) Dong, J.; Liao, J.; He, X.; Hu, Q.; Yu, Y.; Chen, C. Graphene Encircled $KFeSO_4F$ Cathode Composite for High Energy Density Potassium-Ion Batteries. *Chem. Commun.* **2020**, 56, 10050−10053.

(701) Recham, N.; Rousse, G.; Sougrati, M. T.; Chotard, J.-N.; Frayret, C.; Mariyappan, S.; Melot, B. C.; Jumas, J.-C.; Tarascon, J.-M. Preparation and Characterization of a Stable $FeSO_4F$-Based Framework for Alkali Ion Insertion Electrodes. *Chem. Mater.* **2012**, 24, 4363−4370.

(702) Ling, C.; Mizuno, F. Mechanistic Study of the Electrochemical Extraction of K^+ from $KFeSO_4F$. *J. Mater. Chem. A* **2013**, 1, 8000.

(703) Jian, Z.; Luo, W.; Ji, X. Carbon Electrodes for K-Ion Batteries. *J. Am. Chem. Soc.* **2015**, 137, 11566−11569.

(704) Zhou, M.; Bai, P.; Ji, X.; Yang, J.; Wang, C.; Xu, Y. Electrolytes and Interphases in Potassium Ion Batteries. *Adv. Mater.* **2021**, 33, No. e2003741.

(705) Xu, Y.; Ding, T.; Sun, D.; Ji, X.; Zhou, X. Recent Advances in Electrolytes for Potassium-Ion Batteries. *Adv. Funct. Mater.* **2023**, 33, 2211290.

(706) Xiao, N.; Mcculloch, W. D.; Wu, Y. Reversible Dendrite-Free Potassium Plating and Stripping Electrochemistry for Potassium Secondary Batteries. *J. Am. Chem. Soc.* **2017**, 139, 9475−9478.

(707) Zhang, W.; Wu, Z.; Zhang, J.; Liu, G.; Yang, N.-H.; Liu, R.-S.; Pang, W. K.; Li, W.; Guo, Z. Unraveling the Effect of Salt Chemistry on Long-Durability High-Phosphorus-Concentration Anode for Potassium Ion Batteries. *Nano Energy* **2018**, 53, 967−974.

(708) Zhang, W.; Pang, W. K.; Sencadas, V.; Guo, Z. Understanding High-Energy-Density Sn_4P_3 Anodes for Potassium-Ion Batteries. *Joule* **2018**, 2, 1534−1547.

(709) Xie, J.; Li, X.; Lai, H.; Zhao, Z.; Li, J.; Zhang, W.; Xie, W.; Liu, Y.; Mai, W. A Robust Solid Electrolyte Interphase Layer Augments the Ion Storage Capacity of Bimetallic-Sulfide-Containing Potassium-Ion Batteries. *Angew. Chem., Int. Ed.* **2019**, 58, 14740−14747.

(710) Zhang, Q.; Mao, J.; Pang, W. K.; Zheng, T.; Sencadas, V.; Chen, Y.; Liu, Y.; Guo, Z. Boosting the Potassium Storage Performance of Alloy-Based Anode Materials via Electrolyte Salt Chemistry. *Adv. Energy Mater.* **2018**, 8, 1703288.

(711) Wang, H.; Wang, H.; Chen, S.; Zhang, B.; Yang, G.; Gao, P.; Liu, J.; Fan, X.; Huang, Y.; Lin, J.; et al. A Depth-Profiling Study on the Solid Electrolyte Interface: Bis(fluorosulfuryl)imide Anion toward Improved K^+ Storage. *ACS Appl. Energy Mater.* **2019**, 2, 7942−7951.

(712) Deng, L.; Zhang, Y.; Wang, R.; Feng, M.; Niu, X.; Tan, L.; Zhu, Y. Influence of KPF_6 and KFSI on the Performance of Anode Materials for Potassium-Ion Batteries: A Case Study of MoS_2. *ACS Appl. Mater. Interfaces* **2019**, 11, 22449−22456.

(713) Wang, H.; Yu, D.; Wang, X.; Niu, Z.; Chen, M.; Cheng, L.; Zhou, W.; Guo, L. Electrolyte Chemistry Enables Simultaneous Stabilization of Potassium Metal and Alloying Anode for Potassium-Ion Batteries. *Angew. Chem., Int. Ed.* **2019**, 58, 16451−16455.

(714) Liu, S.; Mao, J.; Zhang, Q.; Wang, Z.; Pang, W. K.; Zhang, L.; Du, A.; Sencadas, V.; Zhang, W.; Guo, Z. An Intrinsically Non-flammable Electrolyte for High-Performance Potassium Batteries. *Angew. Chem., Int. Ed.* **2020**, 59, 3638−3644.

(715) Nie, P.; Liu, M.; Qu, W.; Hou, M.; Chang, L.; Wu, Z.; Wang, H.; Jiang, J. Unravelling the Solvation Structure and Interfacial Mechanism of Fluorinated Localized High Concentration Electrolytes in K-ion Batteries. *Adv. Funct. Mater.* **2023**, 33, 2302235.

(716) Yang, H.; Chen, C. Y.; Hwang, J.; Kubota, K.; Matsumoto, K.; Hagiwara, R. Potassium Difluorophosphate as an Electrolyte Additive for Potassium-Ion Batteries. *ACS Appl. Mater. Interfaces* **2020**, 12, 36168−36176.

(717) Qin, L.; Xiao, N.; Zheng, J.; Lei, Y.; Zhai, D.; Wu, Y. Localized High-Concentration Electrolytes Boost Potassium Storage in High-Loading Graphite. *Adv. Energy Mater.* **2019**, 9, 1902618.

(718) Jiang, X.; Zhang, T.; Yang, L.; Li, G.; Lee, J. Y. A Fe/Mn-Based Prussian Blue Analogue as a K-Rich Cathode Material for Potassium-Ion Batteries. *ChemElectroChem* **2017**, 4, 2237−2242.

(719) Bie, X.; Kubota, K.; Hosaka, T.; Chihara, K.; Komaba, S. A Novel K-ion Battery: Hexacyanoferrate(ii)/Graphite Cell. *J. Mater. Chem. A* **2017**, 5, 4325−4330.

(720) Yuan, F.; Li, Z.; Zhang, D.; Wang, Q.; Wang, H.; Sun, H.; Yu, Q.; Wang, W.; Wang, B. Fundamental Understanding and Research

Progress on the Interfacial Behaviors for Potassium-Ion Battery Anode. *Adv. Sci.* **2022**, *9*, No. e2200683.

(721) Xu, C.; Li, B.; Du, H.; Kang, F. Energetic Zinc Ion Chemistry: The Rechargeable Zinc Ion Battery. *Angew. Chem., Int. Ed.* **2012**, *51*, 933−935.

(722) Yang, Y.; Liu, C.; Lv, Z.; Yang, H.; Zhang, Y.; Ye, M.; Chen, L.; Zhao, J.; Li, C. C. Synergistic Manipulation of Zn^{2+} Ion Flux and Desolvation Effect Enabled by Anodic Growth of a 3D ZnF_2 Matrix for Long-Lifespan and Dendrite-Free Zn Metal Anodes. *Adv. Mater.* **2021**, *33*, No. e2007388.

(723) Cao, L.; Li, D.; Pollard, T.; Deng, T.; Zhang, B.; Yang, C.; Chen, L.; Vatamanu, J.; Hu, E.; Hourwitz, M. J.; et al. Fluorinated Interphase Enables Reversible Aqueous Zinc Battery Chemistries. *Nat. Nanotechnol.* **2021**, *16*, 902−910.

(724) Li, D.; Cao, L.; Deng, T.; Liu, S.; Wang, C. Design of a Solid Electrolyte Interphase for Aqueous Zn Batteries. *Angew. Chem., Int. Ed.* **2021**, *60*, 13035−13041.

(725) Sun, W.; Wang, F.; Zhang, B.; Zhang, M.; Kupers, V.; Ji, X.; Theile, C.; Bieker, P.; Xu, K.; Wang, C.; et al. A Rechargeable Zinc-Air Battery Based on Zinc Peroxide Chemistry. *Science* **2021**, *371*, 46−51.

(726) Rubio, S.; Liang, Z.; Liu, X.; Lavela, P.; Tirado, J. L.; Stoyanova, R.; Zhecheva, E.; Liu, R.; Zuo, W.; Yang, Y.; et al. Reversible Multi-Electron Storage Enabled by $Na_5V(PO_4)_2F_2$ for Rechargeable Magnesium Batteries. *Energy Storage Mater.* **2021**, *38*, 462−472.

(727) Tang, X.; Zhou, D.; Zhang, B.; Wang, S.; Li, P.; Liu, H.; Guo, X.; Jaumaux, P.; Gao, X.; Fu, Y.; et al. A Universal Strategy towards High-Energy Aqueous Multivalent-Ion Batteries. *Nat. Commun.* **2021**, *12*, 2857.

(728) Zhao-Karger, Z.; Liu, R.; Dai, W.; Li, Z.; Diemant, T.; Vinayan, B. P.; Bonatto Minella, C.; Yu, X.; Manthiram, A.; Behm, R. J.; et al. Toward Highly Reversible Magnesium-Sulfur Batteries with Efficient and Practical $Mg[B(hfip)_4]_2$ Electrolyte. *ACS Energy Lett.* **2018**, *3*, 2005−2013.

(729) Sun, Y.; Zou, Q.; Wang, W.; Lu, Y.-C. Non-passivating Anion Adsorption Enables Reversible Magnesium Redox in Simple Non-nucleophilic Electrolytes. *ACS Energy Lett.* **2021**, *6*, 3607−3613.

(730) Hou, S.; Ji, X.; Gaskell, K.; Wang, P. F.; Wang, L.; Xu, J.; Sun, R.; Borodin, O.; Wang, C. Solvation Sheath Reorganization Enables Divalent Metal Batteries with Fast Interfacial Charge Transfer Kinetics. *Science* **2021**, *374*, 172−178.

(731) Li, Z.; Fuhr, O.; Fichtner, M.; Zhao-Karger, Z. Towards Stable and Efficient Electrolytes for Room-Temperature Rechargeable Calcium Batteries. *Energy Environ. Sci.* **2019**, *12*, 3496−3501.

(732) Song, H.; Su, J.; Wang, C. Hybrid Solid Electrolyte Interphases Enabled Ultralong Life Ca-Metal Batteries Working at Room Temperature. *Adv. Mater.* **2021**, *33*, No. e2006141.

(733) Kotobuki, M.; Lu, L.; Savilov, S. V.; Aldoshin, S. M. Poly(vinylidene fluoride)-Based Al Ion Conductive Solid Polymer Electrolyte for Al Battery. *J. Electrochem. Soc.* **2017**, *164*, A3868−A3875.

(734) Xu, Z. L.; Park, J.; Wang, J.; Moon, H.; Yoon, G.; Lim, J.; Ko, Y. J.; Cho, S. P.; Lee, S. Y.; Kang, K. A New High-Voltage Calcium Intercalation Host for Ultra-Stable and High-Power Calcium Rechargeable Batteries. *Nat. Commun.* **2021**, *12*, 3369.

(735) Fan, J.; Zhang, Z.; Liu, Y.; Wang, A.; Li, L.; Yuan, W. An Excellent Rechargeable $PP_{14}TFSI$ Ionic Liquid Dual-Ion Battery. *Chem. Commun.* **2017**, *53*, 6891−6894.

(736) Zhang, L.; Li, J.; Huang, Y.; Zhu, D.; Wang, H. Synergetic Effect of Ethyl Methyl Carbonate and Trimethyl Phosphate on BF_4^- Intercalation into a Graphite Electrode. *Langmuir* **2019**, *35*, 3972−3979.

(737) Özmen-Monkul, B.; Lerner, M. M. The First Graphite Intercalation Compounds Containing Tris(pentafluoroethyl)-trifluorophosphate. *Carbon* **2010**, *48*, 3205−3210.

(738) Xiang, L.; Ou, X.; Wang, X.; Zhou, Z.; Li, X.; Tang, Y. Highly Concentrated Electrolyte towards Enhanced Energy Density and Cycling Life of Dual-Ion Battery. *Angew. Chem., Int. Ed.* **2020**, *59*, 17924−17930.

(739) Wang, M.; Jiang, C.; Zhang, S.; Song, X.; Tang, Y.; Cheng, H. M. Reversible Calcium Alloying Enables a Practical Room-Temperature Rechargeable Calcium-Ion Battery with a High Discharge Voltage. *Nat. Chem.* **2018**, *10*, 667−672.

(740) Yu, D.; Zhu, Q.; Cheng, L.; Dong, S.; Zhang, X.; Wang, H.; Yang, N. Anion Solvation Regulation Enables Long Cycle Stability of Graphite Cathodes. *ACS Energy Lett.* **2021**, *6*, 949−958.

(741) Sun, Z.; Zhu, K.; Liu, P.; Chen, X.; Li, H.; Jiao, L. Fluorination Treatment of Conjugated Protonated Polyanilines for High-Performance Sodium Dual-Ion Batteries. *Angew. Chem., Int. Ed.* **2022**, *61*, No. e202211866.

(742) Read, J. A.; Cresce, A. V.; Ervin, M. H.; Xu, K. Dual-Graphite Chemistry Enabled by a High-Voltage Electrolyte. *Energy Environ. Sci.* **2014**, *7*, 617−620.

(743) Wang, Y.; Zhang, Y.; Wang, S.; Dong, S.; Dang, C.; Hu, W.; Yu, D. Y. W. Ultrafast Charging and Stable Cycling Dual-Ion Batteries Enabled via an Artificial Cathode-Electrolyte Interface. *Adv. Funct. Mater.* **2021**, *31*, 2102360.

(744) Wang, Y.; Zhang, Y.; Dong, S.; Zhou, W.; Lee, P. K.; Peng, Z.; Dang, C.; Sit, P. H. L.; Guo, J.; Yu, D. Y. W. An All-Fluorinated Electrolyte Toward High Voltage and Long Cycle Performance Dual-Ion Batteries. *Adv. Energy Mater.* **2022**, *12*, 2103360.

(745) Zhu, J.; Xu, Y.; Fu, Y.; Xiao, D.; Li, Y.; Liu, L.; Wang, Y.; Zhang, Q.; Li, J.; Yan, X. Hybrid Aqueous/Nonaqueous Water-in-Bisalt Electrolyte Enables Safe Dual Ion Batteries. *Small* **2020**, *16*, No. e1905838.

(746) Wrogemann, J. M.; Künne, S.; Heckmann, A.; Rodríguez-Pérez, I. A.; Siozios, V.; Yan, B.; Li, J.; Winter, M.; Beltrop, K.; Placke, T. Development of Safe and Sustainable Dual-Ion Batteries Through Hybrid Aqueous/Nonaqueous Electrolytes. *Adv. Energy Mater.* **2020**, *10*, 1902709.

(747) Rodríguez-Pérez, I. A.; Zhang, L.; Wrogemann, J. M.; Driscoll, D. M.; Sushko, M. L.; Han, K. S.; Fulton, J. L.; Engelhard, M. H.; Balasubramanian, M.; Viswanathan, V. V.; et al. Enabling Natural Graphite in High-Voltage Aqueous Graphite ‖ Zn Metal Dual-Ion Batteries. *Adv. Energy Mater.* **2020**, *10*, 2001256.

(748) Zhang, Z.; Hu, X.; Zhou, Y.; Wang, S.; Yao, L.; Pan, H.; Su, C.-Y.; Chen, F.; Hou, X. Aqueous Rechargeable Dual-Ion Battery Based on Fluoride Ion and Sodium Ion Electrochemistry. *J. Mater. Chem. A* **2018**, *6*, 8244−8250.

(749) Yang, C.; Chen, J.; Ji, X.; Pollard, T. P.; Lu, X.; Sun, C. J.; Hou, S.; Liu, Q.; Liu, C.; Qing, T.; et al. Aqueous Li-Ion Battery Enabled by Halogen Conversion-Intercalation Chemistry in Graphite. *Nature* **2019**, *569*, 245−250.

(750) Wang, H.; Sun, Y.; Li, M.; Li, G.; Xue, K.; Chen, Z.; Yu, D. Y. W. Engineering Solvation Complex-Membrane Interaction to Suppress Cation Crossover in 3 V Cu-Al Battery. *Small* **2020**, *16*, No. e2003438.

(751) Yu, M.; Sui, Y.; Sandstrom, S. K.; Wu, C. Y.; Yang, H.; Stickle, W.; Luo, W.; Ji, X. Reversible Copper Cathode for Nonaqueous Dual-Ion Batteries. *Angew. Chem., Int. Ed.* **2022**, *61*, No. e202212191.